UNIVERSITÄT BONN

Evolution of Very Massive Binary Systems

Masterarbeit in Astrophysik

von Daniel Pauli

angefertigt im Argelander-Institut für Astronomie

vorgelegt der
Mathematisch-Naturwissenschaftlichen Fakultät
der
Rheinischen Friedrich-Wilhelms-Universität Bonn

September 17, 2020

I hereby declare that the work presented here was formulated by myself and that no sources or tools other than those cited were used.

Bonn, _____ _____

Date Signature

1. Gutachter: Prof. Dr. Norbert Langer
2. Gutachter: Prof. Dr. Peter Schneider

acknowledgments

The research included in this thesis could not have been performed if not for the assistance, patience and support of many individuals. First of all I want to wholeheartedly thank Prof. Dr. Nobert Langer for his inexhaustible patience and kindness with which he helped me to carry out my work and to grow as a person in the last year. I also want to thank him for all his good advices and ideas which advanced my scientific work in many good ways. I also want to thank Chen Wang who helped me out when I was lost and came up with new ideas that helped me to make progress in my research. Additionally, I would like to thank David Aguilera-Dena for his helpfulness nature, his tips and all the time he invested to help me. I would also like to thank all the other lovely people of the Institute who had a lot of ideas and helped to improve my results.

Abstract

It is well known that the population of Wolf-Rayet (WR) stars cannot be explained by single star evolution alone. Especially in low metallicity environments, it is suspected that a large fraction of the WR stars is formed in binary systems. However, the binary formation channel is so far not well explored. Here, we want to remedy this by using large grids of binary evolution models, as well as single star evolution models, in order to build a synthetic WR population that can be compared to the presumably complete sample of WR stars observed in the Large Magellanic Cloud.

In this thesis, we use the publicly available MESA code to compute large grids of detailed evolutionary binary models. For those models which enter a common envelope evolution, we apply a simple energy criterion to to investigate which of them may avoid merging and contribute short-period WR binaries. The majority of the remaining models are calculated through Roche-lobe overflow and mass transfer, and through the WR+OB star phase.

We find that only a small fraction of binary systems with an initial primary mass near $10\,M_{\odot}$ are expected to survive a common envelope evolution without merging. Their contribution to the observed WR population is therefore neglected. The systems which undergo stable mass transfer, on the other hand, are shown to produce WR+OB star binaries within a large range of orbital periods. We build a synthetic WR population based on these binary models, augmented with WR stars produced by single star models, which reproduces the WR population of the Large Magellanic Cloud to significant detail. However, our models overpredict the number of long-period WR binaries, arguably due to an observational bias towards short periods. Our models also underpredict the shortest-period WR binaries. This might indicate a lack of understanding of the common envelope evolution, with potential implications for the progenitors of double black hole mergers.

Contents

1 Introduction

After the big bang, the universe consisted of hydrogen and helium. The early universe lacked heavier elements, which are called metals in astronomy. The first stars that were formed are metal-free. The heaviest elements, like carbon, oxygen, and nitrogen as well as iron, are formed inside the cores of massive stars. Nowadays, one observes that the interstellar medium, which is material located between the stars, contains fractions of these heavy elements. In the late phases of a massive star, it is expected to have an iron core and shells with heavier elements on top. It can be interpreted as an onion-like structure with the lightest elements on top and the heaviest elements in the core. If a star explodes as a supernova the core collapses and the remaining material is transferred into the interstellar medium and alters the chemical composition. Furthermore, massive stars develop strong stellar winds which lead to strong mass-loss rates. These mass-loss rates also contribute to the enrichment of the interstellar medium. Therefore, massive stars play a crucial role in the formation of the universe.

Some properties of stars are metallicity dependent, as the mass-loss rates. The mass-loss rates increase with increasing metallicity. If the mass-loss rates get strong enough a star might be able to strip of its hydrogen-rich envelope and to become a helium star. If this helium star has an optically thick wind, it can be observed as a Wolf-Rayet star. These stars have winds that are much stronger than the winds of core hydrogen burning stars and therefore have a larger impact on the enrichment of the interstellar medium. The Small Magellanic Cloud (SMC) and the Large Magellanic Cloud (LMC) are dwarf galaxies that orbit our galaxy. Both have different metallicities, the SMC has $\sim 1/7$ and the LMC $\sim 1/3$ of the solar metallicity. From observations, it is known that the total number of Wolf-Rayet stars decreases with decreasing metallicity. As Wolf-Rayet stars are expected to dominate the feedback processes into the interstellar medium, it is of major interest to test if the theoretical models are capable to reproduce the observed populations.

By only taking single stellar models into account it gets clear that these models alone can not explain the observed Wolf-Rayet populations. From observations, it is known that about half of the stars that are formed will be in a binary system. The evolution of a star in a binary system differs from the single star scenario as both stars are able to interact during their evolution. For example, if one of the stars expands, at some point mass will be transferred from the expanding star on the other one. During this mass transfer phase, it is possible that the hydrogen-rich envelope of the donor star will be removed. This leads to an additional formation channel of Wolf-Rayet stars. Moreover, it is possible if the mass transfer is unstable, that both stars orbit inside a common envelope. This is followed by a spiral-in process where the orbital energy is deposited inside the envelope. If the common envelope cannot be ejected both stars merge. However, if the common envelope can be ejected the binary system is expected to consist of a helium star and its companion with a tight orbit. Therefore, it is im-

portant to understand the outcomes of the common envelope evolution of massive post main-sequence stars with a main-sequence companion in order to understand how this channel contributes to the Wolf-Rayet population. As one can see there are many possibilities of how a Wolf-Rayet can be formed. However, the impact of the different formation channels is rather unknown and needs to be studied in more detail.

To tackle these questions concerning the outcomes of a common envelope evolution of a post main-sequence star and a main sequence companion as well as the different formation channels of Wolf-Rayet in the LMC large grids of detailed binary models, including single star models, are used in this thesis. In the later analysis, the used single star and binary physics are explained in more detail so that the reader will get familiar with the most important mechanisms during the evolution of a single star as well as of a star in a binary system. In this thesis binary models at SMC and LMC metallicity are used to study the outcomes of a common envelope evolution of a post main-sequence star with a main-sequence companion in order to determine if these systems are able to produce Wolf-Rayet stars or not. Furthermore, it will be studied, how the binding and orbital energy changes during a mass transfer phase and if this can lead to more successful common envelope ejections. Regarding the Wolf-Rayet population of the LMC, a new grid of binary models with more accurate mass-loss rates for the Wolf-Rayet phase is calculated. These binary models will be used for a population synthesis to check if the models are capable to explain the observed luminosity distribution of the Wolf-Rayet stars in the LMC.

2 Theoretical Background

The basic concepts that go into a physical description of single stars are covered in Section 2.1. Section 2.2 contains a description of the most important properties of a binary system. A detailed description of the concept of a common envelope phase, a phase where two stars orbit inside a shared envelope, is given in Section 2.3.

2.1 Single Stars

In the current section, the basic physical principles of the structure and evolution of single stars will be described. For a more detailed overview, see Pols (2009). The first question that should be answered, is how to define a star. A simple way to define a star is to say it is a spherical body out of gas which is bound gravitationally by itself. Furthermore, a star produces energy via complex fusion processes in its center which is then radiated away from the surface of the star. When a molecular cloud is gravitationally disturbed and collapses several stars can be formed. The gas collapses until the internal pressure stabilizes the object and a star is formed. The star contains all the elements of the molecular cloud, mostly hydrogen and helium. Fusion processes in the interior of the star can take place once the temperature is large enough. At first, the hydrogen in the core of the star is burned, which takes about 90% of its total lifetime. However, as the amount of the available hydrogen is finite, an end of core hydrogen burning will be reached. If the core temperature is high enough advanced fusion processes will take place. The collapse of the molecular cloud is a short-lived phase while core hydrogen burning takes place for a long time. This implies the following two things: First, the timescales during the evolution of a star can be totally different and therefore have to be discussed in more detail. Second, the structure of the star evolves with time. For example, most of the hydrogen is turned into helium, which alters the chemical composition in the cores of stars.

2.1.1 Timescales of Stellar Evolution

In the evolutionary phases of a star, there are three different timescales that determine the duration. The main goal of a star is to achieve stability or equilibrium. The timescales that describe the duration of a certain phase are therefore a measure of how long it takes to reach a certain state of equilibrium. In order to discuss this in a simple way, it is assumed that a star is spherically symmetric, meaning that all physical quantities only depend on the radius or mass coordinate. Equilibrium is given if the total change in energy is constant for example when the force of the internal pressure cancels out the gravitational force throughout the whole star.

Hydrostatic Equilibrium

If a star has no internal energy source one can assume that there are only the gravitational force and a pressure gradient present throughout the star. If both balance each other in such a way that there is no acceleration in the stellar interior and therefore no expansion or contraction can be observed, the star is in hydrostatic or mechanical equilibrium.

Dynamical Timescale

If a star is not in hydrostatic equilibrium it will expand or contract until the state of equilibrium will be maintained. The time a star needs to get back into hydrostatic equilibrium is called the dynamic timescale which is given by the following formula

$$\tau_{\text{dyn}} = \sqrt{\frac{R^3}{GM}} \tag{2.1}$$

in which R represents the radius and M is the mass of the star, G represents the gravitational constant. A typical value for the dynamical timescale of a sun-like star is in the order of 30 minutes which is short compared to the total lifetime of a star. Therefore, one can assume that almost all stars are in hydrostatic equilibrium. If a star is unable to retain hydrostatic equilibrium it is expected to collapse or explode.

Thermal Equilibrium

Nuclear fusion processes in the interior of the star serve as internal energy sources. Their energy will be radiated away at the surface of the star, keeping the total energy constant. This implies that it is impossible for the star to contract and cool while holding the total energy constant. Therefore stars with internal energy sources that keep the total energy constant are in thermal equilibrium.

Thermal Timescale

As the dynamical timescale is a measurement of the duration of a star to retain hydrostatic equilibrium after a perturbation, the thermal timescale covers the time it takes a star to get into thermal equilibrium. If the nuclear source in the interior of a star is absent the star will get its energy from gravitational contraction until it is able to retain thermal equilibrium again. The thermal timescale can be expressed as

$$\tau_{\text{th}} = \frac{E_{\text{int}}}{L} = \frac{GM^2}{2RL} \tag{2.2}$$

and only depends on the mass M, the radius R, and the luminosity L of the star. A typical estimate for the thermal timescale of a star like our sun is in the order of 10 million years. This is much larger than the dynamical timescale $\tau_{\text{th}} \gg \tau_{\text{dyn}}$.

As a star will produce its energy most of the time via nuclear fusion, it is common to assume that a large fraction of the stars is in thermal equilibrium. This brings us to the next and last timescale, the nuclear timescale.

Nuclear Timescale

As already mentioned above, as long as a star is able to get its energy from nuclear fusion processes it remains in thermal equilibrium. Therefore, it is reasonable to ask how long a star can maintain in thermal equilibrium. The answer is given by the nuclear timescale which can be expressed as

$$\tau_{\mathrm{nuc}} = \frac{E_{\mathrm{nuc}}}{L} = \Phi f_{\mathrm{nuc}} \frac{Mc^2}{L} \tag{2.3}$$

where Φ is the fraction of rest mass released by the fusion process that is converted to energy and f_{nuc} is the fraction of the total mass of the star that can be used for nuclear fusion processes. A typical value for a hydrogen burning sun-like star is in the order of 10 billion years. For more advanced burning stages this time reduces drastically by a factor of 10 or more. However, the nuclear timescale is still larger than the thermal timescale $\tau_{\mathrm{nuc}} \gg \tau_{\mathrm{th}}$.

2.1.2 Stellar Structure

The changes in the stellar structure of a star, like an expansion or contraction, are caused by changes in the density profile, opacities, or chemical composition. These changes can originate from energy transport mechanisms present in the different regions of a star as well as mixing processes. To get familiar with the evolution of the stellar structure and therefore the star itself it is important to understand how these processes change the stellar structure. These ideas will be discussed in this section.

Energy Transport

In the previous section, it was already mentioned that the produced energy in the core has to be radiated away at the surface of the star in order to be in thermal equilibrium. Therefore, it is important to understand which processes can transport energy in a star. There are mainly two energy transport mechanisms present in stars, radiative and convective energy transport.

The used description of radiative energy transport is based on the assumption that a photon travels only a certain distance before interacting with its surrounding. This distance is called mean free path. If the mean free path is much smaller than the radius of the star, which is true for most of the radiation, the photons get scattered and do a 'random walk' and slowly diffuse outwards.

The second kind of energy transport is convection. If the temperature gradient of the gas is not large enough to support energy transport via radiation, the mean free path

for the photons gets smaller than the mean free path of the gas-particle, which leads to instabilities in the gas. These instabilities can be understood as bubbles of gas that are heated and rise up, cool, and fall back down again. This phenomenon is known as convection and similarly occurs when boiling water in a pot.

Following the descriptions of convective and radiative energy transport, it gets evident that these two mechanisms are strongly dependent on the temperature gradient and therefore on the distance a photon can travel before interacting with the surroundings.

Opacity

To determine which energy transport mechanism is present in each region of the star one uses the opacity κ. This can be understood as a measure of how large a temperature gradient must be to carry a given luminosity by radiation. There are different sources that contribute to the opacity: Electron scattering, free-free, bound-free, and bound-bound absorption. Talking about all of them in detail extends beyond the reasonable bounds of this thesis. Still, it is worth mentioning that the different opacities depend on the chemical composition, density, and temperature. Or simply spoken, the opacity throughout a star is not constant.

Eddington Luminosity

As there are regions in the star where energy can be transported via radiation, the pressure term contains an additional term of the radiation itself which acts as an outward force. As the stellar surface is always radiative, one can think of an upper limit for the luminosity that is needed to gravitationally unbind the star. This limit is called the Eddington limit or Eddington luminosity

$$L_{\mathrm{Edd}} = \frac{4\pi c G M}{\kappa} \tag{2.4}$$

and it depends on the opacity κ at the surface and the mass M of the star. Because of the mass-luminosity relation for main-sequence stars, an upper limit for the luminosity implies that there must be an upper limit for the initial mass. Nevertheless, observations show that there are more massive stars than the limit would allow which alludes to the next section.

Inflation

The Eddington limit as it is defined in Equation 2.4 is only valid for the stellar surface, yet it is possible to rewrite this as a local limit within the star. The opacity is not constant throughout the star, implying that it is possible that the local Eddington limit is reached before reaching the Eddington limit at the surface of the star. If this happens the gravitational force that stabilizes the star will be overcome by the internal pressure.

For a star to be stable there must be an additional term in form of an extra pressure gradient acting inwards. This is understood as a density inversion, a region inside the star where the density increases instead of decreases, so that hydrostatic equilibrium can be maintained. Further, as the opacity in these regions is very high the diffusive process of radiative energy transport gets very inefficient and the energy gets transported by convection. Still, the stability of this is not very well understood as small perturbations would lead to instabilities and maybe to pulsations or ejection of the inflated regions of the stars (Sanyal et al. 2015).

Convective Overshooting

nside a convective region, the material is moved, which is a very efficient way to transport energy. At the boundary of a convective region where it transitions into a radiative region this transport of material may lead to some complications, as it is possible that some bubbles of material shoot out of the convective region into the radiative one. This process is called convective overshooting. Of course, these overshooting bubbles are slowed down as the acceleration changes sign in the radiative region. The importance of overshooting should not be underestimated: For example, massive stars have a convective core and a radiative envelope. If the core is overshooting material into the radiative envelope, the matter of the envelope gets mixed into the core which feeds the core with additional hydrogen and leads to longer burning phases. This example illustrates how mixing processes influence the evolution of stars and therefore, the next part will focus on the different kinds of mixing processes.

Mixing Processes

Another aspect of convection, besides the efficient energy transport it induces, is mixing. As the material is moved in a convective region there is also a mixing process going on which is very efficient and acts on a dynamical timescale leading to a homogeneous chemical composition in the convective region.

If a region is stable against convection, it still can have some mixing processes. For example, a displaced blob of material can exchange heat with its surrounding. This mixing process is called semiconvection. This process takes place on timescales shorter than the thermal timescale but much longer than the dynamical timescale and is, therefore, less efficient than convective mixing. However, this process can still have a strong impact on the late phases of the main sequence for massive stars and on core helium burning phases (Heger et al. 2000).

Another mixing process that is mainly important for stars in binary systems is thermohaline mixing. This process occurs as well as semiconvection in regions that are stable against convection. However, these regions additionally need an increasing molecular weight meaning that the heavier elements are located on top of lighter elements. As in most single stars, the heavy elements are in the core thermohaline mixing is less

important for them. However, in a binary system mass gets transferred from one star to the other, which may lead to the formation of an increasing molecular weight. It is important to mention that the constraints on the efficiency of thermohaline mixing and semiconvection are highly uncertain (Heger et al. 2000).

The last mixing process that needs to be mentioned it rotational mixing. For a fast rotating star, the centrifugal force is of major importance and leads to an additional mixing process. If the rotation rate of a star is fast enough, the entire star can be mixed so that all hydrogen can be burned. This is called chemical homogeneous evolution (Heger et al. 2000). As well as the previously mentioned mixing processes rotational mixing also occurs in radiative regions of a star. This process becomes more important for massive stars with radiative envelopes as well as for stars in binary systems that are tidally locked and are able to maintain their initial high rotation rate.

2.1.3 Evolution of Massive Stars

To discuss the evolution of stars, the so-called Hertzsprung-Russell Diagram (HRD) in which the luminosity of a star is plotted against the effective temperature is used. Observationally these two values correspond to the absolute magnitude and color of a star. Historically stars are classified by their color and characteristics in their spectra into different types: O, B, A, F, G, K, and M type stars. O and B type stars, sometimes also called OB stars, have the highest effective temperature and are the most massive stars.

The radius of a star can also be inferred from the HRD as the luminosity and the effective temperature of a black body are linked via the Stefan-Boltzmann law

$$L = 4\pi\sigma R^2 T_{\mathrm{eff}}^4 \tag{2.5}$$

As this thesis focuses on very massive stars in binary systems this section only covers the evolutionary phases for single stars with masses above $10\,M_\odot$ in some detail. Furthermore, as only stars with low metallicity will be discussed in this work the evolutionary tracks for stars of different mass at LMC metallicity are shown in Figure 2.1.

A star goes through many different phases during its evolution. After the collapse of the molecular cloud and the formation of the star, it is able to start hydrogen burning, given that its core is dense and hot enough. The star is now located on the zero-age main-sequence (ZAMS) which is labeled as point 1 in Figure 2.1. A star spends about 90% of its lifetime with core hydrogen burning and can be found on the main sequence where it fuses hydrogen to helium. However, as the amount of hydrogen that can be burned is finite, core hydrogen burning will come to an end leaving a helium core in the center of the star. This is associated to point 2, the terminal age main sequence (TAMS). This is followed by a short contraction phase, which causes a rise in core temperature until the star can start shell hydrogen burning on top of the helium core,

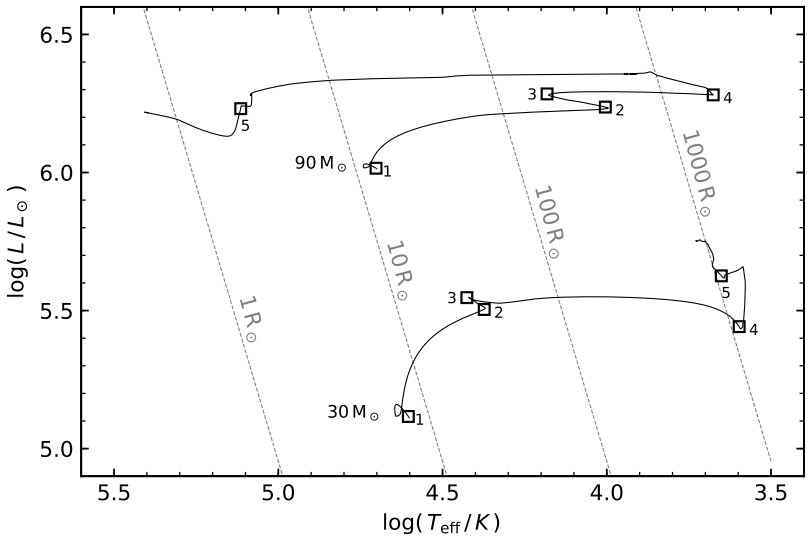

Figure 2.1: Stellar evolutionary tracks of a $30\,M_\odot$ and $90\,M_\odot$ star with overshooting and mass-loss at LMC metallicity as solid lines. The models, which are calculated in the later analysis, are shown until carbon depletion. The squares mark the most characteristic evolutionary phases of the stars.

labeled as point 3. Shell hydrogen burning feeds the helium core with more nuclear supplies and raises the core temperature. Additionally, the stellar surface cools as the envelope expands. If a central temperature of about 10^8 K is reached the helium core can be ignited, see point 4. After core helium burning more advanced burning stages, like carbon burning labeled as point 5, take place until the iron core gets unstable and collapses, leading to a supernova explosion.

Even though the evolutionary phases of the core are the same for massive stars, their evolutionary tracks differ a lot as it can be seen by comparing both tracks in Figure 2.1. One might argue that this is caused by the different mixing processes which are more or less efficient in each star. Although these effects might contribute, there is a much stronger effect coming from stellar winds. Particles near the surface of the star can be accelerated and be gravitationally unbound so that the star loses mass. This is called a stellar wind. Depending on the mechanism that drives the wind this can be very efficient and a star can lose several solar masses already at the main-sequence. In order to understand the influence of stellar winds on the evolutionary phases, a brief summary of the most important wind schemes will be given in the next section.

Stellar Winds and mass-loss

All stars have winds which become important during the different evolutionary phases

of their life. Massive stars can have such strong winds that will remove several solar masses of the envelope even when they are still core hydrogen burning.

Hot and luminous stars like O and B stars can drive their wind by radiation. In this case, the radiation gets absorbed by outflowing atoms which are accelerated. In combination with the effect of Doppler broadening of the spectral lines this forms an efficient way to drive the wind of a star. However, as mainly the heavy elements absorb these photons, this effect is metallicity dependent. In this work the wind recipe for O and B type stars from Vink et al. (2001) is used.

In the temperature range of $27\,500\,\mathrm{K} \leq T_{\mathrm{eff}} \leq 50\,000\,\mathrm{K}$ one uses the equation

$$\begin{aligned}\log \frac{\dot{M}}{M_\odot\,\mathrm{yr}^{-1}} = \; & -6.697 + 2.194 \log \frac{L}{10^5\,L_\odot} - 1.313 \log \frac{M}{30\,M_\odot} - 1.226 \log \frac{v_\infty / v_{\mathrm{esc}}}{2.0} \\ & + 0.933 \log \frac{T_{\mathrm{eff}}}{40\,000\,\mathrm{K}} - 10.92 \left[\log \frac{T_{\mathrm{eff}}}{40\,000\,\mathrm{K}}\right]^2 + 0.85 \log \frac{Z}{Z_\odot} \end{aligned} \tag{2.6}$$

which contains the luminosity L, the mass M, the effective temperature T_{eff}, the terminal wind velocity v_∞ and the escape velocity v_{esc} of the star, as well as the initial metallicity Z.

For the temperature range that spans over $12\,500\,\mathrm{K} \leq T_{\mathrm{eff}} 22\,500\,\mathrm{K}$ the mass-loss rate is given by

$$\begin{aligned}\log \frac{\dot{M}}{M_\odot\,\mathrm{yr}^{-1}} = \; & -6.688 + 2.210 \log \frac{L}{10^5\,L_\odot} - 1.339 \log \frac{M}{30\,M_\odot} - 1.601 \log \frac{v_\infty / v_{\mathrm{esc}}}{2.0} \\ & + 1.07 \log \frac{T_{\mathrm{eff}}}{40\,000\,\mathrm{K}} + 0.85 \log \frac{Z}{Z_\odot} \end{aligned} \tag{2.7}$$

with the same meaning of the symbols as in the equation before.

For the next evolutionary phase, the red super gaint (RSG) phase, the winds are driven by a combination of two effects, stellar pulsations and radiation pressure on dust particles in the outermost regions of the star. For the RSG winds the prescription of Nieuwenhuijzen & de Jager (1990) is used in case it is larger than the mass-loss rate from Vink et al. (2001)

$$\begin{aligned}\log \frac{\dot{M}}{M_\odot\,\mathrm{yr}^{-1}} = \; & -14.02 + 1.24 \log \frac{L}{L_\odot} + 0.16 \log \frac{M}{M_\odot} - 1.61 \log \frac{T_{\mathrm{eff}}}{40\,000\,\mathrm{K}} \\ & + 0.81 \log \frac{R}{R_\odot} + 0.85 \log \frac{Z}{Z_\odot} \end{aligned} \tag{2.8}$$

Again the symbols have the same meaning as above, but additionally for the RSG the mass-loss rate depends on the radius R of the star.

If a star can lose all or most of its hydrogen-rich envelope, for example in a RSG phase or due to binary interaction, only its helium core will be left. Helium burning takes

place at higher temperatures and removing the hydrogen-rich envelope gives the possibility to look at the bare helium core. Therefore, it is possible to see an evolution towards hotter temperatures as it can be seen for the $90\,M_\odot$ star in Figure 2.1. Massive helium stars with optically thick winds are called Wolf-Rayet stars. In optically thick winds all short wavelengths will be absorbed by the wind material and their recombination leads to an emission feature in the observed spectrum, corresponding to the elements present in this wind. A cascading process sets in as photons can be absorbed and re-emitted several times, leading to high mass-loss rates. However, there are large uncertainties in these estimations as it is unclear how strong the winds are clumped. In this thesis, two different mass-loss recipes are used for the Wolf-Rayet mass-loss rates which are compared in the later analysis.

The first recipe that is used are the mass-loss rates by Hamann (1995)

$$\log \frac{\dot{M}}{M_\odot\,\mathrm{yr}^{-1}} = -11.95 + 1.5\log\frac{L}{L_\odot} - 2.85X_\mathrm{s} + 0.85\log\frac{Z}{Z_\odot} + \log\frac{1}{D} \tag{2.9}$$

In this equation X_s is the hydrogen mass fraction at the surface of the star and D as the clumping factor. L is the luminosity of the star and Z the initial metallicity.

The second mass-loss recipe that is used in this work is from Yoon (2017) where the mass-loss rates are assigned according to the Wolf-Rayet phases, which will be explained in the next section. For the hydrogen-free WN phase in which the helium surface mass fraction is $Y_\mathrm{s} = 1 - Z$ the authors use the mass-loss rate from Hamann et al. (2006)

$$\log \frac{\dot{M}}{M_\odot\,\mathrm{yr}^{-1}} = -11.32 + 1.18\log\frac{L}{L_\odot} + 0.60\log\frac{Z}{Z_\odot} + 0.5\log\frac{10}{D} \tag{2.10}$$

For the later WC phase in which the helium surface composition is $Y_\mathrm{s} < 0.9$ the following formula of Tramper et al. (2016) is used

$$\log \frac{\dot{M}}{M_\odot\,\mathrm{yr}^{-1}} = -9.20.32 + 0.85\log\frac{L}{L_\odot} + 0.44\log Y_\mathrm{s} + 0.25\log\frac{Z}{Z_\odot} + 0.5\log\frac{10}{D} \tag{2.11}$$

In both equations the symbols have the same meaning as in the equations above. As these two equations are only valid in a specific range, an interpolation in the transition phase has to be performed.

For the hydrogen-rich WN phase this work uses the mass-loss rates of Nugis & Lamers (2000)

$$\log \frac{\dot{M}}{M_\odot\,\mathrm{yr}^{-1}} = -11.0 + 1.29\log\frac{L}{L_\odot} + 1.5\log Y_\mathrm{s} + 0.5\log\frac{Z}{Z_\odot} + 0.5\log\frac{10}{D} \tag{2.12}$$

Before moving on to the next section it is important to keep in mind that the mass-loss rates of massive stars are not fully understood yet and therefore there are high uncertainties, which will also be discussed in the later analysis.

2.1.4 Wolf Rayet Stars

As already mentioned above Wolf-Rayet stars (WR) are helium stars that have stripped off most or all of their hydrogen-rich envelope and have optically thick winds with emission features. Therefore, it is possible to measure their carbon, nitrogen, and oxygen (CNO) abundances and to divide them into different categories as the CNO abundance change during their evolution. One, therefore, distinguishes between WN, with the subclasses WNL and WNE, WC, and WO stars.

WNL stars show emission features of nitrogen and have some hydrogen left on their surface. Moreover, their helium and nitrogen abundances are increased which can be explained by the CNO cycle. WNE stars show the same feature as WNL stars but they lack hydrogen.

During helium burning most of the nitrogen is consumed and therefore the next stage is a WC star, with enhanced helium, carbon, and oxygen on its surface but no nitrogen. WO stars have even stronger oxygen emission lines corresponding to the depletion of helium and the products of carbon burning.

2.2 Binary Stars

As the last section consisted of a detailed explanation of the single stellar evolution it is now important to understand the physical properties of binary systems, which will be used in the later analysis. A binary system in astrophysics consists of a doublet of stars which usually have an unequal mass ratio. Moreover, the evolution of these two stars may differ from the single star scenario as they can interact with each other during their lifetime.

2.2.1 Roche Lobe

In a binary system, two stars orbit each other as they are attracted gravitationally by each other. In order to study how this influences the evolution of a star one needs to understand how the total potential influences the structure of the stars in terms of stability. To derive the total potential one might assume that both stars are point masses and that only the gravitational as well as the centrifugal potential contribute to the total potential of the system (Kopal 1955). Following these assumptions the total potential of the binary system can be expressed as

$$\Phi = -\frac{GM_1}{r_1} - \frac{GM_2}{r_2} - \frac{\omega^2 r^2}{2} \tag{2.13}$$

where G is the gravitational constant, M_1 and M_2 are the masses of each binary component, r_1 and r_2 are the distances to the center of mass, ω is the orbital angular velocity

and r is the distance to the rotational axis of the system. According to the aforementioned assumptions, the orbital angular velocity can be described by the Keplerian angular velocity $\omega = \sqrt{GM/a^3}$, where $M = M_1 + M_2$ is the total mass and a is the separation of the system.

A close system is defined as a system bound tight enough to interact through mass transfer. The most important mechanism for this is Roche lobe overflow (Paxton et al. 2015). In these systems, it can be assumed that the orbit gets circular due to tidal interaction and synchronized co-rotation of the stars. Following this assumption, it is possible to define equipotential surfaces in a co-moving frame. In Figure 2.2 an illustration of these surfaces is given which showcase crossing points, the Lagrangian points. The first Lagrangian point L_1 lies at the intersection of the innermost equipotential surface between the two stars. This surface around each star marks the so-called Roche lobe, which is pear-shaped. This process is mostly modeled in 1D so that the limiting Roche lobe radius R_{RL} is defined as that of a sphere with the same volume as the lobe (Tauris & van den Heuvel 2006). As a consequence of this, the radius can be approximated following the prescription of Eggleton (1983) to

$$R_{RL} = \frac{0.49\,q^{2/3}}{0.6\,q^{2/3} + \log(1 + q^{1/3})} \cdot a \tag{2.14}$$

and depends on the mass ratio q of both stars and the orbital separation a. This approximation is accurate more than 1% over the whole parameter space of $0 < q < \infty$.

If a star grows enough in size, its radius approaches the Roche lobe radius. The matter that was bound to the star but now exceeds the lobe is in an unstable situation so that mass transfer from the filling star to the companion is initiated. The mass of the first star is transferred through the first Lagrangian point. This phenomenon is called Roche lobe overflow (RLOF). In a binary system one can distinguish between three types of systems detached, semi-detached, and over-contact as the illustration in Figure 2.3 shows. If none of the stars fill their Roche lobe, the system is called detached. If one star overflows its Roche lobe and transfers mass to the companion, the system is semi-detached and if both stars overflow their Roche lobes, the system is called over-contact binary (Marchant 2016).

2.2.2 Case A, B and C

In the beginning, stars in a binary system evolve in the same way as single stars do. However, at some point, the more massive star will fill its Roche lobe, either because its radius grows or because the orbital separation shrinks sufficiently for mass transfer to start. Therefore, the evolution of each stellar component as well as the evolution of the binary system depends on the structural evolution of the donor star. As soon as the donor overfills its Roche lobe the stellar structure of both stars changes. During

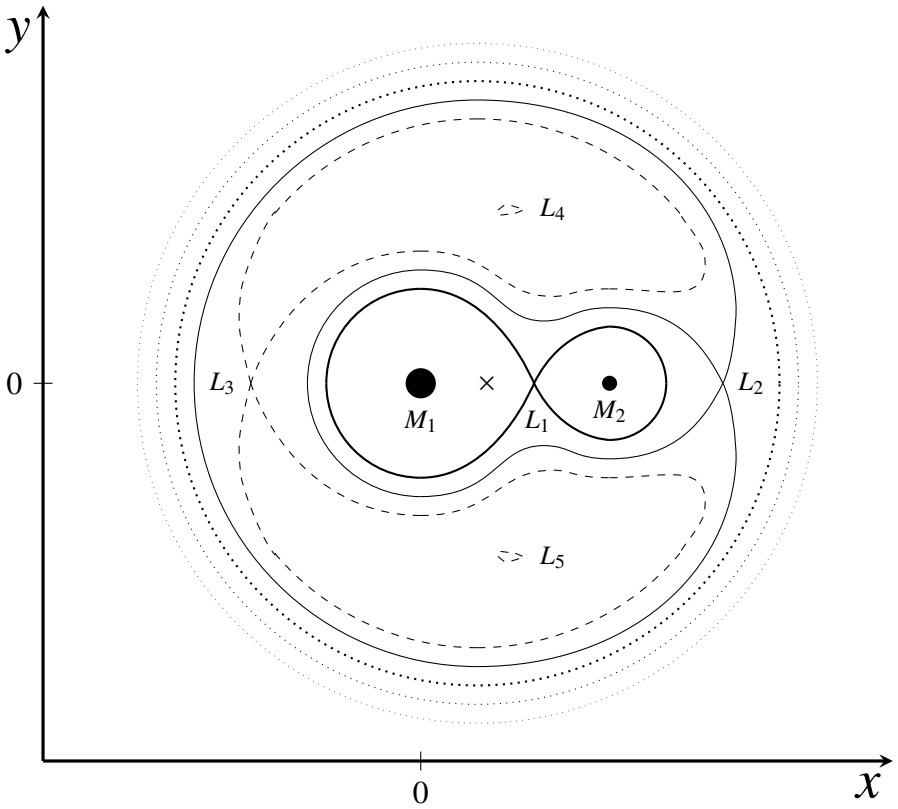

Figure 2.2: Sketch of the equipotential surfaces as a cross-section in the equatorial plane is shown as a contour plot. M_1 and M_2 mark the different binary components with their respective mass, $\times$ denotes the center of mass and the characteristic Lagrangian points are labeled as L_1, L_2, L_3, L_4 and L_5. The principles the sketch draws upon are the same as in Tauris & van den Heuvel (2006).

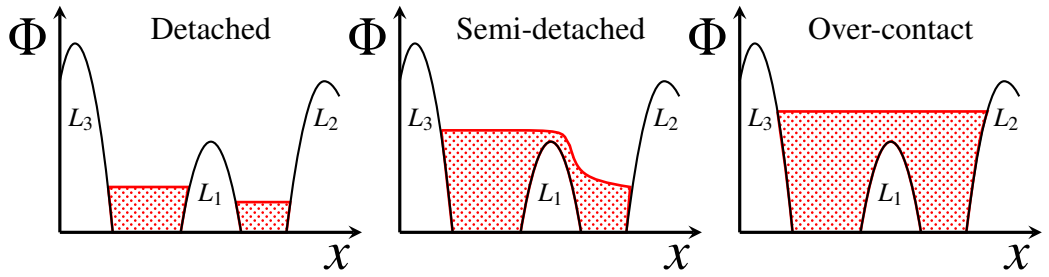

Figure 2.3: Sketch of the Roche potential Φ as a function of position through the axis x. The extends of both binary components in the potential Φ are depicted in red. Shown are the three distinct phases of detachment, semi-detachment and over-contact. L_1, L_2 and L_3 indicate the Lagranigan points which are contained in this plane, for comparison see Figure 2.2. The principles the sketch draws upon are the same as in Marchant (2016).

the mass transfer phase the binary parameters as the binary separation change as well which will be shown later on.

Kippenhahn & Weigert (1967) were the first to do a detailed analysis of interacting binaries and their evolution and made a case comparison resulting in the so-called case A and B scenarios. Later on, these scenarios have been extended by case C.

- **Case A:** The system is close enough to allow the more massive donor star to fill its Roche lobe. This initializes a first rapid mass transfer on the thermal timescale, the so-called fast case A, resulting in a semi-detached phase. If the mass ratio inverts, and the system is still semi-detached mass is transferred from the now less massive donor to the more massive companion on a nuclear timescale, the so-called slow case A.

- **Case B:** After hydrogen depletion in the core, the core contracts, and the envelope expands strongly until the helium core gets ignited. During this expansion phase, it is likely that the donor star fills its Roche lobe which is followed by a rapid phase of mass transfer. Moreover, this expansion phase is also expected to happen in many case A systems which are then called a case AB.

- **Case C:** After helium depletion in the core, the star may start to expand again, for example in an AGB phase, while helium is burned in the shells. If the donor star fills its Roche lobe during this phase it is called case C mass transfer.

While case A mass transfer is most likely to happen for systems with a small initial period, case B and C mass transfer can happen for larger initial periods of up to ten years. It is important to mention that during a mass transfer phase most of the hydrogen-rich envelope will be stripped of the donor star, which has a major impact on the evolution of the star compared to the single star scenario. At a later point in this thesis, this behavior will be discussed in more detail in regard to the grids used for the analysis.

2.2.3 Tidal Forces

Tidal locking is a phenomenon appearing in binary systems that have a short orbital period and preferably stars with convective envelopes. If a star rotates, tides form which then raises bulges that interact with convective motions to dissipate energy leading to a synchronization of the orbital and rotational periods of stars. During this process the orbit gets circularized. For stars with radiative envelopes or large orbital separations, this process is less efficient. The MESA stellar evolution code (Paxton et al. 2015) used in this thesis calculates the timescale of synchronization as an extension of the formula from Hut (1981)

$$\frac{1}{\tau_{\text{sync}}} = \frac{3}{q^2}\frac{MR^2}{I}\frac{k}{T}\frac{R^6}{a^6} \tag{2.15}$$

in which q is the mass ratio, MR^2/I is the radius of gyration, k/T the viscous dissipation time, R the radius of the star, and a the orbital separation. This formula has to be calculated for each stellar component separately. The fact that the separation has a dependence to the power of six underlines the statement that systems with higher orbital periods must not be tidally locked. However, if mass transfer happens, the orbital separation shrinks and the stars may get locked and the orbit circularized.

2.2.4 Accretion and Stellar Spin

Due to the fact that both stars rotate, the transferred material also carries a specific angular momentum. As a consequence, the angular momentum is added to the accretor's momentum leading to a spin-up of the star. The material can be transferred via two methods: Either via ballistic or Keplerian disk mass transfer which have different efficiencies for the angular momentum transport. To distinguish which process is taking place the minimum distance approach of the accretion stream as described in Paxton et al. (2015) is used. It can be written as the following formula

$$R_{\min} = 0.425\, a \left(q_2 + q_2^2\right)^{1/4} \qquad \text{with} \qquad 0.0667 \leq q_2 \leq 15 \tag{2.16}$$

This minimum distance $R_{\min}$, depending on the orbital separation a and mass ratio $q_2 = M_2/M_1$, is compared to the radius of the accretor, R_2. If the radius is larger than the minimum distance $R_2 > R_{\min}$, the accretion is treated as ballistic and if the radius is smaller $R_2 < R_{\min}$, mass transfer happens through a Keplerian disk.

As angular momentum is transferred during RLOF the accretor spins up very fast and reaches critical rotation. This accretion induced spin-up may lead to rapid rotating massive stars and has a major influence on its evolution. Moreover, the spin-up leads to a stop of the accretion on the companion unless it is able to lose angular momentum. Using this assumption the accretion rate and the amount of accreted material is rather low. Another effect is that compared to the conservative case, in which all infalling matter is accreted, a lot of material is lost from the system leading to a high system mass-loss rate and a widening of the orbit.

2.2.5 Orbital Angular Momentum Equations

In binary evolutionary codes it is possible to either set the initial rotational velocity by hand or to synchronize the rotational velocity with the orbital angular momentum which is given by (Paxton et al. 2015)

$$J_{\text{orb}} = M_1 M_2 \sqrt{\frac{Ga}{M_1 + M_2}} \tag{2.17}$$

Just as important as the initial rotation of a star is the evolution of the orbital angular momentum, which is dependent on the orbital separation. As the orbital angular momentum changes with time, this implies that the Roche lobe radius, which directly depends on the orbital separation, changes. Moreover, this means that the change in orbital angular momentum has a direct impact on the possibility of mass transfer to take place. The change of orbital angular momentum following (Paxton et al. 2015) can be expressed as

$$\dot{J}_{\mathrm{orb}} = \dot{J}_{\mathrm{gr}} + \dot{J}_{\mathrm{mb}} + \dot{J}_{\mathrm{ls}} + \dot{J}_{\mathrm{ml}} \tag{2.18}$$

It can be seen as an addition of different effects that will be explained in the following sections.

Gravitational Wave Radiation

When Einstein published his theorem of General Relativity, he also proposed that due to the fact that nothing can move faster than with the speed of light, changes in the gravitational field have a finite velocity and that these changes must be radiated away via gravitational waves. This effect is contained in the first term of Equation 2.18 and is shown in the following equation

$$\dot{J}_{\mathrm{gr}} = \frac{32\,G^{7/2}}{5\,c^5}\,\frac{M_1 M_2\,\sqrt{M_1 + M_2}}{a^{7/2}} \tag{2.19}$$

in which M_1 and M_2 are the masses of each binary component, a is the binary separation, G represents the gravitational constant and c is the speed of light (Landau & Lifshitz 1971). The effect of gravitational wave radiation gets dominant in very close binaries as it depends on the separation with a power of -3.5, which is why wide orbits have almost no orbital angular momentum decay through this channel.

Magnetic Braking

As stars consist of charged particles it is possible that they develop a magnetic field. If these fields are able to couple with the stellar wind, this leads to a spin-down of the stars rotation (Skumanich 1972). The effect of magnetic braking gets strongest for low mass stars with masses of about $1.5\,M_\odot$ and below, as their outflows happen due to coronal winds while having subphotospheric convection zones (Pantolmos & Matt 2017). The effect of magnetic fields on rapid rotating stars is still rather unknown. However, assuming that the system is tidally synchronized, meaning that the rotation of a star is synchronized with the orbital angular momentum, implies the following: If a star that is tidally locked with the orbit slows down due to magnetic braking, the change in the angular momentum of the star will correspond to a change in the orbital angular momentum of the binary. Therefore, the expression of Rappaport et al.

(1983), who assumed that the system is tidally synchronized, can be used to describe the change of the orbital angular momentum in response to the magnetic braking of a stellar component

$$\dot{J}_{\rm mb} = -6.82 \times 10^{34} \frac{M_1}{M_\odot} \left(\frac{R_1}{R_\odot}\right)^{\gamma} \left(\frac{1\,\mathrm{d}}{P_{\rm orb}}\right)^{3} [\mathrm{dyn\,cm}] \tag{2.20}$$

In this equation M_1 is the mass and R_1 the radius of the primary star, $P_{\rm orb}$ is the orbital period of the system and γ the radius exponent. The exponent can be approximated to $\gamma = 4$ (Verbunt & Zwaan 1981). For the secondary star the change in orbital angular momentum can be derived following the same recipe as above.

Angular Momentum Exchange (Spin Orbit Coupling)

Stars expand or contract during their evolutionary phases. These changes in radius also have a direct impact on the rotation of a star. Due to tidal interaction or mass transfer, the change in the angular momentum of a star can be pumped directly into the orbital angular momentum of the system. The effect of this angular momentum exchange is most efficient in tight systems as the tidal torque is strongest here. This effect may lead to an orbit widening during mass transfer, if the stars are tidally locked and may lead to a stable mass transfer phase (Tauris & van den Heuvel 2006). The change in orbital angular momentum due to spin-orbit coupling following the implementation of Paxton et al. (2015) can be written as

$$\dot{J}_{\rm ls} = -\frac{1}{\delta t}\left(\delta S_1 + \frac{\dot{M}_{1,\rm w}}{\dot{M}_1} S_{1,\rm lost} + \delta S_2 + S_{2,\rm lost}\right) \tag{2.21}$$

and depends on the spin angular momentum of each stellar component δS_1 and δS_2, as well as the amounts of lost spin angular momentum, $S_{1,\rm lost}$ and $S_{2,\rm lost}$ for a given time step δt in which mass is lost from the system $\dot{M}_1$. For the more massive donor star also mass-loss due to stellar winds $\dot{M}_{1,\rm w}$ is taken into account which is neglected for the secondary in this case. Additionally, the mass that is lost due to mass transfer is ignored in this simplification.

Mass loss

The angular momentum changes of a single star are mainly caused by stellar winds that carry most of the momentum and spin down the star. This also affects the binary evolution, following the description of Soberman et al. (1997) and Paxton et al. (2015), the change in the orbital angular momentum, due to mass-loss from a wind originating from a stellar component or a circumbinary toroid with radius $R_{\rm t} = \gamma^2 a$, is given by

$$\dot{J}_{\rm ml} = \sqrt{Ga}\,\frac{(\dot{M}_{1,\rm w}+\alpha\dot{M}_{\rm RLOF})M_2^2+(\dot{M}_{2,\rm w}+\beta\dot{M}_{\rm RLOF})M_1^2+\delta\gamma\dot{M}_{\rm RLOF}(M_1+M_2)^2}{(M_1+M_2)^{3/2}} \tag{2.22}$$

with dependence on the mass of each binary component M_1 and M_2 as well as on the mass lost due to winds $\dot{M}_{1,\rm w}$ and $\dot{M}_{2,\rm w}$. Moreover, the equation depends on the orbital separation of the binary system a, the mass transfer rate from Roche lobe overflow $\dot{M}_{\rm RLOF}$ and the fractions α, β and δ lost from a direct fast wind, the mass ejected from the vicinity of the accretor and from the surrounding toroid, respectively. The efficiency of mass transfer is therefore given as

$$f = 1-\alpha-\beta-\delta \tag{2.23}$$

According to this definition, the mass-loss rates of both stars can be written as (Marchant 2016)

$$\dot{M}_1 = \dot{M}_{1,\rm w}+\dot{M}_{\rm RLOF} \qquad \text{and} \qquad \dot{M}_2 = \dot{M}_{2,\rm w}-f\dot{M}_{\rm RLOF} \tag{2.24}$$

As already mentioned before, mass-loss rates from stellar winds for massive stars with masses above about $10\,M_\odot$ are already important during the main sequence. As the mass-loss rates are large during most of the time of a massive star the change of orbital angular momentum is dominated by this term.

Binary Separation and Orbital Angular Momentum

As the orbital angular momentum equation (see Equation 2.17) also depends on the binary separation, one can rewrite this formula to display the change of binary separation. A simple logarithmic differentiation, in which the eccentricity is neglected ($\epsilon = 0$), is given by Tauris & van den Heuvel (2006)

$$\frac{\dot{a}}{a} = 2\frac{\dot{J}_{\rm orb}}{J_{\rm orb}} - 2\frac{\dot{M}_1}{M_1} - 2\frac{\dot{M}_2}{M_2} + \frac{\dot{M}_1+\dot{M}_2}{M_1+M_2} \tag{2.25}$$

The change of binary separation divided by the binary separation depends on the change of orbital angular momentum $\dot{J}_{\rm orb}$, the orbital angular momentum $J_{\rm orb}$, the mass lost from the primary and secondary $\dot{M}_1$ and $\dot{M}_2$, their masses M_1 and M_2. The evolution of the binary separation during mass transfer will be discussed in the next section.

2.2.6 Mass Transfer

When a donor star expands and fills its Roche lobe mass transfer sets in as it has been discussed above. However, if mass is removed from the surface of the star, it is perturbed and wants to return to equilibrium. First, the star responds on one of the shortest timescales and restores hydrostatic equilibrium. Afterwards, thermal equilibrium will be restored. Moreover, if mass is transferred between the two stars or lost from the system, changes in the binary separation and also in the Roche lobe radius occur. As long as the Roche lobe of the donor star is able to enclose the star itself, mass can be transferred in a stable way (Soberman et al. 1997). Therefore, the stability of mass transfer and response of the Roche lobe radius to mass transfer will be discussed in the following sections.

Stability

Stable mass transfer is only possible while the donor star is enclosed by its Roche lobe it is useful to investigate the change of the radius of the star and the change of the Roche lobe radius. As the change in radius is defined over the mass-radius relationship, $R \propto M^{\zeta}$, it is useful to have a closer look at the corresponding exponents for the response of the Roche lobe ζ_{RL} and the growing donor star ζ_{donor}. When rewriting the power-law the exponents can be expressed as

$$\zeta_{\mathrm{RL}} = \frac{\partial \ln R_{\mathrm{RL}}}{\partial \ln M_1} \qquad \text{and} \qquad \zeta_{\mathrm{donor}} = \frac{\partial \ln R_1}{\partial \ln M_1} \tag{2.26}$$

with R_1 and M_1 the radius and mass of the donor star and R_{RL} as the Roche lobe radius (Soberman et al. 1997). At the onset of mass transfer, the radius of the donor star is equivalent to the Roche lobe radius, $R_1 = R_{\mathrm{RL}}$, therefore, it is required for stable mass transfer that the following criterion must be fulfilled

$$\zeta_{\mathrm{RL}} \leq \zeta_{\mathrm{donor}} \tag{2.27}$$

The exponent ζ_{donor} describing the response of the donor stars radius must have a value between the adiabatic and thermal exponent of the star as it tries to maintain equilibrium (Tauris & van den Heuvel 2006).

Radiative and Convective Envelopes

The decision which of both exponents, the adiabatic or thermal, can be used as an approximation for the mass-radius exponent of the donor star ζ_{donor} strongly depends on the equations of state. Therefore, whether or not mass transfer is stable also depends on the energy transport mechanism in the outer regions of the donor's envelope. For the envelope of a star, there are two main mechanisms: Energy transport by radiation

or by convection. For simplicity, one can assume that the mass losing star is an isentropic polytrope. For this model, the pressure term does not depend on temperature T and therefore, the mechanical structure of the star can be calculated. Following this assumption, the pressure P is a function of density ρ and is given by

$$P(\rho) = K\rho^{\gamma_{\mathrm{ad}}} = K\rho^{1+1/n} \tag{2.28}$$

and depends only on the adiabatic exponent γ_{ad} which can be expressed using the polytropic model index n ranging from 1.5 - 3. The adiabatic mass-radius exponent ζ_{ad} can then be formulated as (Soberman et al. 1997)

$$\zeta_{\mathrm{ad}} = \frac{n-1}{n-3} \tag{2.29}$$

For a fully convective star, which is a quite good approximation for a red giant star, the adiabatic exponent is $\gamma_{\mathrm{ad}} = 5/3$ and the polytropic model index is $n = 1.5$. As a consequence, the adiabatic mass-radius exponent $\zeta_{\mathrm{ad}} = -1/3$ is rather small and the star expands rather quickly, which implies that the Roche lobe radius has to expand quickly to have stable mass transfer (Soberman et al. 1997). If the Roche lobe radius cannot expand fast enough, a common envelope will form.

Contrary, for a fully radiative star the polytropic model index is $n = 3$ and the adiabatic exponent is $\gamma_{\mathrm{ad}} = 4/3$. If now on the surface of the star mass is reduced by mass transfer, the underlying material is brought out of pressure equilibrium and expands without filling the region from which the material has been removed. During this phase, the adiabatic exponent is slightly smaller $\gamma_{\mathrm{ad}} < 4/3$ which leads to a contraction on the dynamical timescale and to a positive adiabatic mass-radius exponent $\zeta_{\mathrm{ad}} > 0$ (Soberman et al. 1997).

Of course, no real star is fully convective or radiative throughout its entire stellar structure. However, the assumption made above should give the reader a feeling about the stability of mass transfer. It is important to keep in mind that mass transfer is likely to be stable for radiative envelopes while mass transfer can, but must not be unstable for convective envelopes.

Response of the Binary Separation to Mass Transfer

In this section, the influence of mass transfer on the binary separation will be discussed. For simplicity, all effects on the change of angular momentum like spin-orbit coupling are neglected. Following Tauris & van den Heuvel (2006) and Soberman et al. (1997) only orbital angular momentum exchange due to mass-loss will be taken into account. Therefore, all other terms of Equation 2.18 will be set to zero ($\dot{J}_{\mathrm{gr}} = \dot{J}_{\mathrm{mb}} = \dot{J}_{\mathrm{ls}} = 0$).

Furthermore, effects from a direct fast wind and the circumbinary toroid are also neglected. This implies that in systems with orbital periods larger than a few days the mass transfer coefficients also vanish, $\alpha = \delta = 0$. Therefore, Equation 2.22 can be simplified to

$$\frac{\dot{J}_{\mathrm{orb}}}{J_{\mathrm{orb}}} = \frac{\beta q^2}{1+q}\frac{\dot{M}_2}{M_2} \tag{2.30}$$

Following this, it is possible by using Equation 2.24 and the partial derivatives $\partial \ln a = \dot{a}/a$ and $\partial \ln q = \dot{q}/q$ to reformulate Equation 2.25 to

$$-\frac{\partial \ln a}{\partial \ln q} = 2 + \frac{q}{q+1} + \frac{3\beta q - 5q}{q(1-\beta)+1} \tag{2.31}$$

For a more detailed derivation consider Tauris & van den Heuvel (2006) and Soberman et al. (1997). This analytical solution describes the change of binary separation and its dependence on the mass ratio q as well as on the fraction of ejected mass from the accretor β. Keep in mind that the mass ratio and the fraction of ejected mass from the accretor change during mass transfer. The behavior of the change in binary separation is shown in Figure 2.4 for different values of β. It seems to be a general rule that while the donor star is more massive than the accretor ($q > 1$) the binary separation shrinks, while for donor stars that are less massive than the accretor ($q < 1$) the separation widens.

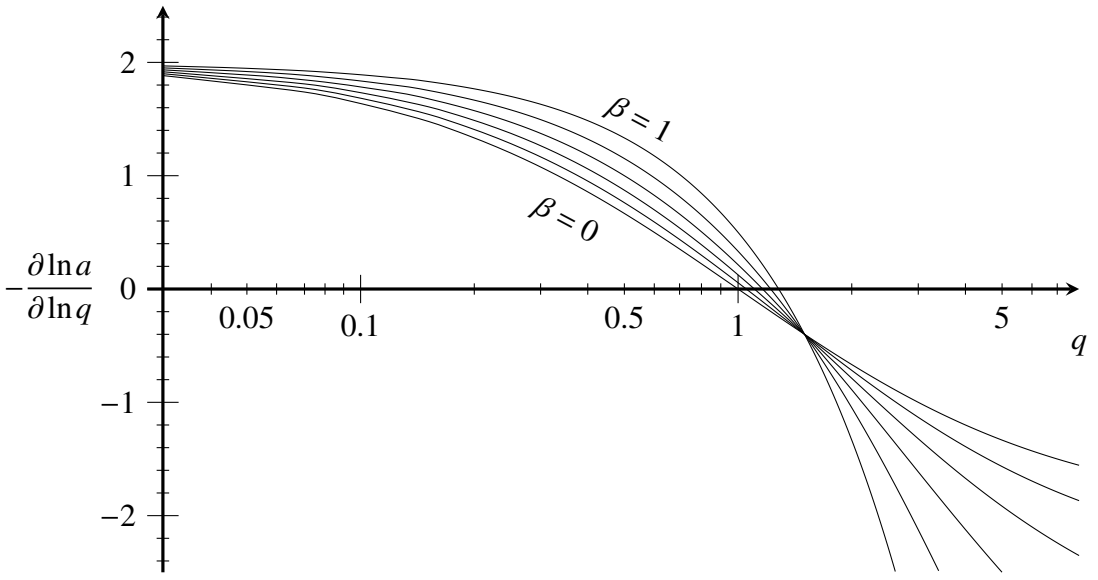

Figure 2.4: Plot of the change in binary separation $-\partial \ln a/\partial \ln q$ as a function of mass ratio q. The different curves correspond to different values of β starting from $\beta = 0$ to $\beta = 1$ in steps of $\Delta\beta = 0.2$. If $-\partial \ln a/\partial \ln q$ is positive the orbit widens, if it is negative the orbit shrinks.

As a matter of fact, the mass ratio is not constant during mass transfer. Therefore, as mostly mass is transferred from the more massive star to the less massive one the mass transfer phase leads to an orbital shrinking. However, at some point, the mass ratio changes and the donor star will be less massive implying that in the end phase of mass transfer it is possible to have an orbital widening. Note, that this is not a necessary step to happen, as the initial mass ratio can be very extreme so that it may not get inverted during the mass transfer phase.

2.2.7 Limitations on Mass Transfer Rates and Accretion

Stellar evolution codes, like MESA, solve the fundamental differential equations of state to calculate the evolution of the stars and of the binary system. However, the code cannot decide whether or not the mass transfer or the amount of accreted mass is physically reasonable. In the previous section, some limitations like the spin-up of the accretor were already mentioned. Anyhow, there are some more physical phenomena which also have to be taken into account.

Eddington Accretion Limit

The first limitation is the accretion rate near the Eddington limit. This limit is mostly important for compact companions. However, it can also be applied to a normal star. It is based on the principle that matter which falls onto the companion during mass transfer gets heated and releases large amounts of the gained gravitational energy as X-Ray radiation (Quast et al. 2019). The Eddington accretion rate is defined as the mass that can be accreted until the Eddington luminosity is reached

$$\dot{M}_{\mathrm{edd}} = \frac{4\pi c R_2}{\kappa} \tag{2.32}$$

and depends on the radius R_2 and the surface opacity κ of the accreting star. For most systems, the envelope and therefore the transferred material mostly consists of hydrogen. Therefore, the electron scattering opacity is a good approximation for κ. In this case, the Eddington accretion limit only depends on the radius of the secondary. This implies that more compact objects only accrete small fractions of the infalling material and the rest is converted into high energy radiation, X-rays, while for more extended objects almost all material can be accreted according to this limit.

Moreover, as this limit also regulates the efficiency of mass transfer and it is useful to redefine the quantity of efficiency as the following (Paxton et al. 2015)

$$f = \min(1 - \alpha - \beta - \delta, |\dot{M}_{\mathrm{edd}}/\dot{M}_{\mathrm{RLOF}}|) \tag{2.33}$$

Limitations on Mass Transfer Rates

As soon as the accretor spins up during mass transfer it cannot accrete any longer. This implies that the transferred material from the donor star needs to be lost from the system somehow. Therefore, a physically reasonable limit is needed. One reasonable approach is to assume that all material will be accelerated from a Keplerian disc at the surface of the accretor via a radiation driven wind. Following the approach of Marchant (2016) who ignored the gravitational attraction of the donor star the limitations can be expressed as

$$\log \frac{\dot{M}}{M_\odot\,\mathrm{yr}^{-1}} = -7.19 + \log \frac{L_1 + L_2}{L_\odot} - \log \frac{M_2}{M_\odot} + \log \frac{R_2}{R_\odot} \tag{2.34}$$

and depends on the luminosities of both binary components, L_1 and L_2, the mass of the accretor M_2, and its radius R_2. However, this is a rather strict limit. A less restrictive limit could include that the material will be accelerated at the edge of the accretion disc in a way that instead of R_2 the Roche lobe radius R_{RL} can be used in Equation 2.34. If the mass transfer rate is higher than this limit, it is assumed that the instreaming material can neither be accreted nor ejected and results in a common envelope phase (Marchant 2016).

2.3 Common Envelope Evolution (CEE)

In the previous section, the stability of mass transfer has been discussed. However, the possibility of an unstable mass transfer needs to be taken into account as well. An unstable mass transfer can occur either due to the rapid expansion of the donor star which expands faster than the Roche lobe or due to accretion on the secondary with a mass transfer rate above the aforementioned limits. The result of an unstable mass transfer is a common envelope phase. During this phase, a spiral-in process takes place where the orbital energy is deposited in the envelope which may lead to a successful ejection. Otherwise, the two stars will not survive the common envelope phase and result in a merger (Ivanova et al. 2013).

Common envelope evolution is a complex three-dimensional problem and requires accurate models to predict the exact outcome of such a system. One dimensional codes, like MESA, are not able to calculate the outcomes yet. Nonetheless, there is a classic way to estimate the fate of a common envelope system. For this, one has to compare the binding energy of the envelope and the orbital energy that can be released due to the spiral-in process. By assuming that all orbital energy will be deposited in the envelope it is possible to get a first impression of whether or not such a system can survive.

2.3.1 Orbital Energy

The maximum orbital energy that can be released during the spiral-in process, is given by the energy difference of the system in the initial state, at the formation of the common envelope, to the final state, in which the larger star just fills its Roche lobe. Therefore, the orbital energy that can be used to unbind the envelope is given by (Webbink 1984)

$$E_{\mathrm{orb}} = E_{\mathrm{init}} - E_{\mathrm{final}} = -\frac{GM_1M_2}{2a_{\mathrm{init}}} + \frac{GM_{1,\mathrm{core}}M_2}{2a_{\mathrm{final}}} \tag{2.35}$$

In this formula, M_1 and M_2 are the masses of the primary and secondary, respectively. $M_{1,\mathrm{core}}$ is the mass of the remaining core of the primary as it loses its envelope, a_{init} is the binary separation at the onset of the common envelope phase, and a_{final} is the separation after a successful envelope ejection during which the larger star fills its Roche lobe. In most of the systems, the separation at the onset of the common envelope is large so that the first term of Equation 2.35 is negligibly small and the orbital energy can be approximated to

$$E_{\mathrm{orb}} \approx \frac{GM_{1,\mathrm{core}}M_2}{2a_{\mathrm{final}}} \tag{2.36}$$

However, there is still the question of how to determine the final separation of the system. In the common envelope phase, it is a good approach to assume that for a successful ejection the whole hydrogen-rich envelope has to be removed and that the remnants are a helium star and the main-sequence companion. As a matter of fact, the main-sequence star is in almost all cases larger than the helium star and for a successful common envelope evolution, it must be smaller or equal to its Roche lobe so that $R_{\mathrm{RL}} = R_2$. Using this approach one can use the equation of the Roche lobe radius, Equation 2.14, to calculate the smallest binary separation possible

$$a_{\mathrm{final}} = \frac{0.6q^{2/3} + \log(1+q^{1/3})}{0.49\,q^{2/3}} \cdot R_2 \qquad \text{with} \qquad q = \frac{M_2}{M_{1,\mathrm{core}}} \tag{2.37}$$

Furthermore, it is assumed that the secondary has a density which is higher by some orders of magnitude so that interactions which take place between the secondary and the common envelope can be neglected. Mixing processes that might happen due to the spiral-in process are also not taken into account. However, as this is a simplification for a complex three-dimensional problem it serves as an estimate to obtain a first impression of the amount of orbital energy that can be released during the spiral-in process.

2.3.2 Binding Energy

The binding energy of the envelope of a star can be classically understood as the energy required to overcome the gravitational potential that binds the envelope and can be written as (Ivanova et al. 2013)

$$E_{\text{bind,g}} = -\int_{M_{\text{core}}}^{M_{\text{surf}}} \frac{Gm(r)}{r}\,\mathrm{d}m \tag{2.38}$$

with M_{surf} and M_{core} as the mass coordinate at the surface and the core respectively and $m(r)$ is the mass coordinate at the radius r of the star. If the orbital energy that can be released is greater than the binding energy, the system is expected to survive the common envelope. However, this is the upper limit of the binding energy and there may be more processes that contribute to this term and reduce the binding energy. One example of an additional term that reduces the binding energy is the internal energy of a star. As the internal energy is counteracting the gravitational energy this leads to an additional term in the estimation of the total binding energy. This additional term can be formulated according to Han et al. (1995) as

$$E_{\text{bind,u}} = -\int_{M_{\text{core}}}^{M_{\text{surf}}} \frac{Gm(r)}{r}\,\mathrm{d}m + \alpha_{\text{th}} \int_{M_{\text{core}}}^{M_{\text{surf}}} U(m)\,\mathrm{d}m \tag{2.39}$$

and depends on the fraction α_{th} of the internal energy that can be used to expel the common envelope is rather unknown. There are two extrema, where the internal energy does not contribute to the binding energy $\alpha_{\text{th}} = 0$ or where all of the internal energy $\alpha_{\text{th}} = 1$ can be used to unbind the envelope. The internal energy U of a star includes the basic thermal energy of a perfect gas and the energy of radiation in the star (Tauris & van den Heuvel 2006)

$$U(m) = \frac{3\Re T(m)}{2\mu(m)} + \frac{aT(m)^4}{3\rho(m)} \tag{2.40}$$

with dependence on the temperature T, the mean molecular weight μ, and the density ρ at the given mass coordinate m. The used constants are the ideal gas constant $\Re$ and the radiation density constant a. Other processes that may reduce the binding energy are ignored in this thesis as their trustworthiness is rather vague.

2.3.3 Fate of the Remnants

As discussed above, a common envelope phase can only end with a successful ejection of the envelope if the orbital energy is large enough. Otherwise, the system will result

as a merger. This kind of remnant is hard to observe as it looks like a single star, but its internal structure differs a lot. However, the outcomes of a successful ejection are observed more easily.

A small illustration of the basic evolution of a system with a successful common envelope ejection is provided in Figure 2.5. The first outcome after the common envelope phase is a tight binary system with a helium star and a main-sequence companion. If the helium star is massive enough, it may be observed as a Wolf-Rayet star. As this becomes important in the later analysis, one should keep in mind that besides stellar mass-loss rates and mass transfer, common envelope evolution may also be an important channel to produce Wolf-Rayet stars.

Depending on the mass of the helium star, its fate will be a white dwarf, a neutron star, or a black hole. Usually, before the helium star will become one of these compact objects it will explode as a supernova (SN). However, it is still unknown how strong a kick introduced by a supernova is and if a system will get disrupted or not. Under the assumption that the system will survive the supernova, the binary system consists now out of a compact object and a main-sequence companion which is hard to observe as the compact object is very faint. Anyhow, if the main sequence companion starts to expand, it may overflow the Roche lobe and initiate a phase of mass transfer. If the mass transfer can be stable, it may be possible to observe this system as an X-ray binary. If the mass transfer is unstable, another common envelope phase may be initiated leading to another helium star or a merger.

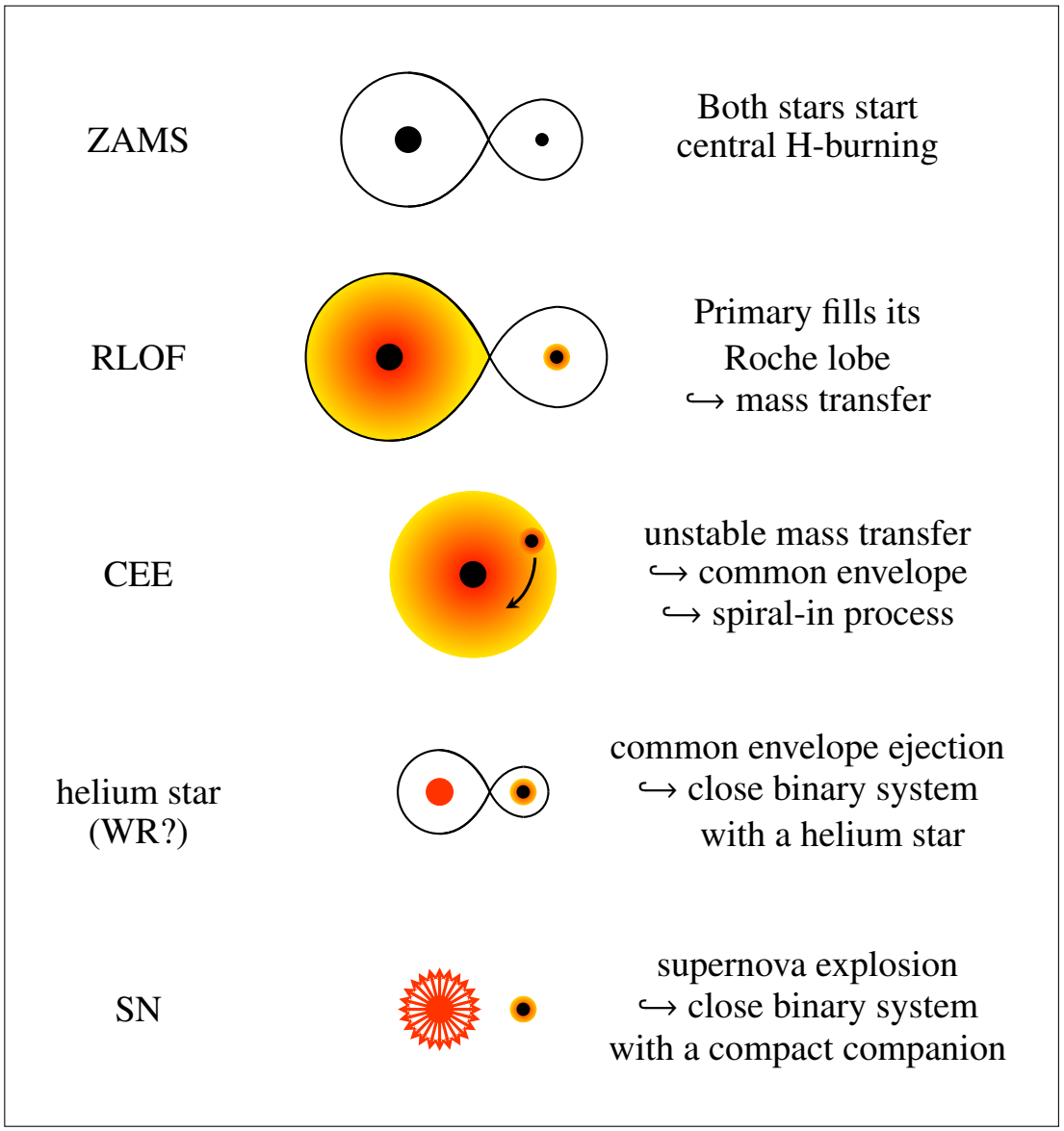

Figure 2.5: Sketch of the evolution of a binary system with a common envelope phase. At first, both stars evolve independently. After core hydrogen depletion of the primary, it will fill its Roche lobe, and mass transfer starts. If the mass transfer is unstable it comes to the formation of a common envelope followed by a spiral-in process. If the envelope can be ejected the resulting orbital separation is reduced to the order of some days or less. The remnants of the common envelope evolution are a helium star and a main-sequence star. Depending on the helium stars mass, this channel may produce Wolf-Rayet stars. However, the Wolf-Rayet phase is short compared to hydrogen burning and the primary explodes in the end as a supernova before the secondary can fill its Roche lobe. This will lead to a binary system with a compact companion. When the secondary fills its Roche lobe mass can be transferred which may be seen as an X-ray binary.

3 Evolutionary Properties of Massive Binary Models

The aim of this thesis is to study the properties of very massive binary systems at low metallicity. Before starting the first analysis of these binary systems a brief overview of previously calculated model grids of detailed binary-evolution calculations (simply called binary grids from here on) with SMC and LMC metallicity is given in Section 3.1. Section 3.2 covers the preparations that are made in order to extend the existing binary grid of Marchant (2016) to initial primary masses of about $70\,M_\odot$. In addition, this section also shows the results of the newly computed grid and compares the corresponding phase diagram with the SMC grid. A more detailed analysis of the influence of inflation on mass transfer and the reliability of the upper limit on mass transfer is given in Section 3.3.

3.1 Previous Works

Large binary grids covering different initial primary masses, mass ratios, and orbital periods provide an ideal theoretical base to test how well the predicted models compare to large samples of observed stars. In the recent work of Wang et al. (2020) a dense model grid with SMC metallicity is used to explain the extensions of the main-sequence turn off region of young star clusters. Marchant (2016) calculated a dense model grid at LMC metallicity to study the surface abundances in massive interacting binary systems. Since they are used in the later analysis to study the effect of metallicity on the evolution of massive binary systems, in the following sections both grids will be introduced.

3.1.1 The LMC binary grid

Marchant (2016) was the first who used the Modules for Experiments in Stellar Astrophysics (MESA) (Paxton et al. 2013, 2015, 2018) code to calculate a large grid of binary models. The resulting grid covers initial primary masses in the range of $M_{1,\mathrm{i}} \simeq 10\,\mathrm{M}_\odot - 40\,\mathrm{M}_\odot$, in steps of $\Delta\log(M_{1,\mathrm{i}}/M_\odot) = 0.05$. Furthermore, the grid spans over the wide range of $P_\mathrm{i} \simeq 1.4\,\mathrm{d} - 3000\,\mathrm{d}$ for initial orbital period in small steps of $\Delta\log(P_\mathrm{i}/\mathrm{d}) = 0.025$. Regarding the initial mass ratios a range of $q_\mathrm{i} = 0.025 - 0.975$ in steps of $\Delta q_\mathrm{i} = 0.025$ is covered. It is assumed that the binary models are tidally synchronized at the ZAMS to avoid the need of an extra parameter for the initial rotation. It is worth mentioning that this is not a good assumption for the wider systems. However, rotation is not that important that it matters much. The binary models are calculated with the MESA code version 8845 and include the physics of mass-loss, rotation, inflation, and binary interaction.

To model the stellar wind mass-loss the models follow the prescription of Brott et al. (2011). The mass-loss rates of Vink et al. (2001) are used for hydrogen-rich main-sequence stars . For lower temperatures below the bi-stability jump, a jump in temper-

ature where the mass-loss rates suddenly drop (see Vink et al. (2001)), the maximum value of Vink et al. (2001) or Nieuwenhuijzen & de Jager (1990) is used. The Wolf-Rayet mass-loss rates of Hamann et al. (1995) are used for stars with a surface hydrogen abundance below 0.4. In the transition phase where a star has a surface hydrogen abundance between 0.4 and 0.7, the wind mass-loss rate is interpolated between the recipes of Vink et al. (2001) and Hamann et al. (1995).

Rotational mixing, which gets more important for massive stars, is modeled as a diffusive process including the effects of dynamical and secular shear instabilities, the Goldreich-Schubert-Fricke instability, and Eddington-Sweet circulations (Heger et al. 2000). In addition to the angular momentum transport by rotation, the transport via magnetic fields from the Tayler-Spruit dynamo (Spruit 2002) is included.

Convection is modeled according to the Ledoux criterion and the mixing length theory (Böhm-Vitense 1958) with a mixing length parameter of $\alpha = l/H_\mathrm{P} = 1.5$. For hydrogen burning cores a steep overshooting is used so that the convective core is extended by $0.335 H_\mathrm{P}$ (Brott et al. 2011) where H_P is the pressure scale height at the boundary of the convective core. Thermohaline mixing is included with an efficiency parameter of $\alpha_\mathrm{th} = 1$ (Kippenhahn et al. 1980). Semiconvection is treated as an inefficient mixing process with a parameter of $\alpha_\mathrm{sc} = 0.01$ (Langer et al. 1983).

Binary interactions are modeled as described in Section 2.2. Mass transfer is modeled by using the 'contact' scheme from MESA. This is an implicit method in which the mass transfer rate is adjusted so that the radius of the donor star stays inside the Roche lobe. Moreover, it enables models to have a contact phase where mass is exchanged efficiently, leading to a mass ratio close to $q = 1$ (Marchant et al. 2016).

Figure 3.1 shows the final states of the binary models with an initial primary mass of $M_{1,\mathrm{i}} = 10\,M_\odot$ in form of a phase diagram. The phase diagrams for the remaining initial primary masses can be found in Appendix A. In contrast to Marchant (2016) where the phase diagrams were published first this plot includes an additional label. The different labels and their corresponding implications for the evolutionary stage of the binary are listed below:

- **Both dep. C**:
  Both stars are calculated until carbon depletion in their core. Due to convergence problems stellar models with helium core masses above $M_\mathrm{He} > 14\,M_\odot$ are calculated to core helium depletion instead. When the primary depleted carbon the companion is modeled as a single star, ignoring the possibility of the formation of a binary with compact object due to the uncertainties of a supernova kick.
- **L2 overflow**:
  During a contact phase both stars overfill their Roche lobe and mass is overflowing the second Lagrangian point L_2. The system is suspected to merge.

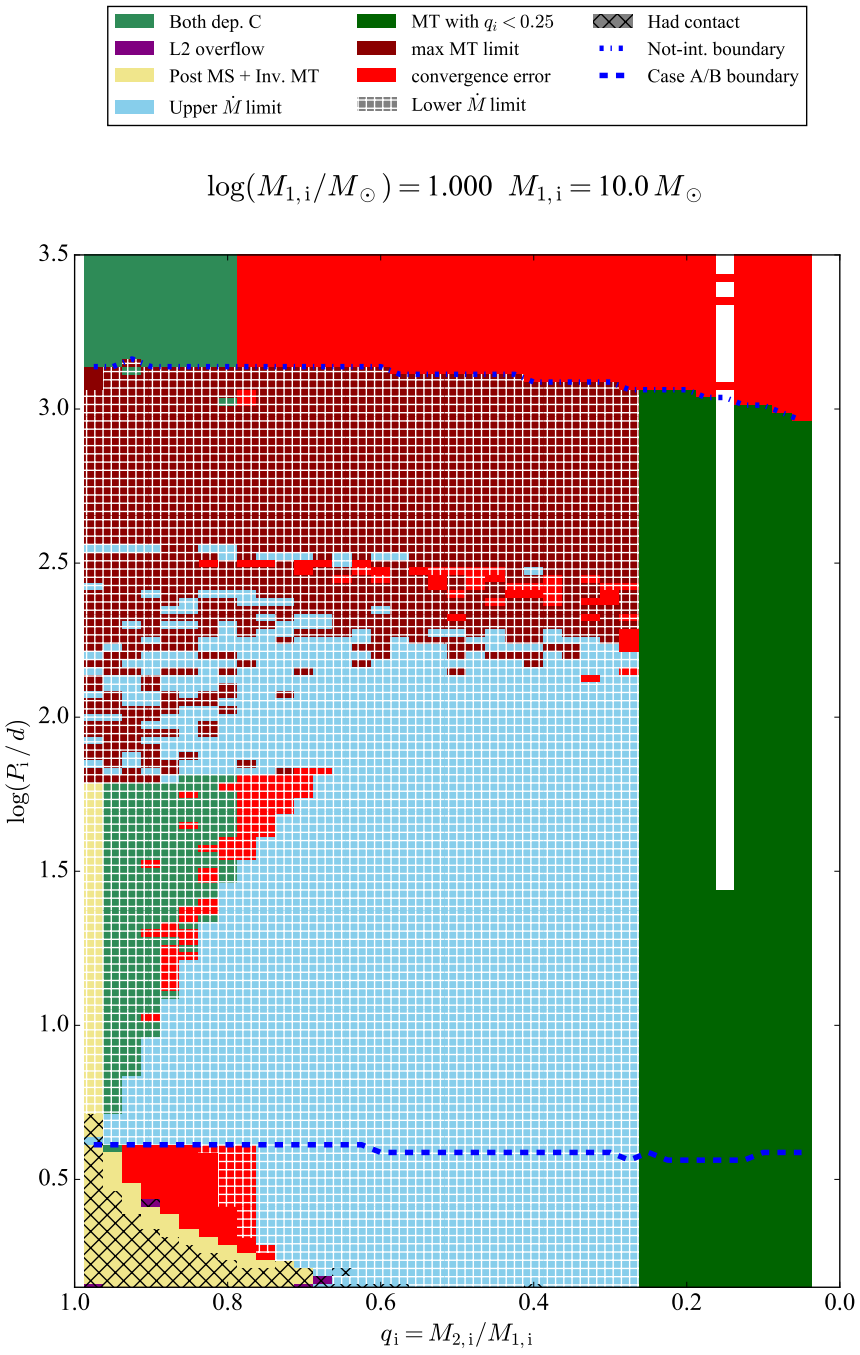

Figure 3.1: Phase diagram of binary models with fixed initial donor mass of $M_{1,\mathrm{i}} = 10\,M_\odot$. The initial mass ratio q_i is plotted versus the initial orbital period P_i. All models are calculated at LMC metallicity. The different phases are indicated in the legend and a more detailed description can be found in Section 3.1.1.

- **Post MS + Inv. MT**:
  Inverse mass transfer from the secondary to a post main-sequence primary. These systems are suspected to have an unstable mass transfer and to merge, leading to the formation of a post main-sequence star.

- **Lower $\dot{M}$ limit**:
  The limit of Equation 2.34 has been reached. Note that the models reaching this condition continue the calculation. This label has to be understood as a warning that radiation may not be able to drive a wind to expel the transferred material from the system.

- **Upper $\dot{M}$ limit**:
  The less restrictive limit of Equation 2.34 is reached. The transferred material can neither be expelled nor accreted anymore. Therefore, the formation of a common envelope is suspected.

- **MT with $q_i < 0.25$**:
  It is assumed that a mass transfer phase for systems with extreme mass ratios below $q_i < 0.25$ are will fill the Roche lobe of the secondary quickly leading to a common envelope phase and a potential merger.

- **max MT limit**:
  This is the additional label mentioned above. Binary systems that trigger this condition have a mass transfer rate that exceeds $0.1\,M_\odot\,\mathrm{yr}^{-1}$. These systems are suggested to form a common envelope.

- **convergence error**:
  The calculation has stopped due to numerical issues and did not converge. This likely happens in the late phases of the evolution or late stages of mass transfer.

- **Had contact**:
  Both stars had a contact phase. Note that this does not imply that this system results in a merger.

- **Not-int. boundary**:
  Systems above this line are not interacting during their entire life. They evolve as single stars.

- **Case A/B boundary**:
  Boundary line between systems undergoing Case A and Case B mass transfer.

To get a better understanding of the implications of the phase diagram the most characteristic regions of Figure 3.1 will be described in more detail.

Binary systems with initial orbital periods beneath the 'Case A/B' boundary already have a mass transfer phase during their time on the main-sequence. One can see that most of the systems with very tight orbits and mass ratios close to $q_i \to 1$ have a con-

tact phase. During this phase much mass is transferred, leading to a mass ratio close to $q = 1$ after the mass transfer phase. Therefore, it is possible for most systems that either the secondary fills its Roche lobe and inverse mass transfer sets in, or mass is overflowing through the second Lagrangian point during the contact phase. Both scenarios are suspected to result in a merger. For systems with initially more extreme mass ratios $q_\mathrm{i} \to 0$, the secondary is not luminous enough so that infalling material cannot be transferred to infinity by a radiation driven wind. These systems are also suspected to form a common envelope and to merge. Only a certain fraction of the binary systems with wide enough orbits and large enough mass ratios can have a successful mass transfer phase where both stars can be modeled until carbon depletion. It is worth mentioning that the accretion efficiency is large for case A systems and decreases with increasing initial orbital period whereas the mass transfer rate grows with increasing initial orbital period.

Binary systems that have a mass transfer phase while they evolve off the main-sequence are located between the 'Case A/B' boundary and the 'not-interacting' boundary. These systems are too wide to have a contact phase and only binary models with initial mass ratios of $q_\mathrm{i} \simeq 1$ are expected to have an inverse mass transfer phase. Models with extreme mass ratios $q_\mathrm{i} \to 0$ are still unable to drive a wind that transfers the infalling material to infinity as they reach the upper limit on mass transfer. For binary systems with large initial orbital periods, the mass transfer rate gets too high so that the upper limit on mass transfer is reached too. Therefore, only a certain fraction of binary systems is suspected to be able to evolve both stars until carbon depletion. For the systems with the widest orbits, the maximum value for mass transfer is triggered. These systems are expected to be evolved into a red supergiant phase and have large convective envelopes. The stability of mass transfer of these systems is briefly discussed in the later analysis.

Binary systems with an initial orbital period larger than the 'not-interacting' boundary evolve as single stars. As the stars are tidally synchronized their initial rotation is rather small and they can be considered as non-rotating single stars.

3.1.2 The SMC binary grid

C. Wang has also calculated a dense grid of detailed binary evolutionary models with SMC metallicity which is not published yet. As in the later analysis, the binary models are used to study the common envelope evolution a short overview over the grid will be given. The binary grid covers the initial primary mass range of $M_{1,\mathrm{i}} \simeq 7\,\mathrm{M}_\odot - 89\,\mathrm{M}_\odot$ in steps of $\Delta\log(M_{1,\mathrm{i}}/\,M_\odot) = 0.05$. The range of initial orbital periods spans over $P_\mathrm{i} \simeq 1\,\mathrm{d} - 3000\,\mathrm{d}$ in steps of $\Delta\log(P_\mathrm{i}/\mathrm{d}) = 0.025$. The initial mass ratios are only calculated in the range of $q_\mathrm{i} = 0.30 - 0.95$ as systems with smaller mass ratios are expected to merge anyways. The bin width is $\Delta q_\mathrm{i} = 0.05$.

The binary models include the same physics of mass-loss, rotation, inflation, and bi-

nary interaction as the LMC binary grid from Marchant (2016). The models are also calculated with the MESA version 8845. However, to be able to reproduce the WO binary AB8 it was argued by Wang et al. (2019) that a more efficient semiconvection with a parameter of $\alpha_{\rm sc} = 1.0$ is needed. Even though the grid has been used in the aforementioned paper, the corresponding phase diagrams are not published yet. As in the later analysis, the effect of metallicity will be discussed and the phase diagrams should be compared to the LMC grid the corresponding phase diagrams are created. The binary models with initial primary mass $M_{1,\rm i} = 10\,M_\odot$ are shown in Figure 3.2 and for binary systems with initial primary mass $M_{1,\rm i} = 60.3\,M_\odot$ is shown in Figure 3.3. The phase diagrams with the remaining initial primary masses are listed in Appendix B.

By comparing the phase diagrams for initial primary mass of $M_{1,\rm i} = 10\,M_\odot$ of the SMC and LMC in Figure 3.2 and 3.1, respectively, one can see that for these binary models the final states of their binary evolution does not differ. This should not be surprising as the effect of semiconvection is strongest for the late evolutionary phases of a star where it is unlikely to have a mass transfer rate. In addition to that, no effect of metallicity on the evolution can be seen, which is not surprising as these effects are strongest for the most massive stars.

The phase diagram for systems with initial primary mass of $M_{1,\rm i} = 60.3\,M_\odot$ is shown in Figure 3.3. However, a comparison of the two phase diagrams is not possible yet as the LMC grid does not cover this high masses. The grid needs to be extended to study the effect of metallicity in some more detail which leads directly to the next section.

3.2 Extending the LMC grid

As already mentioned, in order to study the effects of metallicity the aforementioned LMC grid needs to be extended to higher initial primary masses. The extension of a binary model grid is not an easy task. Therefore, several preparations need to be made to be sure that the calculated models can avoid numerical issues and lead to the desired output.

3.2.1 Preparations

Most of the used physics, like the mass-loss rates, rotation, inflation, and binary interaction, are fixed. However, following the argumentation of Wang et al. (2019) one might consider using a higher semiconvection efficiency in order to produce WC stars. Furthermore, increasing the initial primary mass also implies that the secondary masses increase. In the LMC grid some of the most massive stars are only calculated until core helium depletion and to avoid convergence errors. Therefore, one might need to consider applying the same criterion for the secondaries if they exceed a certain core mass limit. For the above-mentioned grids, both authors used the MESA version 8845. However, by now newer versions are available that have improved resolutions during the mass transfer phases and might be a better choice.

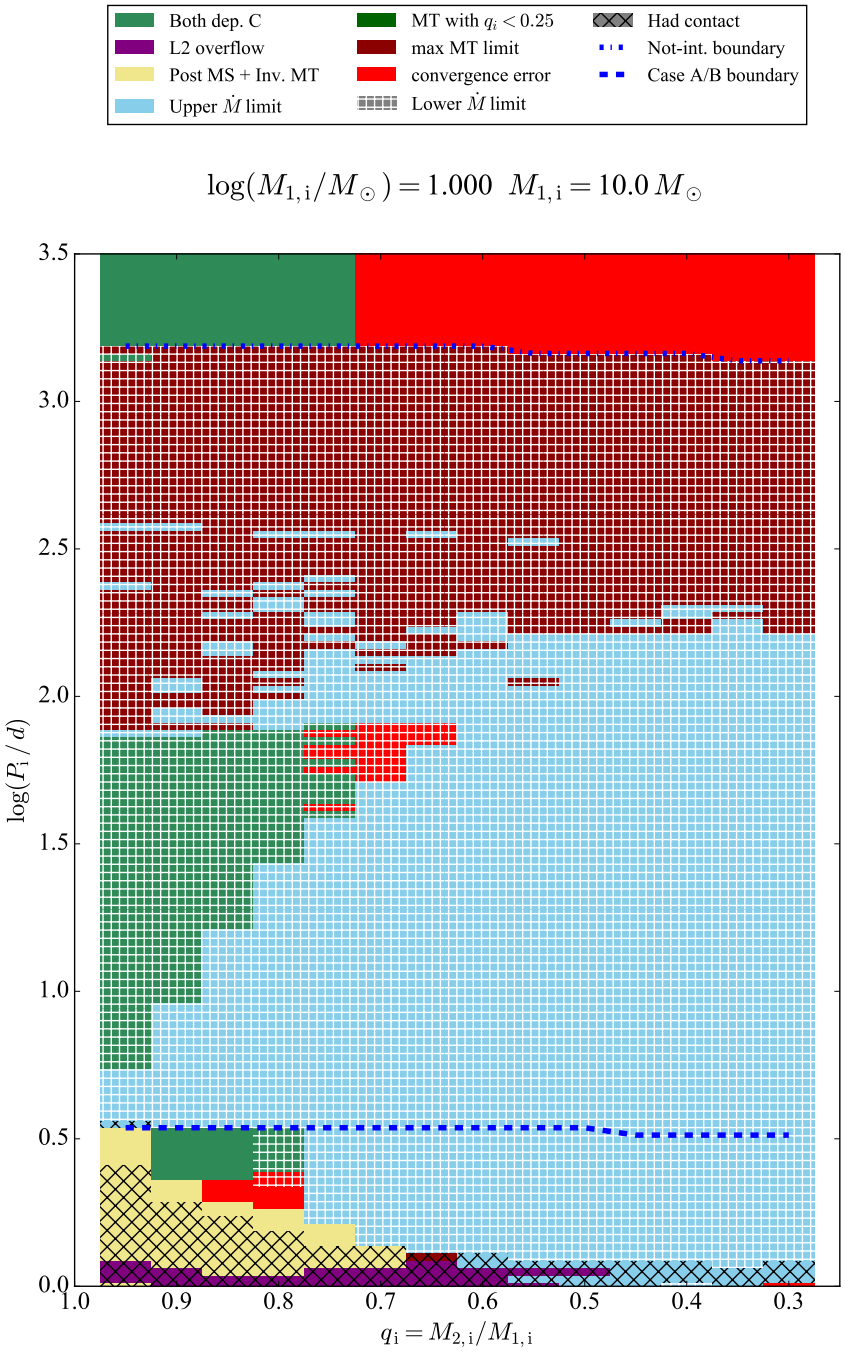

Figure 3.2: Phase diagram of binary models with fixed initial donor mass of $M_{1,\mathrm{i}} = 10\,M_\odot$. The initial mass ratio q_i is plotted versus the initial orbital period P_i. All models are calculated at SMC metallicity. The different phases are indicated in the legend and a more detailed description can be found in Section 3.1.1.

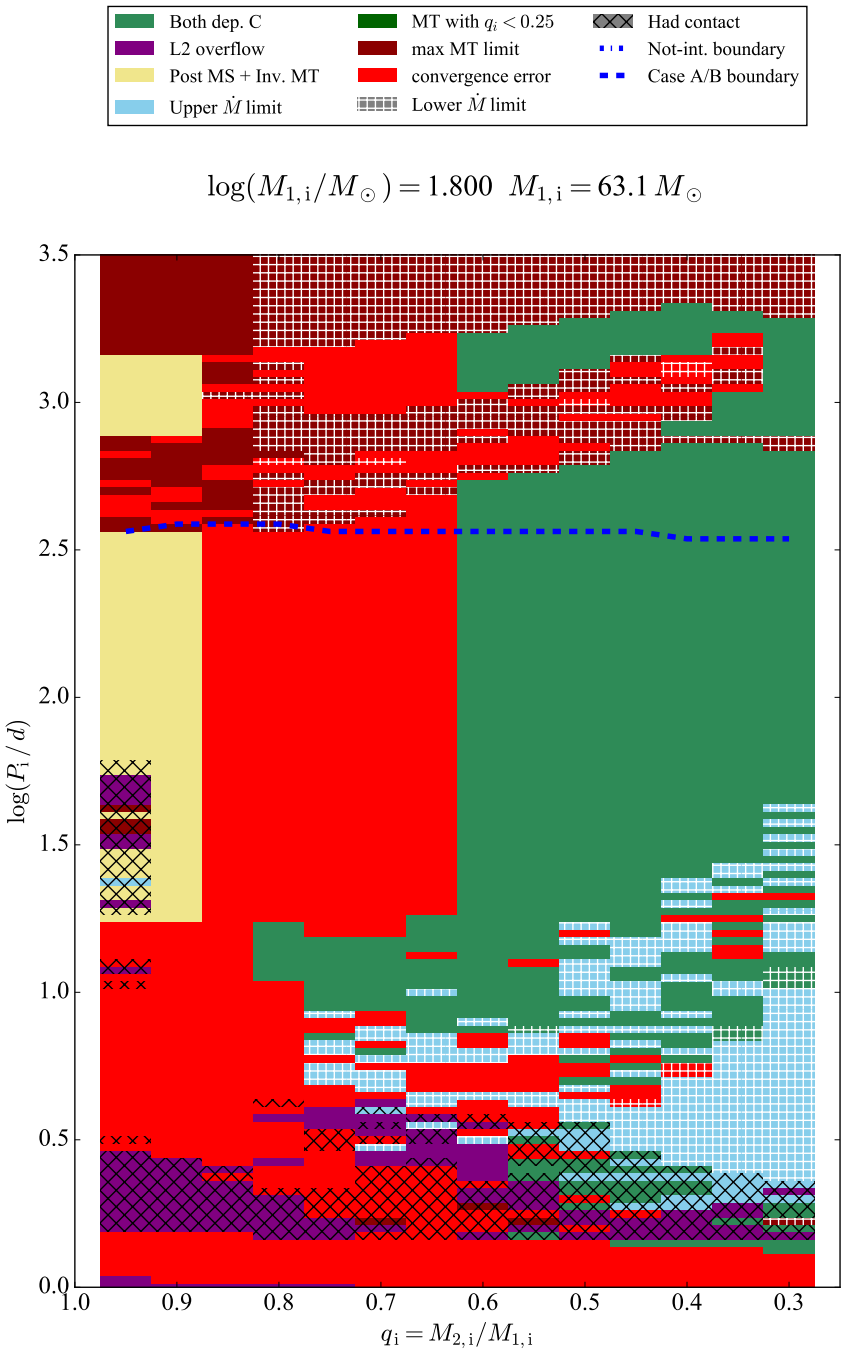

Figure 3.3: Phase diagram of binary models with fixed initial donor mass of $M_{1,\mathrm{i}} = 60.3\,M_\odot$. The initial mass ratio q_i is plotted versus the initial orbital period P_i. All models are calculated at SMC metallicity. The different phases are indicated in the legend and a more detailed description can be found in Section 3.1.1.

Semiconvetion

Semiconvective mixing is not expected to have a major influence on the stellar structure during core hydrogen burning and gets more important in the late evolutionary phases of a star. Therefore, changing the efficiency of semiconvection should not lead to large discrepancies with the aforementioned LMC grid. As the mass-loss rates for massive stars get weaker with decreasing metallicity, higher initial masses are needed to produce single WR stars. Massive binary systems are suspected to contribute to the WR population which will be discussed in more detail in the later analysis. However, it is important to study the influence of the semiconvection efficiency on the predicted WR populations.

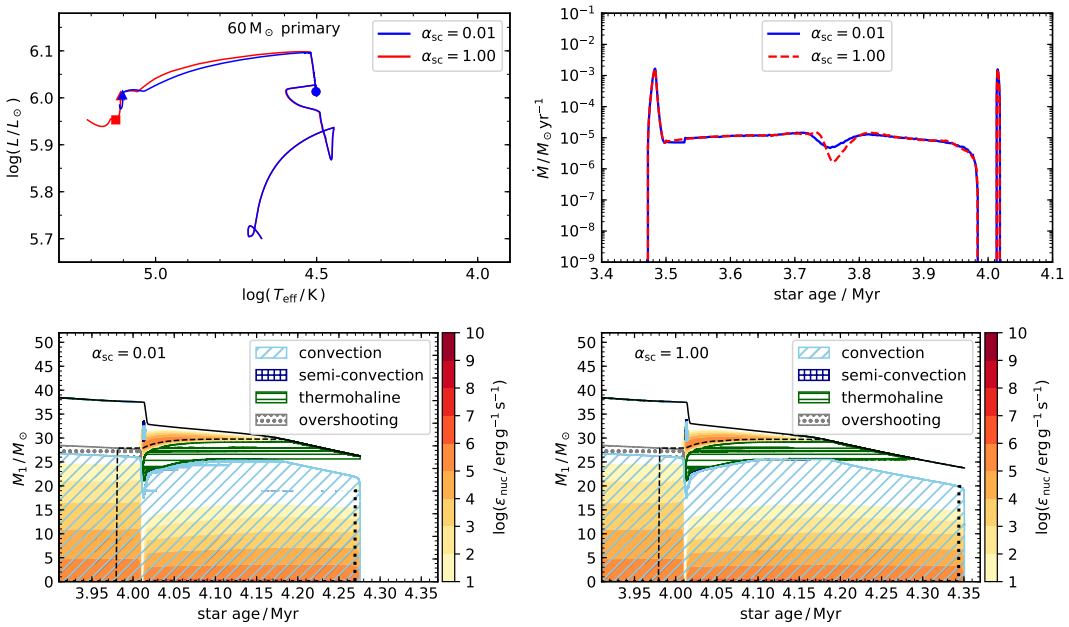

Figure 3.4: *Upper left:* Evolutionary tracks of primary of a binary system with initial masses $M_{1,i} = 60\,M_\odot$ and $M_{1,i} = 42\,M_\odot$ and initial period of 10 d for semiconvection efficiency parameters of $\alpha_{sc} = 0.01$ and $\alpha_{sc} = 1.00$. The circle denotes the point at which the surface hydrogen mass fraction drops below $X_H \leq 0.3$, which is associated to the WNL phase. The triangle marks the point at which the hydrogen-rich envelope is completely stripped of ($X_H = 0.0$), which is associated to the WNE phase. The square represents the beginning of the WC phase as carbon gets visible on the surface with $X_C \geq 0.01$. *Upper right:* Mass transfer rates of the two systems. *Lower left and right:* Kippenhahn-diagrams covering the core helium burning phase for the primary with different α_{sc} values. The solid line is the surface of the star, the dashed line is the helium core mass, and the dotted line is the carbon core mass.

For the SMC grid Wang et al. (2019) concluded that a semiconvection parameter of $\alpha_{sc} = 0.01$ cannot explain the observed WO binary AB8. To see if a more efficient semiconvection parameter is needed for the LMC systems, two binary systems with

different parameters of $\alpha_{sc} = 0.01$ and $\alpha_{sc} = 1.00$ are calculated and compared in Figure 3.4. In the upper left panel, a HRD of both systems is provided. The transitions into the different WR phases WNL, WNE, and WC are labeled by circles, triangles, and squares, respectively. One can see that only the model with the higher semiconvection efficiency is able to produce a WC star. This can be explained by comparing the two Kippenhahn diagrams in the lower panels of Figure 3.4. Here it becomes evident that the longer core helium burning time, caused by the more efficient semiconvective mixing, allows the star to remove more mass from the stellar surface so that carbon gets visible. By having a look at the upper right panel where the mass transfer rate of both systems is shown, one can see that it is modeled in a similar way so that the discrepancies to the aforementioned LMC grid are minimized. Therefore, it is decided to stick to the larger efficiency parameter of $\alpha_{sc} = 1.00$.

MLT++

For the LMC grid, the primaries with helium core masses above $M_{He} > 14\,M_{\odot}$ are modeled with MLT++. During the late evolutionary stages when the stars have large convective regions it is possible that the sound speed in these regions will be approached which decreases the time steps and leads to convergence errors. To deal with this problem Paxton et al. (2013) developed a treatment of convection that reduces the superadiabaticity in radiation-dominated convective regions, known as MLT++. This leads to an more efficient energy transport so that the MESA code can evolve the star until helium depletion.

The secondaries in the LMC grid never got massive enough to exceed this limit and therefore no such criterion was ever applied. However, as the aim is to extend the grid to higher masses, the secondary masses increase as well, implying that these stars also might struggle during helium burning and cause convergence errors. To analyse these kind of issues two binary models with initial primary mass $M_{1,i} = 60\,M_{\odot}$, initial mass ratio $q_i = 0.7$ and initial period of 10 d are calculated. For one system MLT++ is turned on after helium is ignited in the core and the other one is modeled without MLT++. The corresponding evolutionary tracks in the HRD can be seen in Figure 3.5 where the most important evolutionary phases are labeled by numbers.

One can see that as soon as the helium core is ignited (point 4) the evolutionary tracks differ. This can be explained by the more efficient energy transport of MLT++ that changes the stellar structure so that the radius gets smaller and the star appears hotter compared to the model without MLT++. Furthermore, one can see that the model with MLT++ can be calculated until carbon depletion whereas the model without MLT++ cannot even be calculated until helium depletion. Therefore, it is decided that for the secondaries MLT++ is turned on, if the helium core mass is larger than $M_{He} > 14\,M_{\odot}$. The secondaries will be calculated until carbon depletion.

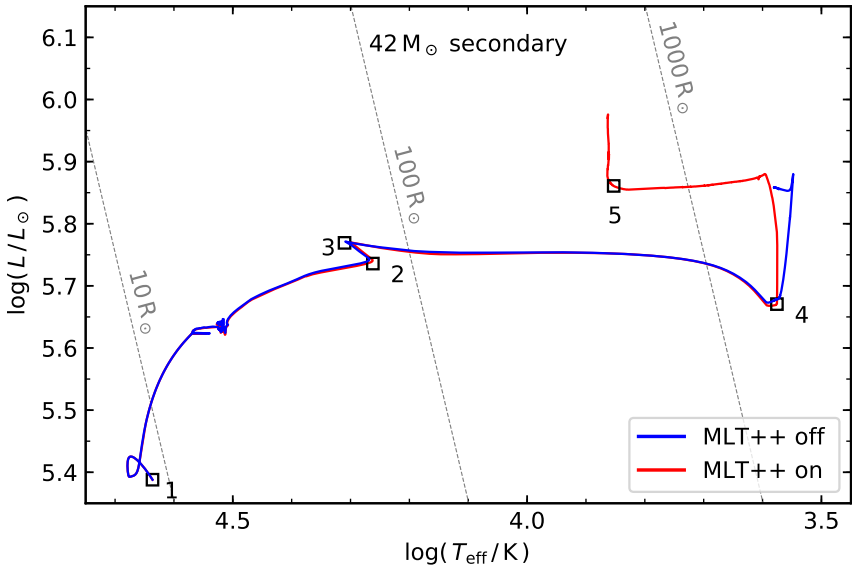

Figure 3.5: Shown are two evolutionary tracks of secondaries where one star is modeled with MLT++ after core helium ignition (red) and one without (blue). The binary system has an initial primary mass of $M_{1,\mathrm{i}} = 60\,M_\odot$, initial mass ratio $q_\mathrm{i} = 0.7$ and initial period of 10 d. The semiconvection efficiency parameter is fixed to $\alpha_\mathrm{sc} = 1$. The numbers 1, 2, 3, 4, 5 correspond to the ZAMS, TAMS, H-shell burning, helium core burning and carbon core burning, respectively.

Numerical Issues During Mass Transfer

While modeling binary systems with initially very massive primaries it became evident that the MESA version 8845, which has been used to calculate the SMC and LMC grid, has some problems if the time steps get to small during the mass transfer phase. In this case, the calculation is stopped. In order to avoid these problems, the newer version 10398 is used as it allows accretion on smaller time steps. An additional reason to use this version is that it fixes a bug that occurred during the contact phase. In the old version, the contact phase was initiated but both stellar components evolved independently.

Even though the newer version allows to have smaller time steps during a mass transfer phase which enables the calculation of almost all systems, new problems arise with this version. For some systems with initially extreme mass ratios $q_\mathrm{i} \rightarrow 0$ the time step during the accretion gets very small leading to some kind of oscillation in the models while they are modeled on a dynamical timescale. This leads to numerical issues where the mass transfer rate is turned off and on again and subsequently shoots up, triggering a limit on the mass transfer rate. In order to avoid these issues the models that showed this behavior are modeled with the old MESA version 8845.

In Figure 3.6 one system that showed this odd behavior is depicted. The binary system has a initial primary mass $M_{1,\mathrm{i}} = 60.3\,M_\odot$, initial mass ratio $q_\mathrm{i} = 0.25$ and initial orbital separation $\log(P_\mathrm{i}/\mathrm{d}) = 1.900$ and is calculated with both versions. On the left side of Figure 3.6 one can see the mass transfer rate and the mass-loss rates of the primary and the secondary. By having a look at the mass accretion of the secondary, one can see that it seems to struggle as some kind of oscillations can be seen. During this phase the time steps get very small, the accretion rate on the secondary oscillates and the mass transfer rate is turned off and on again, followed by a drastic increase which leads to non-physical results. For the older version 8845, the time steps never get that small and the oscillations can be avoided.

In order to check if the MESA version 8845 leads to the same results as the newer version 10398 the most important binary parameters are shown in Figure 3.6. By comparing the slopes of both versions of the mass transfer rate as well as of the mass ratio one can see that the efficiency of mass transfer and the accretion on the secondary modeled in a similar way. Furthermore, one can see that the secondary accretes the same amount of mass and that the mass ratio is for both systems the same. In the lower panels, the orbital separation and period are shown. One can see that the final results seem to be in good agreement. There are some small differences, for example, the mass transfer phase sets in earlier and the accretion is treated in a slightly different way. Nevertheless, as it has no impact on the final binary parameters it can be concluded that the older MESA version 8845 can be used for the systems that show this kind of behavior. All other systems are calculated with the newer version 10398.

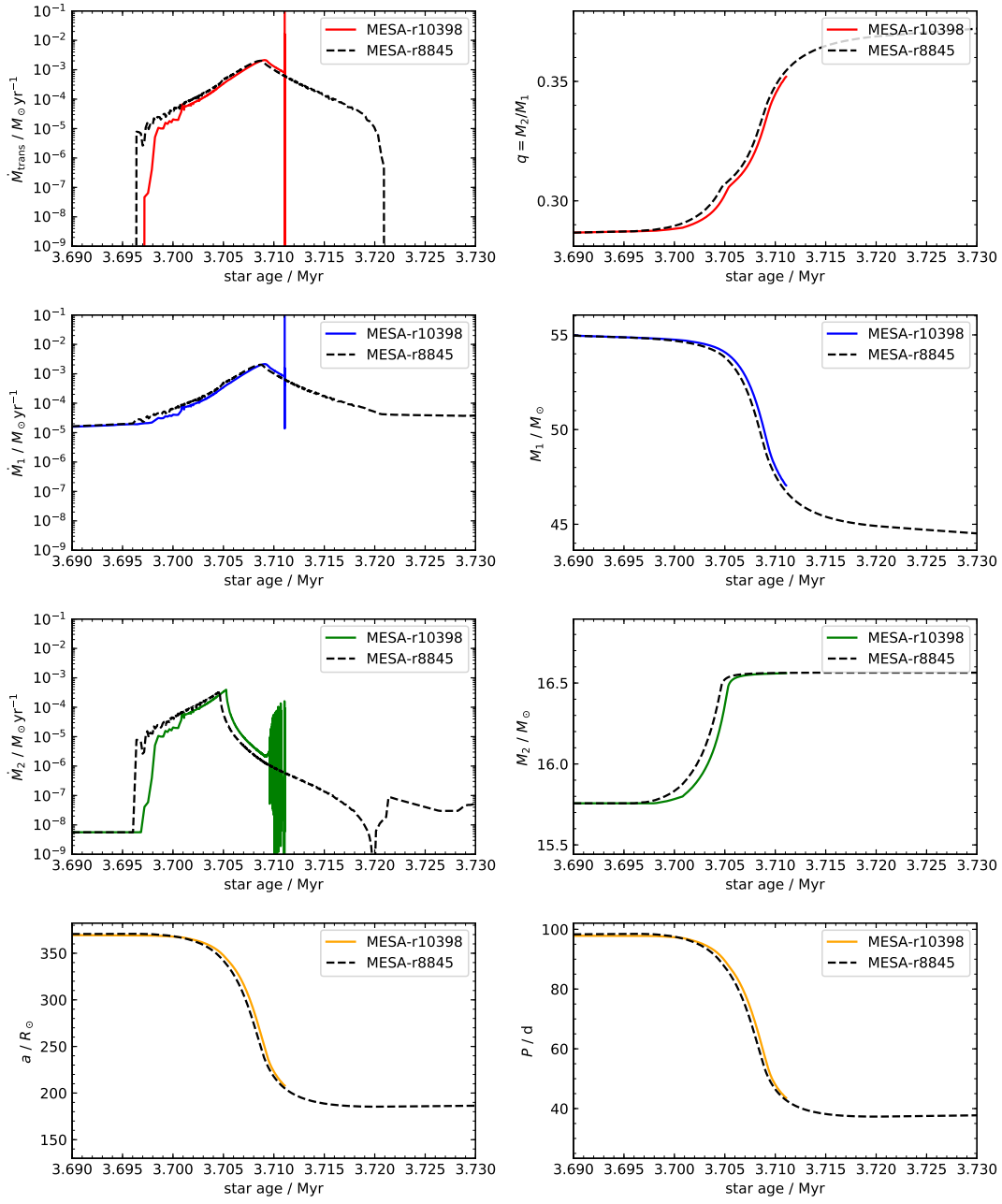

Figure 3.6: Comparison of the binary parameters for the MESA versions 8845 and 10398. The MESA version 8845 is shown as a black dashed line, while version 10398 is shown as a colored solid line. The plot includes the mass transfer rate, the mass-loss rates of each stellar component, the mass ratio as well as the individual masses of the stars and the orbital separation and period.

3.2.2 The Extended LMC Grid

With the aforementioned changes, it is possible to extend the LMC grid. In summary, the changes are as follows: The binary models are calculated with the MESA version 10398. If a model starts to oscillate during mass transfer the older version 8845 is used. To produce WC stars the semiconvection efficiency parameter is set to $\alpha_{\rm sc} = 1$. For helium burning stars with core masses above $M_{\rm He} > 14\,M_\odot$, MLT++ is turned on to avoid convergence errors. The binary models include the same physics of mass-loss, rotation, inflation, and binary interaction as the LMC grid.

The extended grid covers an initial primary mass range $M_{1,\rm i} \simeq 45\,\mathrm{M}_\odot - 71\,\mathrm{M}_\odot$ in steps of $\Delta\log(M_{1,\rm i}/\,M_\odot) = 0.05$. To save computation time, the initial mass ratios cover a range from $q_{\rm i} = 0.25 - 0.95$ in steps of $\Delta q_{\rm i} = 0.05$. The initial orbital periods span over the range of $P_{\rm i} \simeq 1.4\,\mathrm{d} - 10\,000\,\mathrm{d}$ in steps of $\Delta\log(P_{\rm i}/\mathrm{d}) = 0.05$. The upper boundary for the orbital period is chosen in order to include all interacting binary systems.

The phase diagram for binary systems with initial primary mass $M_{1,\rm i} = 60.3\,M_\odot$ is shown in Figure 3.7. The remaining phase diagrams can be found in Appendix C. Comparing this phase diagram with the equivalent of the SMC, shown in Figure 3.3, several differences can be observed. The first thing that should be mentioned is the higher 'Case A/B' boundary. The effect of inflation is metallicity dependent and is present in the LMC models, while the SMC models are still uninflated. Therefore, more binary models with LMC metallicity are expected to fill their Roche lobe while they are on the main-sequence, leading to an up-shift of the 'Case A/B' boundary. Another metallicity dependent property is the mass-loss rate. For the LMC models, the mass-loss rates are higher which means that more mass is lost before the mass transfer begins. This leads to an orbit widening which might help the system to have a stable mass transfer phase. Moreover, more mass is lost from the stars during the mass transfer phase leading to shorter mass transfer phases and therefore potentially more systems that can avoid the upper limit on mass transfer. One can conclude that metallicity driven effects, like inflation and mass-loss have a strong impact on the evolution of massive binary systems.

3.3 Physical Properties of Massive Binary Models

As mentioned in the section above, the influence of metallicity leads to inflated binary models that need to be studied in more detail. Massive stars have fast rotating cores that need to share their angular momentum with the envelope to avoid an angular momentum crisis (Langer 2012). In Section 3.3.1 it will be discussed if the inflated envelope is still coupled with the core during a mass transfer phase and if the mass transfer rates can remove the inflated envelopes of the primaries. From the phase diagrams of the binary grids, it can be seen that almost independently from the initial primary mass

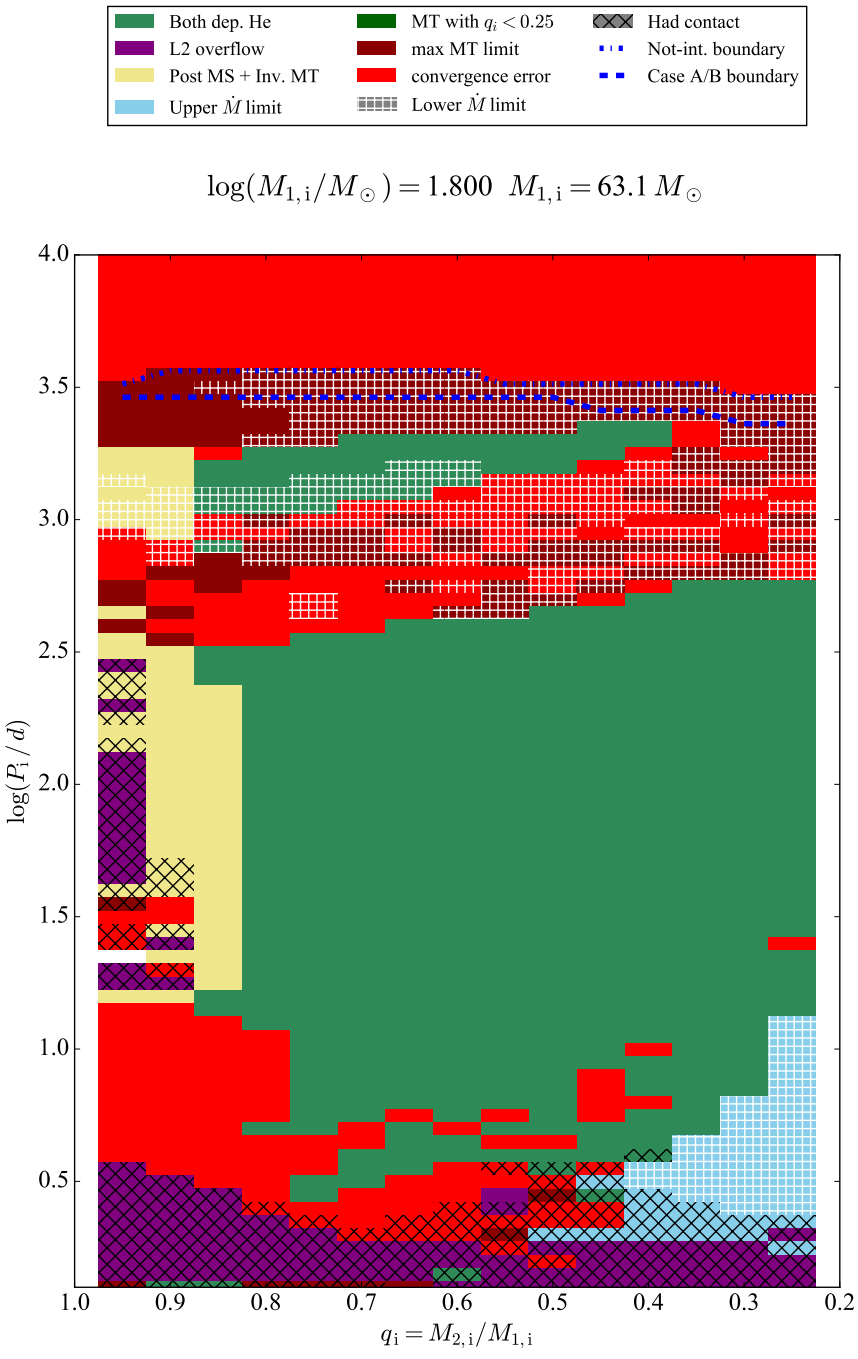

Figure 3.7: Phase diagram of binary models with fixed initial donor mass of $M_{1,\mathrm{i}} = 60.3\,M_\odot$. The initial mass ratio q_i is plotted versus the initial orbital period P_i. All models are calculated at LMC metallicity. The different phases are indicated in the legend and a more detailed description can be found in Section 3.1.1.

most binary systems with initial orbital periods above $P_i \gtrsim 1000\,d$ trigger the maximum mass transfer limit. This seems to be connected with their evolutionary stage and is discussed in some detail in Section 3.3.2. Moreover, by inspecting the phase diagrams of the least and most massive primaries one can see that only a small fraction of the low massive systems can be evolved to carbon depletion whereas for the most massive systems a large fraction can reach this phase. Therefore, the reliability of the upper limit on mass transfer is questioned in Section 3.3.3.

3.3.1 Inflation in Massive Binary Models

Sanyal et al. (2015) discussed the effect of envelope inflation for very massive main-sequence stars at LMC metallicity. As this effect is metallicity driven it gets less important for lower metallicity environments like the SMC. The calculated LMC grid covers initial primary masses of more than $60\,M_\odot$ and therefore the primaries are suspected to have inflated envelopes. These stars get inflated already during the main-sequence implying that mass transfer sets in earlier as in models without inflation.

In the work of Petrovic et al. (2006) it was discussed that large mass-loss rates of stars are capable of removing the inflated envelopes if they exceed the critical value of

$$\dot{M}_{\rm infl} = 4\pi\, r_{\rm core}^2 \rho_{\rm min} \sqrt{\frac{G\,M}{r_{\rm core}}} \tag{3.1}$$

where M is the star mass, $\rho_{\rm min}$ is the lowest density and $r_{\rm core}$ the uninflated radius inside the star. The uninflated radius can be defined as the point where the gas pressure divided by the total pressure gets smaller than $\beta \leq 0.15$ for the first time (Sanyal et al. 2015). As the mass transfer rates are several magnitudes larger than the mass-loss rates of the stars it might be interesting to see if the inflated envelope can be removed during a mass transfer phase.

In Figure 3.8 the evolutionary history of a binary system with an inflated primary star is shown. In the upper left panel, the mass transfer and mass-loss rates of the system are shown as well as the critical values for mass-loss rates for each stellar component. One can see that indeed during the mass transfer phase the critical value is exceeded. In the lower left panel, the strength of the inflation of each star is shown. As expected only the more massive primary shows strong effects of inflation. During the fast case A mass transfer phase the critical value for which the inflated envelope would be removed is exceeded for a short time by the mass transfer rate. However, the time is not long enough and only a small reduction of inflation can be seen in the lower left panel. For the later case AB mass transfer the critical value is exceeded by almost an order of magnitude during the whole mass transfer phase. One can see in the lower left panel that indeed the inflated envelope of the star is removed during this phase.

As the transport of angular momentum is important within a star to avoid an angular momentum crisis, it is of major importance to understand if the inflated envelope still

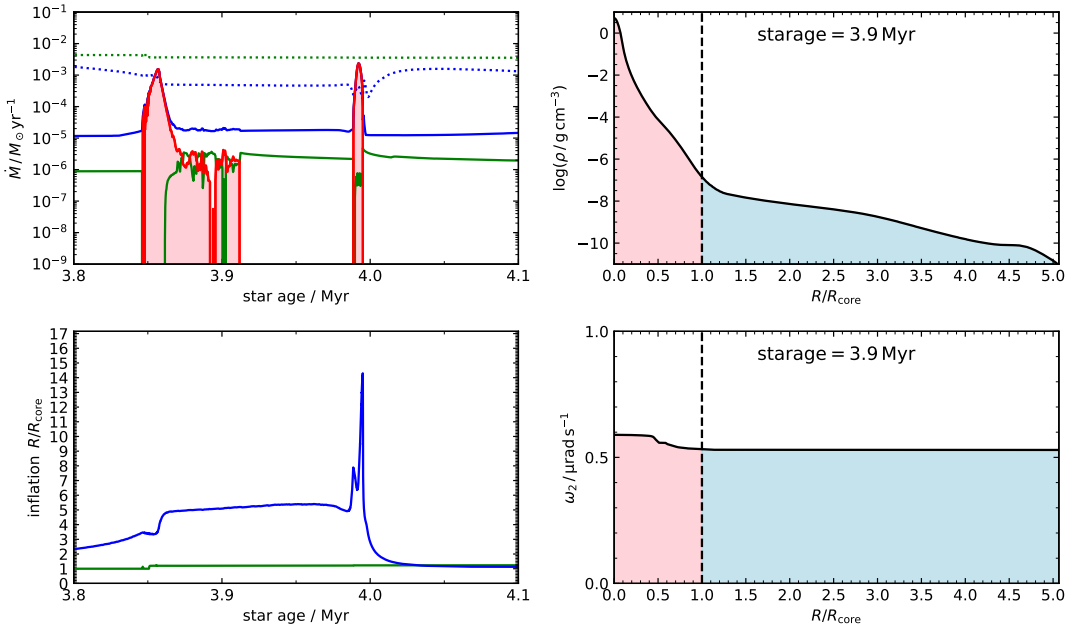

Figure 3.8: Effects of mass transfer rates on the inflation of a binary system with initial primary mass of $M_{1,\mathrm{i}} = 60\,M_\odot$, initial mass ratio $q_\mathrm{i} = 0.7$ and initial orbital period of $P_\mathrm{i} = 100\,\mathrm{d}$. *Upper left*: Mass transfer and mass-loss rates of the primary and secondary. The mass transfer rate is shown as a solid red line, the mass-loss rates of the donor and accretor are shown as blue and green solid lines, respectively. Additionally, the critical value for which the inflated envelope of a star would be removed is shown as dotted blue and green lines for the primary and secondary, respectively. *Lower left*: Inflation of the primary and the secondary as a function of time. *Upper right*: Snapshot of the density profile. The dashed vertical line marks the transition of the uninflated stellar core (pink) and the inflated envelope (blue). *Lower right*: Snapshot of the angular momentum throughout the stellar structure during a mass transfer phase.

can carry the angular momentum of the fast rotating core to the surface or if the envelope and the core are decoupled. To see if the inflated envelope is still able to carry the angular momentum a snapshot of the stellar structure during the slow case A phase is shown on the right side of Figure 3.8. The lower right panel contains information on the angular momentum throughout the star. One can see that the inflated convective envelope carries the angular momentum of the core to the stellar surface. As this system already has gone through an expansion phase, in which the core contracts and spins up and the envelope expands and slows down, the inflated envelope is still coupled to the core and is able to transport the angular momentum. In the upper right panel, one can see the density profile of the inflated star. At the end of the inflated region, a small bump can be identified which is associated with the density inversion that is characteristic for an inflated region.

It is important to mention that the criterion that defines the border of the stellar core and the inflated envelope ($\beta \leq 0.15$) is chosen rather arbitrary and therefore needs to be handled with care. However, the argument that the inflated envelope is coupled to the stellar core still holds, even if the threshold is varied. It also holds true, that the inflated envelope can be removed during a mass transfer phase.

Concerning the stability of mass transfer it is worth mentioning that the inflated envelope is not expected to lead to unstable mass transfer as the inflated region contains less than $< 1\%$ of the total mass. Therefore the mass-radius exponent is not expected to be smaller than the Roche lobes mass-radius exponent.

3.3.2 Mass Transfer During the RSG Phase

In an initially wide binary system with initial periods above $P_\mathrm{i} \gtrsim 1000\,\mathrm{d}$ the primary can evolve to a RSG phase before initiating a mass transfer phase. In this evolutionary phase, the star is extended to several thousand solar radii and has a convective envelope. The RSG is core helium burning and has a hydrogen burning shell. Woods et al. (2011) analyzed the stability of mass transfer in binary systems with a red giant (RG) donor star by using expressions for the mass-radius exponent for condensed polytropes, and the approximation from Soberman et al. (1997) for the Roche lobe mass-radius exponent. They come to the conclusion that only inefficient mass transfer can be stable for RG stars. However, Woods et al. (2011) also note that the used approximation is a more restrictive criterion than is typically used in the literature. To study the behavior of the binary models with a RSG donor star of the LMC grid, the mass-radius exponent of the primary ζ_1 and of the Roche lobe ζ_RL are calculated for each time step by using

$$\zeta_1 = \frac{\mathrm{d}\log R_1}{\mathrm{d}\log M_1} \qquad \text{and} \qquad \zeta_\mathrm{RL} = \frac{\mathrm{d}\log R_{\mathrm{RL},1}}{\mathrm{d}\log M_1} \tag{3.2}$$

where M_1 is the primary mass, R_1 is the primary radius and $R_{\mathrm{RL},1}$ is the Roche lobe of the primary. As an implicit method is used to model the mass transfer one would expect that during a mass transfer phase $\zeta_1 \gtrsim \zeta_\mathrm{RL}$.

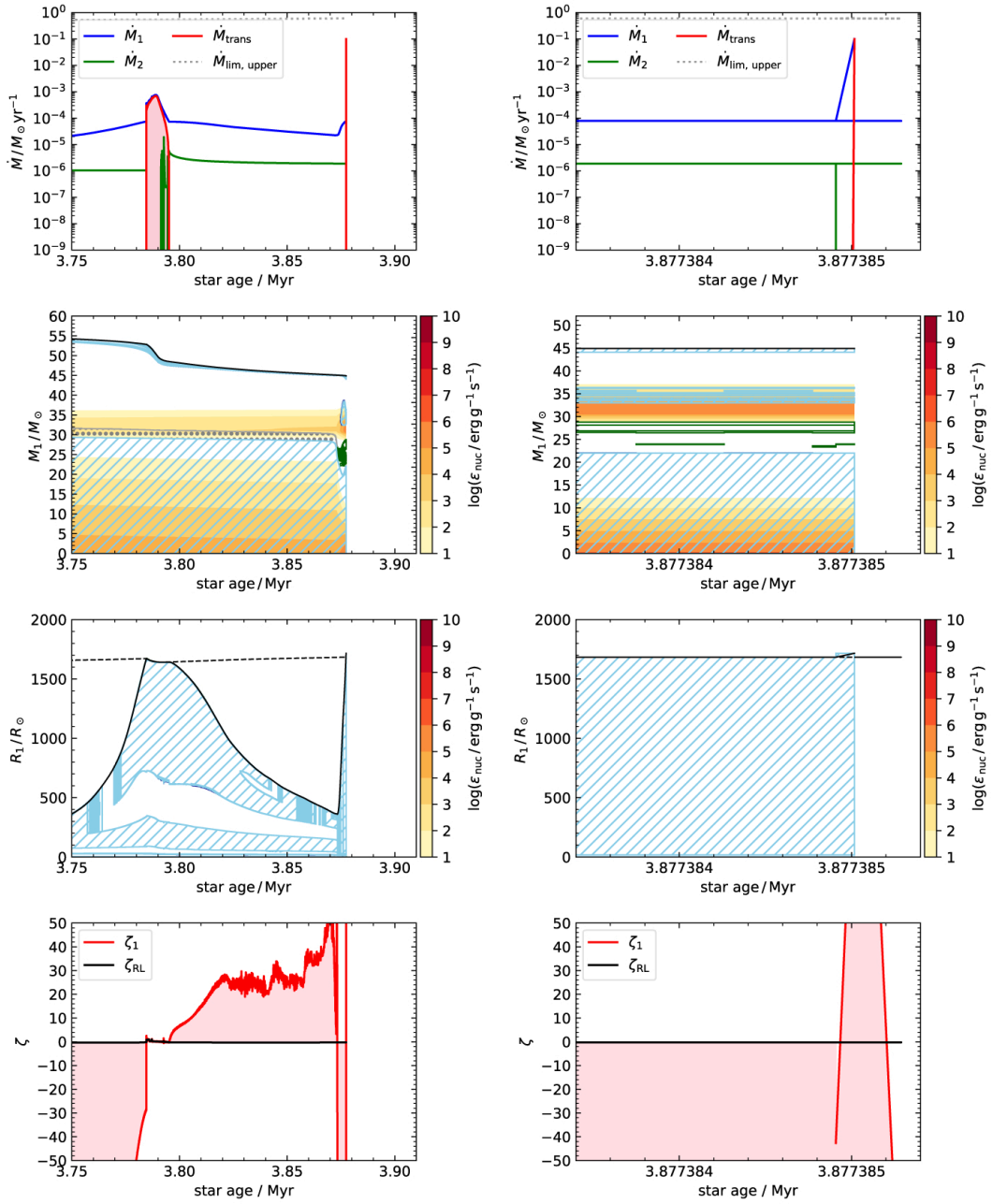

Figure 3.9: Binary system with initial primary mass of 60.3 $M_\odot$, initial mass ratio of $q = 0.7$ and initial orbital period of $\log(P_{\rm i}/{\rm d}) = 3.400$ at LMC metallicity. *Upper left*: Mass transfer and mass-loss rates of the system. *Upper middle left*: Kippenhahn diagram of the primary with the mass coordinate on the y-axis. The convective regions are marked by dashed light blue hatches, semiconvective regions are marked in dark blue, thermohaline mixing is marked by green regions, and overshooting by dotted gray hatches. *Lower middle left*: Kippenhahn diagram of the primary with the radius coordinate on the y-axis. The labels have the same meaning as before. The dashed black line is the Roche lobe radius. *Lower left*: Mass radius exponent of the primary (ζ_1) in red and the Roche lobe ($\zeta_{\rm RL}$) in black. *Right panels*: Zoomed versions of the left panels.

In figure Figure 3.9 a binary system with initial primary mass of 60.3 $M_\odot$, initial mass ratio of $q = 0.7$ and initial orbital period of $\log(P_i/\mathrm{d}) = 3.400$ of the LMC grid is shown. In the upper left panel, the mass transfer and mass-loss rates are shown. One can see that the systems have a stable case A mass transfer and stops as soon as the next mass transfer phase is initiated. In the upper middle panel, the Kippenhahn diagram of the primary with the mass coordinate is shown. One can see that during the first mass transfer phase the star is still core hydrogen burning. In the zoomed-in plot on the right side, one can see that the star is core helium burning during the second mass transfer phase.

In the lower middle panel, one can see the same Kippenhahn diagram with the radius coordinate on the y-axis. The primary already expands on the main-sequence which initiates the first mass transfer phase. The dashed black line marks the Roche lobe radius and it can be seen that the mass transfer rate is adjusted in such a way that the star is held underneath the Roche lobe radius. This phase is followed by a contraction phase until core helium depletion. As a result, the star expands on the dynamical timescale. During this expansion phase, the second mass transfer phase is initiated. By inspecting the lower middle right panel, one can see that for the last time step the star expands above the Roche lobe radius.

In the lower left panel, the mass-radius exponents are shown for each time step. The mass-radius exponent of the primary ζ_1 is shown as a solid red line and the Roche lobes mass-radius exponent ζ_{RL} is shown as a solid black line. In order to know if ζ_1 is larger or smaller than ζ_{RL} the area between the two lines is shaded in pink. One can see that during the first mass transfer phase $\zeta_1 \approx \zeta_{\mathrm{RL}}$ as expected. In the lower right panel, one can see the zoomed-in version for the second mass transfer phase. One should mention that during this phase the model already struggles as for the last time-step the model got into convergence errors and re-tries with a different approach that initiated the mass transfer phase. This can be seen, as the curves have two data points for one time-step. Anyhow, one can see that for the last time step the mass-radius exponent of the primary is smaller than the Roche lobes mass-radius exponent $\zeta_1 < \zeta_{\mathrm{RL}}$ which implies an unstable mass transfer phase leading to a common envelope formation.

One should note that it is not fully understood yet if the problems during this phase are really caused by the faster expanding star or if the problems are of numerical nature. Nevertheless, for the later analysis, it is assumed that these stars have an unstable mass transfer phase leading to the formation of a common envelope.

3.3.3 Reliability of the Upper Limit on Mass Transfer

For the binary models with the initially least massive primaries, one can see that a large fraction of the systems triggers the upper limit on mass transfer. This implies that about 90% of all systems are expected to go through a common envelope evolution. Therefore, one might need to reconsider the reliability of this limit. If this limit is ex-

ceeded, it is assumed that both stars are unable to drive a wind that moves the infalling material to infinity. The upper limit on mass transfer is given by Equation 2.34 and depends on the luminosities of both stars. During a mass transfer phase, the primary star is perturbed and drops out of equilibrium, leading to a drop in luminosity. This causes a drop in the upper limit on mass transfer during the mass transfer phase.

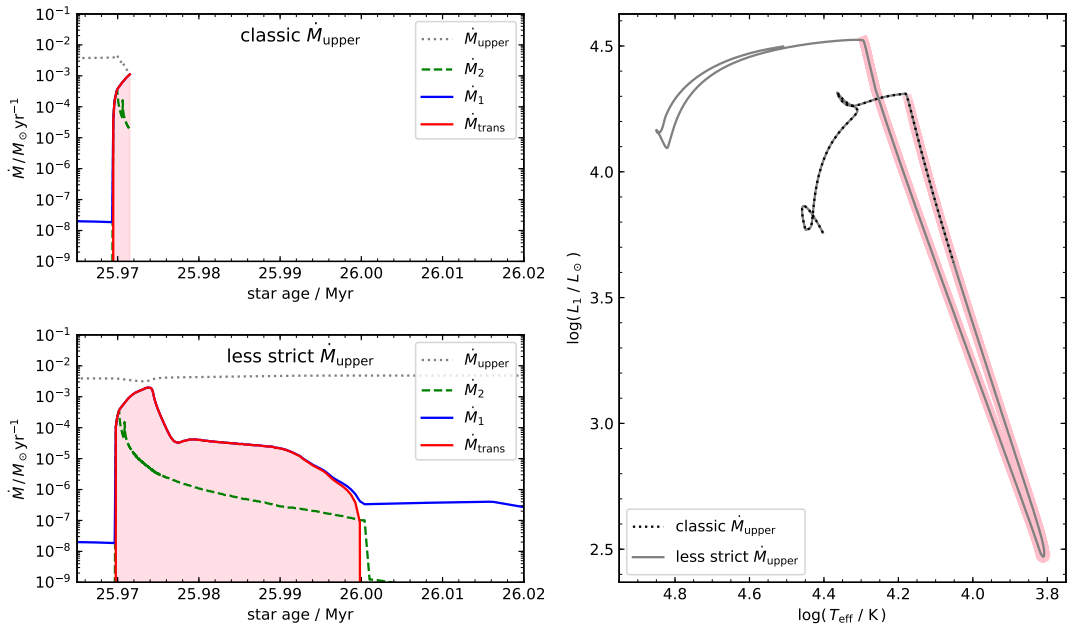

Figure 3.10: Mass transfer rates and HRD of a binary system with initial primary mass of $M_{1,\mathrm{i}} = 10\,M_\odot$, initial mass ratio of $q_\mathrm{i} = 0.6$ and initial orbital period of $P_\mathrm{i} = 10\,\mathrm{d}$ with different criteria for the upper limit on mass transfer. *Upper left*: The upper mass transfer limit is treaded as in Equation 2.34. The system terminates as soon as the limit is reached. *Lower left*: Less strict limit that assumes that the mass can be transferred to infinity after the mass transfer phase when the luminosity of both stars is bright enough. *Right*: HRD of both systems. As the luminosity drops during the mass transfer phase for the classical case the upper limit on mass transfer is reached.

In Figure 3.10 two binary systems with initial primary mass of $M_{1,\mathrm{i}} = 10\,M_\odot$, initial mass ratio of $q_\mathrm{i} = 0.6$ and initial orbital period of $P_\mathrm{i} = 10\,\mathrm{d}$, that have different criteria for the upper limit on mass transfer, are shown. The classical upper limit, given by Equation 2.34, and the corresponding mass transfer rates are shown in the upper left panel. Indeed, during the mass transfer phase, a drop in the classical limit can be observed. On the right panel, the evolutionary tracks of the primaries in the HRD are shown. One can see that for the system that is calculated with the classical limit the luminosity drops.

For the second system, a less strict limit is introduced. The luminosity of the system drops during the mass transfer phase but recovers after the fast mass transfer phase.

This is why, it is assumed that the system transports the infalling material only to a finite distance during the mass transfer phase and as soon as the luminosity rises again, the material will be transferred to infinity. Instead of using the current luminosity, the luminosity in Equation 2.34 is fixed to the value of both stars had at the onset of mass transfer. Therefore, no sharp drop of the upper limit is expected to happen during the mass transfer phase. The mass transfer phase for the system with the less strict limit is shown in the lower left panel of Figure 3.10. Evidently, the system is able to avoid the limit and also the formation of a common envelope. The evolutionary track of the primary is shown in the right panel, validating that after the mass transfer phase the model is even brighter than before, leading to an even higher upper limit of mass transfer.

To test how this new limit changes the fraction of binary systems that avoid the upper limit on mass transfer and therefore the formation of a common envelope, 15 binary models are calculated using the new limit. The initial primary mass for all binary systems is $M_{1,\mathrm{i}} = 10\,M_\odot$. The initial mass ratios cover a range from $q_\mathrm{i} = 0.4 - 0.8$ in steps of $\Delta q_\mathrm{i} = 0.1$. The initial orbital periods cover a range from $\log(P_\mathrm{i}/\mathrm{d}) = 1.000 - 2.000$ in steps of $\Delta\log(P_\mathrm{i}/\mathrm{d}) = 0.500$.

In order to see how the fraction of models that can avoid the upper limit changes the models are plotted over the phase diagram of the LMC grid. The result can be seen in Figure 3.11 where each model is marked by a circle. If a system exceeds the less strict limit on mass transfer, it is crossed out. The boundary for which all systems are expected to exceed the upper limit is marked by a dashed black line. There are still many systems left that form a common envelope. However, the number of systems that can be evolved to carbon depletion of both stars, following this less strict limit, is doubled. Anyhow, this limit is based on very rough assumptions that are not tested yet. Therefore, is recommended to stick to the more reliable upper limit on the mass transfer rates given by Equation 2.34. Nevertheless, one should keep in mind that in case a larger fraction of binary models that can avoid the formation of a common envelope is needed, this less strict limit can be used.

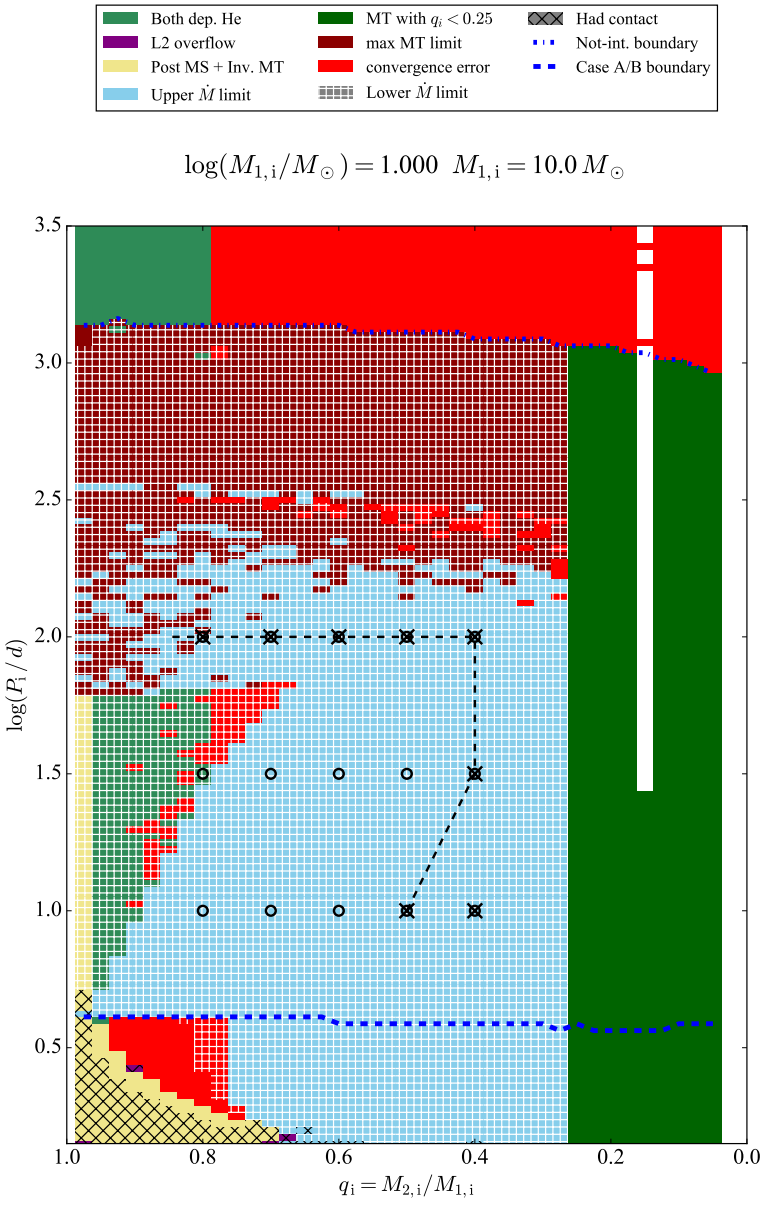

Figure 3.11: Phase diagram of binary models with fixed initial donor mass of $M_{1,\mathrm{i}} = 10\,M_\odot$. The initial mass ratio q_i is plotted versus the initial orbital period P_i. All models are calculated at LMC metallicity. The different phases are indicated in the legend and a more detailed description can be found in Section 3.1.1. The circles mark the systems that are calculated with the less strict upper limit for the mass transfer rate and the crossed-out circles are binary systems that trigger this limit. The dashed black line marks the bounds of the new binary models that could be calculated until carbon depletion if this limit would be used.

4 Common Envelope Evolution for Post Main-Sequence Stars with Main-Sequence Companions

In the previous section, it has already been mentioned that some binary models are expected to go through a common envelope evolution. Many systems with two hydrogen burning stars are suspected to merge. However, there are several binary systems with a post main-sequence donor star that form a common envelope. These systems might be able to eject the common envelope and form a binary consisting of a helium star and a main-sequence companion. Therefore, these systems should be studied in more detail. In Section 4.1 the change of the binding and orbital energies during a mass transfer phase is discussed. Furthermore, it is determined how the fraction of binary systems that can eject the common envelope depends on the current energies in the system. In Section 4.2 the influence of metallicity on the common envelope evolution is discussed by comparing the predictions from the SMC and LMC grids. The resulting binary parameters of systems, that are able to eject the common envelope, are presented in Section 4.3. In Section 4.4 a brief summary of the results is provided.

4.1 Changes of the Binding and Orbital Energy Ratio During Mass Transfer

Section 3.1 and 3.2 show the phase diagrams of the binary models with the initially least massive primary stars. Most of these binary models exceed a limit on mass transfer and are suspected to enter a common envelope phase. If both stellar components are main-sequence stars, they are expected to merge. However, if the primary has evolved off the main-sequence, it is possible that during the spiral-in process the hydrogen-rich common envelope is stripped off. The resulting binary is expected to consist of a helium star and a main-sequence companion in a tight orbit.

In the classical approach, the binding energy and the orbital energy of the system are calculated according to Equation 2.36 and 2.39. For the primary's core mass $M_{1,\mathrm{core}}$ the helium core mass is used which is defined by the boundary where the hydrogen mass fraction drops below 1%. Wellstein (2001) discussed that for close binary systems a large fraction of mass is transferred before the systems enter a common envelope phase whereas for wide binary systems the formation of the common envelope coincides with the onset of mass transfer as the primary has evolved to a RSG phase (see Section 3.3.2). The binary models of Wellstein (2001) are modeled with conservative mass transfer. This is contrary to the models used in this thesis, which only accrete a small fraction of the infalling material. However, the mass that is transferred from the primary which cannot be accreted by the secondary is lost from the system. Therefore, the binding energy is expected to be lowered during a mass transfer phase. This implies that it might be possible that systems that are predicted to merge by the classical

approach might have a successful envelope ejection when taking into account a prior mass transfer phase.

In the lower panel of Figure 4.1 the evolution of the ratio of the binding energy to the orbital energy is shown for a binary model of the extended LMC grid. The initial primary mass is $M_{1,\mathrm{i}} = 63.1\,M_\odot$ and the initial mass ratio and orbital period are $q_\mathrm{i} = 0.7$ and $\log(P_\mathrm{i}/\mathrm{d}) = 2.7$, respectively. The binding energies are calculated with and without the contribution of internal energies and are labeled $E_{\mathrm{bind,u}}$ and $E_{\mathrm{bind,g}}$, respectively. The energy evolution is shown right before the onset of case AB mass transfer. In the upper panel, the evolutionary track of the primary in the HRD is shown. It can be seen that the track has a loop-like feature. This can be explained by the contraction after case A mass transfer followed by an expansion when hydrogen is depleted in the core. This expansion leads to the case AB mass transfer. The mass-loss and mass transfer rates can be found in the middle panel. By inspecting the middle and lower panel, one can see that before mass transfer sets in the ratio of binding energy to orbital energy increases rapidly and reaches a maximum at the onset of mass transfer. During the mass transfer phase the ratio decreases by a factor of 2. This confirms the expectation from above.

In order to study whether this has an effect on the fraction of binary systems that are able to eject their common envelope or not, the previous grids will be used. For this purpose, the SMC models are used because they contain information about the binding energies of the envelope at each time step. Here, the binary models with initial primary mass $M_{1,\mathrm{i}} = 10\,M_\odot$ are used, because a large fraction of these models is expected to enter a common envelope phase. As the impact of metallicity is small for these models the results can also be applied for the LMC grid.

To study the evolution of the binding and orbital energies of the system, the energies are plotted as a function of the initial orbital period. The result can be seen in the upper panels of Figure 4.2. The initial mass ratios cover the range of $q_\mathrm{i} = 0.3 - 0.9$ in steps of $\Delta q_\mathrm{i} = 0.1$ and are indicated by their shade of color. Binary systems with initial mass ratios $q_\mathrm{i} = 0.3$ have the highest transparency while systems with mass ratios $q_\mathrm{i} = 0.9$ have the highest opacity. Only the binary models that enter the common envelope phase with a post main-sequence donor star are shown which explains the lack of case A systems.

By comparing the binding energies of the envelope at the beginning of the mass transfer in the upper left panel with the binding energies at the formation of the common envelope in the upper right panel, it can be seen that the binding energies in the later case are fanned out and do not lie on a straight line. However, this fanning out can only be observed for binary systems with initial orbital periods below $\log(P_\mathrm{i}/\mathrm{d}) \lesssim 2.5$. The scatter of the binding energies originates from the lower value of the upper limit on mass transfer which depends on the luminosity and mass of the secondary and therefore implicitly on the mass ratio. The boundary at $\log(P_\mathrm{i}/\mathrm{d}) \approx 2.5$ can be explained as

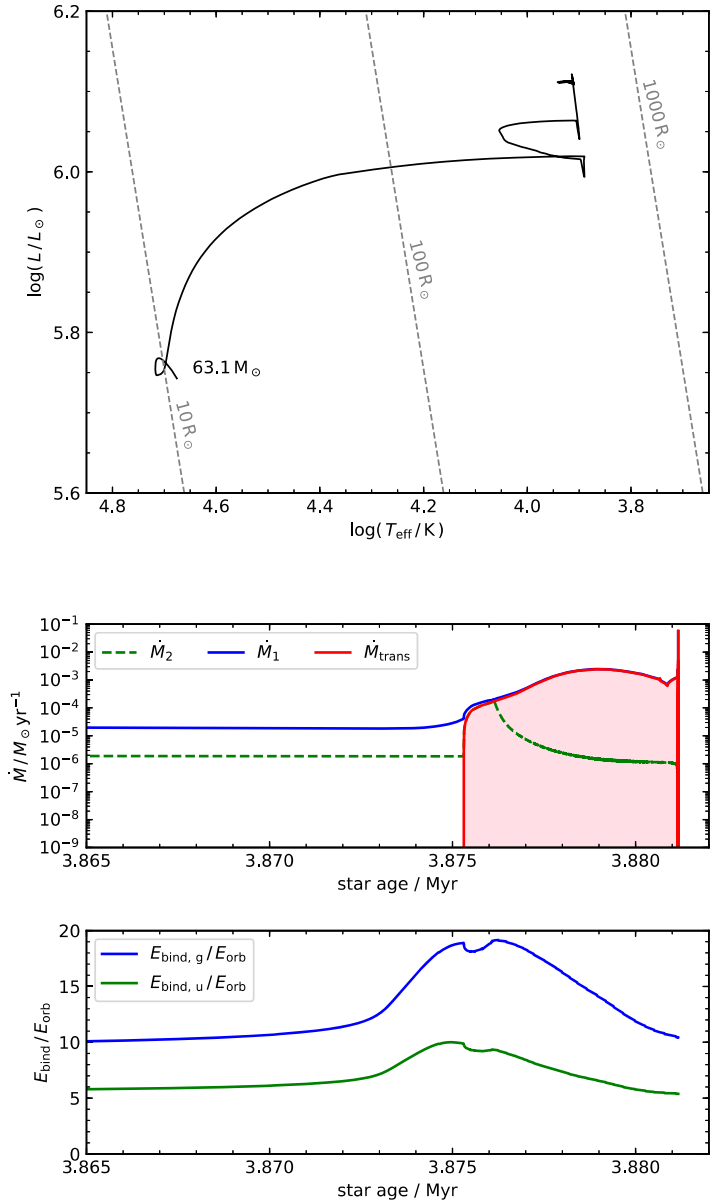

Figure 4.1: Binary model with initial primary mass $M_{1,\mathrm{i}} = 63.1\,M_\odot$. The initial mass ratio is $q_\mathrm{i} = 0.7$ and the initial orbital period is $\log(P_\mathrm{i}/\mathrm{d}) = 2.7$ ($P_\mathrm{i} \approx 500\,\mathrm{d}$). *Upper panel*: Evolutionary track of the primary in the HRD as solid black line. Lines of equal stellar radius are plotted as dashed gray lines. *Middle panel*: Mass transfer and mass-loss rates during the case AB mass transfer. *Lower panel*: Binding energies divided by the available orbital energy of the system. Binding energies without a contribution of the internal energy ($\alpha_\mathrm{th} = 0$) is shown as solid blue line. Binding energies taking into account all internal energies ($\alpha_\mathrm{th} = 1$) is shown as solid green line.

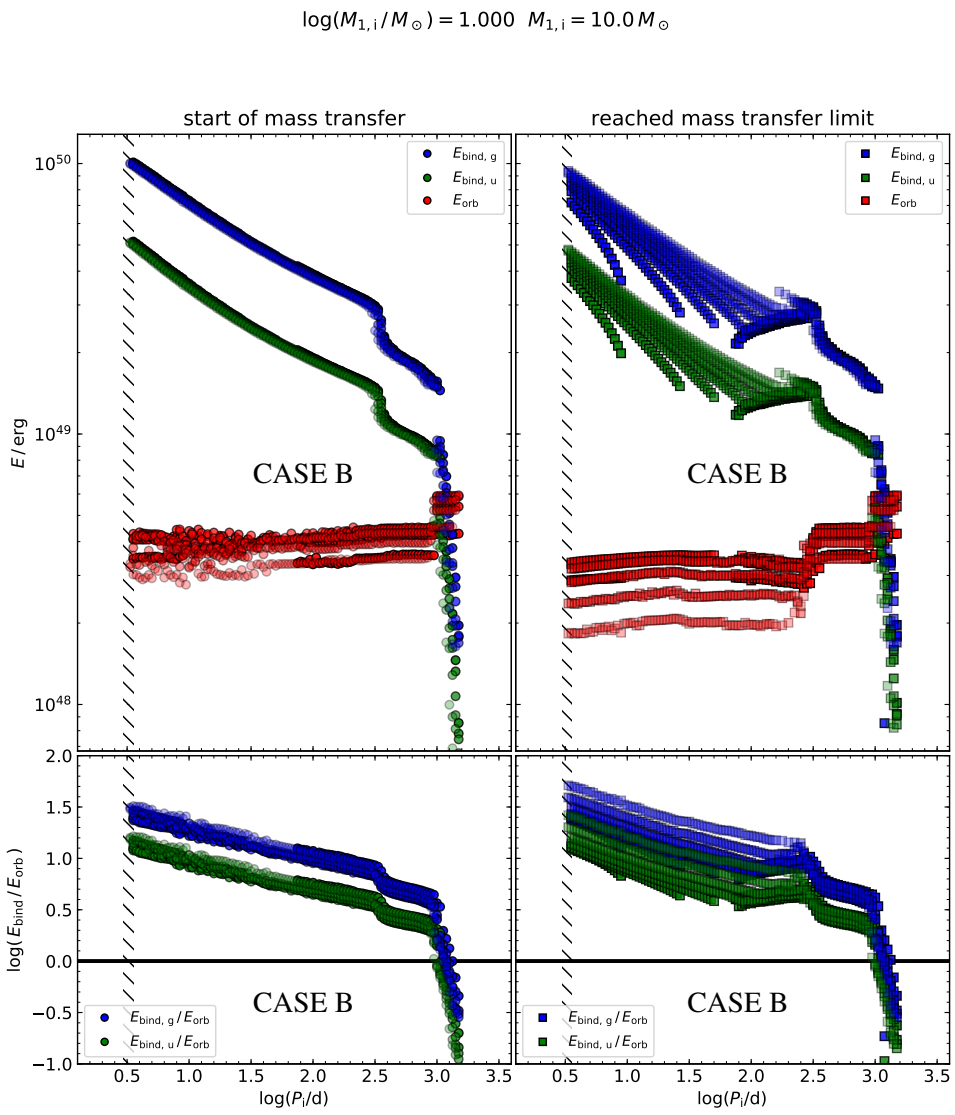

Figure 4.2: Binding and orbital energies of binary models with initial primary mass $M_{1,\mathrm{i}} = 10\,M_\odot$. On the left side, the energies are calculated at the onset of mass transfer and on the right side at the moment when the mass transfer rate exceeds one of the limitations. In the upper panels, the binding energies with and without the contribution of the internal energy as well as the available orbital energy are shown in green, blue, and red, respectively. In the lower panel, the logarithm of the ratio of the binding energy to the orbital energy of each system is shown. The initial mass ratios are indicated by their shade of color. The model with the most extreme initial mass ratio $q_\mathrm{i} \to 0$ is the faintest and the model with a mass ratio close to $q_\mathrm{i} \to 1$ is the most colorful one. The hatched line marks the 'Case A/B' boundary.

the transition between binary systems that have a mass transfer phase before the formation of the common envelope and binary systems that enter the common envelope as soon as mass transfer is initiated.

One can see that the reduction of the binding energy for binary systems with initial mass ratio $q_\mathrm{i} \to 1$ is the strongest. However, as mass is removed from the binary system, this also leads to a reduction of the orbital energy which is strongest for the binary systems with extreme initial mass ratio $q_\mathrm{i} \to 0$. In order to make a more reliable statement on how strong the effect on the reduction of the energies is, one needs to take into account the ratio of the binding energy to the orbital energy. The logarithm of this ratio is shown in the lower panels of Figure 4.2. One can see that the ratio is reduced by up to a factor of 3 for binary systems with an initial mass ratio $q_\mathrm{i} \to 1$. Anyhow, the binary systems with initial mass ratio $q_\mathrm{i} \to 0$ show the opposite behavior. The ratio increases for the most extreme cases by a factor of 1.5.

Even though for some systems the ratio of binding energy to orbital energy is reduced by a factor of 3, none of these systems is able to eject the common envelope. The only systems that are able to expel the common envelope are the binary systems with initial orbital periods above $\log(P_\mathrm{i}/\mathrm{d}) \gtrsim 3.0$. Nevertheless, as most of the ratios of binding energies to orbital energies are reduced, this ratio will be calculated in the further analysis at the formation of the common envelope and not at the onset of mass transfer.

4.2 The Influence of Metallicity on the CEE

In Section 3.3 the influence of metallicity on inflation and mass-loss rates has already been mentioned. Furthermore, it has been pointed out that the effects of metallicity are most dominant at the highest initial masses. It was realized that fewer systems enter the common envelope phase. However, it is not clear if there is an effect on the common envelope evolution for different metallicities. Since this thesis presents binary model grids at SMC and LMC metallicity it gives an ideal basis to test if there are any predicted differences on the common envelope evolution.

Before having a look at higher initial primary masses, the energies of the binary systems with initial primary mass $M_{1,\mathrm{i}} = 10\,M_\odot$ will be compared to see if the predictions of both grids are as similar as expected. The corresponding plots for the SMC models can be found on the left side of Figure 4.3, the LMC models are on the right side. Comparing both sides, they look very similar on first glance. Both show the fanned out binding energies, the reduction in orbital and binding energies are rather similar, as well as the boundary at initial periods of $\log(P_\mathrm{i}/\mathrm{d}) \approx 2.5$. However, by having a closer look at the systems with an initial mass ratio above $\log(P_\mathrm{i}/\mathrm{d}) \gtrsim 3.0$ one can see that for the LMC models a smaller fraction is able to eject the common envelope. This can be explained by the different choice of the efficiency factor of semiconvective mixing which is $\alpha_\mathrm{sc} = 1.00$ for the SMC models and $\alpha_\mathrm{sc} = 0.01$ for the LMC models.

Semiconvective mixing gets important for post main-sequence stars and has a major impact on the structure of these stars including the extent of the convective regions in the envelope (Mowlavi & Forestini 1994).

The extended LMC grid uses a semiconvection parameter of $\alpha_{\rm sc} = 1.00$ and is consistent with the SMC grid. Therefore, no discrepancies can be caused by this effect for the most massive primary stars. The impact of metallicity on the common envelope evolution will be discussed for the binary models with initial primary mass $M_{1,\rm i} = 63.1\,M_\odot$. The corresponding plots can be found in Figure 4.4. For the SMC models, the case A binary systems with initial orbital periods smaller than $\log(P_{\rm i}/{\rm d}) \lesssim 1.5$ are left out, because they trigger the upper limit on mass transfer by their winds, as they evolve towards a WR phase. This seems to be a numerical issue, that does not occur in the LMC grid.

One can see that for the SMC grid only case B systems enter a common envelope phase with a post main-sequence primary and a main-sequence companion. As expected, for the LMC models one can see that there are less common envelope systems. There are several models that enter the common envelope phase during case AB mass transfer. One can see that the binding energies are rather similar for both metallicities. However, the orbital energies for the LMC models are a bit smaller for the case AB systems which might be caused by the prior case A mass transfer.

Contrary to the initially less massive binaries non of these binary models can successfully eject the common envelope. However, the ratio of binding energy, including the internal energy, to the orbital energy is smaller than a factor of 3 for most systems. Taking into account that these are only approximations this is not a large value. Even though the results would imply that no binary system at the largest initial primary masses can eject the common envelope, there are many explanations that can lead to a successful ejection that are not taken into account here. For example, during a RSG phase, there might be eruptions that additionally remove parts of the envelope. These eruptions are only barely understood and it is unclear if they can occur during a common envelope phase. Another example is, that it is assumed that the radius of the common envelope is given by the radius of the primary at the formation of the star. However, the primary is forced to stay underneath the Roche lobe during the mass transfer phase. Therefore, it could be possible that the common envelope is much more extended and has a different binding energy. These are only two examples that show how large the uncertainties of the results are. Anyway, as not many binary systems consisting of a helium star and a main-sequence companion are observed the results are not bad at all. Nevertheless, it should be kept in mind that there are several effects that are not included in our analysis.

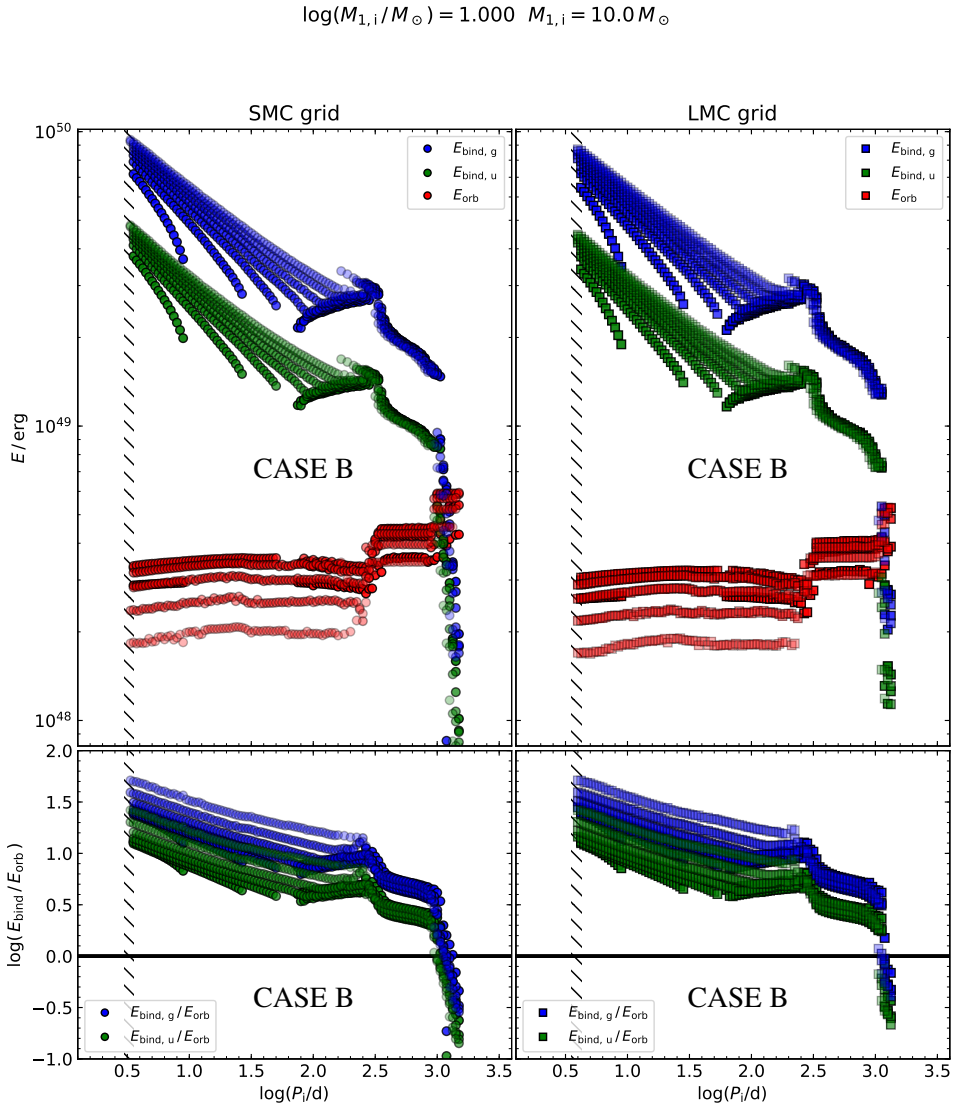

Figure 4.3: Binding and orbital energies of binary models with initial primary mass $M_{1,\mathrm{i}} = 10\,M_\odot$. On the left side the energies of the SMC binary models and on the right side, the energies of the LMC binary models are shown. In the upper panels, the binding energies with and without the contribution of the internal energy as well as the available orbital energy are shown in green, blue, and red, respectively. In the lower panel, the logarithm of the ratio of the binding energy to the orbital energy of each system is shown. The initial mass ratios are indicated by their shade of color. The model with the most extreme initial mass ratio $q_\mathrm{i} \to 0$ is the faintest and the model with a mass ratio close to $q_\mathrm{i} \to 1$ is the most colorful one. The hatched line marks the 'Case A/B' boundary.

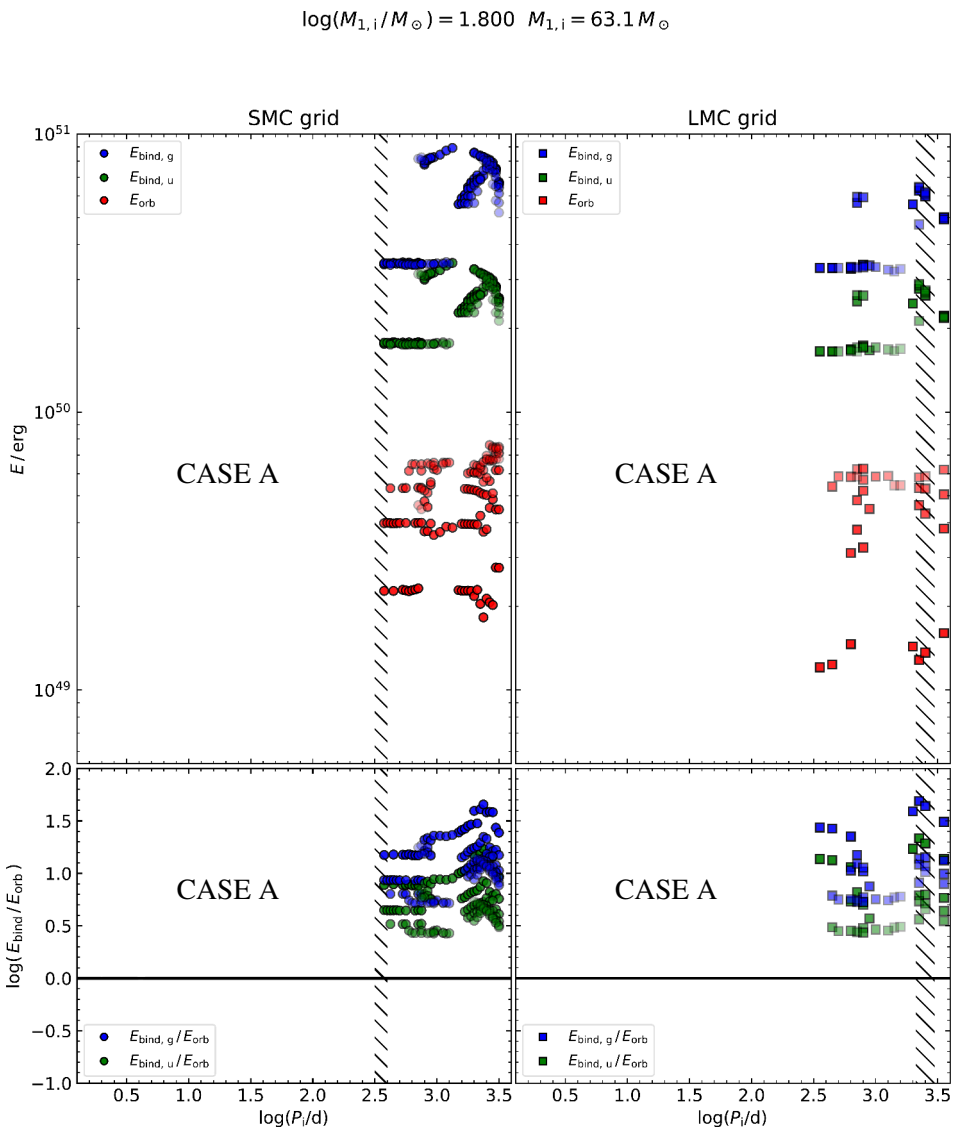

Figure 4.4: Binding and orbital energies of binary models with initial primary mass $M_{1,\mathrm{i}} = 60.3\,M_\odot$. On the left side the energies of the SMC binary models and on the right side, the energies of the LMC binary models are shown. In the upper panels, the binding energies with and without the contribution of the internal energy as well as the available orbital energy are shown in green, blue, and red, respectively. In the lower panel, the logarithm of the ratio of the binding energy to the orbital energy of each system is shown. The initial mass ratios are indicated by their shade of color. The model with the most extreme initial mass ratio $q_\mathrm{i} \to 0$ is the faintest and the model with a mass ratio close to $q_\mathrm{i} \to 1$ is the most colorful one. The hatched line marks the 'Case A/B' boundary.

4.3 Post Common Envelope Parameter

Even though only a small fraction of the common envelope systems is expected to have a successful ejection, it still is interesting in which parameter range the mass ratios and orbital periods are after the ejection. The final binary parameters are calculated according to Equation 2.37 for the binary models that have an orbital energy that is larger than the binding energy with respect to the internal energy $E_{\mathrm{orb}} > E_{\mathrm{bind,u}}$.

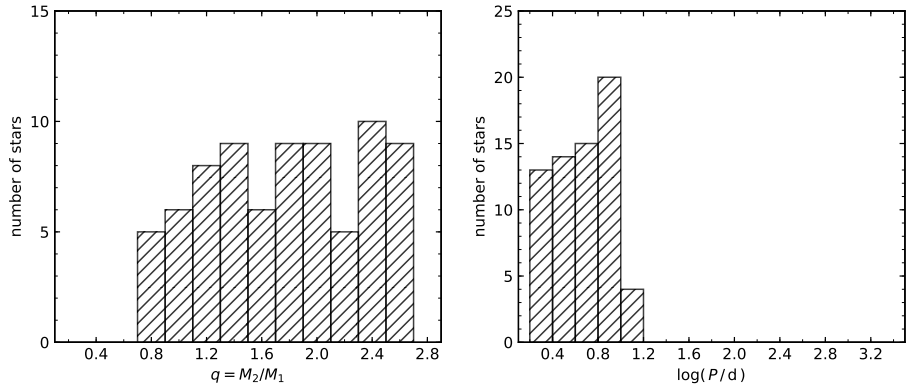

Figure 4.5: Post common envelope parameters for binary models with initial primary mass $M_{1,\mathrm{i}} = 10\,M_\odot$. Left: Histogram of the distribution of the resulting mass ratios. Right: Histogram of the resulting orbital period distribution.

The resulting binary parameters for the models with initial primary mass $M_{1,\mathrm{i}} = 10\,M_\odot$ are presented in Figure 4.5. On the left side, one can see the final mass ratios which seem to be distributed uniformly for mass ratios above $q \gtrsim 1$. This implies, under the assumption that the helium core has almost the same mass for all models, that a successful ejection for these systems is independent of the initial mass ratio. The final orbital periods are, as expected, in the order of a few days $P = 1.5\,\mathrm{d} - 10\,\mathrm{d}$. Using a different selection criterion, for example taking into account the binding energy without any contribution of the internal energy $E_{\mathrm{bind,g}}$ would lead to closer orbits as more orbital energy needs to be deposited in the envelope in order to eject it.

4.4 Summary

In this section, it was established that for binary systems with intermediate orbital periods the ratio of the binding energy to the orbital energy can be reduced by up to a factor of 3 due to a prior mass transfer phase. It is therefore important to estimate this ratio at the formation of the common envelope and not at the onset of mass transfer. However, the effect is too small to lead to a successful envelope ejection for the studied systems. A successful ejection is most likely during the RSG phase of a primary where the binding energy of the envelope is smallest. Anyhow, for the initially most massive

primary stars, no successful ejections are predicted using this method. Nevertheless, there are large uncertainties in the process of a common envelope evolution that might not be taken into account and would lead to a successful ejection. The final mass ratios are expected to be distributed uniformly and the orbital periods are expected to be in the order of a few days.

5 Population synthesis of WR stars in the LMC

Due to their high mass-loss rates during their entire life, massive single stars are able to strip off their hydrogen-rich envelope leading to the formation of a WR star. mass-loss is weaker for low metallicity environments and plays a crucial role in the stripping process. Therefore, the minimum initial mass that is needed by a single star to form a WR wind increases with decreasing metallicity. Observations show that there are WR stars that cannot be explained by a single star channel (Shenar et al. 2020). In order to explain these WR stars, it is assumed that most of them have formed due to binary interaction that removes the hydrogen-rich envelope. In this thesis, a large grid of very massive binary systems, including single star models, is calculated. Therefore, these binary models in combination with single star models can be used for a population synthesis to see if the observed WR population of the LMC can be reproduced.

Section 5.1 gives a brief overview of the observed WR stars, separated by their individual subclasses, that are used in the later analysis. In Section 5.2 it will be tested if the binary models are able to explain the observed luminosity range of the WC stars by comparing the evolutionary tracks and the evolutionary stages of the stellar models to the observed WR stars. It will be seen that the binary models of the previously calculated binary grid are not able to explain the observed WC stars. With the objective to determine if a stellar model appears as a WR star or not, a criterion based on the optical thickness of the stellar wind will be introduced in Section 5.3. In Section 5.4 a new grid of binary models that uses a different mass-loss recipe for the WR stars is presented. A discussion of the matches and discrepancies between the synthesized models and the observations is given in Section 5.5. Section 5.6 provides a short summary of the results of the performed stellar population synthesis.

5.1 Observations

As already mentioned, classical Wolf-Rayet stars are core helium burning stars that have lost their hydrogen-rich envelope. Furthermore, these stars have very strong optically thick winds which make it impossible to directly observe their surface. Nevertheless, it is possible to obtain the properties of the star from stellar atmospheric models. From these models one can determine the luminosity L, the "stellar radius" $R_\star$, and "stellar temperature" $T_\star$, which are associated with the radius and the temperature of the star at a given optical depth inside the wind. The following section presents the results of recent works that studied WN and WC stars in the LMC.

5.1.1 The WN sample

Hainich et al. (2014) performed an analysis of the known 108 WN type stars in the LMC. The sample contains 17 confirmed binaries and 22 WR stars which are suspected to be in a binary system. The sample of the WN type stars is suspected to be nearly

complete. Hainich et al. (2014) analyzed the WN spectra with the help of the Potsdam Wolf-Rayet (PoWR) atmospheric models and determined their stellar properties. The results of the most important parameters from that paper which are used during the later analysis are listed in Table 1. The uncertainties of the parameters are not discussed in Hainich et al. (2014), however from the results of the galactic WN stars which are studied by Hamann et al. (2019) one can estimate the typical uncertainties to be $\Delta \log(L/L_\odot) = 0.2$ for the luminosities and $\Delta \log(T_\star/kK) = 0.05$ for the temperatures. The uncertainties in the temperature that is available in the literature correspond to the spacing of the atmospheric models that are used for the analysis. As the uncertainty of the temperature is rather small it should be handled with care.

A HRD with all observed WN stars is shown in Figure 5.1. One can see that the hydrogen-free WN stars are all located at higher temperatures while hydrogen-rich stars have cooler stellar temperatures. Another feature that can be seen is that the WN stars only populate the bright part of the HRD. No WR star is observed with a luminosity below $\log(L/L_\odot) \leq 5.25$. This threshold is understood as a transition from optically thin to optically thick winds which makes the WR stars visible in the optical range. One can see that the most luminous stars are in binary systems whereas the less luminous stars are either apparently single or in a binary system. Furthermore, one can see that the faintest star is an apparently single star.

5.1.2 The WC sample

In addition to the WN stars the LMC contains 24 known WC type stars. Only a small fraction of them have been analyzed with the PoWR code by Gräfener et al. (2013) and Ramachandran et al. (2018). However, the absolute visual magnitudes of all 24 WC stars are obtained by Bartzakos et al. (2001a). With the aim of calculating the absolute visual magnitudes of the observed stars a bolometric correction of $M_{\mathrm{bol}} = 4.5$ (Smith et al. 1994) is applied. The results are listed in Table 2. The uncertainties in the estimates of the luminosities are about $\Delta \log(L/L_\odot) = 0.3$, which is similar to the uncertainties from stellar atmospheric models (Sander et al. 2012). Reference values from Gräfener et al. (2013) and Ramachandran et al. (2018) are listed in addition to the calculated luminosities in Table 2. One can see that the discrepancy for the single stars is rather small and within the given uncertainties, although the obtained luminosity for BAT99 53 differs by $\Delta \log(L/L_\odot) = 0.5$. As only information about the luminosity of the WC stars is available, the positions in the HRD in Figure 5.1 are indicated by arrows. Evidently, the most luminous WC stars are in binary systems. This could cause a systematic error because the spectrum might be diluted by the companion. Anyhow, the WC stars cover almost the same luminosity range as the WN stars. The faintest observed WC star has a luminosity of $\log(L/L_\odot) = 5.4$. This threshold can be explained by the fact the least massive stars that can produce WN stars neither have strong enough winds to strip their helium envelope nor efficient enough mixing to have a carbon mass fraction at the surface that could be observed via the characteristic

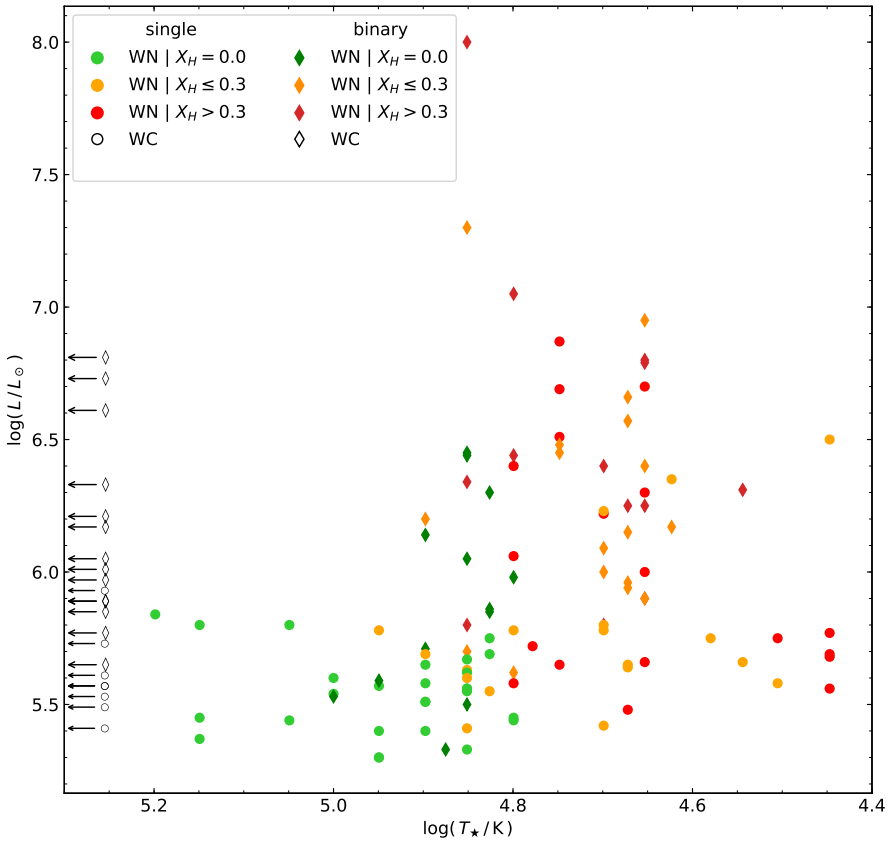

Figure 5.1: Luminosity of the observed WN and WC stars plotted against the stellar temperature. Circles denote apparently single stars and diamonds WR stars in binary systems. Hydrogen-free WN stars are marked in green, hydrogen-rich WN stars are colored by their surface hydrogen abundance in orange and red for $X_\mathrm{H} \leq 0.3$ and $X_\mathrm{H} > 0.3$, respectively. Since only the luminosities of the WC stars are available, their corresponding positions in the HRD are marked with arrows at the given luminosity.

emission lines of WC stars (Langer 2012). For the upper luminosity limit, one might argue that the most massive stars have such massive envelopes that they are unable to fully strip them and therefore never appear as hydrogen-free WN or WC star (Langer 2012).

5.2 Problems with the Previous Grid

With the objective to get a first impression of how the previously calculated binary models compare to the observations, the stellar evolutionary tracks of the primaries for systems with initial mass ratio $q_\mathrm{i} = 0.7$ and an initial orbital period of $P_\mathrm{i} = 100\,\mathrm{d}$ are shown in Figure 5.2. The stellar evolutionary tracks are color-coded according to their surface hydrogen and carbon mass fraction in order to distinguish the different WR phases. The WN phases are divided into three groups: Stars with a surface hydrogen mass fraction in the range of $0.3 < X_\mathrm{H} \leq 0.7$ are colored red, stars with a surface hydrogen mass fraction of $0.0 < X_\mathrm{H} \leq 0.3$ are colored orange, and stars without hydrogen on the surface $X_\mathrm{H} = 0.0$ are colored green. If in addition to that a star has a surface carbon mass fraction of $X_\mathrm{C} \geq 0.01$, it is associated to a WC phase and is colored in blue. In the background, the observed WR stars are plotted. One can see that only the model with initial primary mass $M_{1,\mathrm{i}} = 70.8\,M_\odot$ can produce a WC star. The rest of the models cannot explain the less luminous WC stars. This is indeed a problem and the grid cannot be used to reproduce the observed WR stars.

The origin of this problem most likely lies in the large uncertainties of the Wolf-Rayet winds which are the main mechanism of the envelope stripping process. For the Wolf-Rayet mass-loss rates many different recipes that assume different clumping factors inside the wind or differentiate between the individual WR phases are available in the literature. In the work of Yoon (2017) the most popular mass-loss recipes for WN and WC stars are combined to get a more sustainable mass-loss recipe. Moreover, the influence of the clumping factor is discussed and it is recommended to use a clumping factor of $D = 4$ to reproduce the observations of the galactic WN and WC stars.

As the mass-loss recipe that is used for the previous grid is mostly thought to be valid for WN stars and uses a clumping factor of $D = 10$, it should be no surprise that the models do not fit the observations. In order to check whether the mass-loss recipe of Yoon (2017) with a clumping factor of $D = 4$ can produce the observed WR stars in the LMC, binary models with an initial mass ratio of $q_\mathrm{i} = 0.7$ and an initial orbital period of $P_\mathrm{i} = 100\,\mathrm{d}$ are calculated. The result can be seen in Figure 5.3 with the same color-code as above.

One can see now that the observed luminosity range of the WC stars can be explained by the new models. Only the least massive model does not evolve into a WC star. Even though these exemplary models are not able to produce the faintest WC star, this is not worrisome as the mass transfer efficiency depends on the initial orbital period as well as on the mass ratio. Therefore, binary systems with more efficient mass transfer phases

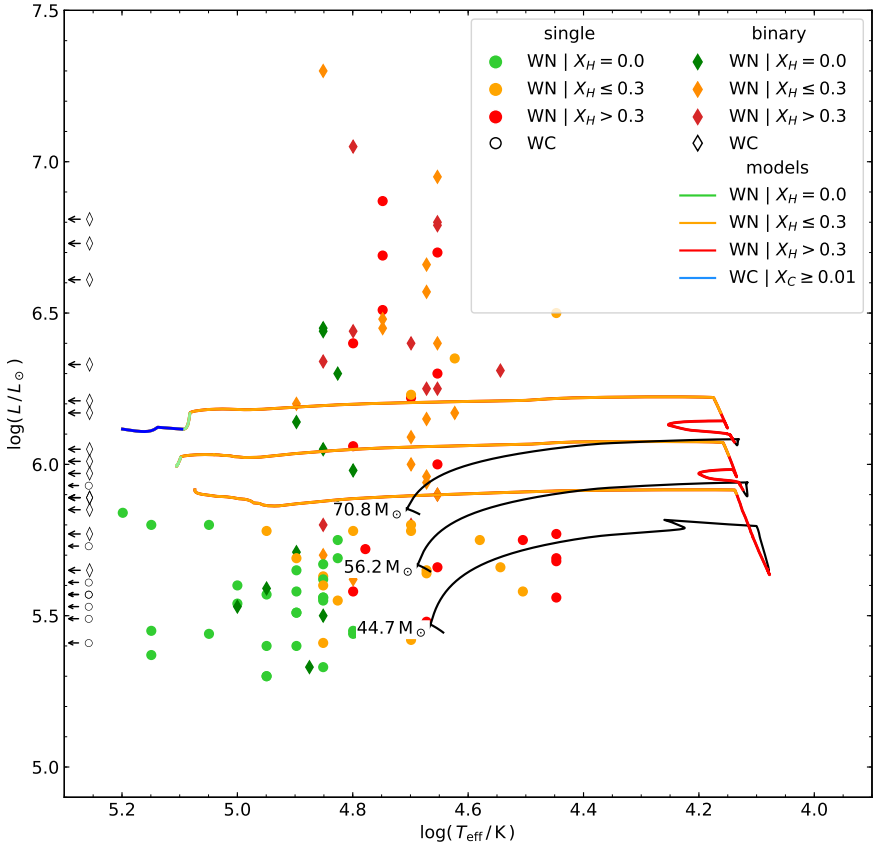

Figure 5.2: Luminosity plotted versus the effective temperature of the binary models. Stellar evolutionary tracks of the binary models are color-coded in green, orange, red and blue to mark the different WR phases. In the background are the observed WN and WC stars with the same labeling as in Figure 5.1. It is assumed that the stellar temperature can be used as the effective temperature of the WR star.

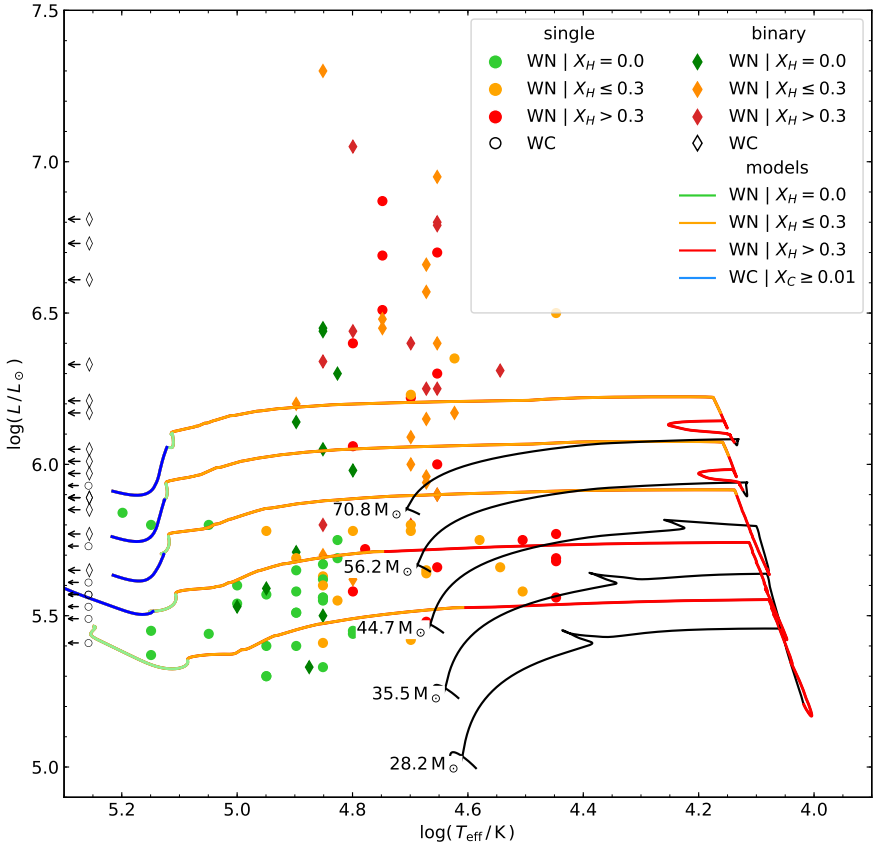

Figure 5.3: Luminosity plottet versus the effective temperature of the binary models. Stellar evolutionary tracks calculated with the mass-loss rates for WR stars according to Yoon (2017). The color-scheme is the same as in Figure 5.2. In the background are the observed WN and WC stars with the same labeling as in Figure 5.1. It is assumed that the stellar temperature can be used as the effective temperature of the WR star.

are likely to produce the fainter WC stars. This leads to the conclusion that the WR mass-loss rates in the previous grid are underestimated and in order to reproduce the observed WR stars one needs to calculate a new grid. However, to save computation time and to decide whether a model will be observed as a WR star or not one needs a criterion that determines the lowest initial mass that is needed to produce a WR star.

5.3 Optical Depth of WR Winds

For a Wolf-Rayet star to be observable as such it needs an optically thick wind that can produce the strong emission lines that are characteristic for these stars. In this section, the optical thickness of the winds, which can be described theoretically, is used as a criterion that determines if a star would be visible as a WR star or not. Shenar et al. (2020) discussed that the luminosity of the faintest observable WR star is inverse proportional to metallicity. They find that the faintest WR stars of the SMC, LMC, and Milkyway (MW) have a luminosity of $\log(L/L_\odot) = 5.6$, 5.25 and 4.9, respectively.

To describe the wind of a WR star is assumed that the wind velocities can be expressed as a β-type wind velocity law

$$v(r) = v_\infty \left(1 - \frac{R}{r}\right)^\beta \tag{5.1}$$

where v_∞ is the terminal wind velocity and β is the exponent of the wind velocity law. R is the radius of the star and r is the radius coordinate. In the works by Gräfener et al. (2017) and Vink et al. (2001) the authors, who analysed WC and OB stars, respectively, use a value of $\beta = 1$. Therefore, in the further analysis, it is assumed that the wind velocity laws of all WR stars can be described by this exponent.

Following this assumption on the wind velocities the optical depth of the wind can be calculated according to Langer (1989)

$$\tau(r) = \frac{-\kappa \dot{M}}{4\pi R(v_\infty - v_0)} \ln\left[1 - \frac{R}{r}\left(1 - \frac{v_0}{v_\infty}\right)\right] \tag{5.2}$$

The optical thickness depends on the opacity κ of the wind, the mass-loss rate $\dot{M}$, the radius of the star R, the radius coordinate r, the terminal wind velocity v_∞ and the expansion velocity at the stellar surface v_0. The opacity of the Wolf-Rayet winds can be approximated by the electron scattering opacity $\kappa_{\mathrm{es}} = 0.20(1 + X_{\mathrm{H}})\,\mathrm{cm^2\,g^{-1}}$. The expansion velocity at the surface of a star is typically $v_0 = 20\,\mathrm{km\,s^{-1}}$ Langer (1989). To get the terminal wind velocity for hydrogen-free WN stars one can use its correlation with the escape velocity which is given by $v_\infty = 1.3\,v_{\mathrm{esc}}$ (Gräfener et al. 2017). The mass-loss rates are calculated according to Equation 2.10 and with the aim of getting the radius of a hydrogen-free WN star the mass-luminosity and the mass-radius relation from Langer (1989) can be used

$$\log \frac{M_{\mathrm{WNE}}}{M_{\odot}} = -0.158206 - 0.053868 \log \frac{L_{\mathrm{WNE}}}{L_{\odot}} + 0.055467 \left(\frac{L_{\mathrm{WNE}}}{L_{\odot}} \right)^2 , \tag{5.3}$$

$$\log \frac{R_{\mathrm{WNE}}}{R_{\odot}} = -0.651411 + 0.639656 \log \frac{M_{\mathrm{WNE}}}{M_{\odot}} - 0.023537 \left(\frac{M_{\mathrm{WNE}}}{M_{\odot}} \right)^2 . \tag{5.4}$$

By combining the above-mentioned equations one can get a theoretical estimate of the optical thicknesses of hydrogen-free WN stars as a function of luminosity and metallicity. The least luminous WR stars of the SMC, LMC and MW are used to see how this theoretical model compares to observations. Figure 5.4 shows the theoretical optical depths of the stellar winds of hydrogen-free WN stars in the plane of the luminosity and metallicity.

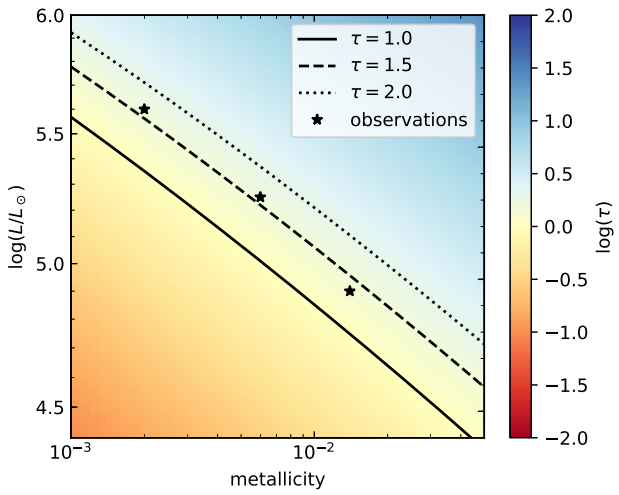

Figure 5.4: Plot of the theoretical optical depth of stellar winds of helium stars as a function of luminosity and metallicity. The metallicity is on the x-axis and the luminosity on the y-axis. The theoretical optical depths of helium stars are shown as colors in the background. The lowest observed hydrogen-free WN star luminosities from Shenar et al. (2020) with 5.6, 5.25, and 4.9 in the SMC, LMC, and MW, respectively are shown as star-shaped symbols. Lines of equal optical thickness of hydrogen-free WN stars are shown for values of τ = 1.0, 1.5 and 2.0 as solid, dashed and dotted lines, respectively.

This simple theoretical model indicates that the threshold optical depth that determines weather a star appears as a WR star is $\tau = 1.5$. This value will be used as a criterion in the later synthesis to determine if a stellar model would be observable as WR star or not. As a new binary grid needs to be calculated in order to reproduce the observed WC luminosity range, this criterion will be used to determine the lowest initial primary mass that is needed for a model to be observable as a WR star.

For the purpose of using this criterion for the calculated binary models, some preparations need to be done. The correlation between the terminal wind velocity and the escape velocity is not constant during the evolution of a star. Therefore, one needs to differentiate between the different evolutionary phases and has to adjust the value of the correlation between the terminal wind velocity and the escape velocity. For OB stars with effective temperatures in the range of $12\,500\,\mathrm{K} \leq T_{\mathrm{eff}} \leq 22\,500\,\mathrm{K}$ Vink et al. (2001) found that the correlation can be expressed as $v_\infty = 1.3\,v_{\mathrm{esc}}$. Regarding hydrogen-rich WN stars, no such correlation has been derived yet. In this work, it is assumed that for these stars the correlation of $v_\infty = 1.3\,v_{\mathrm{esc}}$ that is valid OB type stars and hydrogen-free WN stars holds true for the hydrogen-rich WN stars. For WC stars Gräfener et al. (2013) found a steeper correlation of $v_\infty = 1.6\,v_{\mathrm{esc}}$. Using these correlations and the output from the models it is now possible to calculate a phase diagram that shows which systems will be visible as WR stars.

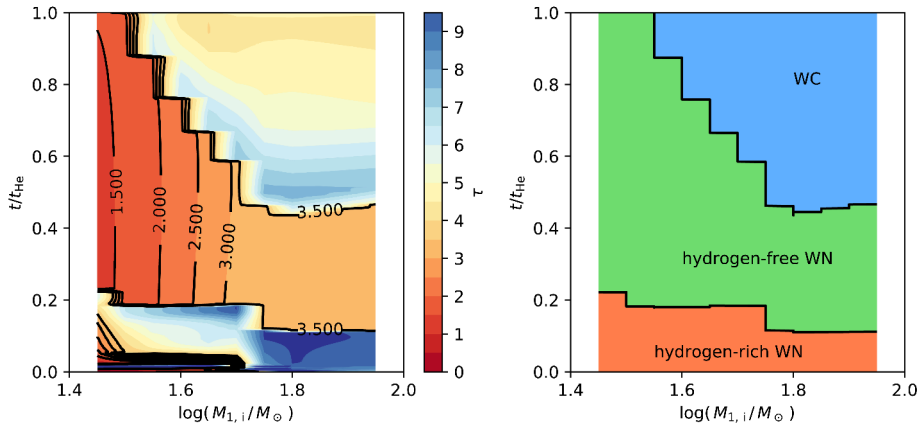

Figure 5.5: Optical depth and phase diagram of binary models with initial primary masses ranging from $\log(M_{1,\mathrm{i}}/\,M_\odot) = 1.450 - 1.950$. All systems have an initial mass ratio of $q_{\mathrm{i}} = 0.5$ and an initial orbital period of $P_{\mathrm{i}} = 10\,\mathrm{d}$. *Left*: On the y-axis is the fraction of the core helium burning time of the primary. On the x-axis is the initial primary mass. The optical depth of the primaries during the different evolutionary stages is shown as contour plot. Highlighted by solid lines are the optical depths up to a value of $\tau = 3.5$. *Right*: Phase diagram of the primary stars with the same axis as in the left panel. The evolutionary stages are separated into hydrogen-rich and hydrogen-free WN stars as well as WC stars in orange, green and blue respectively. The different evolutionary stages are estimated by the surface abundance. Hydrogen-rich WN stars have a surface hydrogen abundance of $0 < X_{\mathrm{H}} \leq 0.3$, hydrogen-free WN stars have $X_{\mathrm{H}} = 0$ and WC stars have $X_{\mathrm{C}} \geq 0.01$.

An exemplary plot of the optical depth of binary models can be found on the left side of Figure 5.5. One can see that stellar models with initial primary masses below $M_{1,\mathrm{i}} \lesssim 28\,\mathrm{M}_\odot$ ($\log(M_{1,\mathrm{i}}/\,M_\odot) \geq 1.450$) have an optical depth below $\tau < 1.5$ and therefore are not observable as Wolf-Rayet stars. On the right side of Figure 5.5 a phase diagram of the models is shown indicating the evolutionary stage of each model by

only taking into account the surface abundances of the stellar model. It can be seen that all primaries of the binary models are able to produce helium stars as they lose their hydrogen-rich envelope. If the calculated optical depth of a primary is larger than $\tau \geq 1.5$ it is assumed that the stellar model has an optically thick wind which is associated to a WR phase. Primary stars with initial masses larger than $M_{1,\mathrm{i}} \gtrsim 35.5\,\mathrm{M}_\odot$ are considered to go through a WC phase during the late stages of core helium burning. It gets evident that for larger initial primary masses the Wolf-Rayet stars will be observed for most of their core helium burning time as WC star. One can see that there is a minimum at around $M_{1,\mathrm{i}} \approx 70.8\,\mathrm{M}_\odot$ after which the fraction of time during which the primary will be seen as WC stars reduces again. This can be explained by the larger hydrogen envelopes and the shorter core helium burning times of more massive stars which make it harder for a WN star to evolve into a WC star.

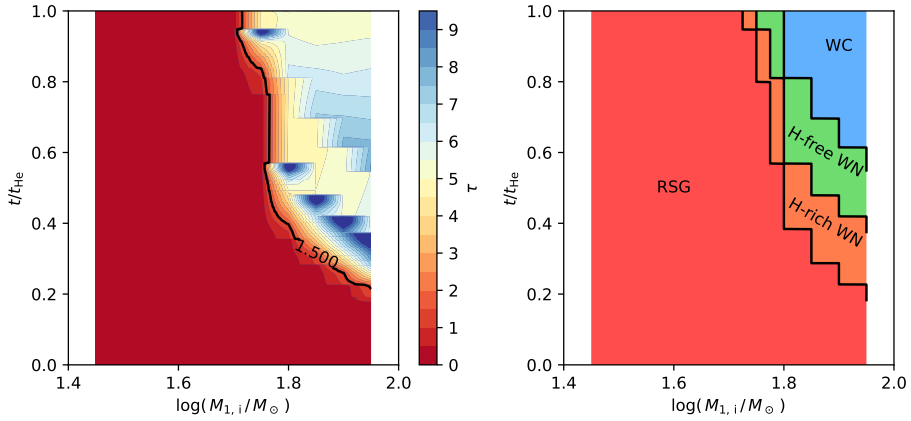

Figure 5.6: Optical depth and phase diagram of single star models with initial primary masses ranging from $\log(M_{1,\mathrm{i}}/M_\odot) = 1.450 - 1.950$. *Left*: On the y-axis is the fraction of the core helium burning time of each stellar model. On the x-axis is the initial star mass. The optical depth of the stellar models during the different evolutionary stages is shown as a contour plot. Highlighted by a solid line is the optical depth of $\tau = 1.5$. *Right*: Phase diagram of the stellar models with the same axis as in the left panel. The evolutionary stages are separated into RSG, hydrogen-rich, and hydrogen-free WN stars as well as WC stars in red, orange, green, and blue respectively. The different evolutionary stages are estimated by the surface abundance and effective temperature. In order to be labeled as a Wolf-Rayet star a stellar model requires an effective temperature above $T_{\mathrm{eff}} > 10\,000\,\mathrm{K}$. Hydrogen-rich WN stars need to have a surface hydrogen abundance between $0 < X_{\mathrm{H}} \leq 0.3$, hydrogen-free WN stars a surface hydrogen abundance of $X_{\mathrm{H}} = 0$ and WC stars surface carbon abundance above $X_{\mathrm{C}} \geq 0.01$. If a stellar model does not fulfill any of the aforementioned criteria it is labeled as RSG.

For comparison, a plot of the theoretical optical depth of the stellar winds of single star models is shown on the left of Figure 5.6. It can be seen that only the single star models with initial mass above $M_{1,\mathrm{i}} \gtrsim 56.2\,\mathrm{M}_\odot$ go trough a Wolf-Rayet phase. Stellar models with initial mass below $M_{1,\mathrm{i}} \lesssim 56.2\,\mathrm{M}_\odot$ are expected to have an optically thin

wind. On the right side of Figure 5.6 the evolutionary phases of the models are shown. It gets evident that all single star models that have an optically thin wind are in an RSG phase. Similar to the binary models one can see that the lightest Wolf-Rayet stars that are formed will only be visible as hydrogen-rich and hydrogen-free WN stars. Stellar models with initial masses above $M_{,\mathrm{i}} \gtrsim 60.3\,\mathrm{M}_\odot$ go trough a WC phase while they are core helium burning. As it is the case for the binary models the fraction of the core helium burning time during which a stellar model is visible as WC star increases with increasing initial star mass.

5.4 The New Grid of Binary Models

Following the discussions above, a new grid for the LMC needs to be calculated in order to produce a synthetic WR population. The grid is calculated with the same input physics as mentioned in Section 3.2 with the mass-loss recipe from Yoon (2017) for the WR phase. The grid covers initial primary masses in the range of $M_{1,\mathrm{i}} \simeq 28\,\mathrm{M}_\odot - 89\,\mathrm{M}_\odot$ in steps of $\Delta\log(M_{1,\mathrm{i}}/\,M_\odot) = 0.05$. The upper limit has been chosen according to the large amount of convergence errors, which occur at these high masses. The initial mass ratio range is the same as for the previous grid and covers the range of $q_\mathrm{i} = 0.25 - 0.95$ in steps of $\Delta q_\mathrm{i} = 0.05$. The initial orbital periods are calculated in the range from $P_\mathrm{i} = 1.4\,\mathrm{d} - 10\,000\,\mathrm{d}$ in steps of $\Delta\log(P_\mathrm{i}/\mathrm{d}) = 0.050$. For comparison with the previous grid the phase diagram for initial primary mass $M_{1,\mathrm{i}} = 60.3\,M_\odot$ is shown in Figure 5.7. The rest of the phase diagrams can be found in Appendix D.

Comparing the phase diagram of the old grid in Figure 3.7 with the new grid in Figure 5.7 one can see that the final states of the binary systems seem to be rather similar. This should not be surprising, as the Wolf-Rayet mass-loss rates only set in in the very late phases of the stellar evolution when no mass transfer phase is expected. However, in the late evolutionary phases when the primary develops a strong WR wind it will lose more mass than its counterpart of the old grid. This implies that the final mass ratios for the binary systems with a WR star are expected to differ between the two grids. Moreover, as mass is lost from the binary system this also leads to an orbital widening. This can be seen in the later analysis in which the WC stars are predicted to have wider orbits than the hydrogen-rich WN stars. The discussion for the common envelope evolution in Section 4 still holds, because the common envelope phase is initiated during a mass transfer phase during which the Wolf-Rayet mass-loss rates are not used.

Additionally to the binary models, the grid also contains single star models, because binary systems with an initial orbital period above $\log(P_\mathrm{i}/\mathrm{d}) \gtrsim 3.5$ are not interacting and therefore modeled as single stars. As the stars are initially tidally synchronized, at this high initial orbital period the stars are almost non-rotating. One can see that some of the non-interacting binary models are labeled as convergence errors. Regarding the single star models the non-interacting binary models with initial mass ratio $q_\mathrm{i} = 0.5$ and

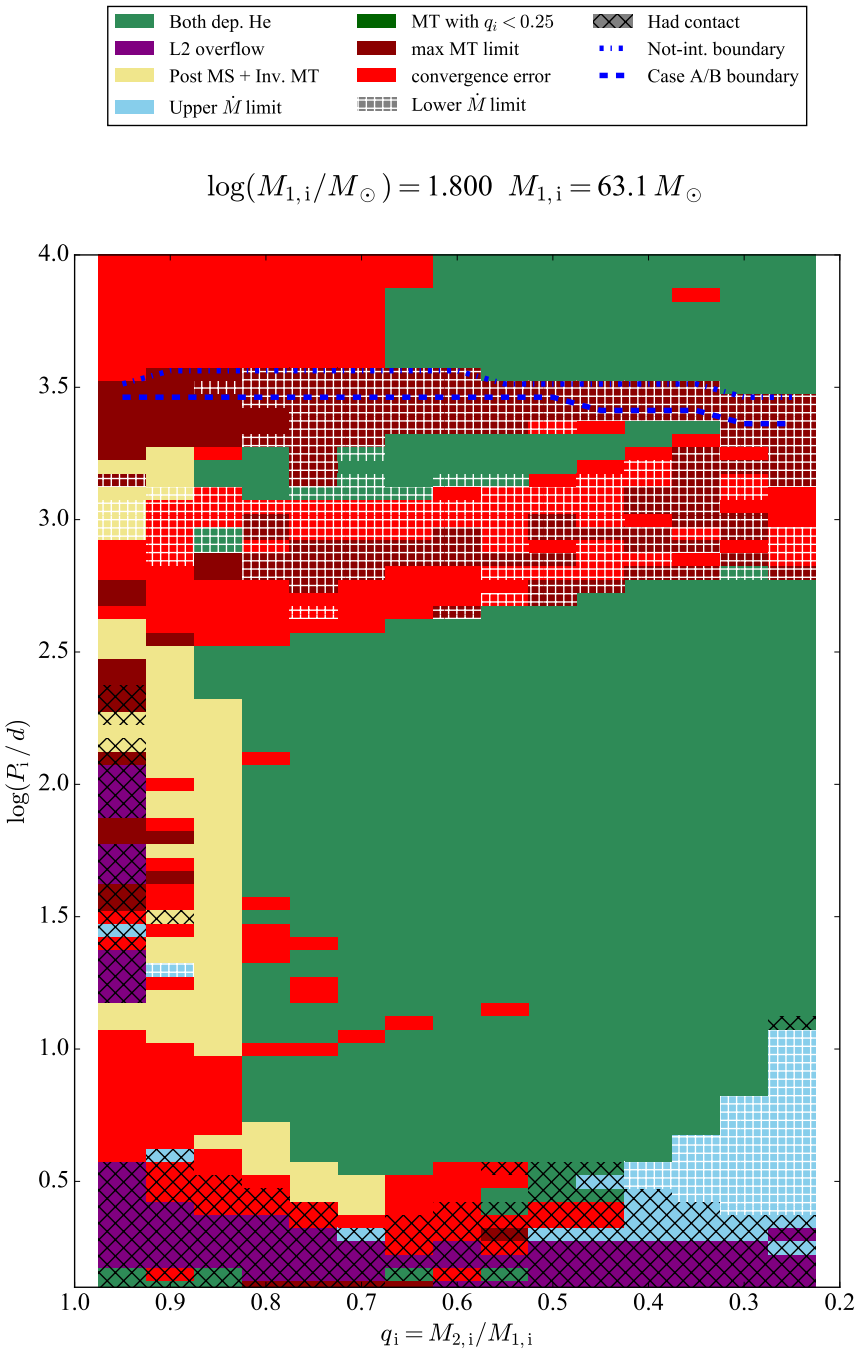

Figure 5.7: The initial mass ratio q_i is plotted versus the initial orbital period P_i. All models are calculated at LMC metallicity. The different phases are indicated in the legend and a more detailed description can be found in Section 3.1.1. The models are calculated with the Wolf-Rayet mass-loss rates from Yoon (2017).

initial orbital period $\log(P_i/\mathrm{d}) = 4.0$ are used. In regards to the models that are labeled with convergence errors, new models are calculated until core helium depletion in the primary, because only the primaries are relevant for the used single star models.

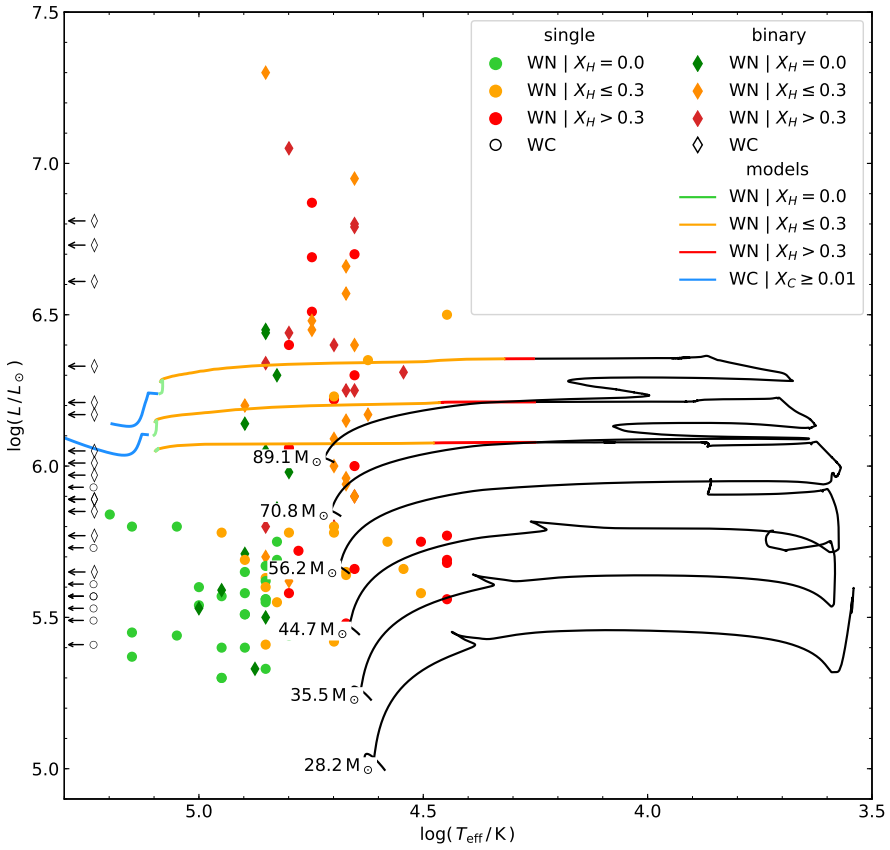

Figure 5.8: Stellar evolutionary tracks of the single star models. The color scheme is the same as in Figure 5.3. Single stars need an initial mass above $M_i \geq 56.2\,M_\odot$ to strip off their hydrogen-rich envelope and to evolve to a WR star.

The evolutionary tracks of the single star models are shown in Figure 5.8. One can see that the single star models are also able to produce WR stars if their initial mass is above $M_i \gtrsim 56.2\,M_\odot$. This leads to the conclusion that below a certain mass and therefore a certain luminosity only binary systems can produce the observed WR stars. After the threshold is reached all stars are able to strip off their hydrogen-rich envelope and the single star channel is expected to mainly contribute to the WR population. Every single star model with a mass above $M_i \gtrsim 56.2\,M_\odot$ can form a WR star whereas

in regards to the binary models the formation of a WR star needs a prior stable mass transfer phase, which implies that only a certain fraction of the binary systems actually form WR stars. This is also discussed by Shenar et al. (2020) who argued that binary models need to have an initial primary mass of $M_{1,\mathrm{i}} = 24\,M_\odot$ to be visible as WR stars and that, depending on the stellar model, the initial mass of a single star must be in the range of $M_\mathrm{i} = 28-75\,M_\odot$. The models used in this thesis require an initial primary mass above $M_{1,\mathrm{i}} = 28\,M_\odot$ to produce a WR star, while a mass $M_\mathrm{i} \gtrsim 56.2\,M_\odot$ is needed for a single star model.

5.5 Stellar Population Synthesis

The newly calculated grids of detailed binary evolutionary models are used for a stellar population synthesis with the aim to understand the importance of the different formation channels of WR stars in low metallicity environments like the LMC. The stellar temperatures, which are assumed to correspond to the effective temperatures of the WR stars, are not available for all observed stars, so only the luminosity of the WR stars will be extracted from the models and compared to the observations. Sana et al. (2013) analyzed the O-star population of the Tarantula Nebula in the LMC including the effect of binary systems. O-type stars are young massive main-sequence stars with initial masses of about $M_\mathrm{i} \gtrsim 30\,M_\odot$ (Weidner & Vink 2010). As the least massive primary stars of the used binary models have an initial mass of $M_{1,\mathrm{i}} = 28\,M_\odot$, the obtained probability distributions of Sana et al. (2013) will be used for the population synthesis. The initial mass function (IMF) of Salpeter (1955) is used for the single stars as well as for the initial primary mass of the binary systems. The IMF can be expressed as $f(M/M_\odot) \propto (M/M_\odot)^{-\alpha}$ with an exponent of $\alpha = 2.3$. Regarding the binary systems it is assumed that the intrinsic orbital period distribution is given by $f(\log(P/\mathrm{d})) \propto \log(P/\mathrm{d})^\pi$ with an exponent of $\pi = -0.45 \pm 0.30$ and the intrinsic mass ratio distribution is given by $f(q) \propto q^\kappa$ with an exponent of $\kappa = -1.0 \pm 0.4$. Sana et al. (2013) determined the intrinsic binary fraction to be $f_\mathrm{bin} = 0.51 \pm 0.04$, but for simplicity the intrinsic binary fraction in this analysis is assumed to be $f_\mathrm{bin} = 0.5$. With the purpose of small statistical fluctuations 7500 binary models with initial primary mass, initial orbital period, and initial mass ratio according to the aforementioned distributions are chosen from the grid. Furthermore, 7500 single star models with initial primary masses according to the IMF are drawn from the set of single star models as well. It is assumed that the LMC has a constant star formation rate. To include a constant star formation in our synthesis for the last 10^7 years, every 50000 years the luminosity of each drawn binary and single star model is added to the synthetic WR population if the star is core helium burning and has an optical depth above $\tau \geq 1.5$.

5.5.1 The First Synthesis

For the observed WR stars, not all temperatures are measured yet. However, as for all WR stars the luminosities are given, it is possible to compare the observed and

predicted luminosity range that is obtained from the population synthesis. As the grid only covers stellar models up to an initial mass of $M_i = 89.1\,M_\odot$, an upper limit for the luminosities that can be compared with the observations is used. Therefore, only WR stars in the range of $\log(L/L_\odot) = 5.05 - 6.35$ are taken into account for the analysis. All WR stars with luminosities above $\log(L/L_\odot) > 6.35$ are discarded.

In order to compare the predictions with the observations, the Wolf-Rayet stars are divided into three subclasses, hydrogen-free WN, hydrogen-rich WN, and WC stars. The observed subsets contain 38 hydrogen-free WN, 48 hydrogen-rich WN, and 19 WC stars in the given luminosity interval. To minimize the statistical fluctuations, more stars are synthesized than are observed. To be consistent with the observed data, the number of synthesized hydrogen-free WN stars is normalized to match the number of observed hydrogen-free WN stars.The normalization factor obtained in this way is then applied to the other subclasses in order to check if the synthesized models can reproduce the number of observed WR subtypes.

Applying this normalization on the synthesized population leads to a star formation rate of SFR $\approx 0.4\,M_\odot\,yr^{-1}$. Harris & Zaritsky (2009) estimated the star formation rate of the LMC to be rather constant at around SFR $\approx 0.2\,M_\odot\,yr^{-1}$ within the last few Gyrs with temporary variations of a factor of 2. They found that the star formation rate increases within the last 5×10^7 Myr to SFR $\approx 0.4\,M_\odot\,yr^{-1}$. The lifetime of a Wolf-Rayet star is expected to be in the order of several Myrs and therefore the required star formation rate of the synthetic population is in good agreement with the observed one.

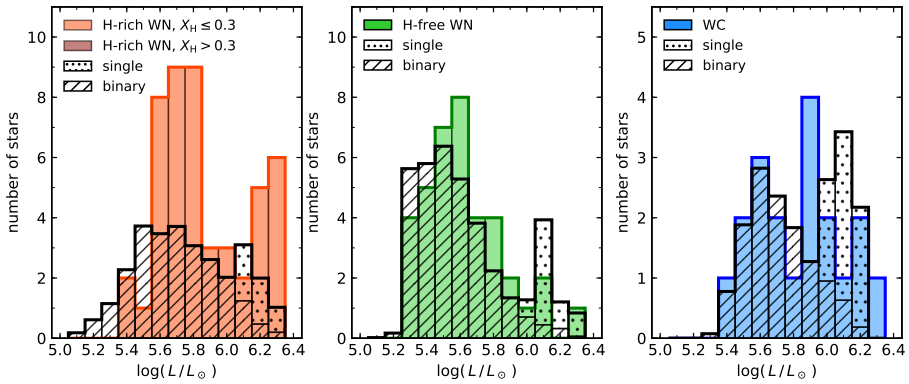

Figure 5.9: Comparison of the luminosity distribution of observed hydrogen-rich WN (orange), hydrogen-free WN (green), and WC (blue) populations for a given luminosity interval with single and binary star models with dotted and dashed hatches, respectively. The total distribution of the synthetic population is marked by a bold black line and the observed one is marked by a bold line in the corresponding color.

The result can be found in Figure 5.9, a histogram of the luminosity distributions of the observed and predicted WR subclasses. The shape of the luminosity distribution

of the hydrogen-free WN stars seems to comply with the observed distribution. This is also true for the subset of WC stars on the right side of Figure 5.9. The second peak of the observed WC luminosity distribution is located at lower luminosities compared to the predicted WR distribution. However, one has to keep in mind that the uncertainties in the estimated luminosities are large. The predicted number of WC stars is 19.25 matches with the number of 19 observed WC stars. Only the hydrogen-rich WN stars in the middle plane are underpopulated. The models only predict 29.30 of 48 observed stars and also the peaks cannot be explained by the models. To understand this discrepancy for the hydrogen-rich WN stars the origin of these stars needs to be discussed.

Comparing the predicted luminosity distributions of WR stars in single or binary systems, one can see in Figure 5.9 that the synthetic WR population is dominated by the binary channel for luminosities below $\log(L/L_\odot) \lesssim 6.0$. As soon as the single stars have strong enough winds to strip off their hydrogen-rich envelopes the WR population gets dominated by the single stars. This can be seen for luminosities higher than $\log(L/L_\odot) \gtrsim 6.0$. Naively one would expect that the number of single WR stars in this luminosity region is approximately the same as the number of WR stars in binary systems. However, this cannot be seen in Figure 5.9. This can be explained by the probability that a binary model evolves into a WR star compared to the probability that a single star evolves into a WR star. The binary models need a prior stable mass transfer in order to produce a WR star, implying that only a certain fraction of the binary models actually evolve into a WR star. Regarding the single star models, each model that has a high enough initial mass can go trough a WR phase, which explains the large contribution of the single stars at the higher luminosities.

5.5.2 The Evolutionary State of Hydrogen-Rich WN Stars

According to the classical WR stars, all of the WR stars that are synthesized from the binary and single star models are core helium burning stars including the hydrogen-rich WN stars. Martins et al. (2013) performed a spectroscopic analysis of H-rich WN stars in the LMC and the Galaxy and concluded that some of the stars must still be core hydrogen burning. de Koter et al. (1997) observed 4 luminous hydrogen-rich WN stars in the LMC and come to the conclusion that these stars must still be core hydrogen burning and have WR-like spectra. They explained this by very strong mass-loss rates that lead to the formation of an optically thick wind.

Therefore, the assumption that all WR stars are core helium burning is wrong. To determine if core hydrogen burning hydrogen-rich WN stars can be explained by the stellar models, the optical depths throughout the entire stellar evolution are calculated. Therefore, more correlations between the terminal wind velocity and the escape velocity are needed. In order to describe these correlations the obtained values of Vink et al. (2001) for the given temperature regimes are used. For a temperature range of $27\,500\,\mathrm{K} \leq T_\mathrm{eff} \leq 50\,000\,\mathrm{K}$ Vink et al. (2001) found that the correlation of $v_\infty = 2.6\,v_\mathrm{esc}$

can be used. For lower temperatures in the range of $12\,500\,\mathrm{K} \leq T_{\mathrm{eff}} \leq 22\,500\,\mathrm{K}$ the wind gets less powerful and the correlation can be expressed as $v_\infty = 1.3\,v_{\mathrm{esc}}$. For the lowest temperatures of RSG $T_{\mathrm{eff}} \leq 10\,000\,\mathrm{K}$ they obtained even less intense winds with $v_\infty = 0.7\,v_{\mathrm{esc}}$.

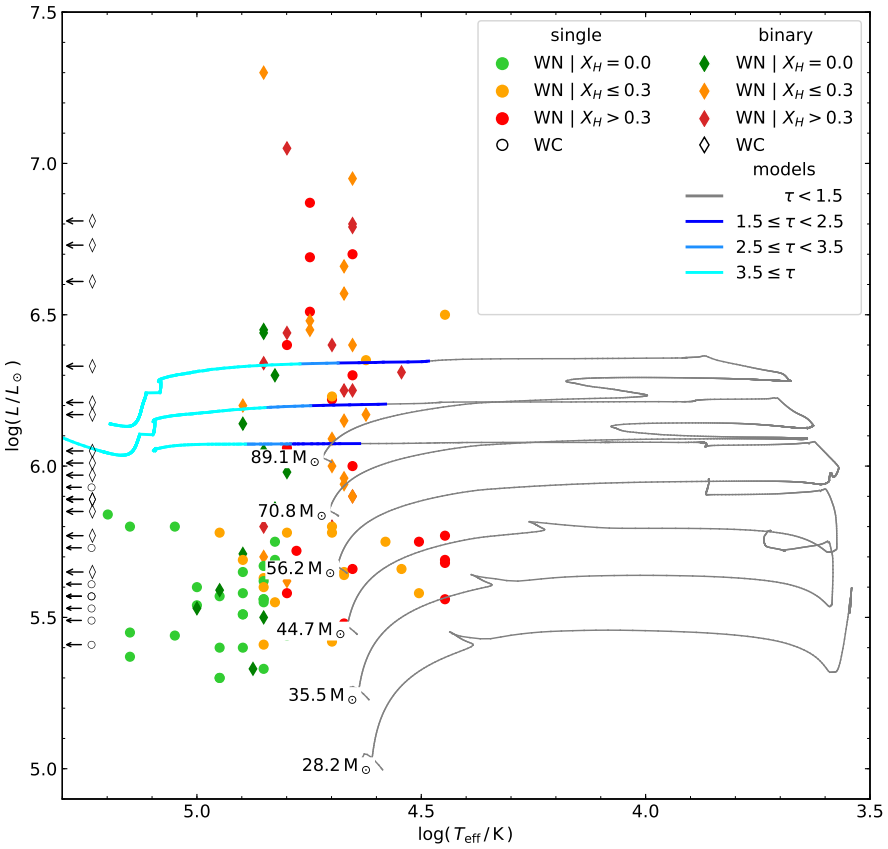

Figure 5.10: HRD with the temperature on the x-axis and luminosity on the y-axis. Stellar evolutionary tracks of the single star models are colored by their optical depth. Stellar models that have an optical depth below $\tau < 1.5$ are shown as gray lines. Stellar models with an optical depth above $\tau \geq 1.5$ are colored in cyan, light blue, and blue. In the background the are the observed WN and WC stars with the same labeling as in Figure 5.1.

However, even with these correlations none of the single star models, shown in Figure 5.10, develops an optically thick wind during the core hydrogen burning. This could have two reasons: First, the used correlations between the terminal wind velocity to the escape velocity are wrong. Second, the mass-loss rate of the O and B type

stars are underestimated. As the optical depth is proportional to the mass-loss rate this seems to be the more relevant point. Bestenlehner (2020) analyzed very massive stars and also found that in order to explain the transition from an O star wind spectrum to a WR-like spectrum, stronger mass-loss rates are required.

5.5.3 The second Synthesis

In the section above, it was discussed that the hydrogen-rich WN stars may have two different evolutionary states and that the modeled grid can only explain core helium burning WN stars. Therefore, in the following analysis, the subsample of hydrogen-rich WN stars is divided into two more subgroups: Hydrogen-rich WN stars with a surface hydrogen abundance of $X_{\mathrm{H}} \leq 0.3$ that are suspected to be core helium burning and super hydrogen-rich WN stars with a surface abundance of $X_{\mathrm{H}} > 0.3$ that are expected to be core hydrogen burning. Using the surface hydrogen abundance is not a very reliable criterion to divide the core hydrogen and core helium burning stars, however, it is a simple approximation and will be used in the further analysis. For the used binary models the detection criterion for a WR star has been modified so that a WR star must have a surface hydrogen abundance of $X_{\mathrm{H}} \leq 0.3$ to be consistent with the definition above.

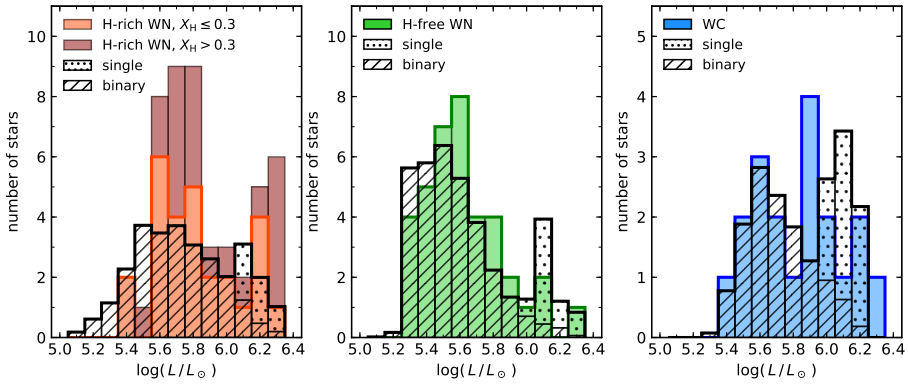

Figure 5.11: Comparison of the luminosity distribution of observed hydrogen-rich WN (orange), super hydrogen-rich WN (red), hydrogen-free WN (green), and WC (blue) populations for a given luminosity interval with single and binary star models with dotted and dashed hatches, respectively. The total distribution of the synthetic population is marked by a bold black line and the observed one is marked by a bold line in the corresponding color. Note, that for the comparison of the hydrogen-rich WN stars the super hydrogen-rich WN stars are not taken into account.

The resulting histograms of the luminosity distributions are shown in Figure 5.11. It is possible to see that the predicted hydrogen-rich WN stars are now in much better agreement with the observed hydrogen-rich WN stars (in orange). From the observed

WN population, one would expect 27 hydrogen-rich WN stars and 21 super hydrogen-rich WN stars. The predictions would expect 29.14 hydrogen-rich WN stars which is in much better agreement than before.

5.5.4 Comparing Observed and Predicted Binary Parameters

Even though the predicted distribution of the WR populations matches the observed distribution, the models would predict a binary fraction of WR stars of about $\approx 80\%$. The observed WR stars only show a binary fraction of $\approx 40\%$ which means that every second binary would be undetected. Furthermore, our models only predict single WR stars at the luminosities above $\log(L\,/\,L_{\odot}) \gtrsim 6$ which is contrary to the observations, at least regarding the WC stars of which the most luminous stars are in a binary. There are several explanations that might be able to verify this appearance. They will be discussed at the end of this section. Before that, the predictions of the used models on mass ratios and orbital periods will be compared with the few that are available from observations.

Hydrogen-rich WN binaries

The hydrogen-rich WN sample is shown in Figure 5.12 in which the mass ratios can be seen in the upper left panel and the orbital periods in the upper right panel. It is important to note that only WR stars in binary systems with a surface hydrogen mass fractions in the range of $0.0 < X_{\mathrm{H}} \leq 0.3$ are included. The binary parameters are listed in Table 1.

Most of the observed binaries have very tight orbits. This is in good agreement with the expectation because the companion in tight systems should be easier to observe, as for example the spectrum is Doppler-shifted or darkened by an eclipsing star in the line of sight. Therefore, one can expect this sample to be more complete for tighter orbits. The observed systems with wide orbits show strong X-ray emission, which is associated with a binary companion. Therefore, the models seem to match the observations very well. However, there are two observed hydrogen-rich stars in very tight orbits that cannot be explained by the binary models. These systems are either core-hydrogen burning and therefore could have a tight orbit, or they might be remnants of a common envelope phase with a very small fraction of hydrogen still left on the stellar surface. Alternatively, they could be systems with an undetected compact object. Another possibility might be given by wind particles that gravitationally torque the binary system and extract angular momentum leading to the formation of tight orbits (Brookshaw & Tavani 1993). However, for such a scenario to be possible, the terminal wind velocity must be in the same order of magnitude as the binary orbital velocity. For our systems the binary orbital velocity is typically in the order of $200\,\mathrm{km\,s^{-1}}$ whereas the terminal wind velocity is much larger up to $v_{\infty} = 2000\,\mathrm{km\,s^{-1}}$. Therefore, such a scenario seems unlikely.

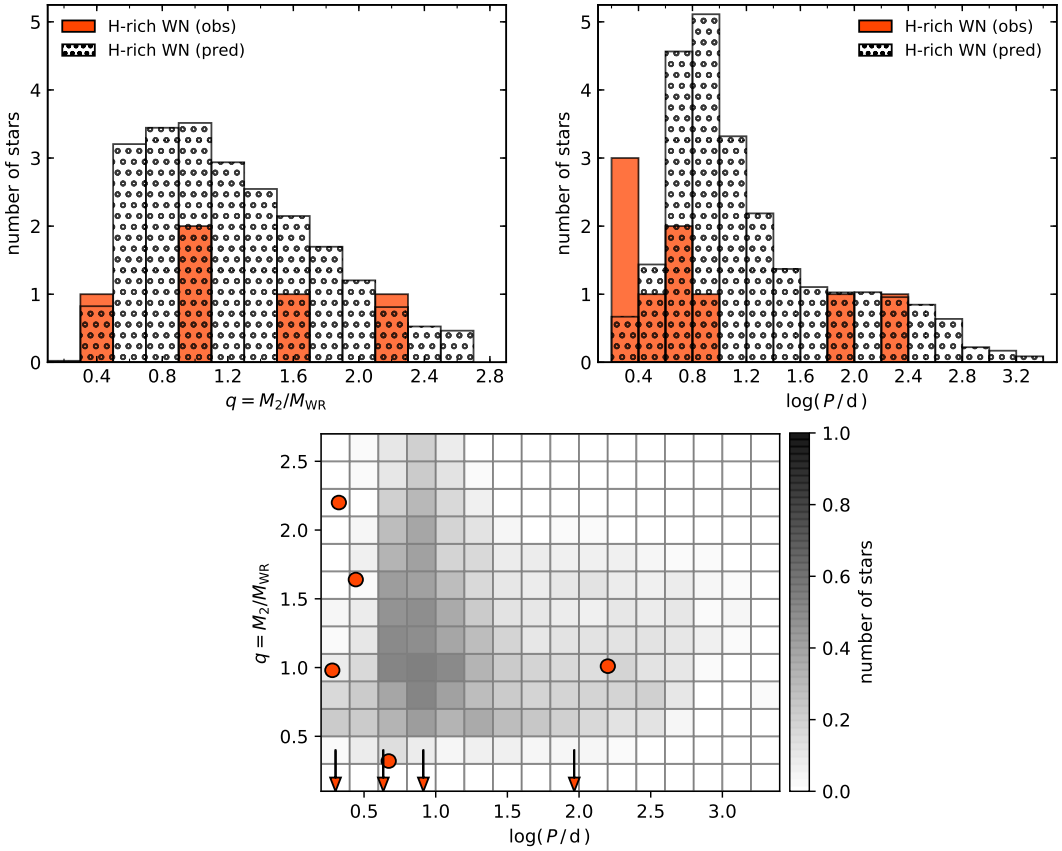

Figure 5.12: *Upper left*: The observed mass ratios of hydrogen-rich WN binaries, with surface hydrogen mass fractions in the range of $0.0 < X_H \leq 0.3$, are shown in orange and the predictions from the stellar synthesis are marked by dotted hatches. *Upper right*: Observed orbital periods of hydrogen-rich WN binaries in orange and the predictions as dotted hatched bins. *Lower panel*: Plot of the mass ratios versus the orbital period. The observed binaries are shown as orange dots if mass ratio and orbital period are known. If only the orbital period is known, it is marked by an arrow. The predicted distribution is shown as a gray-scaled histogram in the background.

For the observed and predicted mass ratios, both distributions show a rather flat behavior and seem not to be in a disagreement at all. Here, one might assume that the systems with the most massive companion stars might be detected because the companions can be visible in the spectrum while less massive companions might be outshined by the WR star. The observed WR binary systems with mass ratios smaller than $q \leq 1.0$ are all detected X-ray binaries. By having a look at the lower left panel of Figure 5.12, one can see the correlations of the mass ratios and the orbital periods. This shows that most of the systems with small orbital periods cover a large range of mass ratios. However, compared to the predicted correlations this seems to be in quite good agreement as one would expect a bias towards smaller periods over a large range of mass ratios.

Hydrogen-free WN binaries

The mass ratios and orbital periods for the hydrogen-free WN stars are shown in Figure 5.13. Even though fewer systems are observed one can see the same structure as for the hydrogen-rich WN stars. In comparison, the binary models predict wider orbits that are caused by strong mass-loss rates. Also, the expected mass ratios are shifted to higher values as the WR star loses mass whereas the companion is expected to have almost the same mass as in the hydrogen-rich WN phase. One can see again that there are tight systems that cannot be explained by the binary models. This time the mass ratio of these systems is unknown, however, a common envelope evolution or a compact companion seem to be likely channels that produce the observed star.

WC binaries

For the WC binaries in the LMC only in three cases the orbital periods are determined which are included in Table 2. The predictions from the stellar synthesis can be found in Figure 5.14. The strong mass-loss rates are expected to widen the orbit of these systems, even more, implying that no binary with orbital periods below $P < 10\,\mathrm{d}$ is expected. However, there are two observed WC binaries in very tight orbits. WR binaries with orbits in the order of a few days are present for all WR phases and cannot be explained by the binary models. Most of these systems consist of a WR star and an OB companion. Even though it was argued in Section 4 that a common envelope evolution for a post main-sequence star with a main-sequence companion seems to be unlikely to end with a successful common envelope ejection, such a scenario cannot be ruled out. It seems like these systems are possible remnants of a common envelope evolution. In Section 4 it was mentioned that a successful ejection is most likely for systems with initially large orbital periods as the primary can evolve to a RSG phase. The RSG phase of stars is very unknown and it is possible that there are pulsations and eruptions that additionally lead to a partial ejection of the envelope and help the system to successfully eject the common envelope and forming a close binary system.

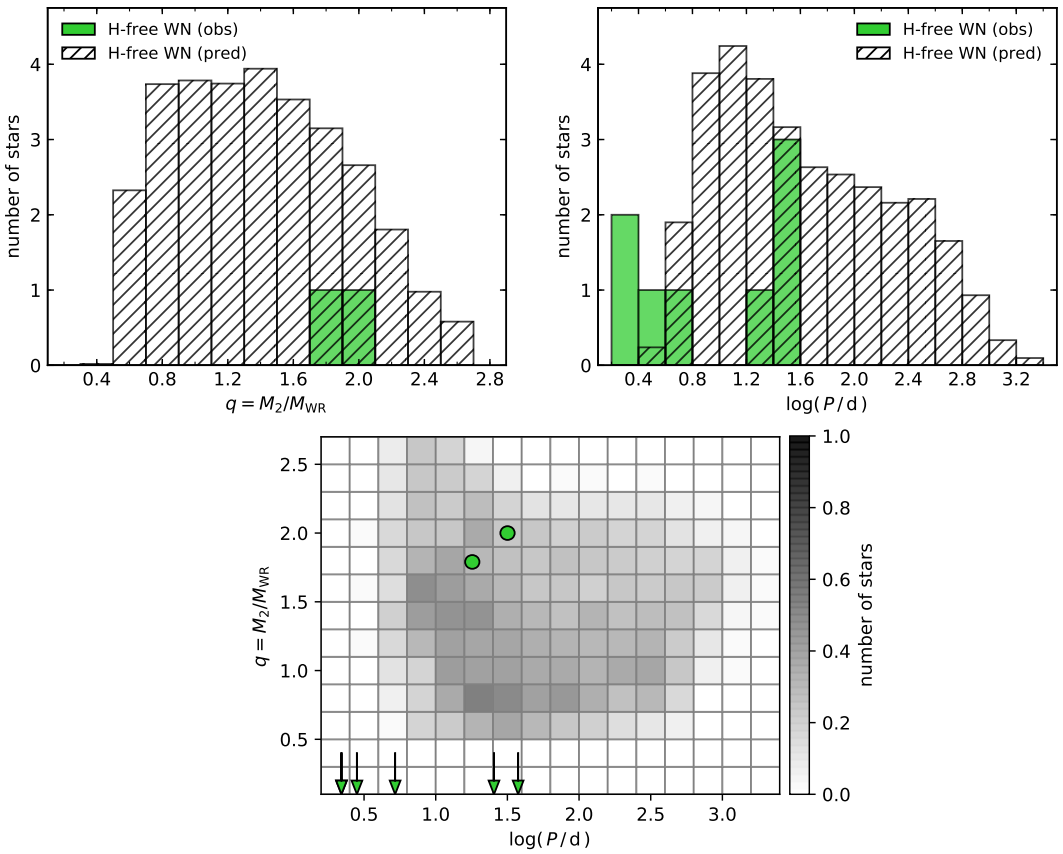

Figure 5.13: *Upper left*: The observed mass ratios of hydrogen-free WN binaries are shown in green and the predictions from the stellar synthesis are marked by dashed hatches. *Upper right*: Observed orbital periods of hydrogen-free WN binaries in green and the predictions as dashed hatched bins. There is a discrepancy for the tightest observed orbits that cannot be explained by the models. *Lower panel*: Plot of the mass ratios versus the orbital period. The observed binaries are shown as green dots if mass ratio and orbital period are known. If only the orbital period is known, it is marked by an arrow. The predicted distribution is shown as a gray-scaled histogram in the background.

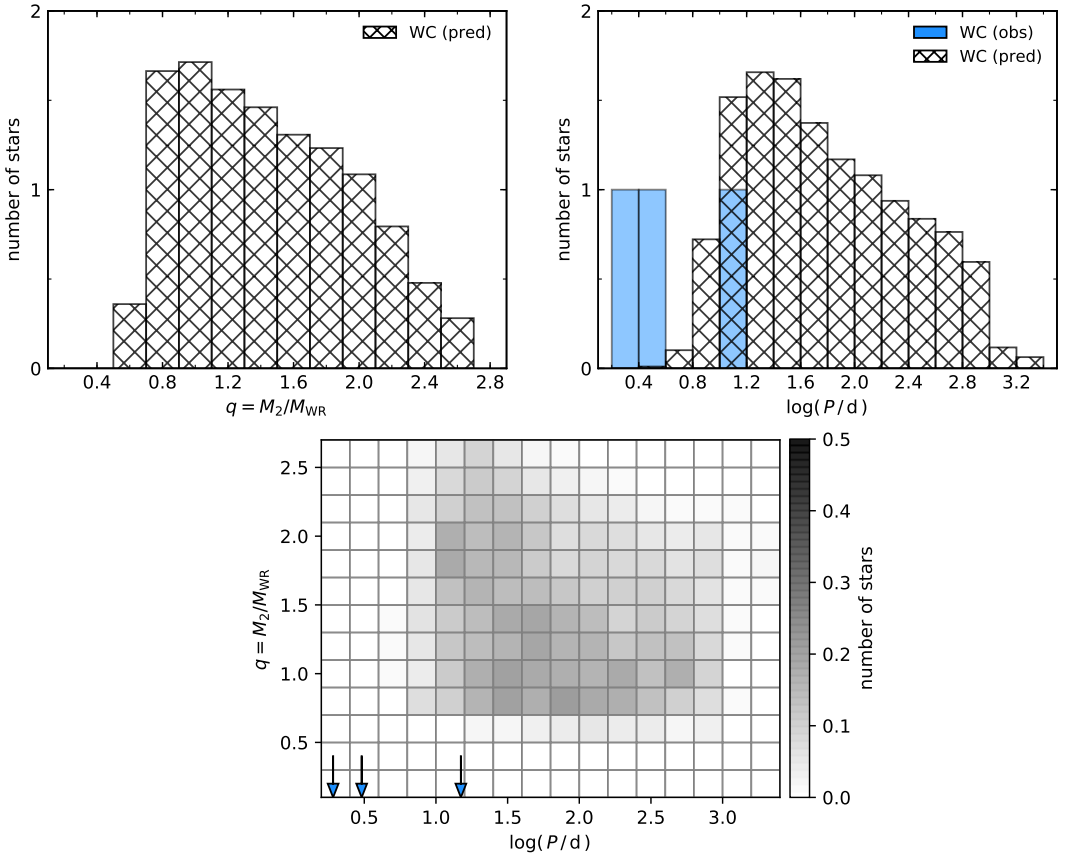

Figure 5.14: *Upper left*: The predicted mass ratios of the WC binaries from the stellar synthesis are marked by cross hatches. *Upper right*: Observed orbital periods of WC binaries in blue and the predictions as crossed hatched bins. There is a discrepancy for the tightest observed orbits that cannot be explained by the models. *Lower panel*: Plot of the mass ratios versus the orbital period. The orbital period is marked by an arrow. The predicted distribution is shown as a gray-scaled histogram in the background.

5.5.5 Conflict Between Observations and Predictions

As already mentioned in the previous section the synthesized models, at least for the WC population, would predict that the most luminous stars should be observed as single stars and the less luminous stars are in binary systems. However, the observations show the opposite. Shenar et al. (2020) also realized this problem and discussed some possibilities which will be listed below:

1. **Binary evolution in disguise**: Some apparent single WR stars still might be products of binary systems even though they are detected as single stars. This scenario was discussed by Schootemeijer & Langer (2018) for the WR stars of the SMC. Moreover, it is possible that the evolution of binary systems leads to the formation of single WR stars, for example, they could be merger products, binaries with a compact object that is X-ray quiet, or products of a three-body interaction that kicked out the companion.
2. **Undetected binaries**: As most of the WR stars are observed in the optical range it might be possible that the WR star gets outshined by its brighter companion.
3. **All WR stars can be formed by single stars**: As it has been seen several times in this chapter the uncertainties in the mass-loss rates are very high and the RSG phase is not very well understood so that it might be that all WR stars can be formed via the single star channel. This would also correspond to the lack of observed luminous RSG.

These are many possible scenarios that can explain the faint apparently single WR stars. However, studying them is beyond the scope of this thesis. The used binary and singe star models are able to explain the observed luminosity range of the WR stars in the LMC. Even though there are some conflicts with the observed single stars which might be explained by the aforementioned scenarios, the results of the population synthesis show that one would expect a large fraction of the WR stars to be in wide orbits with orbital periods above 30 d which are not observed yet. This might correspond to the first scenario of the binary evolution of disguise where the secondary is not detected. Dsilva et al. (2020) analyzed the variations in radial velocities of the northern galactic WC stars in order to flag binary candidates. Dsilva et al. (2020) finds that the WC stars lack binary systems with orbital periods $P \lesssim 100$ d, which indicates that a large number of the WC binaries likely reside in long-period systems. This finding underlines the predicted period distribution of the synthetic WR population.

5.6 Summary

In this section, an overview over the observed WR stars in the LMC was given. In order to compare the calculated grid with the observed WR population, a criterion that determines whether or not a star can be seen as a WR star based on the optical depth of the stellar wind has been introduced. It was realized that the previously used

WR mass-loss rates are underestimated and that one needs to use a clumping factor of $D = 4$ in order to reproduce the observed WR stars. Furthermore, the wind of O and B type stars seem to be underestimated. Also, no main-sequence star can reproduce the observed WR-like spectra of core hydrogen burning stars. However, the binary and single star models can reproduce the observed WR population and also the observed orbital periods astonishingly well. Further, the mass ratios seem to fit the predictions. There are some outliers that might have been formed by a common envelope evolution. The synthesized models cannot explain the observed distribution of apparent single and binary stars, which seems, at least for the WC stars, to be the opposite of the predictions.

6 Conclusions and Outlook

In this thesis, large grids of detailed binary evolution models at SMC and LMC metallicity are used and extended to higher initial primary masses up to $70.8\,M_{\odot}$. These binary models are calculated with the MESA code and include the physics of mass-loss, rotation, inflation, and binary interaction. The final phases of these models are discussed in more detail in Section 3. The two main outcomes of the models are that either both stars can be calculated until core carbon depletion or the binary systems enters a common envelope phase where the simulation is stopped.

For those systems that enter a common envelope phase while both stars are still core hydrogen burning it is assumed that these systems will result in a merger. However, for a binary system consisting of a post main-sequence star and a main-sequence companion the outcome is rather unknown and is discussed in Section 4. During the analysis of those systems, it becomes clear that it is of major importance to calculate the binding and orbital energy at the formation of the common envelope instead of calculating them at the onset of mass transfer, as during the mass transfer phase the ratio of binding energy to orbital energy can reduce by a factor of 3. Even though this ratio could be reduced by a factor of 3, it does not lead to a much larger fraction of successful ejections of the common envelope, as only binary systems in which the primary is evolved to a RSG are able to eject the common envelope. For the highest initial primary masses, the used methods would predict no successful ejections at all. However, there are many unknowns that might contribute to the process. One might think about pulsations that might appear in the late stages of a RSG, where it is unclear if these can also develop during a common envelope phase.

In Section 5 new binary models are calculated with the mass-loss rates of Yoon (2017) with the purpose of understanding the different formation channels of WR stars in low metallicity environments. The models, including single star models calculated with the same physics as the binary models, are used for a population synthesis. The synthesized Wolf-Rayet population is compared to the observed population of Wolf-Rayet stars in the LMC. The obtained luminosity distribution of both populations fits astonishingly well. The synthesized population would predict that all Wolf-Rayet stars with luminosities below $\log(L\,/\,L_{\odot}) \lesssim 6.0$ are in binary systems. However, about half of the observed Wolf-Rayet stars in this luminosity range are apparently single stars. By comparing the predicted orbital periods and mass ratios of the synthesized population with the observed Wolf-Rayet binaries one can see that the binary systems in tight orbits can be partly explained by the synthesized models. Nevertheless, there are some WR binaries that orbital periods within a few days that could not be explained by the binary models and hint at a common envelope evolution of a post main-sequence star with a main-sequence companion. The obtained orbital period and mass-ratio distributions of the synthesized population can be used as predictions. These predictions hint that most of the faint apparently single Wolf-Rayet stars can be in a binary system with a wide

orbit or that these stars have a light companion that cannot be seen in the spectrum. However, in the analysis merger products are completely excluded which might also contribute to the Wolf-Rayet population.

It was realized during the analysis of the common envelope evolution of a post main-sequence star with a main-sequence companion that this channel is only poorly understood, as the observed WR binaries with an O star companion and an orbital period of a few days cannot be explained. Therefore, further studies have to be made in order to understand what we are missing, for example, can pulsations or explosions that are present in a RSG phase help to eject the envelope. If this can be understood in more detail, many systems like the aforementioned WR binaries can be explained as well as high mass X-ray binaries which can form from this channel.

Furthermore, the results of the orbital period distribution of the synthesized WR population would predict intermediate and large orbital periods for the binary systems. It the WR explodes as a supernova, taking into account the unknown parameters of a supernova kick, a binary system with a large orbital period, and a compact object is formed. If the secondary expands and mass transfer is instable this will lead to the formation of a common envelope. It is known from the work of Kruckow et al. (2016) that a successful ejection is possible for these systems. Therefore, this opens a formation channel of double BH merger candidates, which could be studied in more detail in future works.

Additional to the aforementioned studies, the predicted orbital period distributions can be used in combination with the results of Dsilva et al. (2020) to analyze apparently single WR stars in order to detect if they could be in a binary system.

To study the reliability of the predictions one could also calculate grids of detailed binary models at SMC and MW metallicity to see if the used physics, especially the mass-loss rates, can explain the observed WR populations too.

References

Bartzakos, P., Moffat, A. F. J., & Niemela, V. S. 2001a, MNRAS, 324, 18

Bartzakos, P., Moffat, A. F. J., & Niemela, V. S. 2001b, MNRAS, 324, 33

Bestenlehner, J. M. 2020, MNRAS, 493, 3938

Böhm-Vitense, E. 1958, ZAp, 46, 108

Brookshaw, L. & Tavani, M. 1993, ApJ, 410, 719

Brott, I., de Mink, S. E., Cantiello, M., et al. 2011, A&A, 530, A115

de Koter, A., Heap, S. R., & Hubeny, I. 1997, ApJ, 477, 792

Dsilva, K., Shenar, T., Sana, H., & Marchant, P. 2020, A&A, 641, A26

Eggleton, P. P. 1983, ApJ, 268, 368

Gräfener, G., Owocki, S. P., Grassitelli, L., & Langer, N. 2017, A&A, 608, A34

Gräfener, G., Vink, J. S., Harries, T. J., & Langer, N. 2013, VizieR Online Data Catalog, 354, 79083

Hainich, R., Rühling, U., Todt, H., et al. 2014, A&A, 565, A27

Hamann, W.-R. 1995, in IAU Symp., Vol. 163, Wolf-Rayet Stars: Binaries, Colliding Winds, Evolution, ed. K. A. van der Hucht & P. M. Williams (Kluwer, Dodrecht, Holland), 105

Hamann, W.-R., Gräfener, G., & Liermann, A. 2006, A&A, 457, 1015

Hamann, W.-R., Gräfener, G., Liermann, A., et al. 2019, A&A, 625, A57

Hamann, W.-R., Koesterke, L., & Wessolowski, U. 1995, A&A, 299, 151

Han, Z., Podsiadlowski, P., & Eggleton, P. P. 1995, MNRAS, 272, 800

Harris, J. & Zaritsky, D. 2009, AJ, 138, 1243

Heger, A., Langer, N., & Woosley, S. E. 2000, ApJ, 528, 368

Hut, P. 1981, A&A, 99, 126

Ivanova, N., Justham, S., Chen, X., et al. 2013, A&A Rev., 21, 59

Kippenhahn, R., Ruschenplatt, G., & Thomas, H. C. 1980, A&A, 91, 175

Kippenhahn, R. & Weigert, A. 1967, ZAp, 65, 251

Kopal, Z. 1955, Annales d'Astrophysique, 18, 379

Kruckow, M. U., Tauris, T. M., Langer, N., et al. 2016, A&A, 596, A58

Landau, L. D. & Lifshitz, E. M. 1971, The classical theory of fields

Langer, N. 1989, A&A, 210, 93

Langer, N. 2012, ARA&A, 50, 107

Langer, N., Fricke, K. J., & Sugimoto, D. 1983, A&A, 126, 207

Marchant, P. 2016, PhD thesis, Rheinischen Friedrich-Wilhelms-Universität Bonn

Marchant, P., Langer, N., Podsiadlowski, P., Tauris, T. M., & Moriya, T. J. 2016, A&A, 588, A50

Martins, F., Depagne, E., Russeil, D., & Mahy, L. 2013, A&A, 554, A23

Mowlavi, N. & Forestini, M. 1994, A&A, 282, 843

Nieuwenhuijzen, H. & de Jager, C. 1990, A&A, 231, 134

Nugis, T. & Lamers, H. J. G. L. M. 2000, A&A, 360, 227

Pantolmos, G. & Matt, S. P. 2017, ApJ, 849, 83

Paxton, B., Cantiello, M., Arras, P., et al. 2013, ApJS, 208, 4

Paxton, B., Marchant, P., Schwab, J., et al. 2015, ApJS, 220, 15

Paxton, B., Schwab, J., Bauer, E. B., et al. 2018, ApJS, 234, 34

Petrovic, J., Pols, O., & Langer, N. 2006, A&A, 450, 219

Pols. 2009, Stellar Structure and Evolution

Quast, M., Langer, N., & Tauris, T. M. 2019, A&A, 628, A19

Ramachandran, V., Hamann, W. R., Hainich, R., et al. 2018, A&A, 615, A40

Rappaport, S., Verbunt, F., & Joss, P. C. 1983, ApJ, 275, 713

Salpeter, E. E. 1955, ApJ, 121, 161

Sana, H., de Koter, A., de Mink, S. E., et al. 2013, A&A, 550, A107

Sander, A., Hamann, W.-R., & Todt, H. 2012, A&A, 540, A144

Sanyal, D., Grassitelli, L., Langer, N., & Bestenlehner, J. M. 2015, A&A, 580, A20

Schootemeijer, A. & Langer, N. 2018, A&A, 611, A75

Shenar, T., Gilkis, A., Vink, J. S., Sana, H., & Sand er, A. A. C. 2020, A&A, 634, A79

Shenar, T., Sablowski, D. P., Hainich, R., et al. 2019, A&A, 627, A151

Skumanich, A. 1972, ApJ, 171, 565

Smith, L. F., Meynet, G., & Mermilliod, J. C. 1994, A&A, 287, 835

Soberman, G. E., Phinney, E. S., & van den Heuvel, E. P. J. 1997, A&A, 327, 620

Spruit, H. C. 2002, A&A, 381, 923

Tauris, T. M. & van den Heuvel, E. P. J. 2006, Formation and evolution of compact stellar X-ray sources, Vol. 39, 623–665

Tramper, F., Sana, H., & de Koter, A. 2016, ApJ, 833, 133

Verbunt, F. & Zwaan, C. 1981, A&A, 100, L7

Vink, J. S., de Koter, A., & Lamers, H. J. G. L. M. 2001, A&A, 369, 574

Wang, C., Langer, N., Gräfener, G., & Marchant, P. 2019, in IAU Symposium, Vol. 346, IAU Symposium, ed. L. M. Oskinova, E. Bozzo, T. Bulik, & D. R. Gies, 78–82

Wang, C., Langer, N., Schootemeijer, A., et al. 2020, ApJ, 888, L12

Webbink, R. F. 1984, ApJ, 277, 355

Weidner, C. & Vink, J. S. 2010, A&A, 524, A98

Wellstein, S. 2001, PhD thesis, Universität Potsdam

Woods, T., Ivanova, N., Van der Sluys, M., & Chaichenets, S. 2011, The Astrophysical Journal, 744

Yoon, S.-C. 2017, MNRAS, 470, 3970

A The LMC Grid

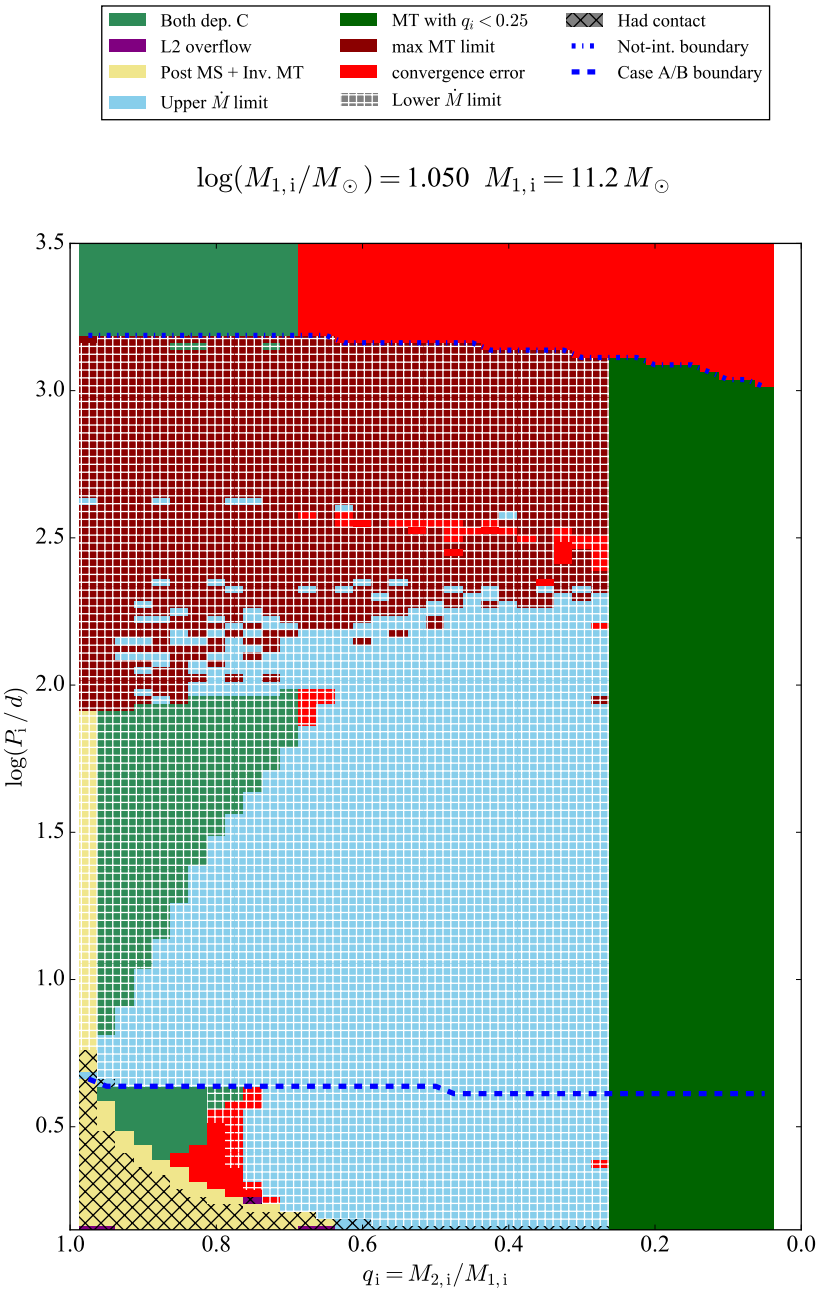

Figure A.1: Phase diagram of binary models with fixed initial donor mass of $M_{1,\mathrm{i}} = 11.2\,M_\odot$. The initial mass ratio q_i is plotted versus the initial orbital period P_i. All models are calculated at LMC metallicity. The different phases are indicated in the legend and a more detailed description can be found in Section 3.1.1.

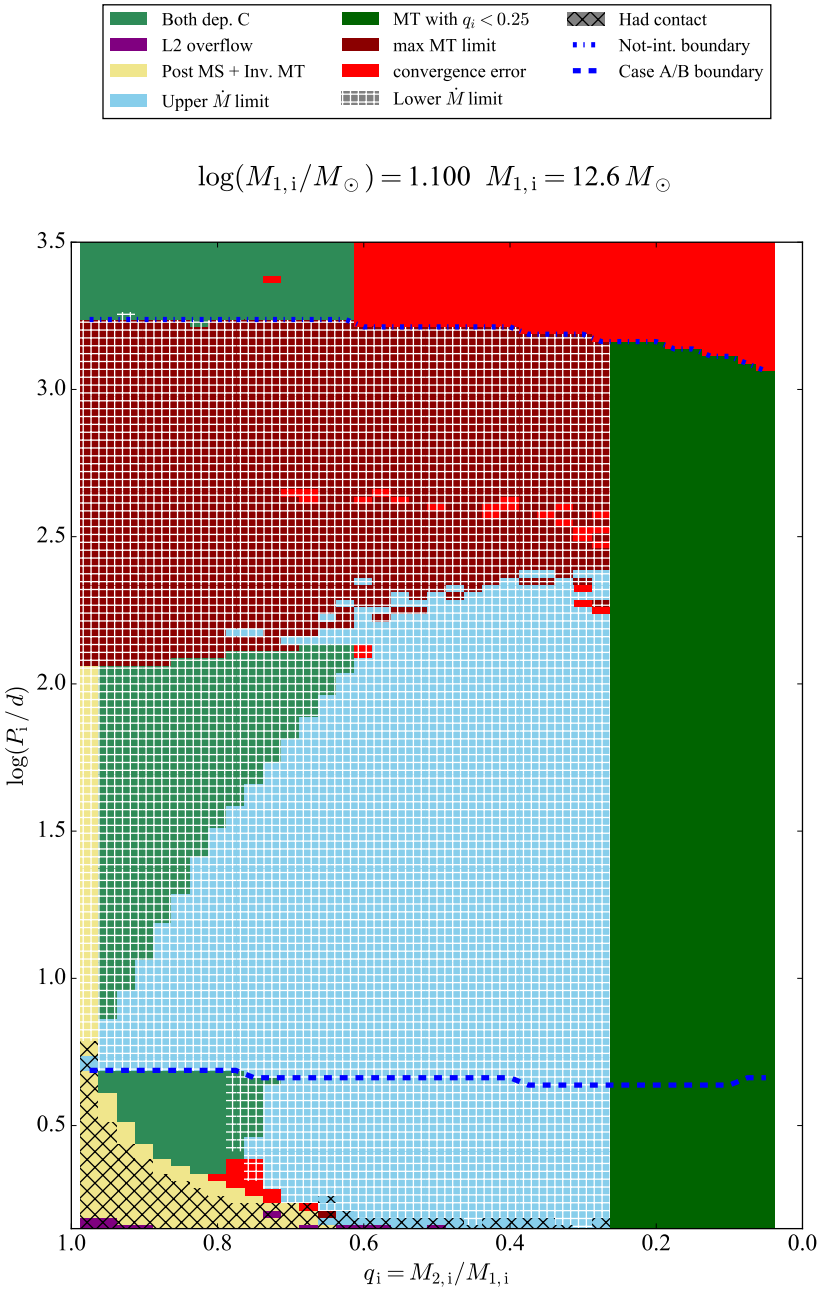

Figure A.2: Phase diagram of binary models with fixed initial donor mass of $M_{1,\mathrm{i}} = 12.6\,M_\odot$. The initial mass ratio q_i is plotted versus the initial orbital period P_i. All models are calculated at LMC metallicity. The different phases are indicated in the legend and a more detailed description can be found in Section 3.1.1.

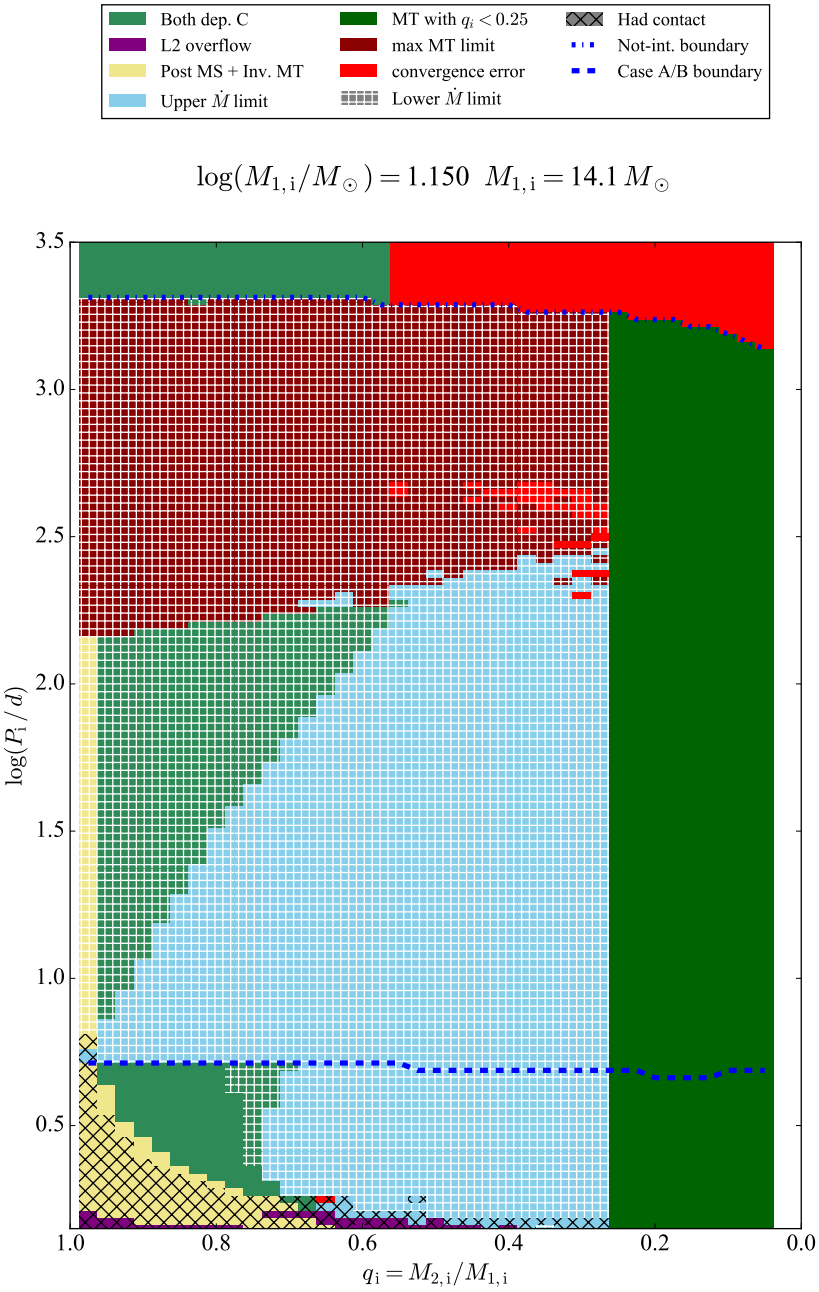

Figure A.3: Phase diagram of binary models with fixed initial donor mass of $M_{1,\mathrm{i}} = 14.1\,M_\odot$. The initial mass ratio q_i is plotted versus the initial orbital period P_i. All models are calculated at LMC metallicity. The different phases are indicated in the legend and a more detailed description can be found in Section 3.1.1.

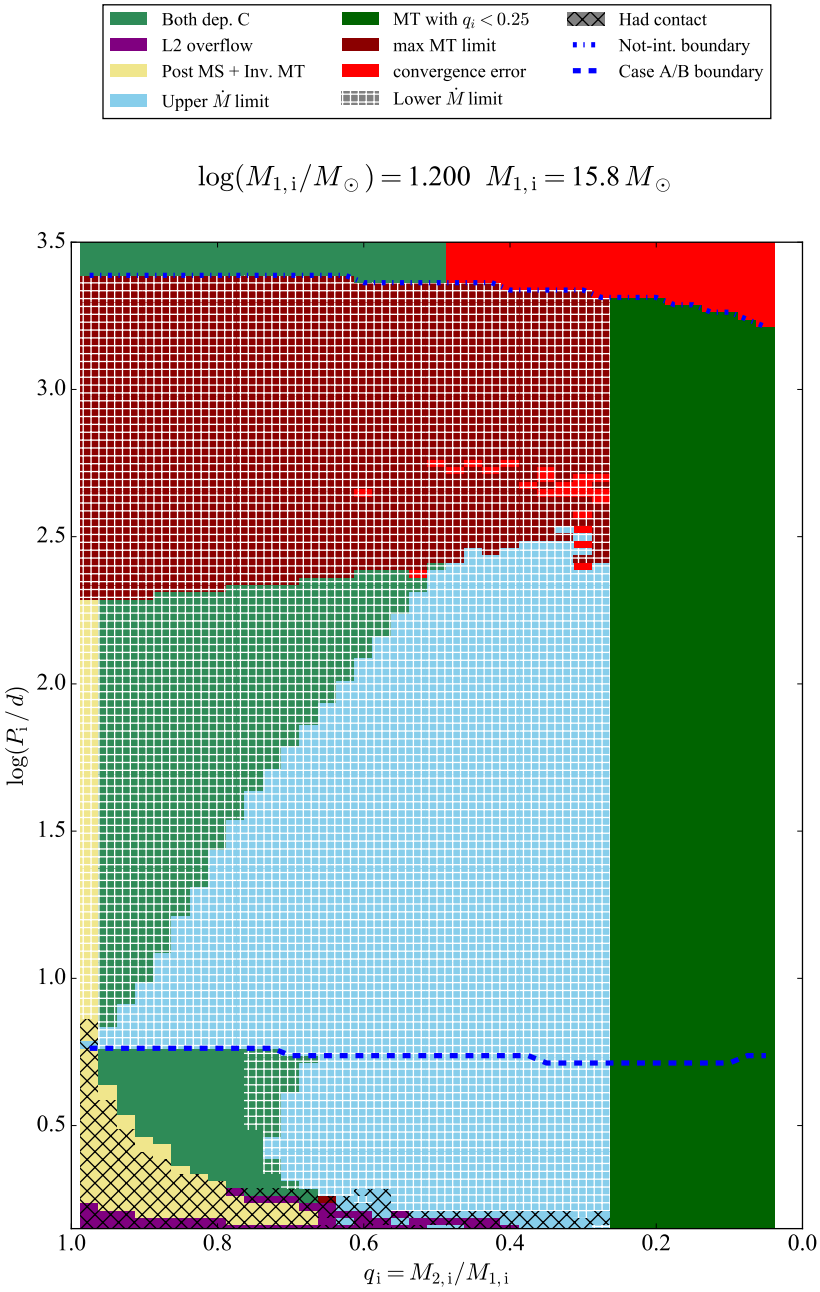

Figure A.4: Phase diagram of binary models with fixed initial donor mass of $M_{1,\mathrm{i}} = 15.8\,M_\odot$. The initial mass ratio q_i is plotted versus the initial orbital period P_i. All models are calculated at LMC metallicity. The different phases are indicated in the legend and a more detailed description can be found in Section 3.1.1.

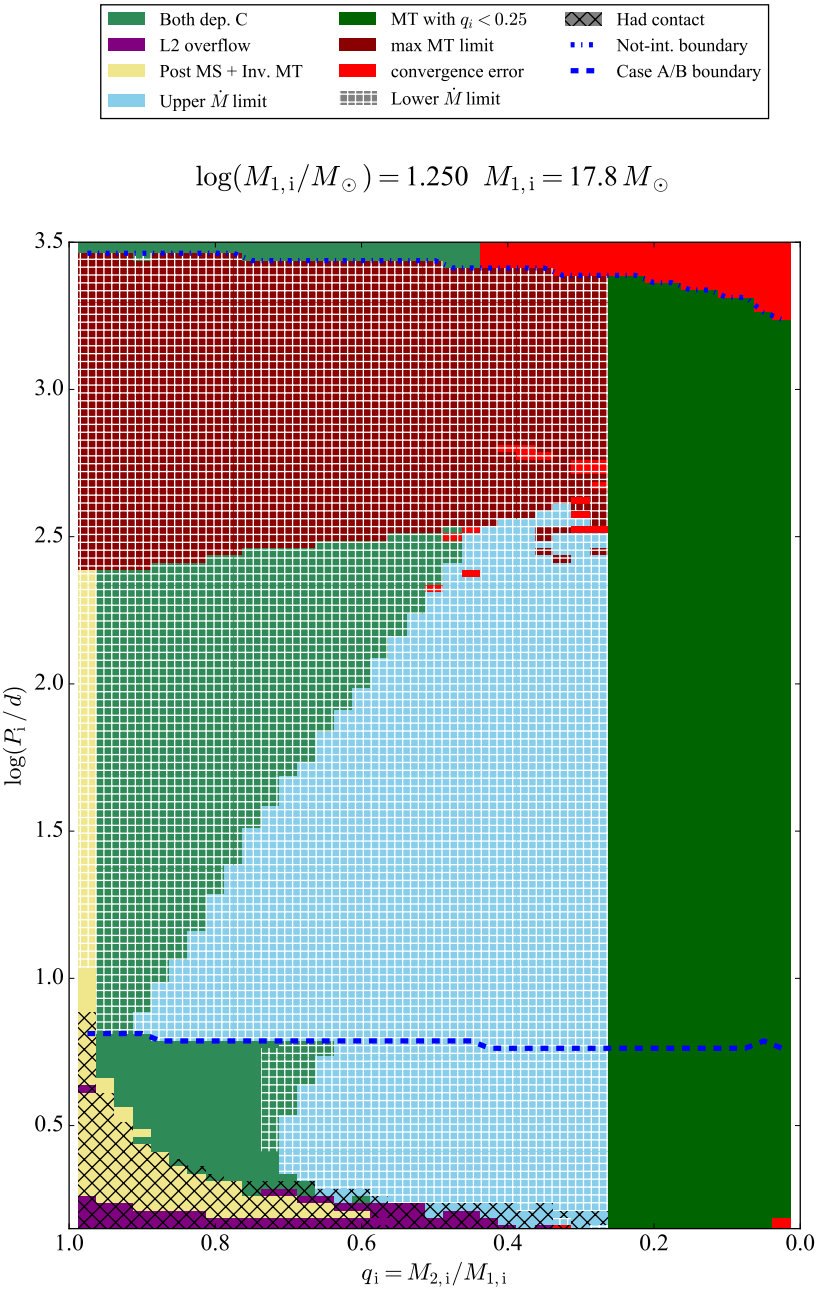

Figure A.5: Phase diagram of binary models with fixed initial donor mass of $M_{1,\mathrm{i}} = 17.8\,M_\odot$. The initial mass ratio q_i is plotted versus the initial orbital period P_i. All models are calculated at LMC metallicity. The different phases are indicated in the legend and a more detailed description can be found in Section 3.1.1.

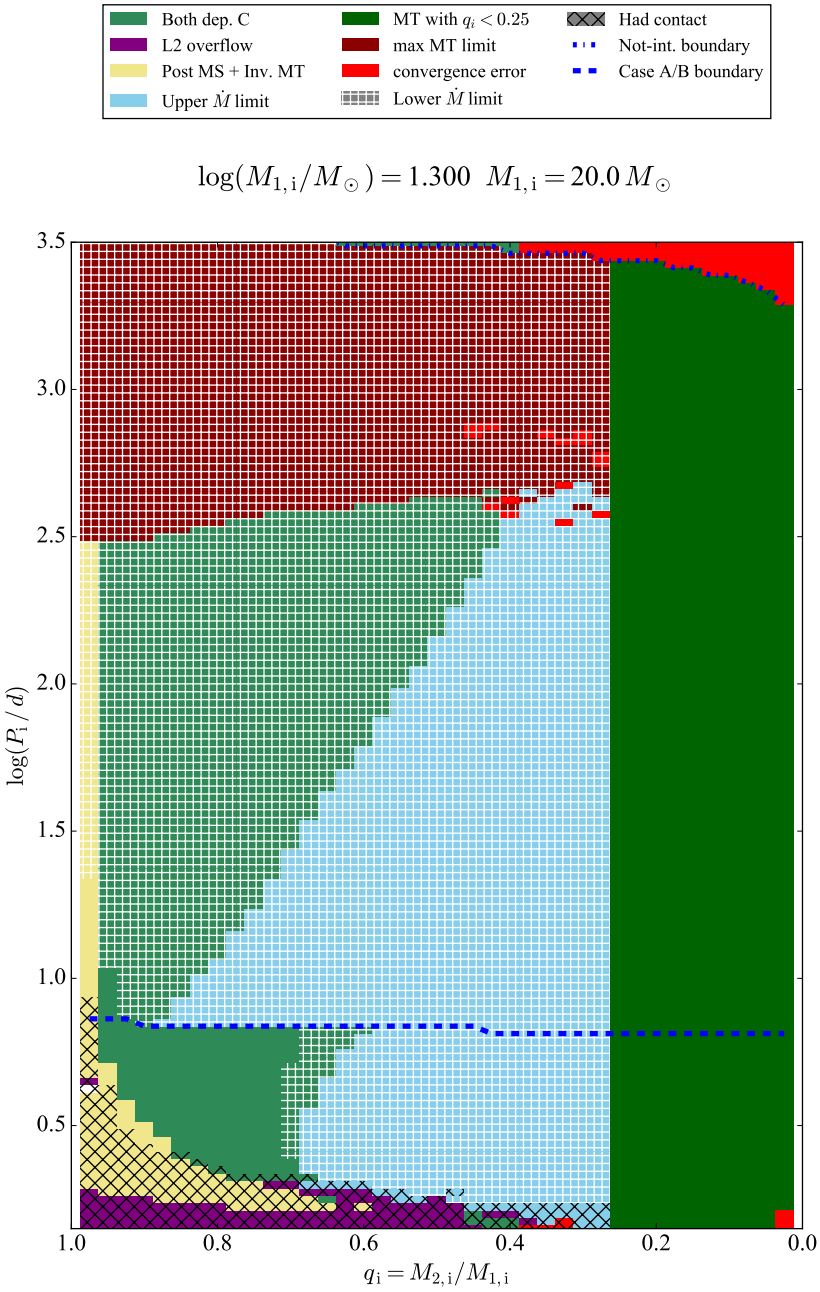

Figure A.6: Phase diagram of binary models with fixed initial donor mass of $M_{1,\mathrm{i}} = 20\,M_\odot$. The initial mass ratio q_i is plotted versus the initial orbital period P_i. All models are calculated at LMC metallicity. The different phases are indicated in the legend and a more detailed description can be found in Section 3.1.1.

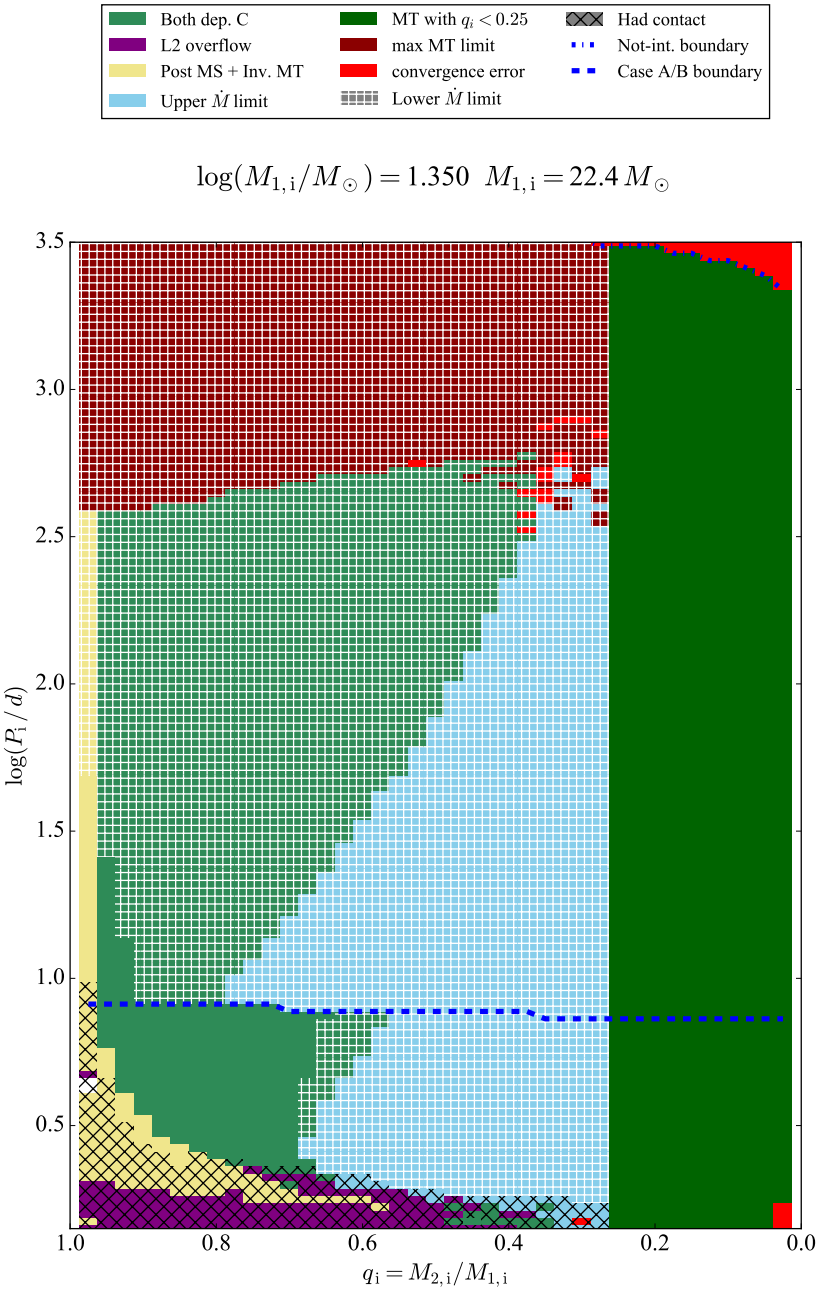

Figure A.7: Phase diagram of binary models with fixed initial donor mass of $M_{1,\mathrm{i}} = 22.4\,M_\odot$. The initial mass ratio q_i is plotted versus the initial orbital period P_i. All models are calculated at LMC metallicity. The different phases are indicated in the legend and a more detailed description can be found in Section 3.1.1.

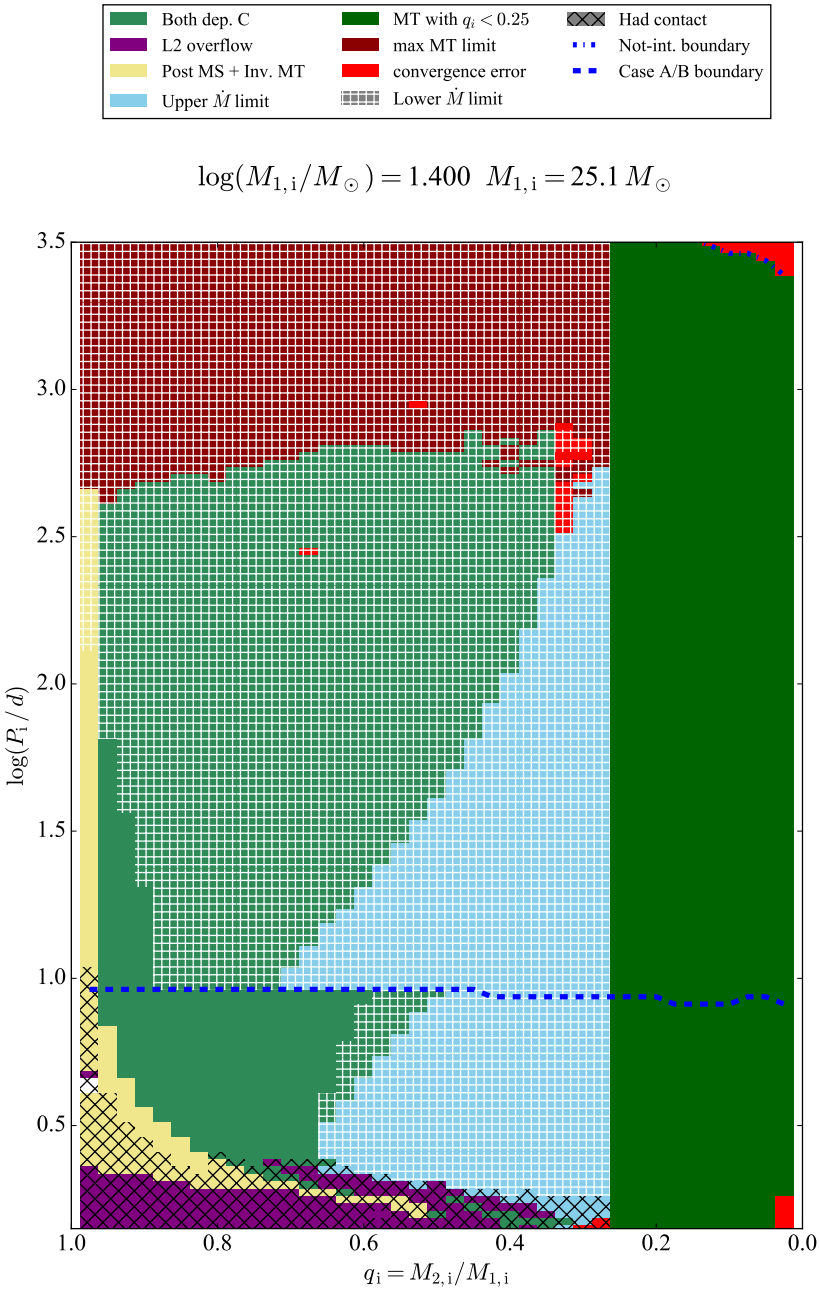

Figure A.8: Phase diagram of binary models with fixed initial donor mass of $M_{1,\mathrm{i}} = 25.1\,M_\odot$. The initial mass ratio q_i is plotted versus the initial orbital period P_i. All models are calculated at LMC metallicity. The different phases are indicated in the legend and a more detailed description can be found in Section 3.1.1.

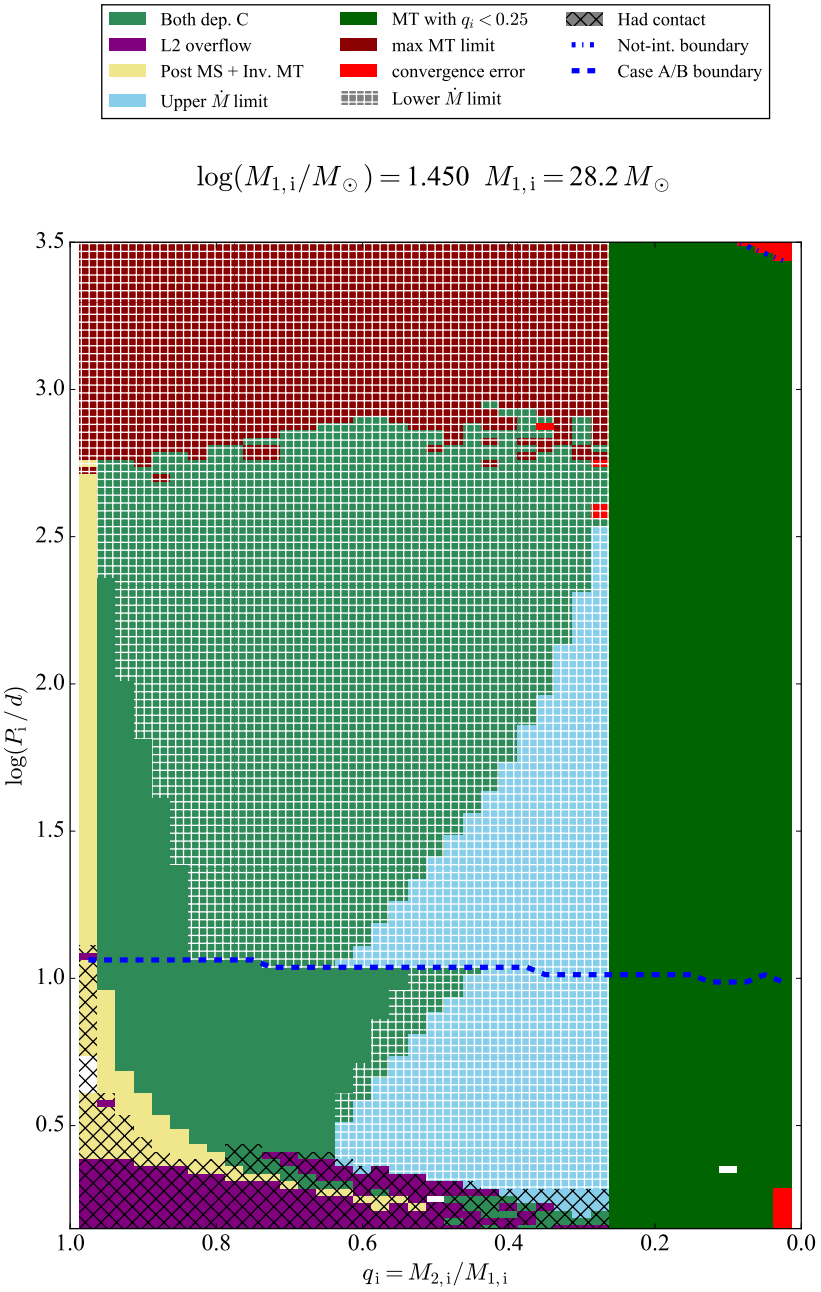

Figure A.9: Phase diagram of binary models with fixed initial donor mass of $M_{1,\mathrm{i}} = 28.2\,M_\odot$. The initial mass ratio q_i is plotted versus the initial orbital period P_i. All models are calculated at LMC metallicity. The different phases are indicated in the legend and a more detailed description can be found in Section 3.1.1.

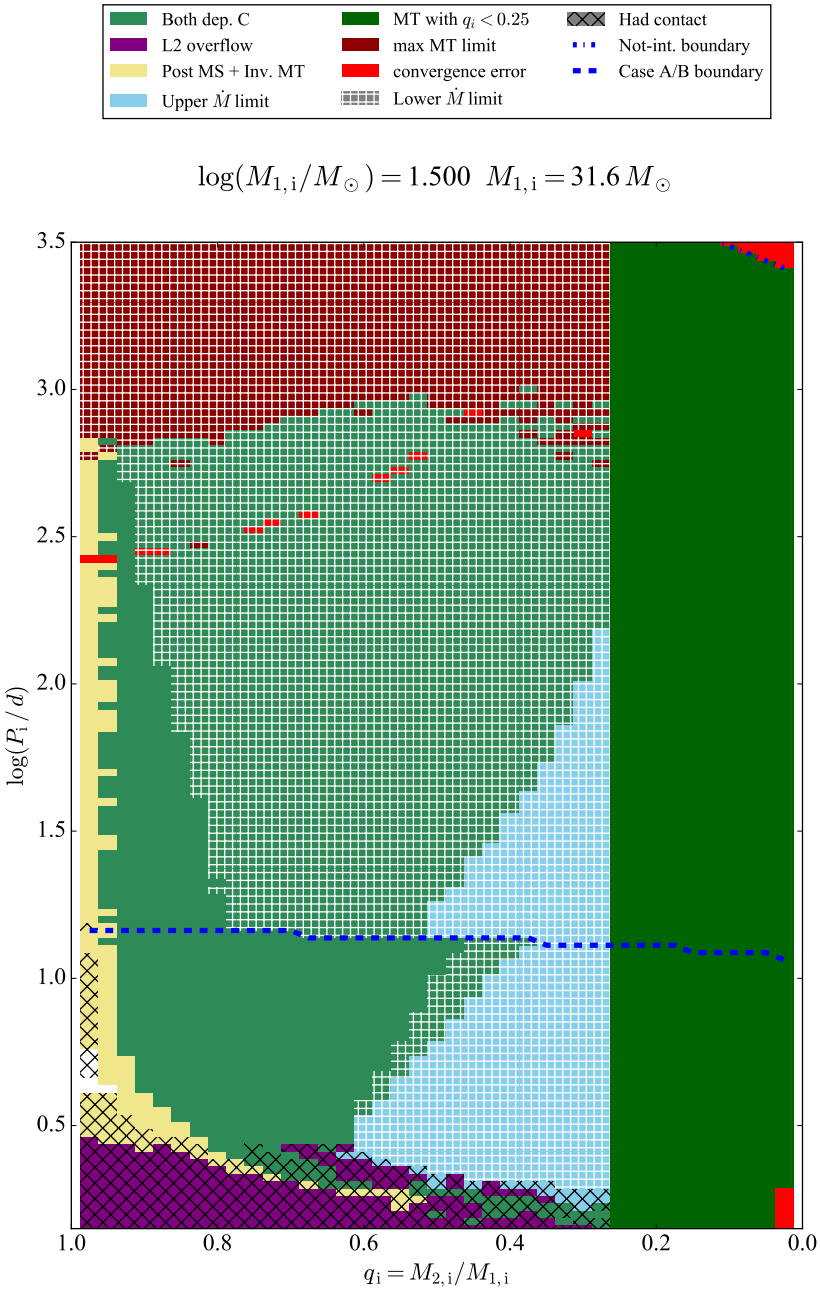

Figure A.10: Phase diagram of binary models with fixed initial donor mass of $M_{1,\mathrm{i}} = 31.6\,M_\odot$. The initial mass ratio q_i is plotted versus the initial orbital period P_i. All models are calculated at LMC metallicity. The different phases are indicated in the legend and a more detailed description can be found in Section 3.1.1.

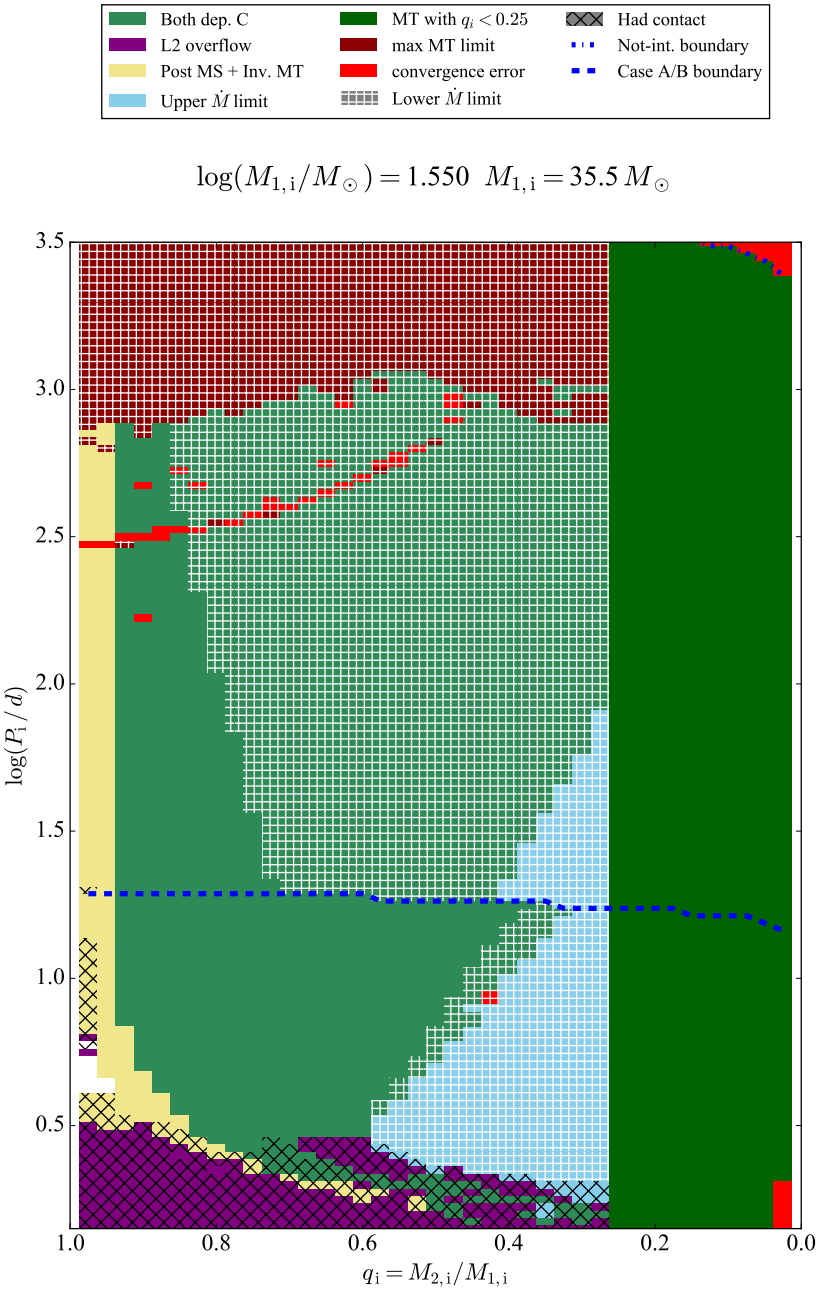

Figure A.11: Phase diagram of binary models with fixed initial donor mass of $M_{1,\mathrm{i}} = 35.5\,M_\odot$. The initial mass ratio q_i is plotted versus the initial orbital period P_i. All models are calculated at LMC metallicity. The different phases are indicated in the legend and a more detailed description can be found in Section 3.1.1.

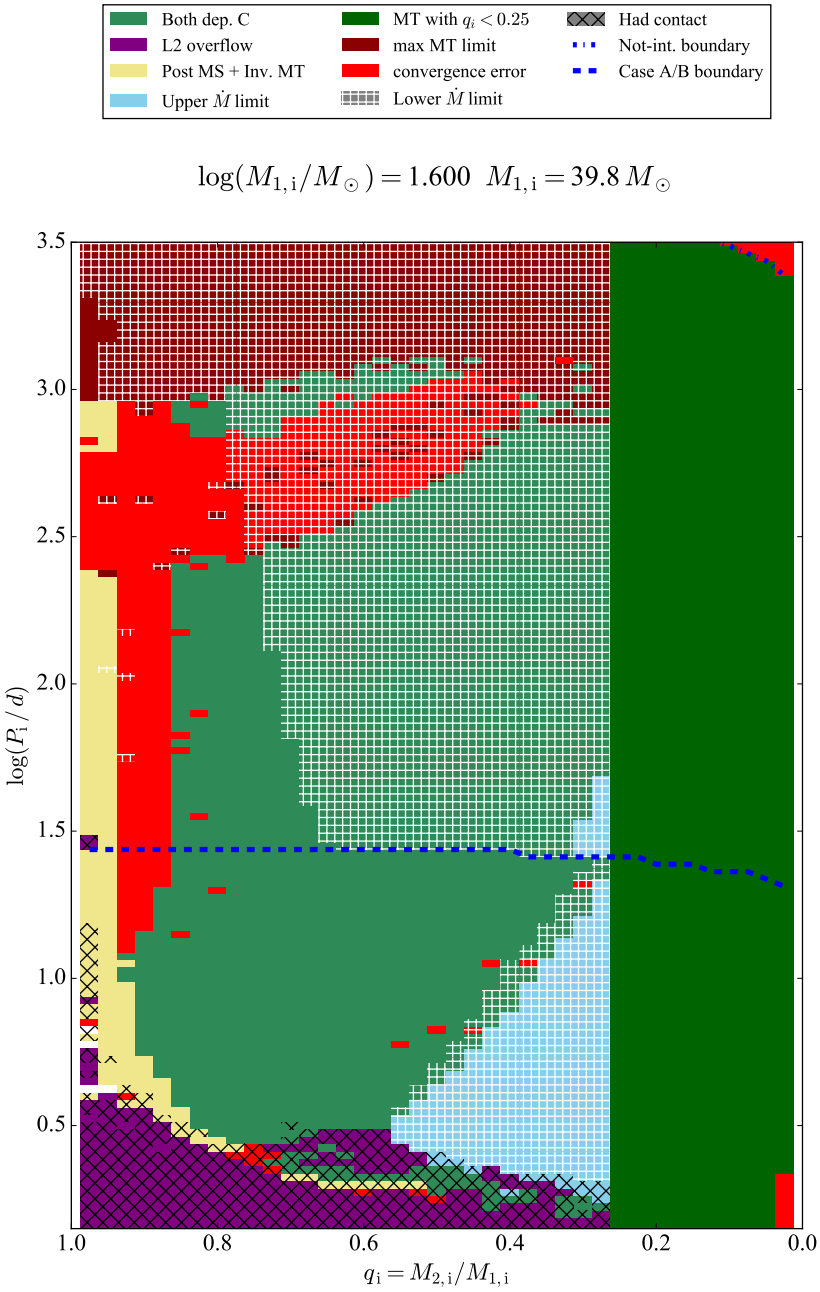

Figure A.12: Phase diagram of binary models with fixed initial donor mass of $M_{1,\mathrm{i}} = 39.8\,M_\odot$. The initial mass ratio q_i is plotted versus the initial orbital period P_i. All models are calculated at LMC metallicity. The different phases are indicated in the legend and a more detailed description can be found in Section 3.1.1.

B The SMC Grid

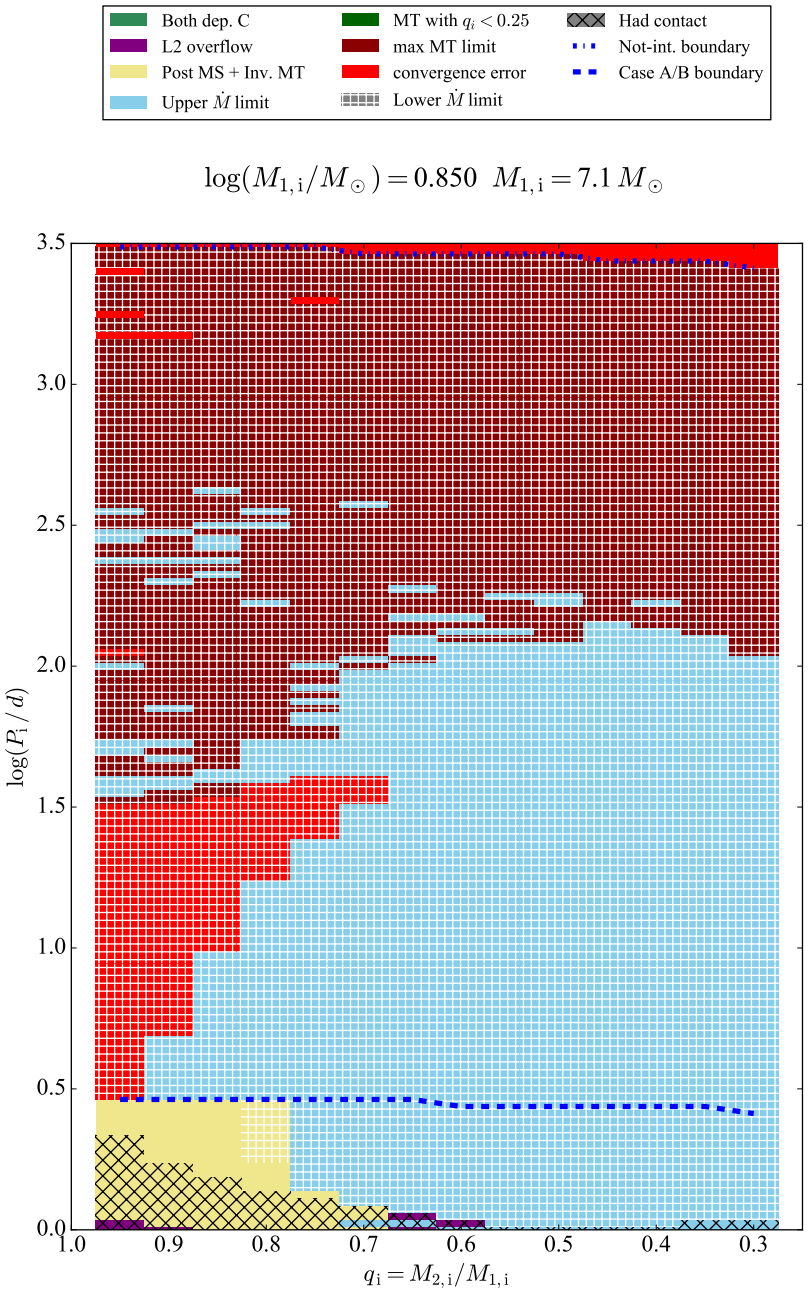

Figure B.1: Phase diagram of binary models with fixed initial donor mass of $M_{1,\mathrm{i}} = 7.1\,M_\odot$. The initial mass ratio q_i is plotted versus the initial orbital period P_i. All models are calculated at SMC metallicity. The different phases are indicated in the legend and a more detailed description can be found in Section 3.1.1.

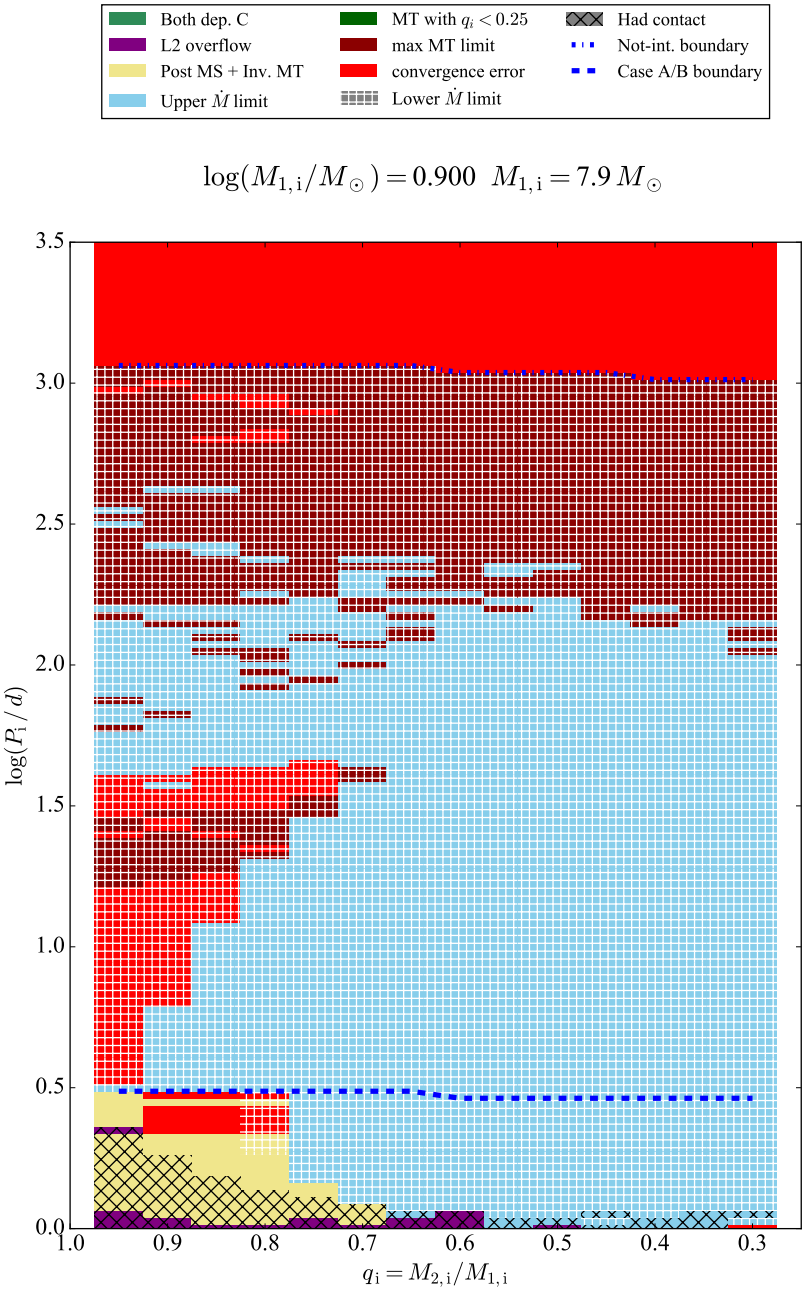

Figure B.2: Phase diagram of binary models with fixed initial donor mass of $M_{1,\mathrm{i}} = 7.9\,M_\odot$. The initial mass ratio q_i is plotted versus the initial orbital period P_i. All models are calculated at SMC metallicity. The different phases are indicated in the legend and a more detailed description can be found in Section 3.1.1.

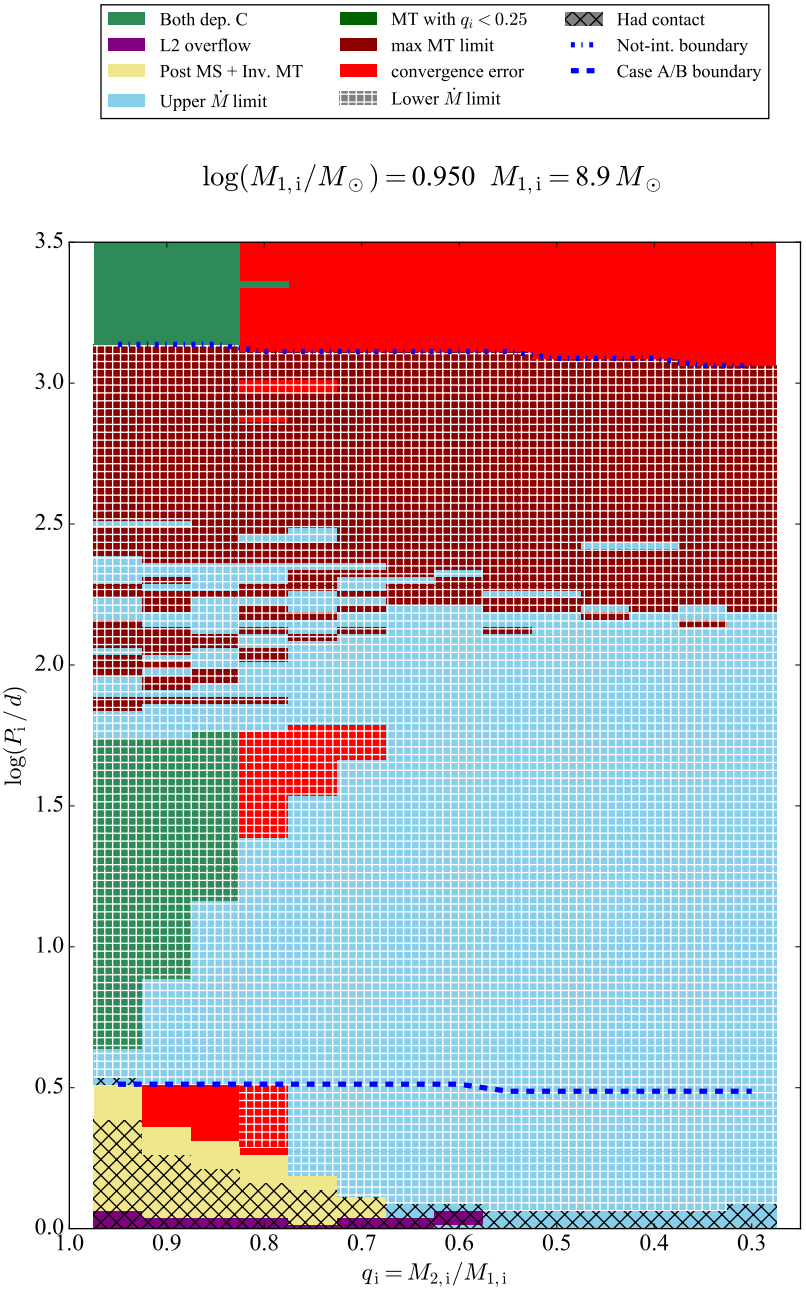

Figure B.3: Phase diagram of binary models with fixed initial donor mass of $M_{1,\mathrm{i}} = 8.9\,M_\odot$. The initial mass ratio q_i is plotted versus the initial orbital period P_i. All models are calculated at SMC metallicity. The different phases are indicated in the legend and a more detailed description can be found in Section 3.1.1.

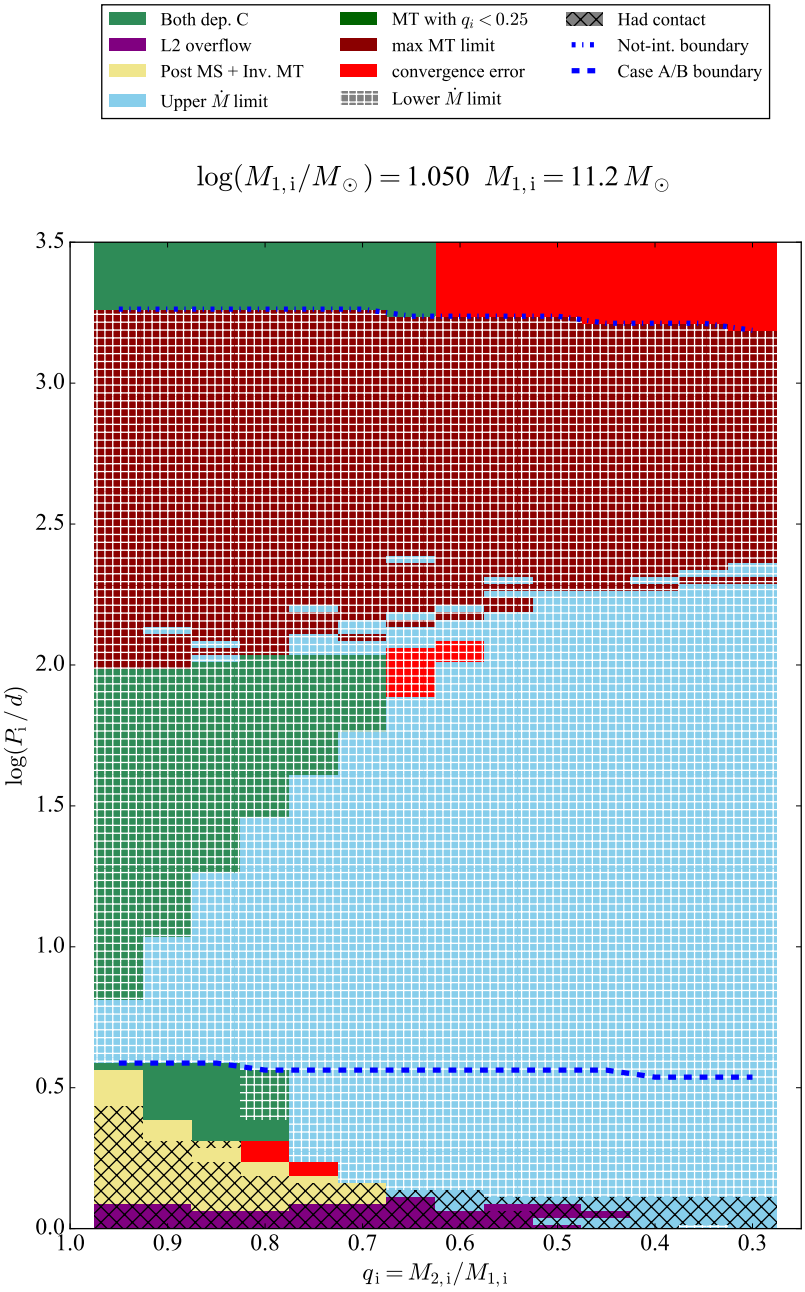

Figure B.4: Phase diagram of binary models with fixed initial donor mass of $M_{1,\mathrm{i}} = 11.2\,M_\odot$. The initial mass ratio q_i is plotted versus the initial orbital period P_i. All models are calculated at SMC metallicity. The different phases are indicated in the legend and a more detailed description can be found in Section 3.1.1.

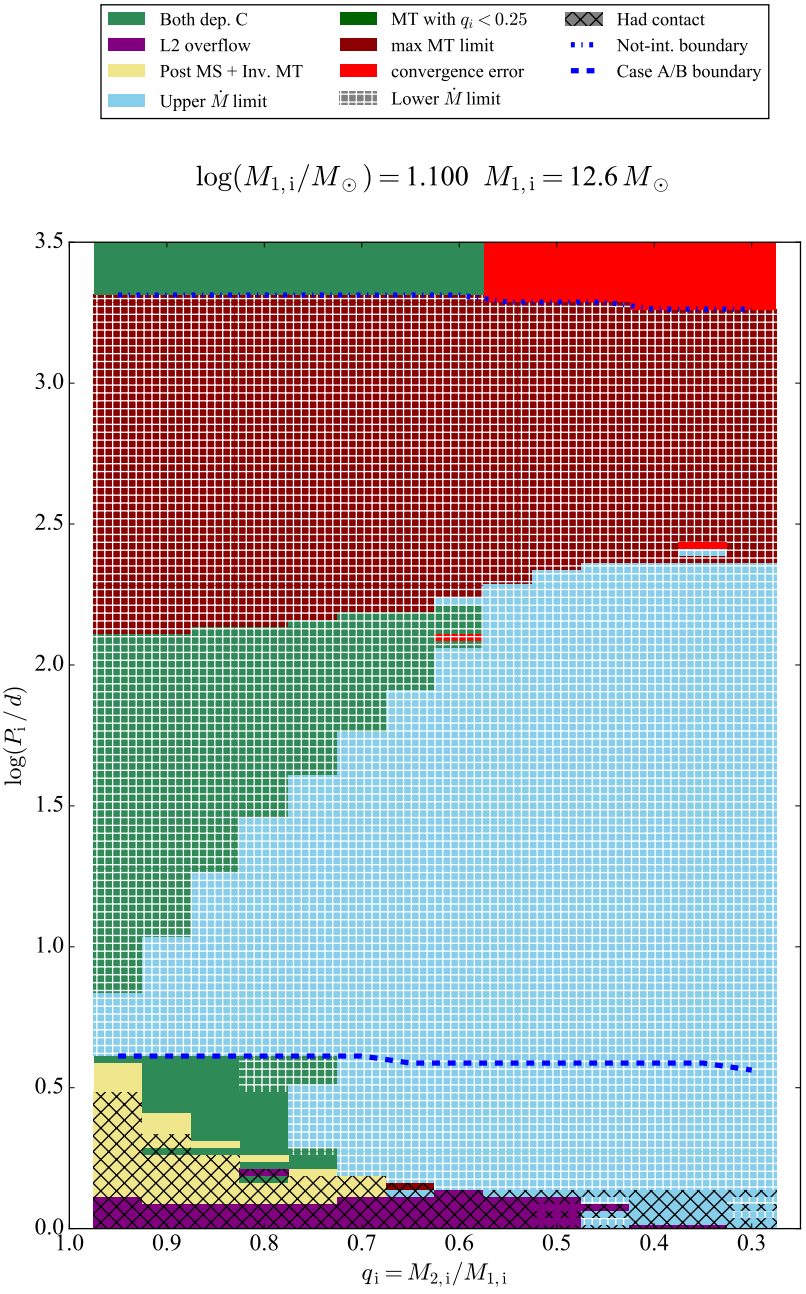

Figure B.5: Phase diagram of binary models with fixed initial donor mass of $M_{1,\mathrm{i}} = 12.6\,M_\odot$. The initial mass ratio q_i is plotted versus the initial orbital period P_i. All models are calculated at SMC metallicity. The different phases are indicated in the legend and a more detailed description can be found in Section 3.1.1.

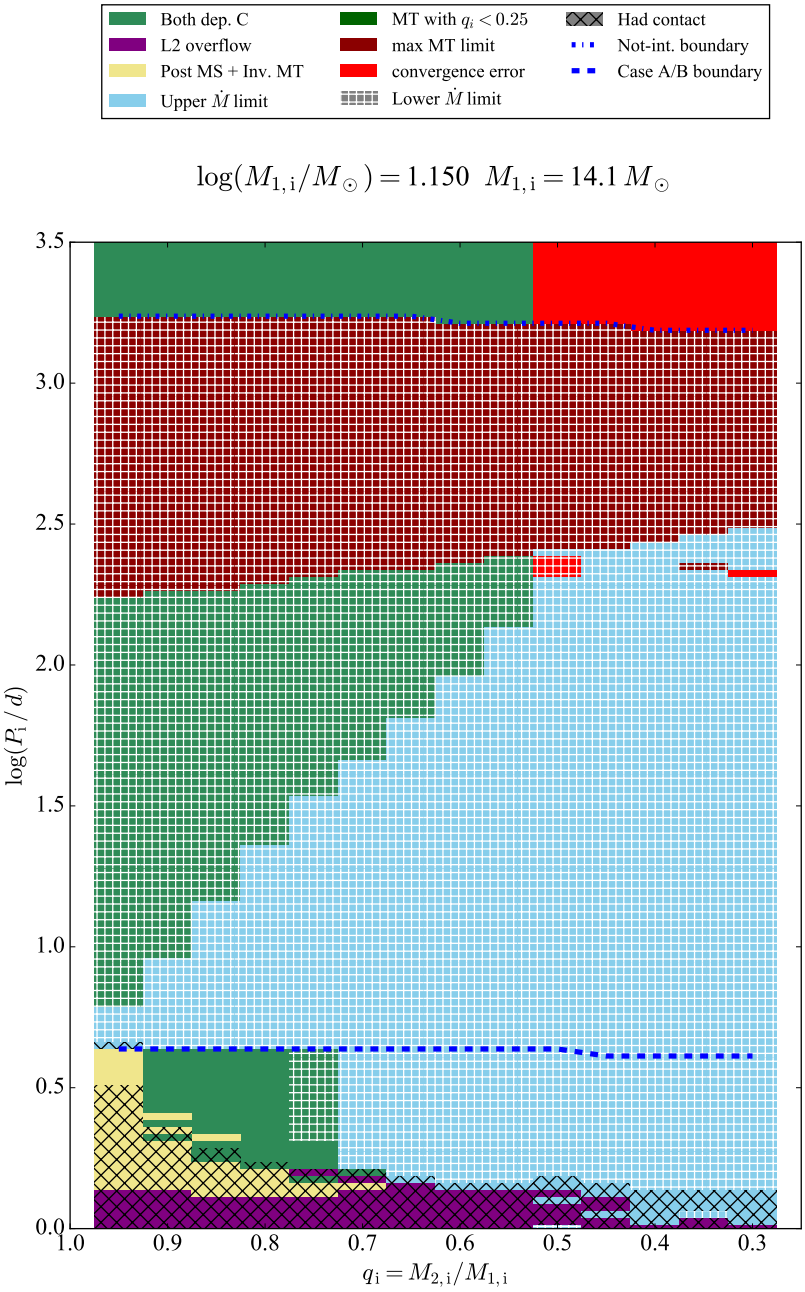

Figure B.6: Phase diagram of binary models with fixed initial donor mass of $M_{1,\mathrm{i}} = 14.6\,M_\odot$. The initial mass ratio q_i is plotted versus the initial orbital period P_i. All models are calculated at SMC metallicity. The different phases are indicated in the legend and a more detailed description can be found in Section 3.1.1.

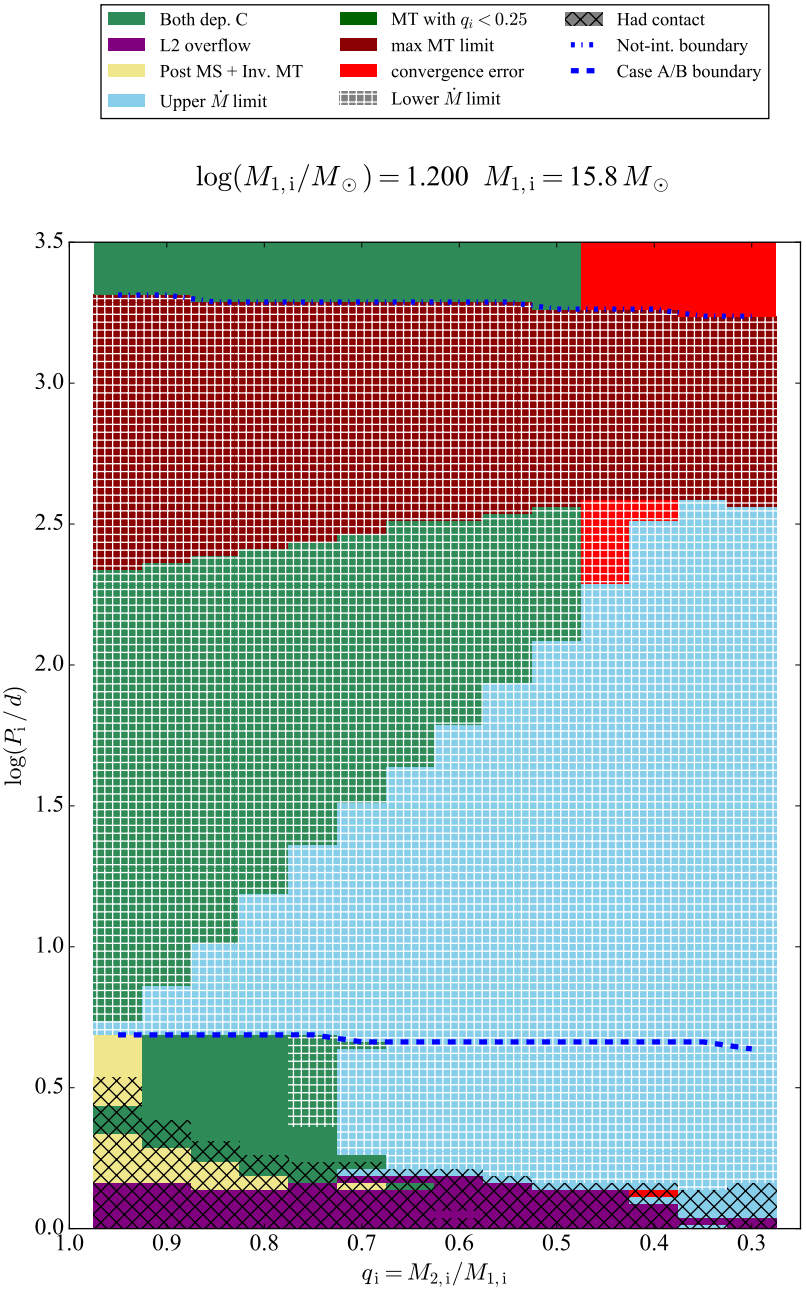

Figure B.7: Phase diagram of binary models with fixed initial donor mass of $M_{1,\mathrm{i}} = 15.8\,M_\odot$. The initial mass ratio q_i is plotted versus the initial orbital period P_i. All models are calculated at SMC metallicity. The different phases are indicated in the legend and a more detailed description can be found in Section 3.1.1.

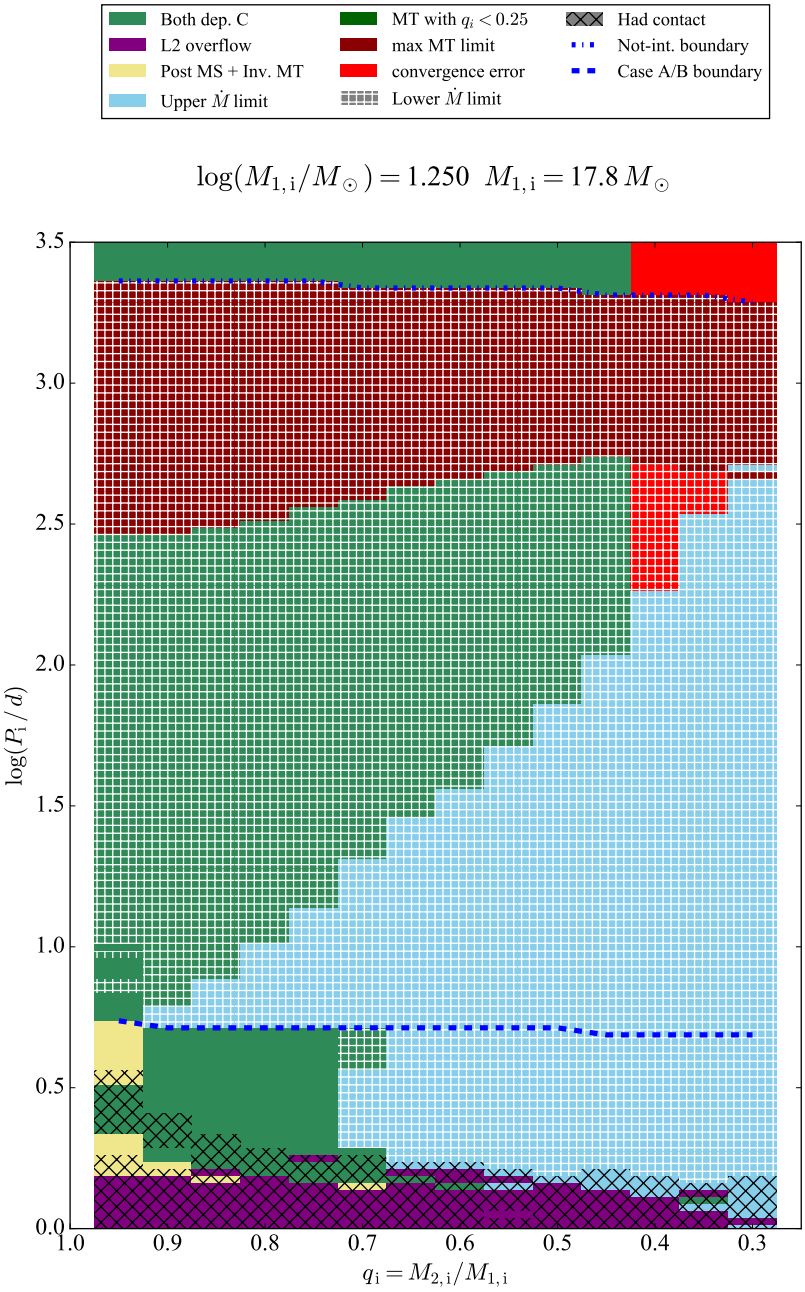

Figure B.8: Phase diagram of binary models with fixed initial donor mass of $M_{1,\mathrm{i}} = 17.8\,M_\odot$. The initial mass ratio q_i is plotted versus the initial orbital period P_i. All models are calculated at SMC metallicity. The different phases are indicated in the legend and a more detailed description can be found in Section 3.1.1.

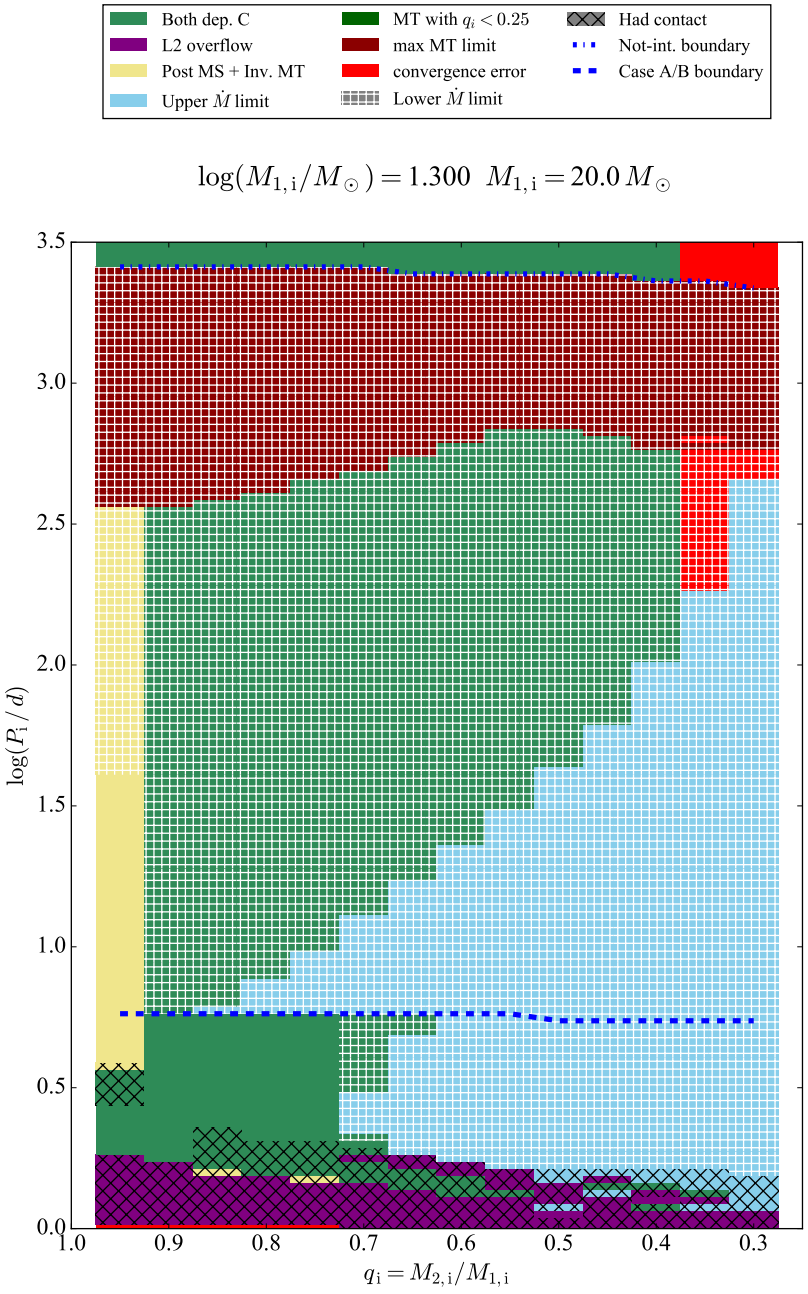

Figure B.9: Phase diagram of binary models with fixed initial donor mass of $M_{1,\mathrm{i}} = 20\,M_\odot$. The initial mass ratio q_i is plotted versus the initial orbital period P_i. All models are calculated at SMC metallicity. The different phases are indicated in the legend and a more detailed description can be found in Section 3.1.1.

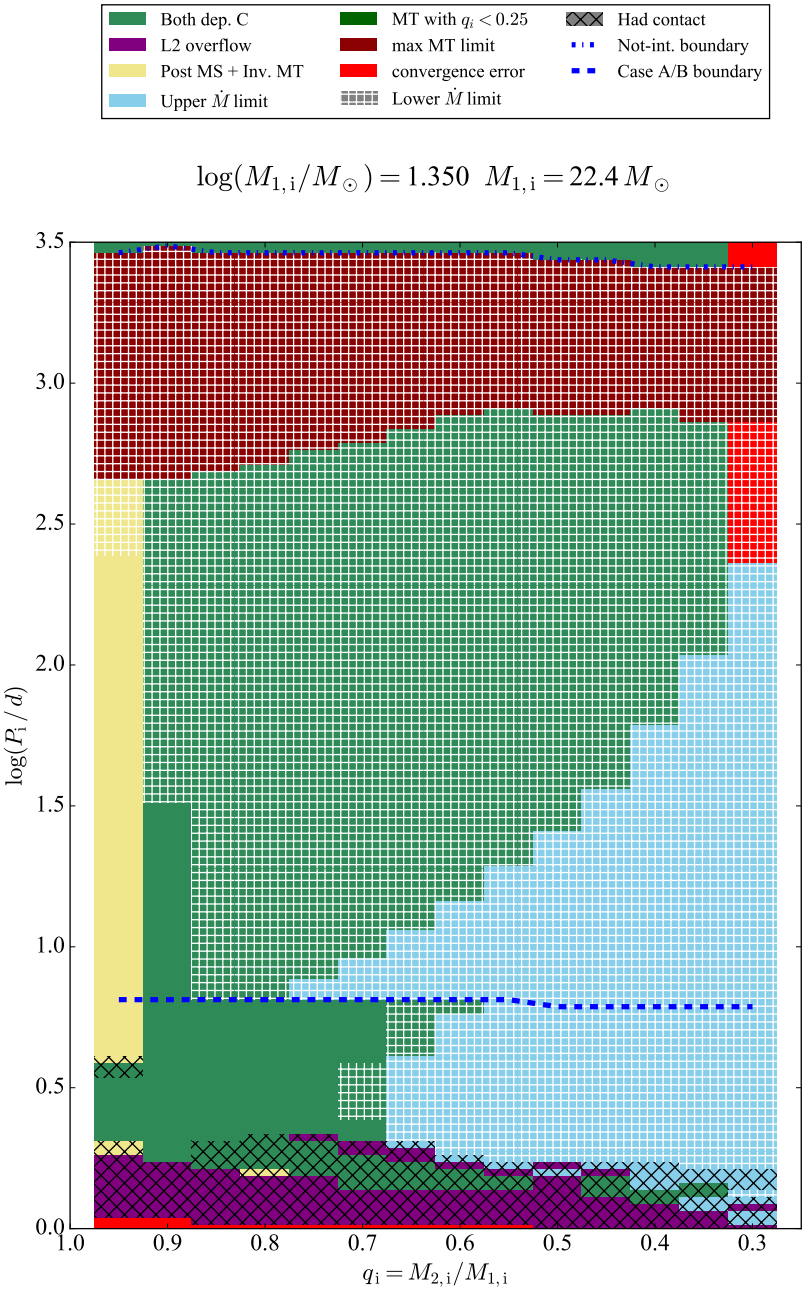

Figure B.10: Phase diagram of binary models with fixed initial donor mass of $M_{1,\mathrm{i}} = 22.4\,M_\odot$. The initial mass ratio q_i is plotted versus the initial orbital period P_i. All models are calculated at SMC metallicity. The different phases are indicated in the legend and a more detailed description can be found in Section 3.1.1.

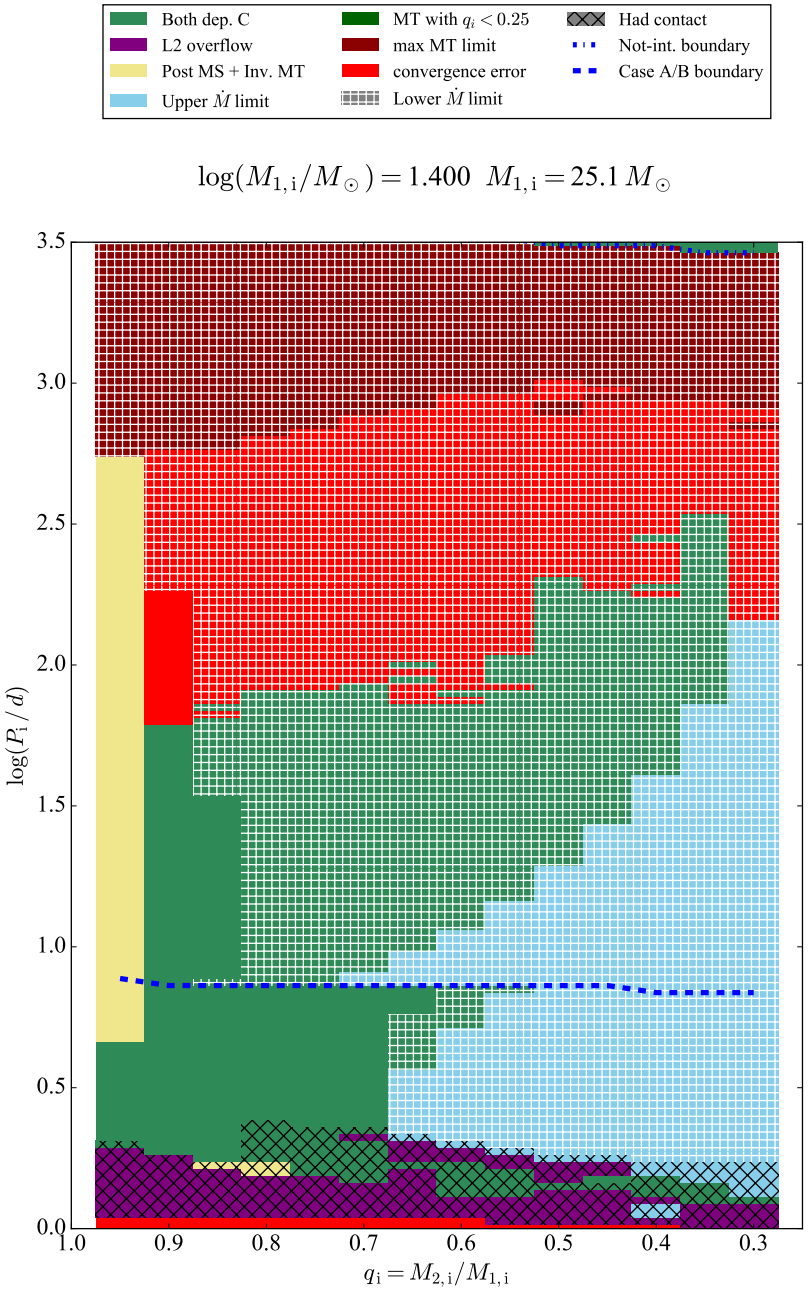

Figure B.11: Phase diagram of binary models with fixed initial donor mass of $M_{1,\mathrm{i}} = 25.1\,M_\odot$. The initial mass ratio q_i is plotted versus the initial orbital period P_i. All models are calculated at SMC metallicity. The different phases are indicated in the legend and a more detailed description can be found in Section 3.1.1.

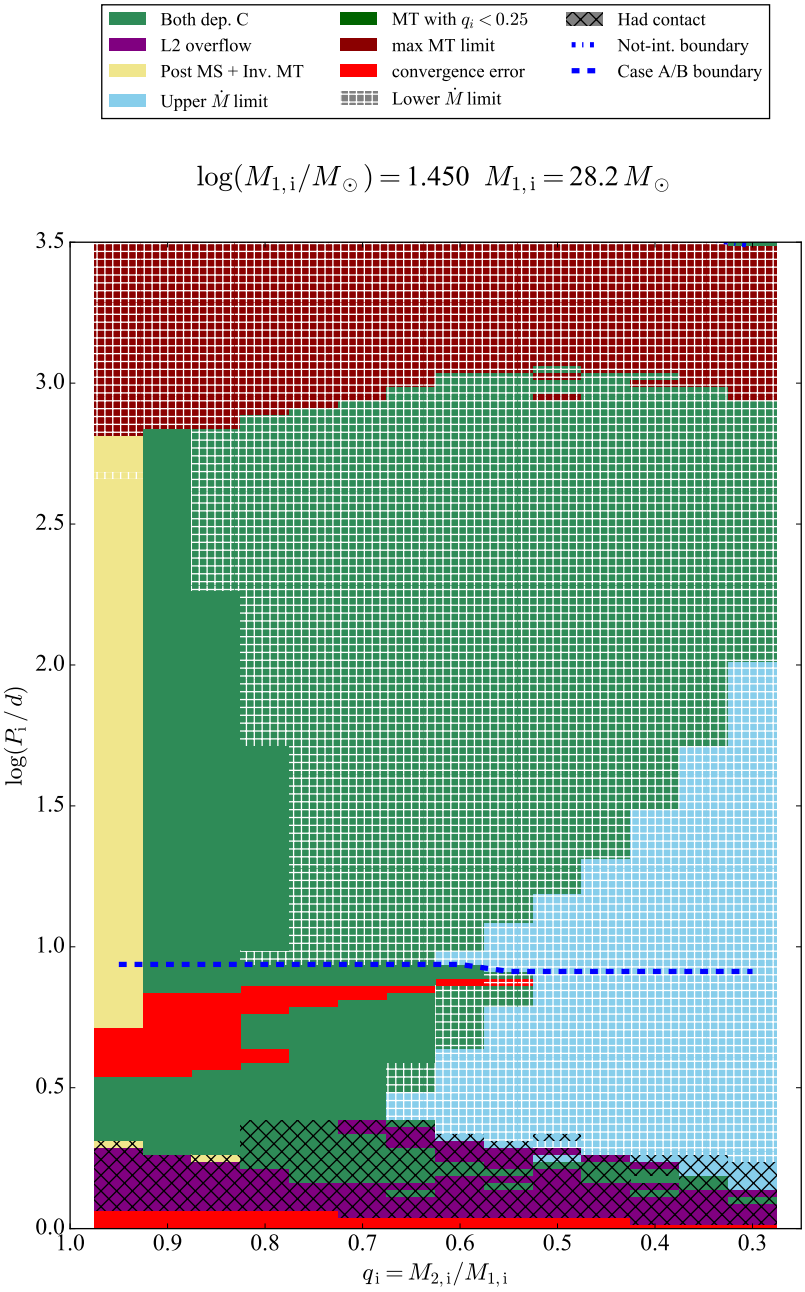

Figure B.12: Phase diagram of binary models with fixed initial donor mass of $M_{1,\mathrm{i}} = 28.2\,M_\odot$. The initial mass ratio q_i is plotted versus the initial orbital period P_i. All models are calculated at SMC metallicity. The different phases are indicated in the legend and a more detailed description can be found in Section 3.1.1.

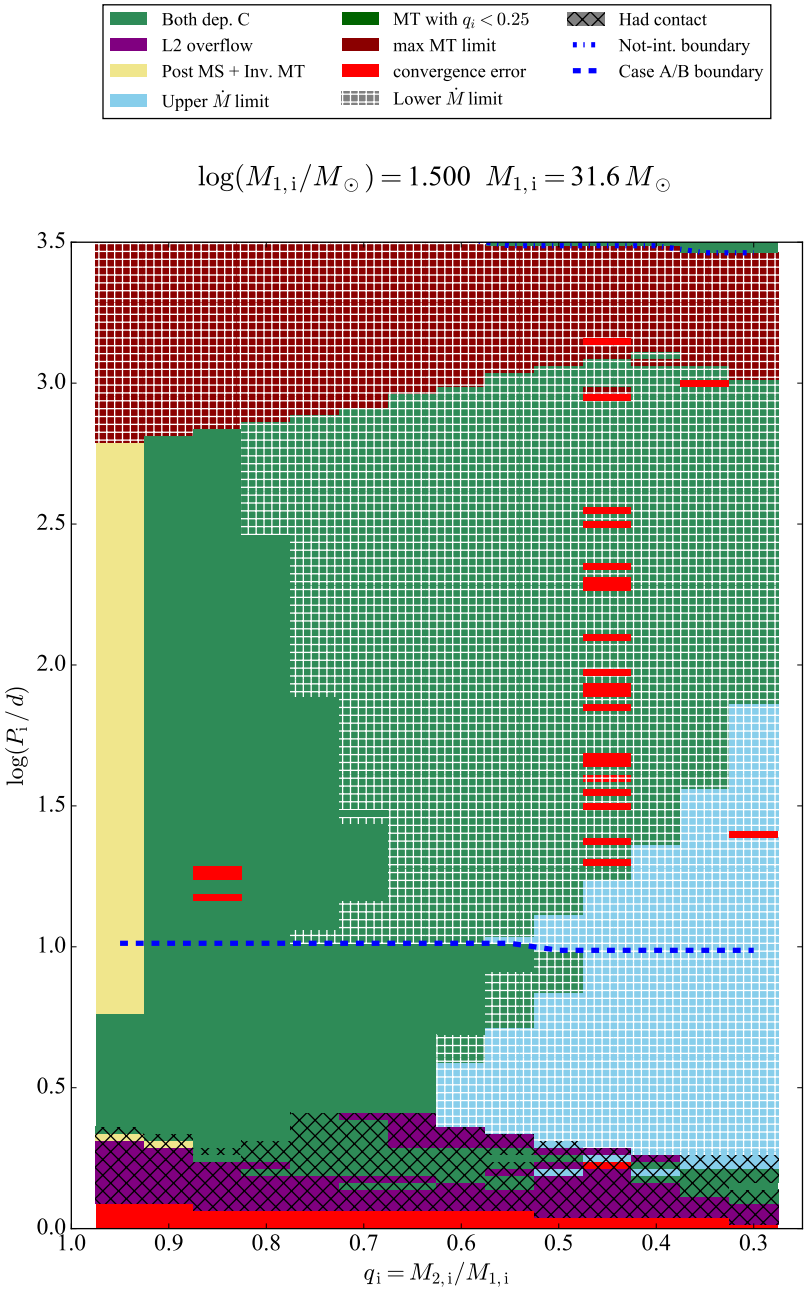

Figure B.13: Phase diagram of binary models with fixed initial donor mass of $M_{1,\mathrm{i}} = 31.6\,M_\odot$. The initial mass ratio q_i is plotted versus the initial orbital period P_i. All models are calculated at SMC metallicity. The different phases are indicated in the legend and a more detailed description can be found in Section 3.1.1.

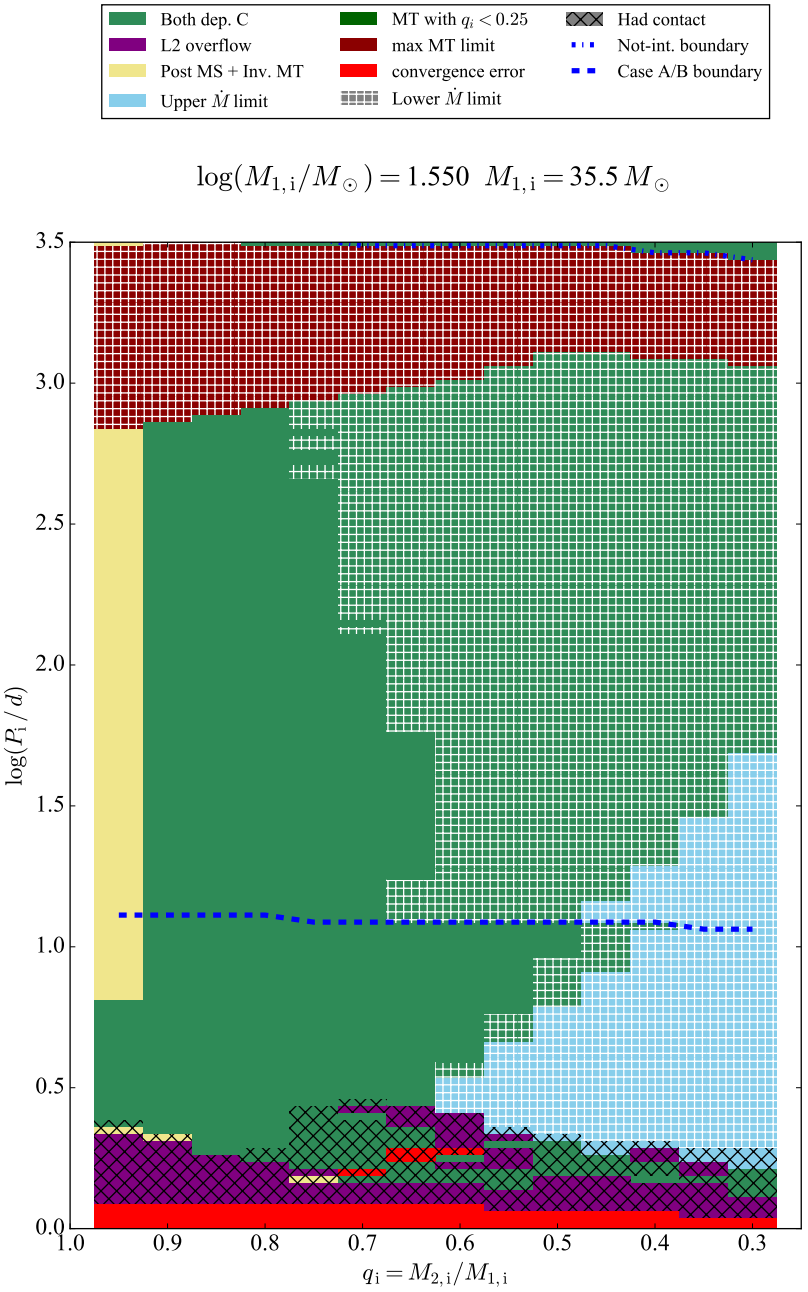

Figure B.14: Phase diagram of binary models with fixed initial donor mass of $M_{1,\mathrm{i}} = 35.5\,M_\odot$. The initial mass ratio q_i is plotted versus the initial orbital period P_i. All models are calculated at SMC metallicity. The different phases are indicated in the legend and a more detailed description can be found in Section 3.1.1.

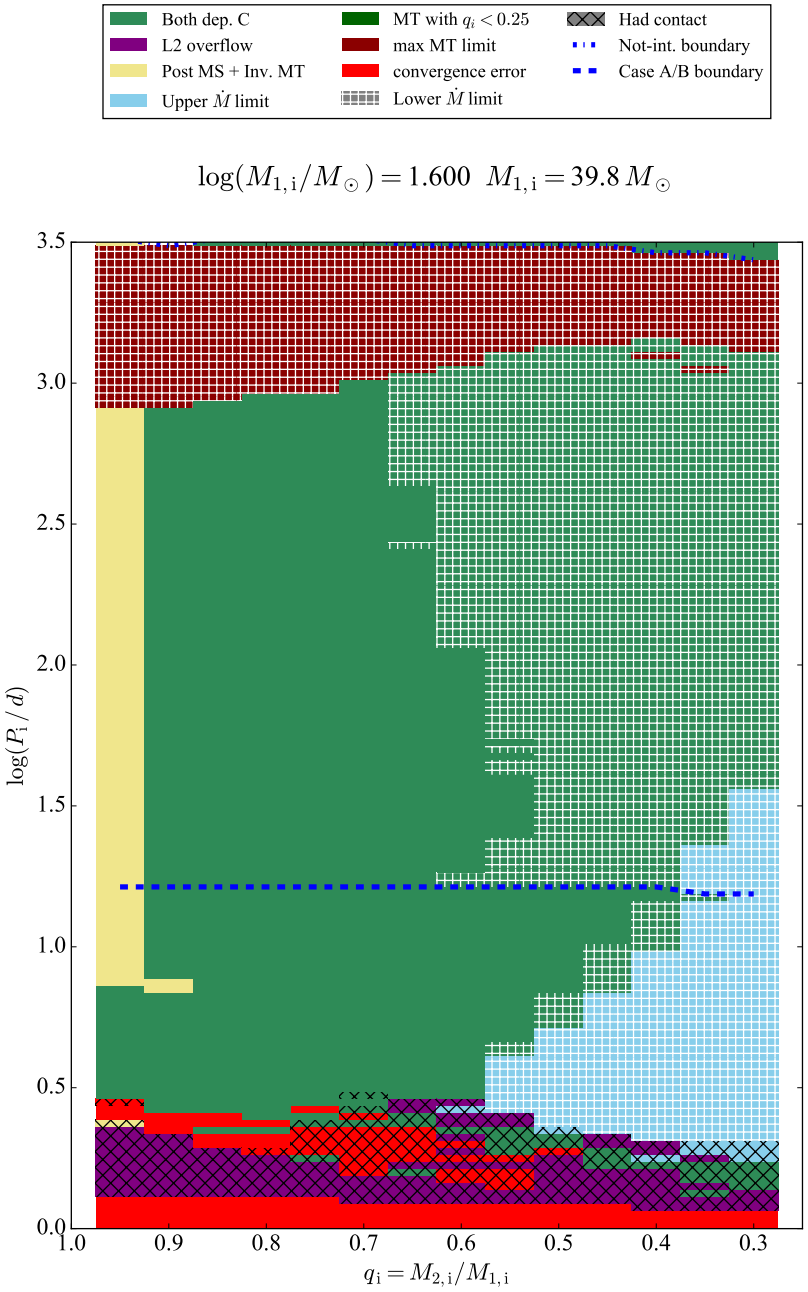

Figure B.15: Phase diagram of binary models with fixed initial donor mass of $M_{1,\mathrm{i}} = 39.8\,M_\odot$. The initial mass ratio q_i is plotted versus the initial orbital period P_i. All models are calculated at SMC metallicity. The different phases are indicated in the legend and a more detailed description can be found in Section 3.1.1.

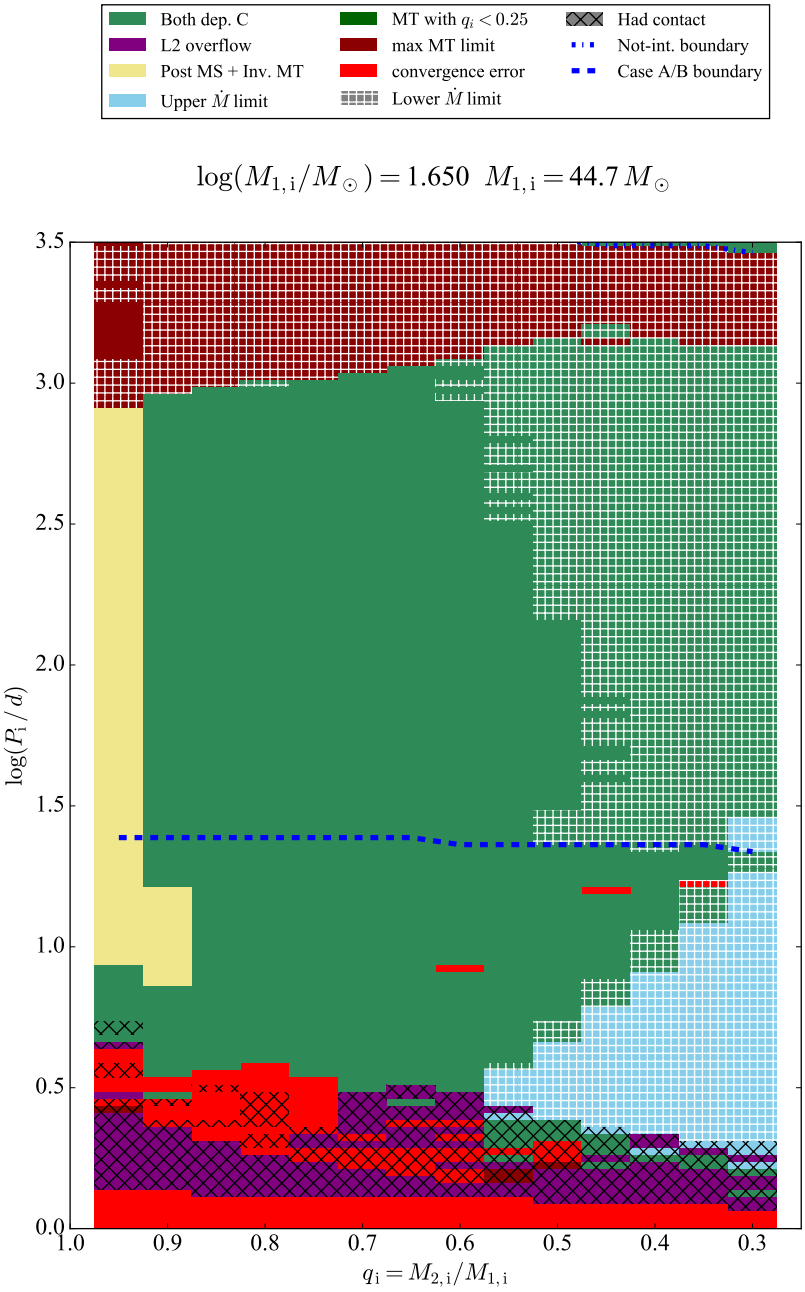

Figure B.16: Phase diagram of binary models with fixed initial donor mass of $M_{1,\mathrm{i}} = 44.7\,M_\odot$. The initial mass ratio q_i is plotted versus the initial orbital period P_i. All models are calculated at SMC metallicity. The different phases are indicated in the legend and a more detailed description can be found in Section 3.1.1.

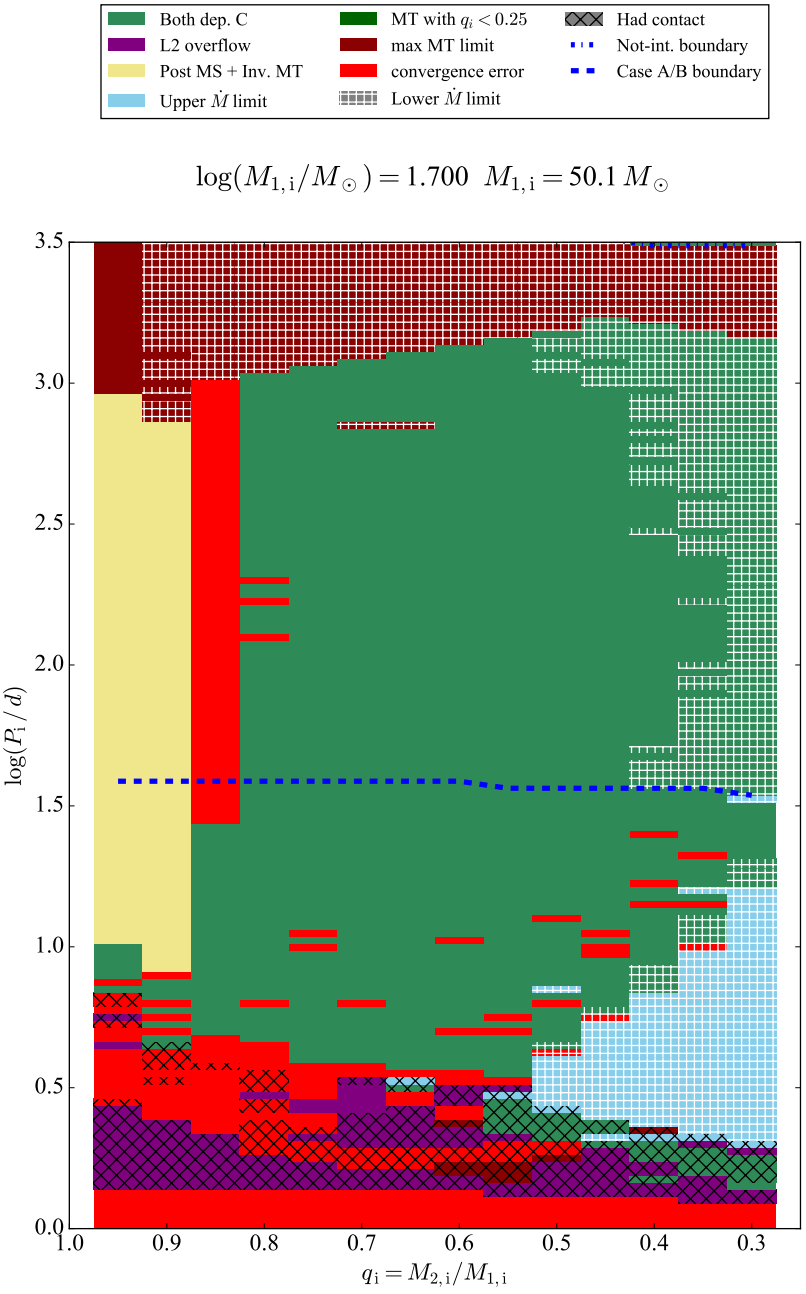

Figure B.17: Phase diagram of binary models with fixed initial donor mass of $M_{1,\mathrm{i}} = 50.1\,M_\odot$. The initial mass ratio q_i is plotted versus the initial orbital period P_i. All models are calculated at SMC metallicity. The different phases are indicated in the legend and a more detailed description can be found in Section 3.1.1.

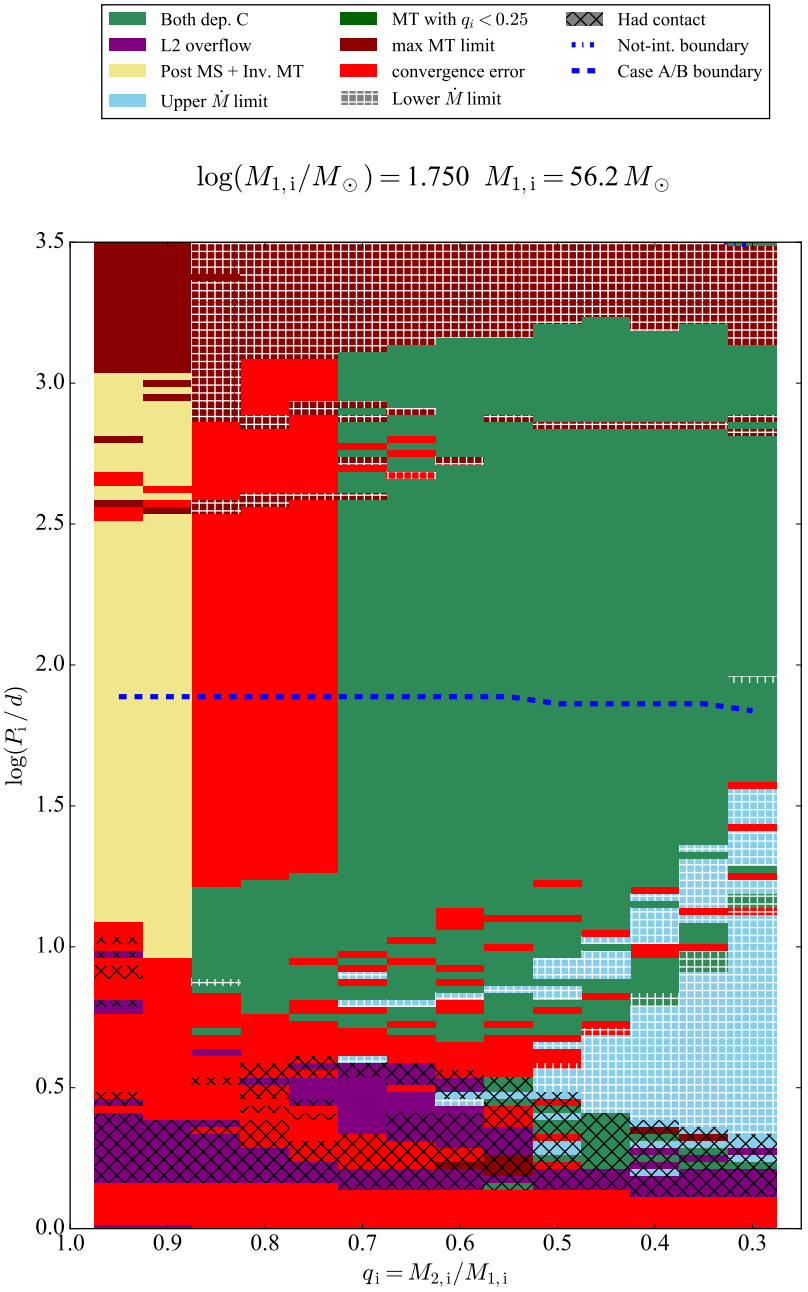

Figure B.18: Phase diagram of binary models with fixed initial donor mass of $M_{1,\mathrm{i}} = 56.2\,M_\odot$. The initial mass ratio q_i is plotted versus the initial orbital period P_i. All models are calculated at SMC metallicity. The different phases are indicated in the legend and a more detailed description can be found in Section 3.1.1.

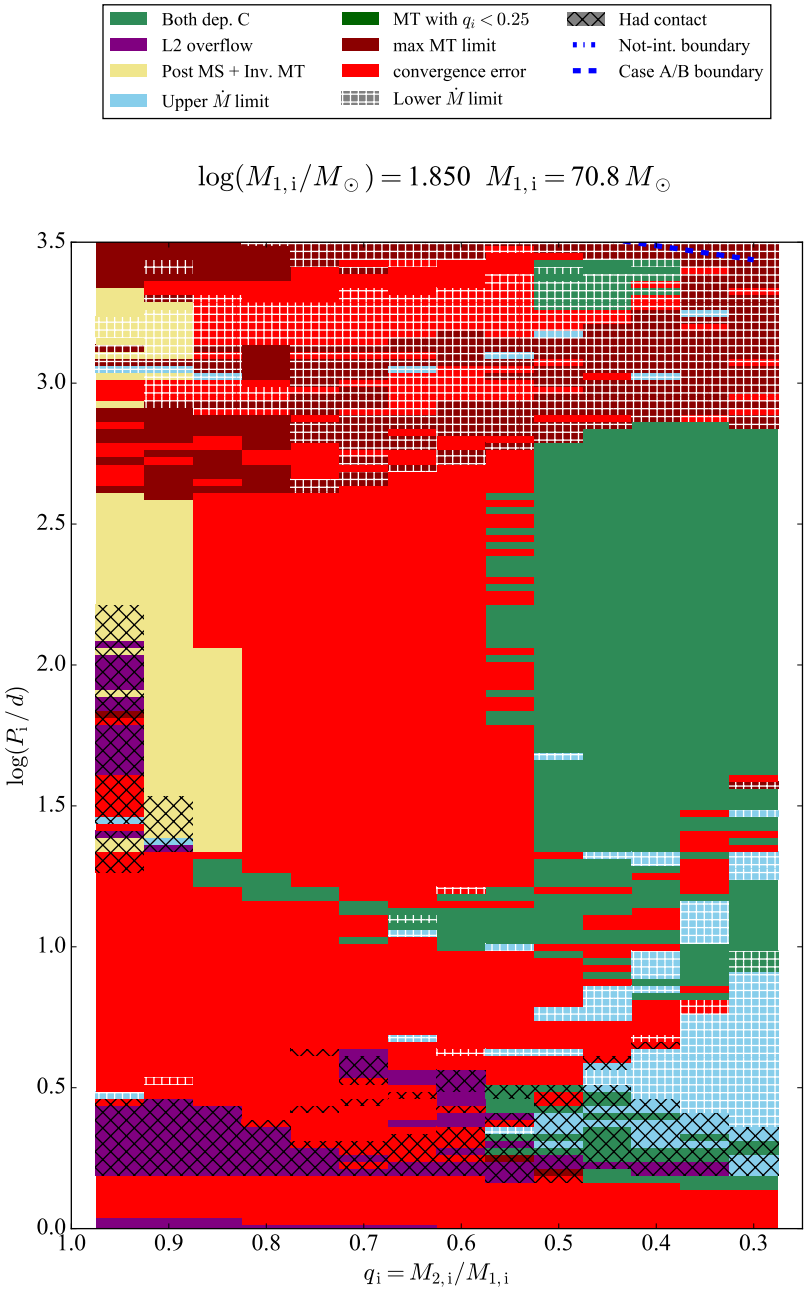

Figure B.19: Phase diagram of binary models with fixed initial donor mass of $M_{1,\mathrm{i}} = 70.8\,M_\odot$. The initial mass ratio q_i is plotted versus the initial orbital period P_i. All models are calculated at SMC metallicity. The different phases are indicated in the legend and a more detailed description can be found in Section 3.1.1.

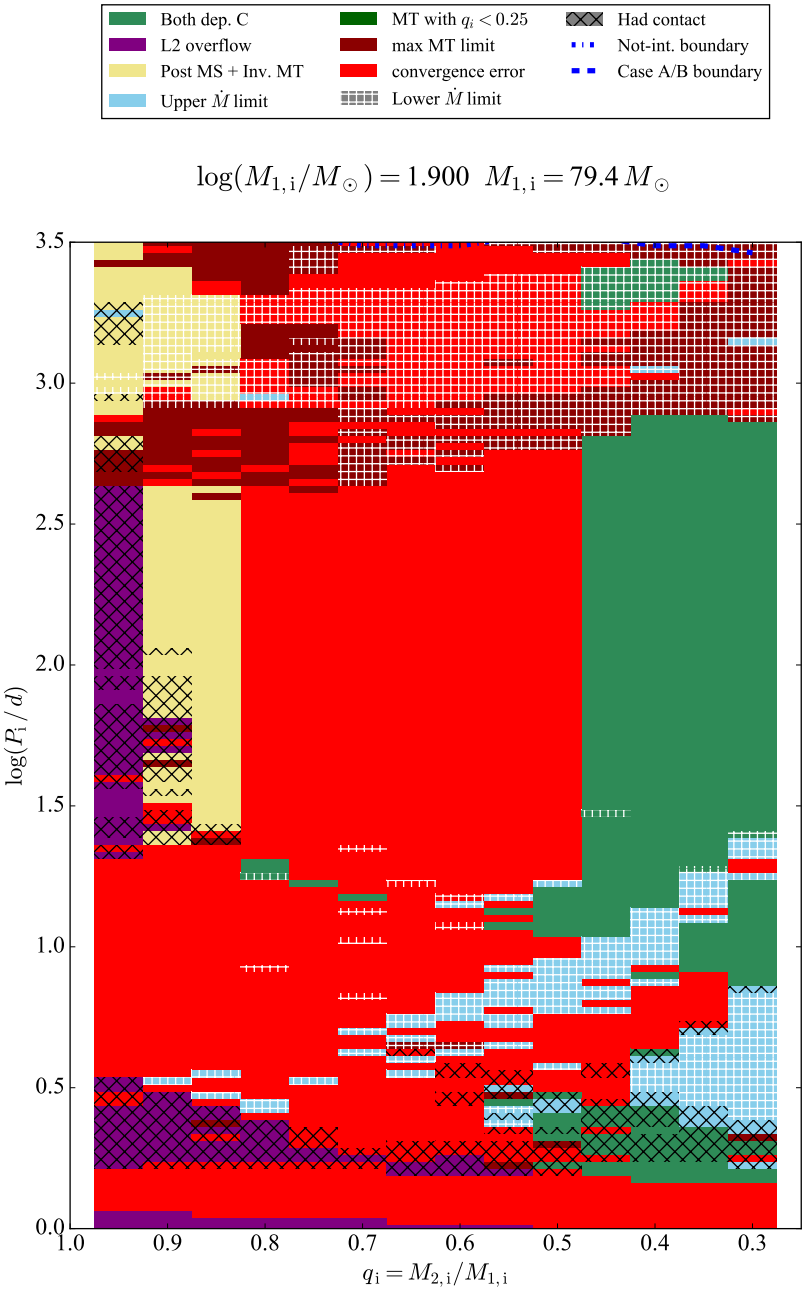

Figure B.20: Phase diagram of binary models with fixed initial donor mass of $M_{1,\mathrm{i}} = 79.4\,M_\odot$. The initial mass ratio q_i is plotted versus the initial orbital period P_i. All models are calculated at SMC metallicity. The different phases are indicated in the legend and a more detailed description can be found in Section 3.1.1.

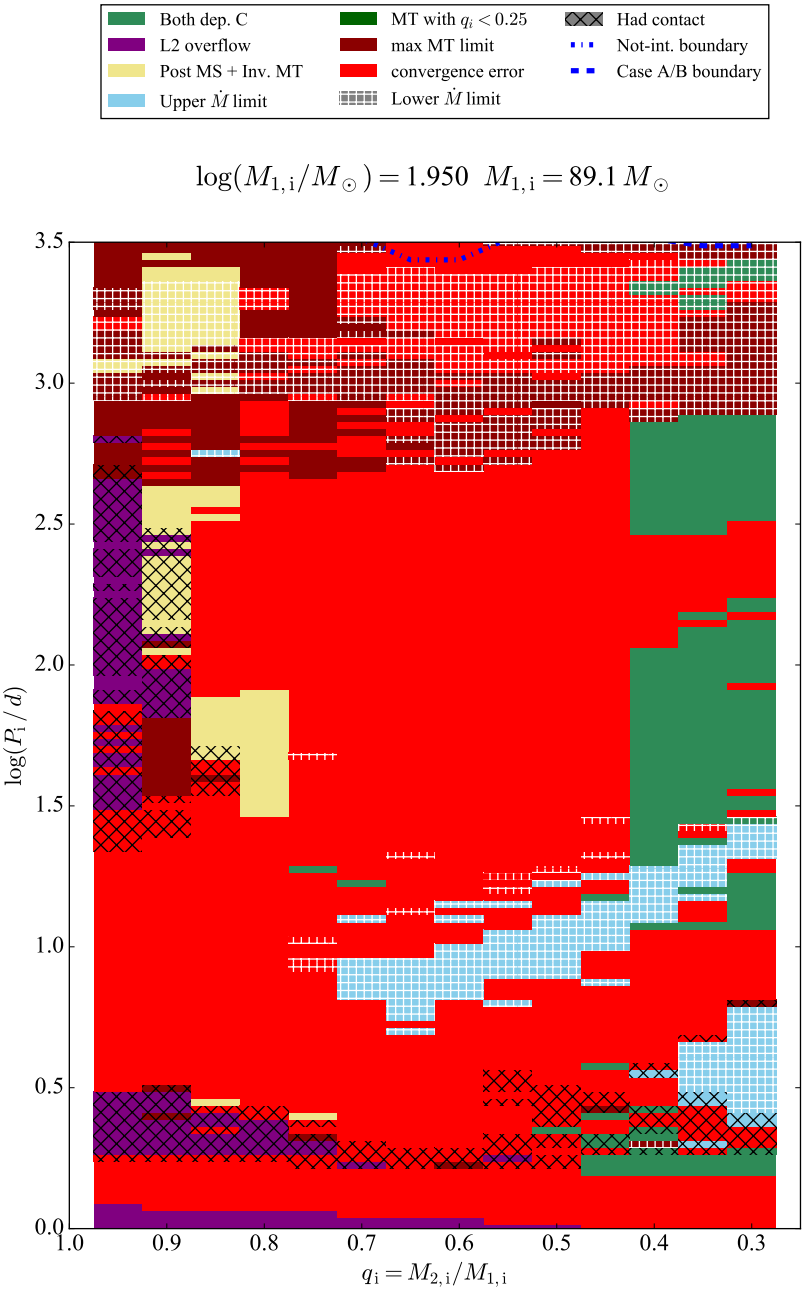

Figure B.21: Phase diagram of binary models with fixed initial donor mass of $M_{1,\mathrm{i}} = 89.1\,M_\odot$. The initial mass ratio q_i is plotted versus the initial orbital period P_i. All models are calculated at SMC metallicity. The different phases are indicated in the legend and a more detailed description can be found in Section 3.1.1.

C Extensions the LMC Grid

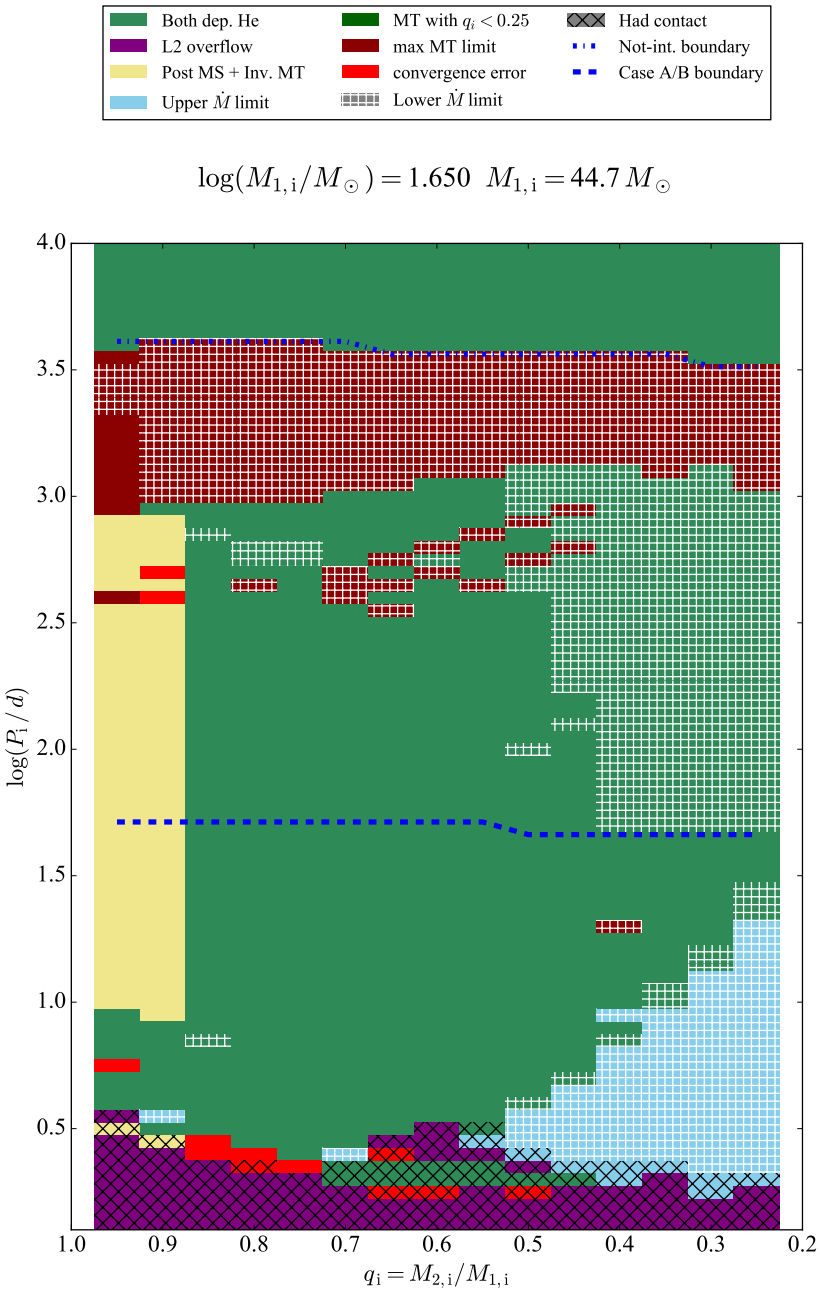

Figure C.1: Phase diagram of binary models with fixed initial donor mass of $M_{1,\mathrm{i}} = 44.7\,M_\odot$. The initial mass ratio q_i is plotted versus the initial orbital period P_i. All models are calculated at LMC metallicity. The different phases are indicated in the legend and a more detailed description can be found in Section 3.1.1.

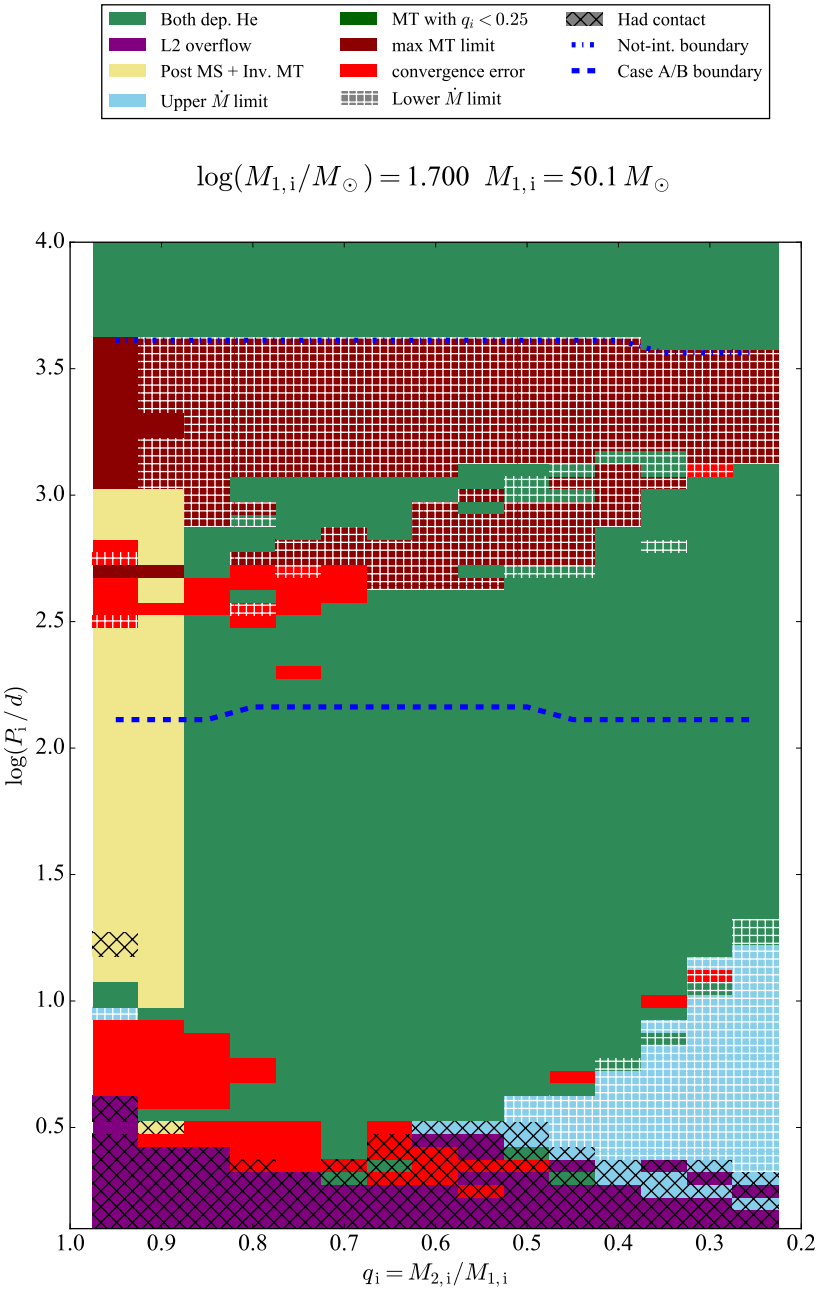

Figure C.2: Phase diagram of binary models with fixed initial donor mass of $M_{1,\mathrm{i}} = 50.1\,M_\odot$. The initial mass ratio q_i is plotted versus the initial orbital period P_i. All models are calculated at LMC metallicity. The different phases are indicated in the legend and a more detailed description can be found in Section 3.1.1.

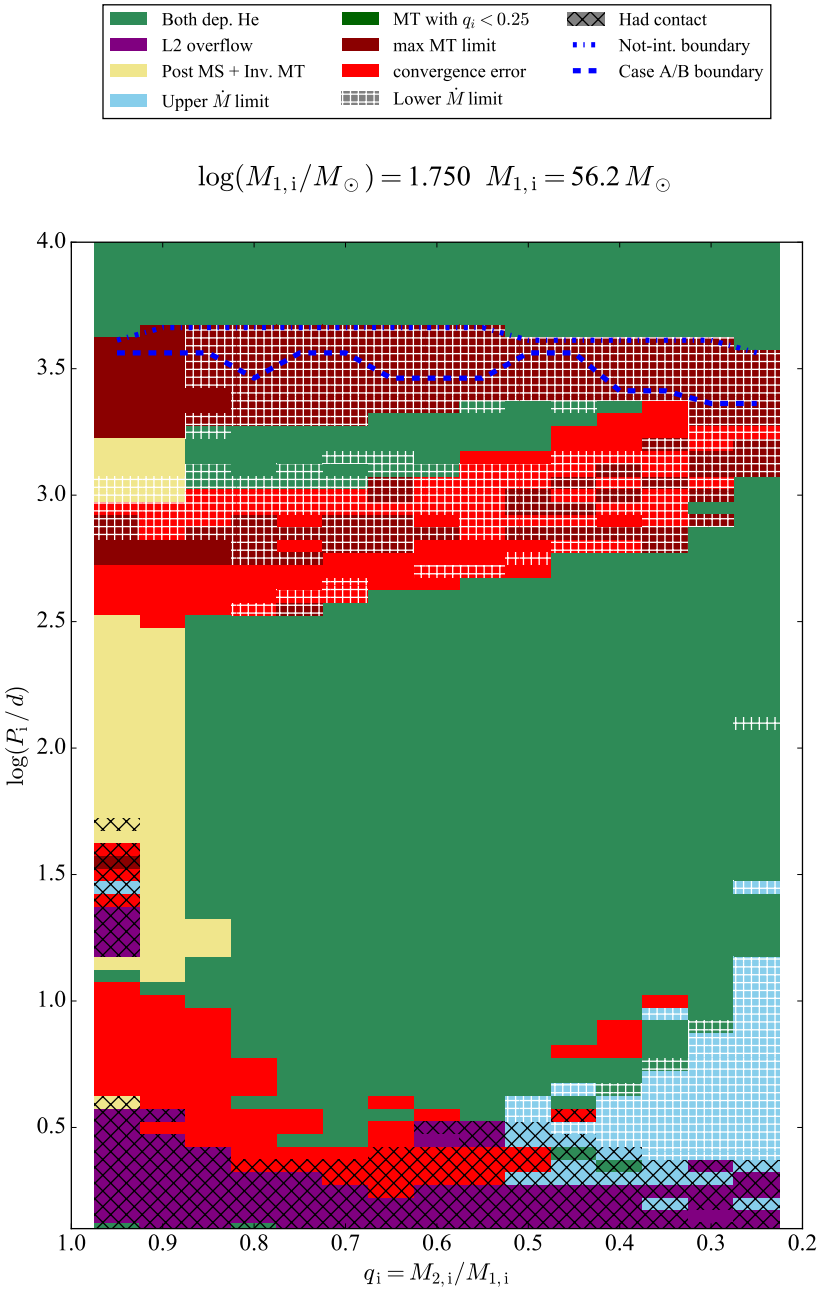

Figure C.3: Phase diagram of binary models with fixed initial donor mass of $M_{1,\mathrm{i}} = 56.2\,M_\odot$. The initial mass ratio q_i is plotted versus the initial orbital period P_i. All models are calculated at LMC metallicity. The different phases are indicated in the legend and a more detailed description can be found in Section 3.1.1.

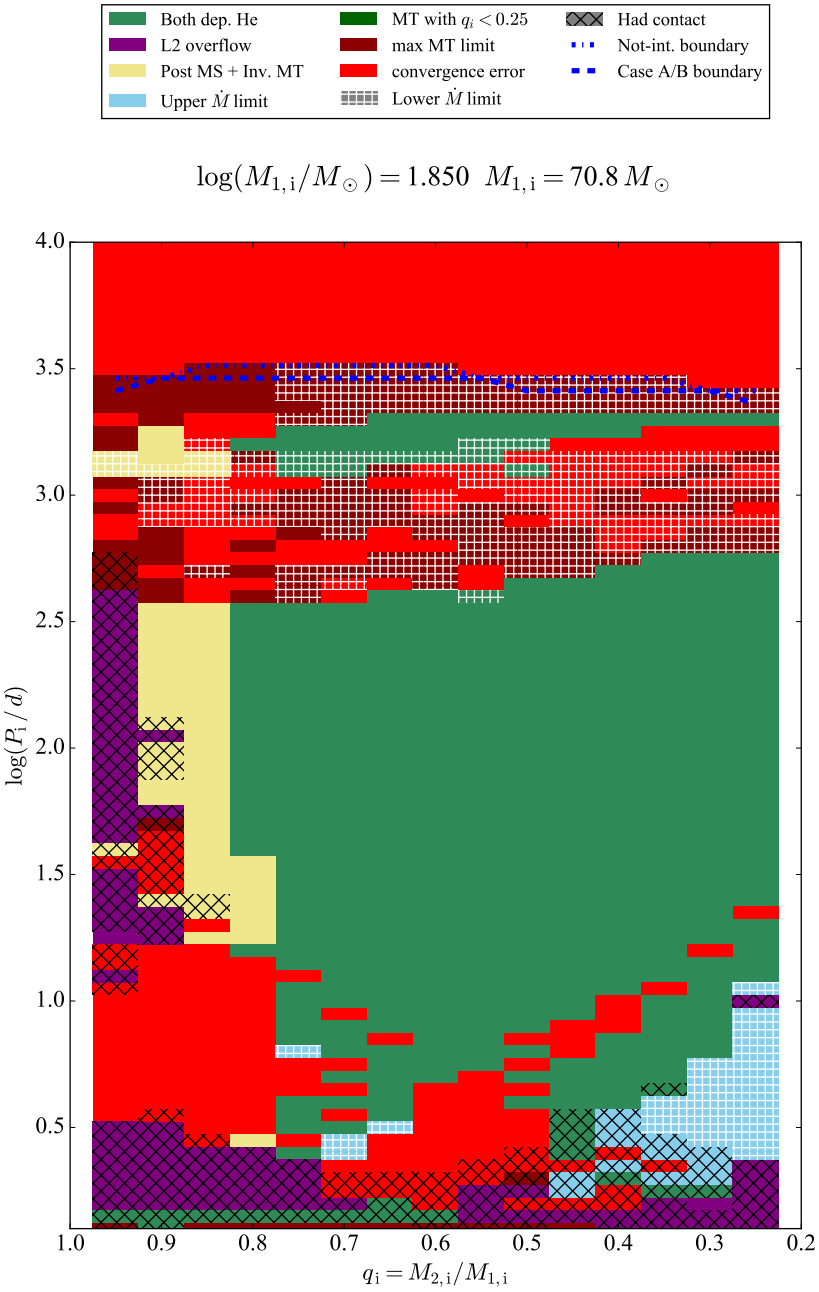

Figure C.4: Phase diagram of binary models with fixed initial donor mass of $M_{1,\mathrm{i}} = 70.8\,M_\odot$. The initial mass ratio q_i is plotted versus the initial orbital period P_i. All models are calculated at LMC metallicity. The different phases are indicated in the legend and a more detailed description can be found in Section 3.1.1.

D LMC Grid for WR stars

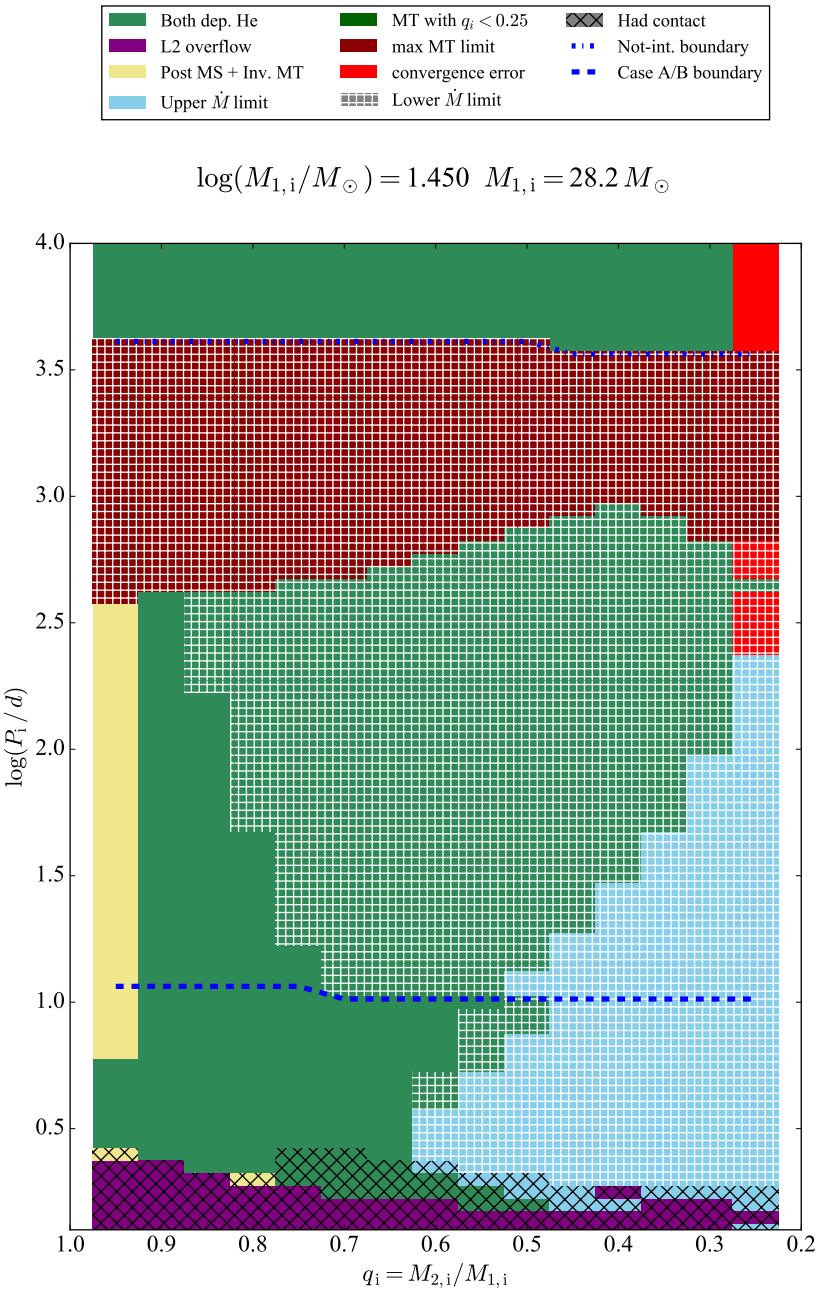

Figure D.1: Phase diagram of binary models with fixed initial donor mass of $M_{1,\mathrm{i}} = 28.2\,M_\odot$. The initial mass ratio q_i is plotted versus the initial orbital period P_i. All models are calculated at LMC metallicity. The different phases are indicated in the legend and a more detailed description can be found in Section 3.1.1.

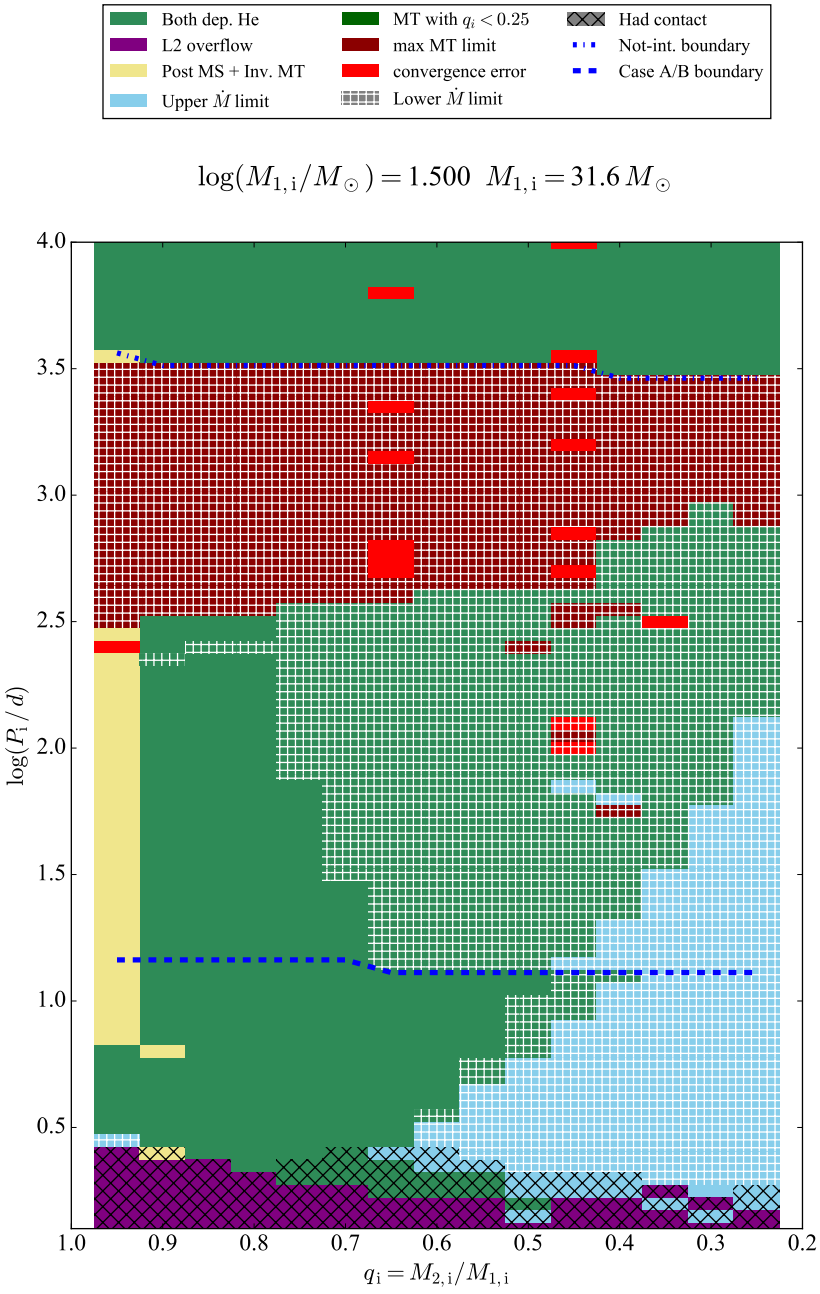

Figure D.2: Phase diagram of binary models with fixed initial donor mass of $M_{1,\mathrm{i}} = 31.6\,M_\odot$. The initial mass ratio q_i is plotted versus the initial orbital period P_i. All models are calculated at LMC metallicity. The different phases are indicated in the legend and a more detailed description can be found in Section 3.1.1.

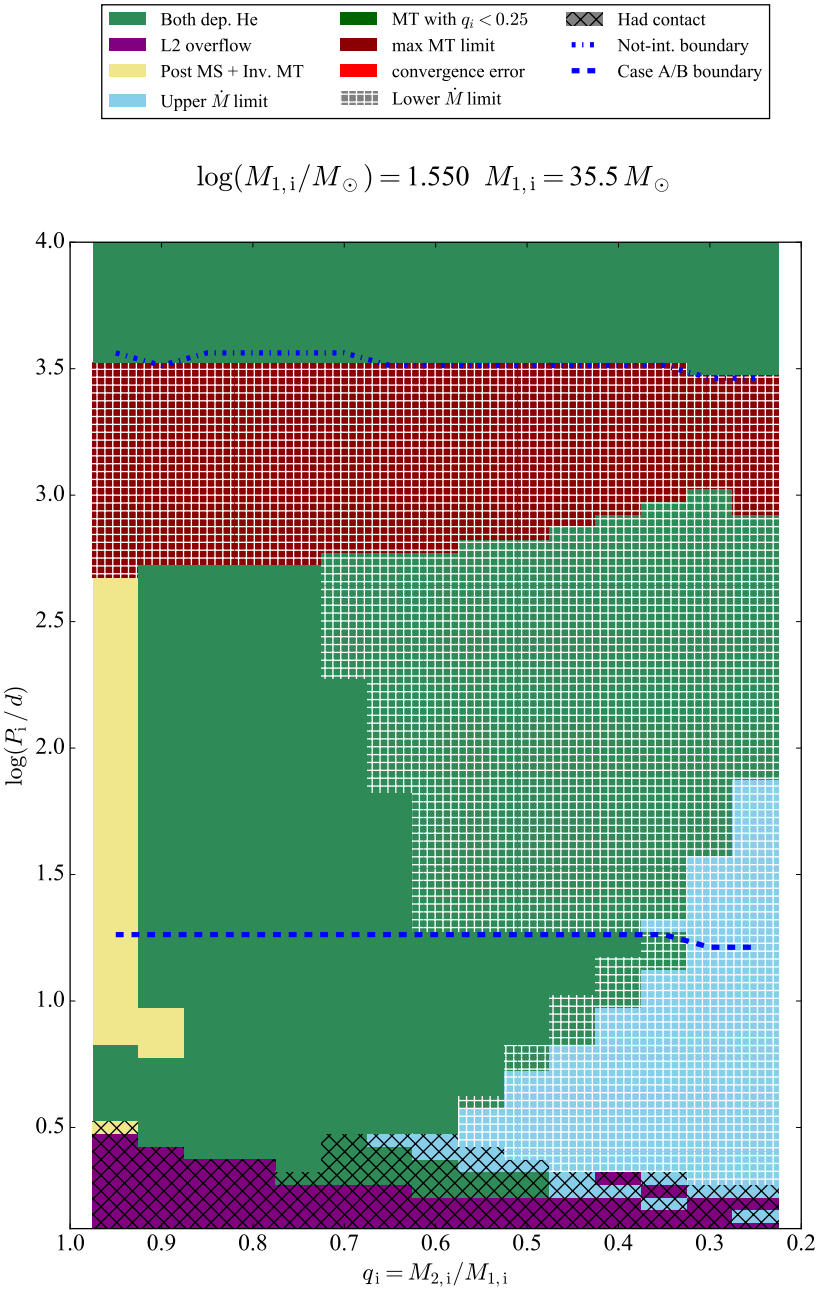

Figure D.3: Phase diagram of binary models with fixed initial donor mass of $M_{1,\mathrm{i}} = 35.5\,M_\odot$. The initial mass ratio q_i is plotted versus the initial orbital period P_i. All models are calculated at LMC metallicity. The different phases are indicated in the legend and a more detailed description can be found in Section 3.1.1.

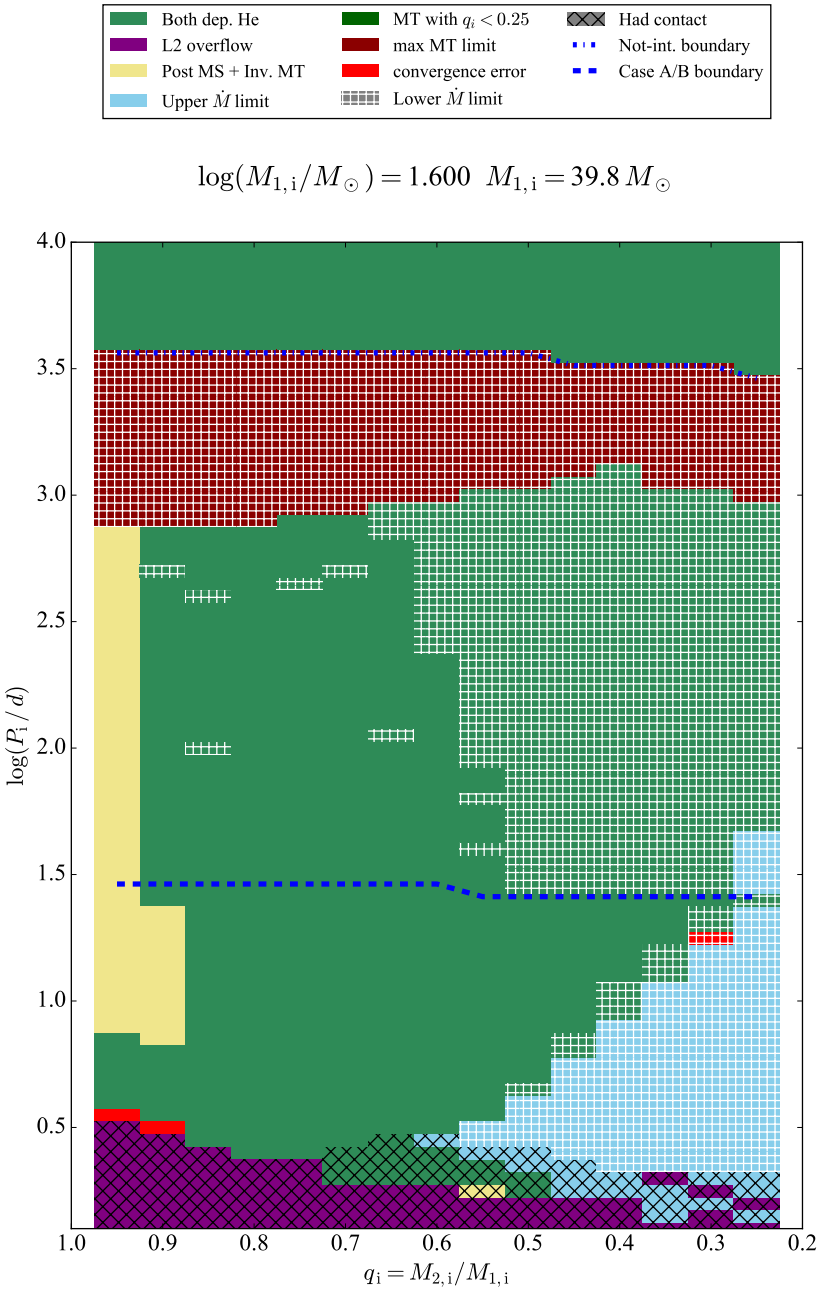

Figure D.4: Phase diagram of binary models with fixed initial donor mass of $M_{1,\mathrm{i}} = 39.8\,M_\odot$. The initial mass ratio q_i is plotted versus the initial orbital period P_i. All models are calculated at LMC metallicity. The different phases are indicated in the legend and a more detailed description can be found in Section 3.1.1.

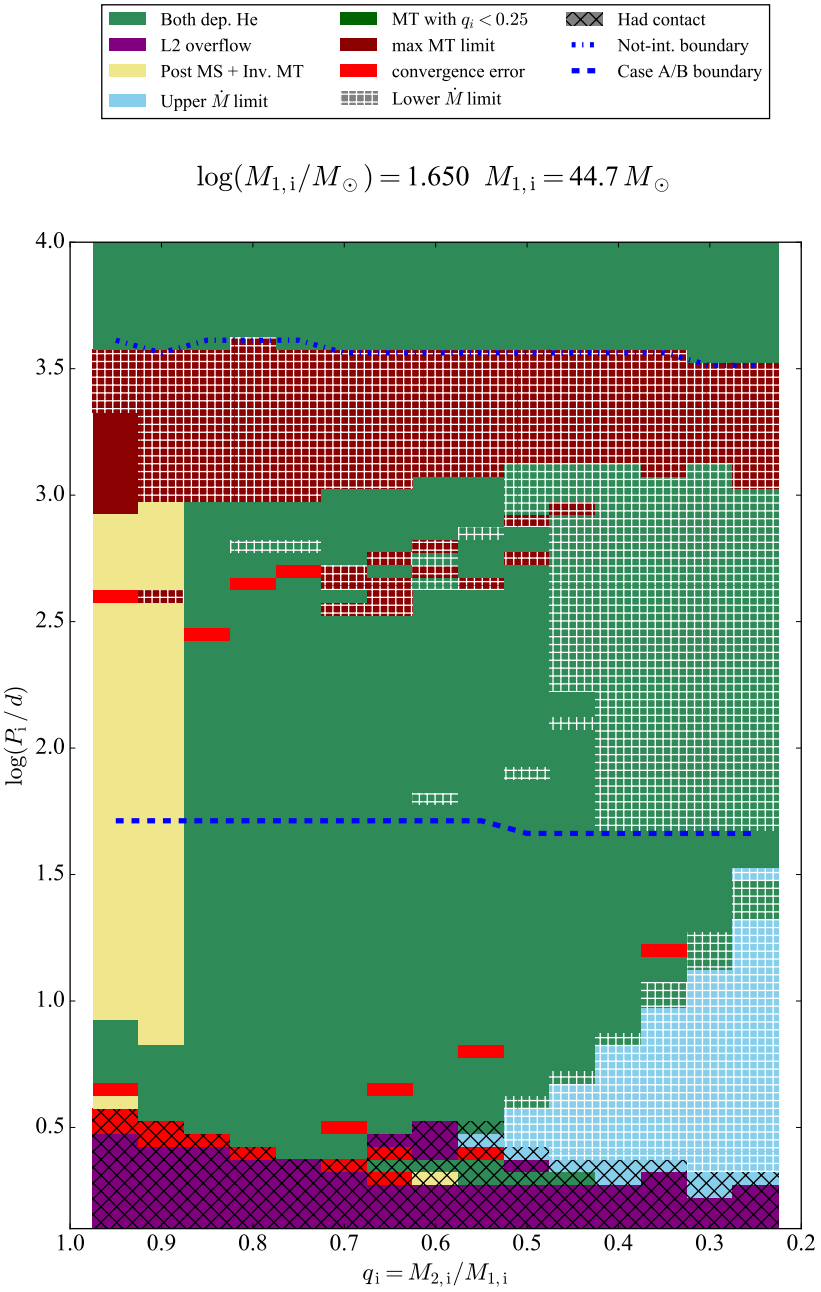

Figure D.5: Phase diagram of binary models with fixed initial donor mass of $M_{1,\mathrm{i}} = 44.7\,M_\odot$. The initial mass ratio q_i is plotted versus the initial orbital period P_i. All models are calculated at LMC metallicity. The different phases are indicated in the legend and a more detailed description can be found in Section 3.1.1.

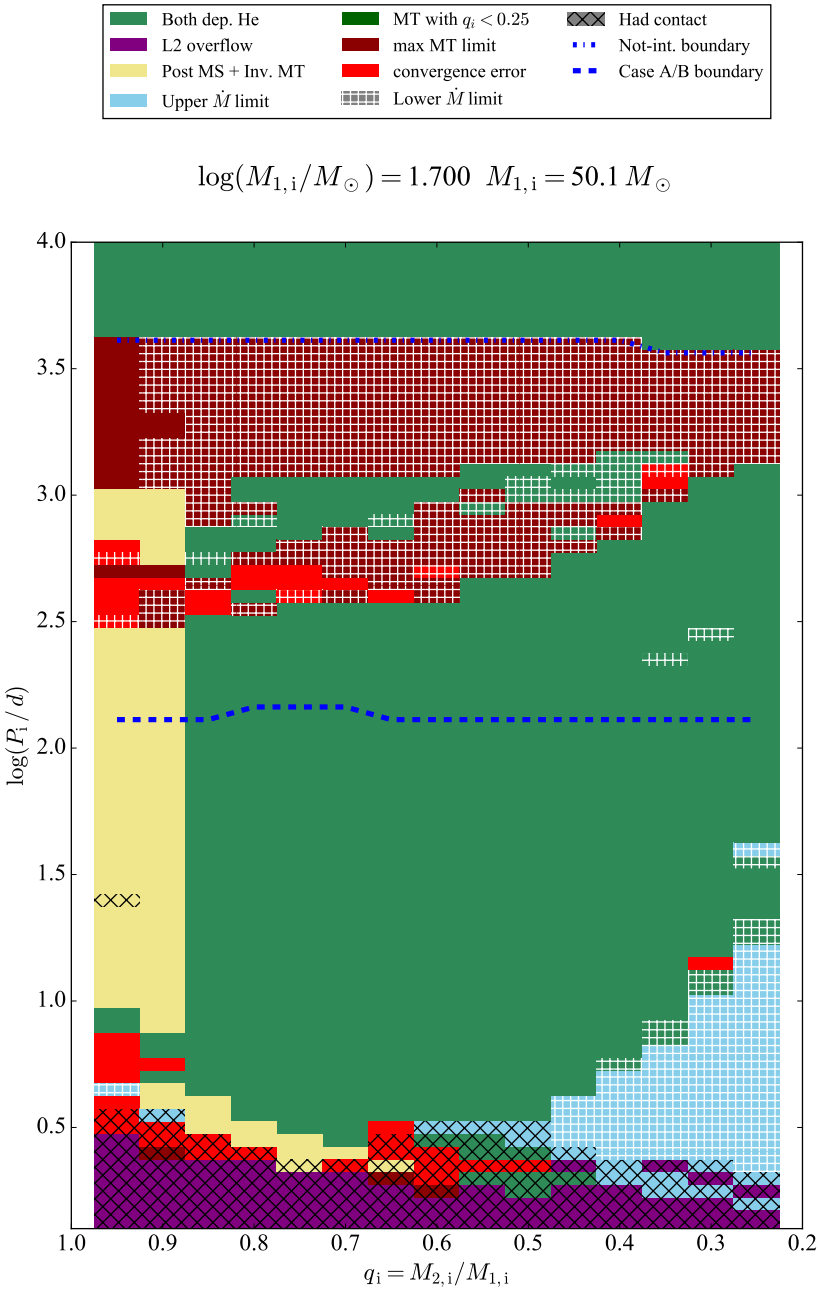

Figure D.6: Phase diagram of binary models with fixed initial donor mass of $M_{1,\mathrm{i}} = 50.1\,M_\odot$. The initial mass ratio q_i is plotted versus the initial orbital period P_i. All models are calculated at LMC metallicity. The different phases are indicated in the legend and a more detailed description can be found in Section 3.1.1.

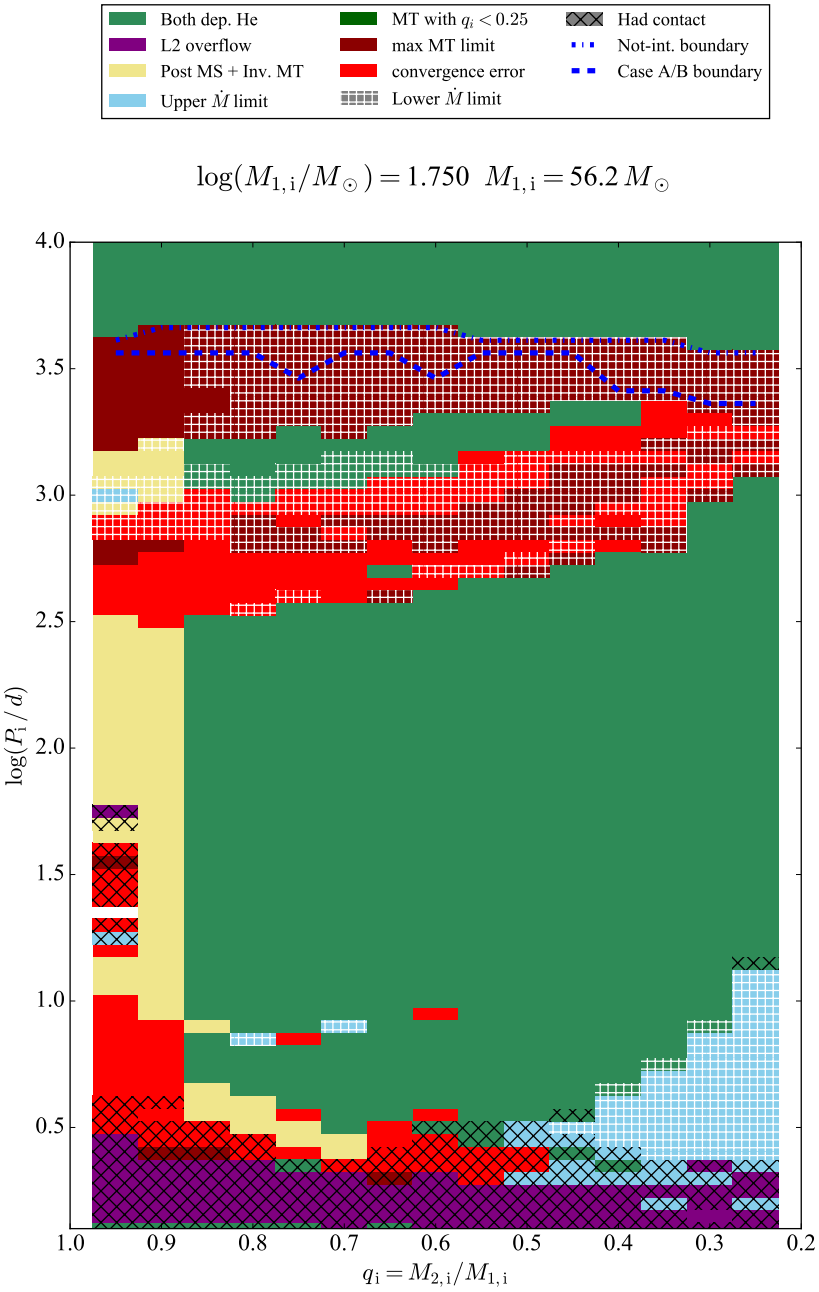

Figure D.7: Phase diagram of binary models with fixed initial donor mass of $M_{1,\mathrm{i}} = 56.2\,M_\odot$. The initial mass ratio q_i is plotted versus the initial orbital period P_i. All models are calculated at LMC metallicity. The different phases are indicated in the legend and a more detailed description can be found in Section 3.1.1.

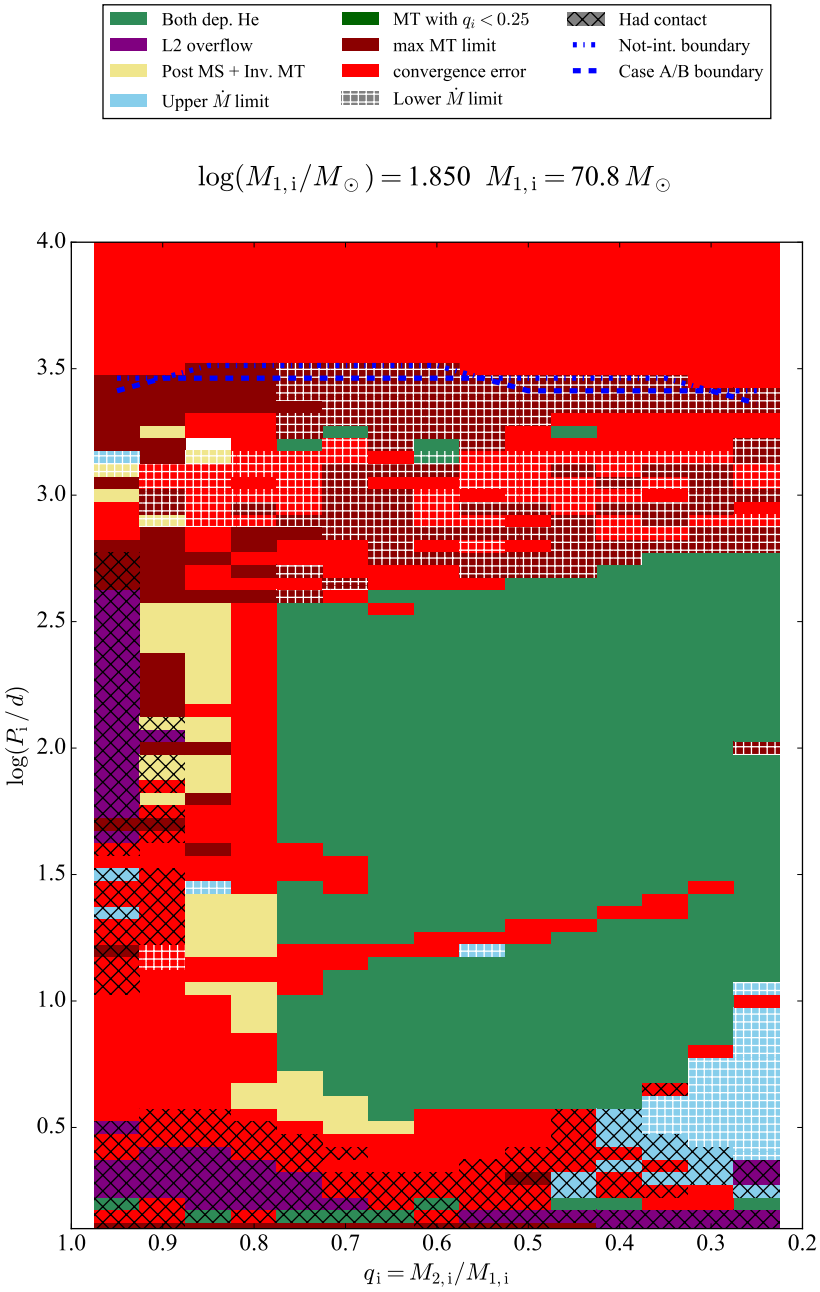

Figure D.8: Phase diagram of binary models with fixed initial donor mass of $M_{1,\mathrm{i}} = 70.8\,M_\odot$. The initial mass ratio q_i is plotted versus the initial orbital period P_i. All models are calculated at LMC metallicity. The different phases are indicated in the legend and a more detailed description can be found in Section 3.1.1.

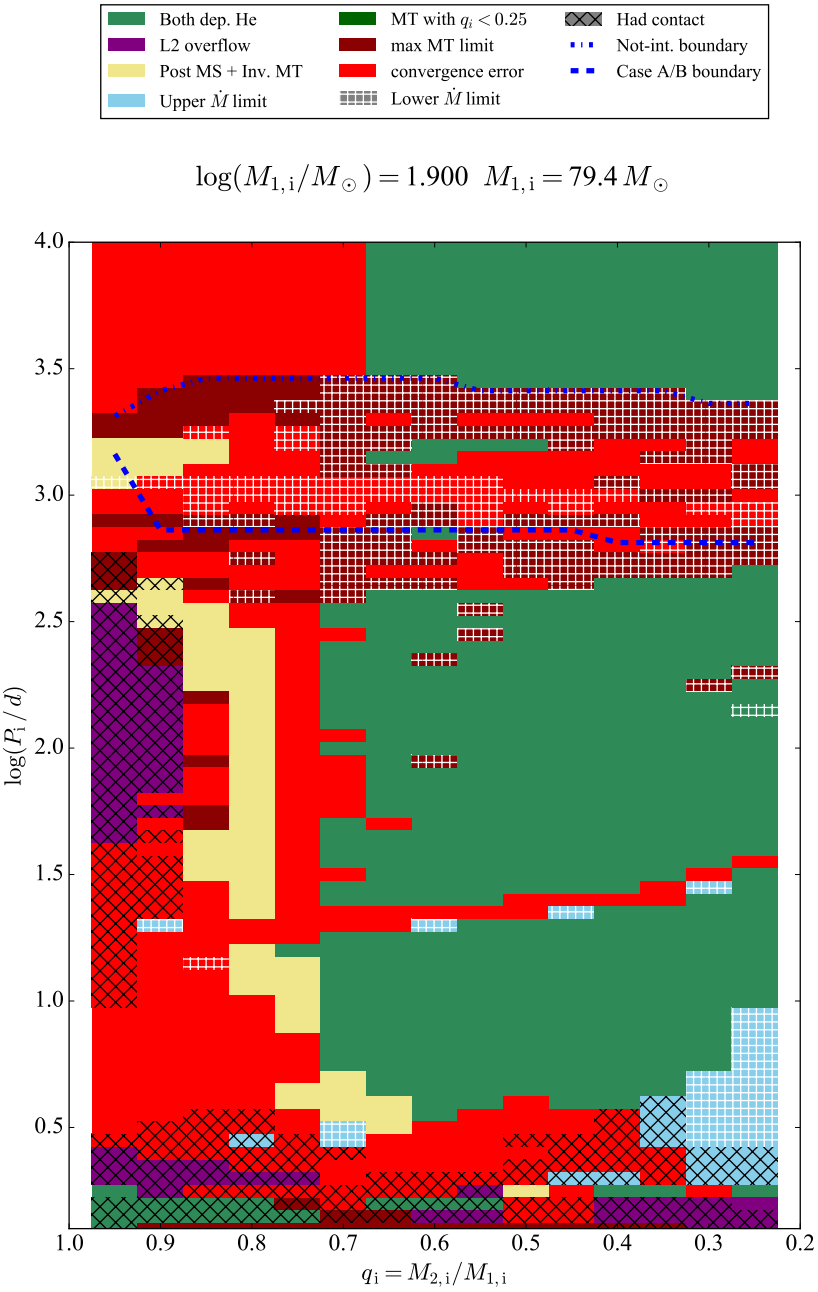

Figure D.9: Phase diagram of binary models with fixed initial donor mass of $M_{1,\mathrm{i}} = 79.4\,M_\odot$. The initial mass ratio q_i is plotted versus the initial orbital period P_i. All models are calculated at LMC metallicity. The different phases are indicated in the legend and a more detailed description can be found in Section 3.1.1.

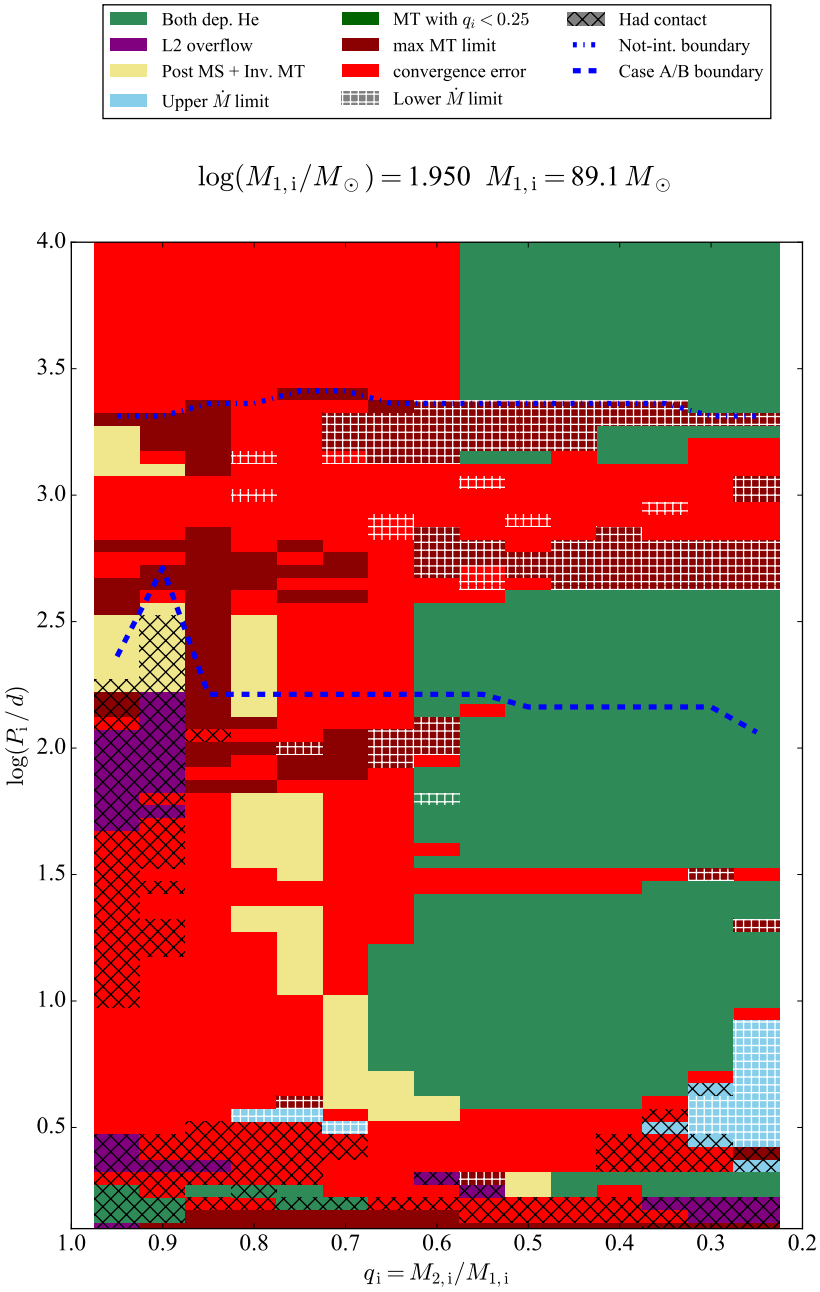

Figure D.10: Phase diagram of binary models with fixed initial donor mass of $M_{1,\mathrm{i}} = 89.1\,M_\odot$. The initial mass ratio q_i is plotted versus the initial orbital period P_i. All models are calculated at LMC metallicity. The different phases are indicated in the legend and a more detailed description can be found in Section 3.1.1.

E Tables with the Observed Data of WN and WC Stars in the LMC

Table 1: Parameters for WN stars in the LMC.

BAT99	spectral subtype[a]	$T_\star$[a] [kK]	$\log(L)$[a] [$L_\odot$]	X_H[a]	Binary?[a]	P[b] [d]	q[b] [M_2/M_{WR}]
1	WN3b	89	5.30	0.0	-	-	-
2	WN2b(h)	141	5.37	0.0	-	-	-
3	WN4b	79	5.51	0.0	-	-	-
5	WN2b	141	5.45	0.0	-	-	-
6	O3f*+O	56	6.45	0.2	x	2.00	-
7	WN4b	158	5.84	0.0	-	-	-
12	O2If*/WN5	50	5.80	0.5	x	3.24	-
13	WN10	28	5.56	0.4	-	-	-
14	WN4o(+OB)	67	5.86	0.0	?	-	-
15	WN4b	89	5.57	0.0	-	-	-
16	WN7h	50	5.80	0.3	-	-	-
17	WN4o	67	5.69	0.0	-	-	-
18	WN3(h)	71	5.63	0.2	-	-	-
19	WN4b+O5:	79	6.14	0.0	x[c]	17.99	1.79
21	WN4o(+OB)	67	6.30	0.0	?	-	-
22	WN9h	32	5.75	0.4	-	-	-
23	WN3(h)	71	5.55	0.0	-	-	-
24	WN4b	100	5.54	0.0	-	-	-
25	WN4ha	67	5.55	0.2	-	-	-
26	WN4b	71	5.62	0.0	-	-	-
27	WN5b(+B1Ia)	71	7.30	0.2	?	-	-
29	WN4b+OB	71	5.50	0.0	x	2.20	-
30	WN6h	47	5.65	0.3	-	-	-
31	WN4b	75	5.33	0.0	?	-	-
32	WN6(h)	47	5.94	0.2	x	1.90	0.98
33	Ofpe/WN9?	28	6.50	0.2	-	-	-
35	WN3(h)	71	5.60	0.1	-	-	-
36	WN4b/WCE+OB	79	5.71	0.0	?	-	-
37	WN3o	79	5.65	0.0	-	-	-
40	WN4(h)a	63	5.62	0.2	?[c]	-	-
41	WN4b	100	5.60	0.0	-	-	-
42	WN5b(h)(+B3I)	71	8.00	0.4	?[c]	-	-
43	WN4o+OB	67	5.85	0.0	x	2.82	-
44	WN8ha	45	5.66	0.4	-	-	-

[a] Values adopted from Hainich et al. (2014). [b] Values taken from Shenar et al. (2019). [c] Showing X-ray emission (see Hainich et al. (2014)).

Table 1 continued

BAT99	spectral subtype [a]	$T_\star$ [a] [kK]	$\log(L)$ [a] [$L_\odot$]	X_H [a]	Binary? [a]	P [b] [d]	q [b] [M_2/M_WR]
46	WN4o	63	5.44	0.0	-	-	-
47	WN3b	89	5.59	0.0	?[c]	-	-
48	WN4b	89	5.40	0.0	-	-	-
49	WN4:b+O8V	71	6.34	0.6	x	31.69	2.00
50	WN5h	56	5.65	0.4	-	-	-
51	WN3b	89	5.30	0.0	-	-	-
54	WN8ha	38	5.75	0.2	-	-	-
55	WN11h	28	5.77	0.4	-	-	-
56	WN4b	71	5.56	0.0	-	-	-
57	WN4b	79	5.40	0.0	-	-	-
58	WN7h	47	5.64	0.3	-	-	-
59	WN4b+O8:	71	6.45	0.0	?	2.20	-
60	WN4(h)a	63	5.78	0.2	-	-	-
62	WN3(h)	71	5.41	0.1	-	-	-
63	WN4ha:	63	5.58	0.4	-	-	-
64	WN4o+O9:	71	6.05	0.0	x	37.59	-
65	WN4o	67	5.75	0.0	-	-	-
66	WN3(h)	89	5.78	0.2	-	-	-
67	WN5ha	47	5.96	0.3	?[c]	-	-
68	O3.5If*/WN7	45	6.00	0.6	-	-	-
71	WN4+O8:	63	5.98	0.0	x	5.21	-
72	WN4h+O3:	71	5.80	0.4	?	-	-
73	WN5ha	60	5.72	0.4	-	-	-
74	WN3(h)a	79	5.69	0.2	-	-	-
75	WN4o	71	5.56	0.0	-	-	-
76	WN9ha	35	5.66	0.2	-	-	-
77	WN7ha	45	6.79	0.7	x[c]	3.00	1.66
78	WN6(+O8V)	71	5.70	0.2	?[c]	-	-
79	WN7ha+OB	42	6.17	0.2	?[c]	-	-
80	WN5h:a	45	6.40	0.2	?[c]	-	-
81	WN5h	47	5.48	0.4	-	-	-
82	WN3b	100	5.53	0.0	?[c]	-	-
86	WN3(h)	71	5.33	0.0	-	-	-
88	WN4b/WCE	112	5.80	0.0	-	-	-
89	WN7h	50	5.78	0.2	-	-	-
91	WN6(h)	50	5.42	0.2	-	-	-
92	WN3:b(+O)+B1Ia	45	6.95	0.2	x[c]	4.31	-
93	O3If*	45	5.90	0.6	?[c]	-	-
94	WN4b	141	5.80	0.0	-	-	-

[a] Values adopted from Hainich et al. (2014). [b] Values taken from Shenar et al. (2019). [c] Showing X-ray emission (see Hainich et al. (2014)).

Table 1 continued

BAT99	spectral subtype [a]	$T_\star$ [a] [kK]	$\log(L)$ [a] [$L_\odot$]	X_H [a]	Binary? [a]	P [b] [d]	q [b] [M_2/M_WR]
95	WN7h+OB	50	6.00	0.2	x	2.11	2.20
96	WN8	42	6.35	0.2	-	-	-
97	O3.5If*/WN7	45	6.30	0.6	-	-	-
98	WN6	45	6.70	0.6	-	-	-
99	O2.5If*/WN6	45	5.90	0.2	x[c]	92.6	-
100	WN7	47	6.15	0.2	?[c]	-	-
102	WN6	45	6.80	0.4	?[c]	-	-
103	WN5(h)+O	47	6.25	0.4	x[c]	2.75	1.94
104	O2If*/WN5	63	6.06	0.4	-	-	-
105	O2If*	50	6.40	0.6	?[c]	-	-
106	WN5h	56	6.51	0.4	-	-	-
107	O6.5Iafc+O6Iaf	35	6.31	0.4	x[c]	153.89	0.81
108	WN5h	56	6.87	0.4	-	-	-
109	WN5h	56	6.69	0.4	-	-	-
110	O2If*	50	6.22	0.7	-	-	-
111	WN9ha	45	6.25	0.7	?[c]	-	-
112	WN5h	56	6.48	0.2	?[c]	8.2	-
113	O2If*/WN5	50	6.09	0.2	x[c]	4.70	0.32
114	O2If*/WN5	63	6.44	0.4	?[c]	-	-
116	WN5h:a	63	7.05	0.4	?[c]	154.55	0.92
117	WN5ha	63	6.40	0.4	-	-	-
118	WN6h	47	6.66	0.2	x[c]	-	-
119	WN6h+?	47	6.57	0.2	x[c]	158.76	1.01
120	WN9h	32	5.58	0.3	-	-	-
122	WN5h	50	6.23	0.2	-	-	-
124	WN4	63	5.45	0.0	-	-	-
126	WN4b+O8:	71	6.44	0.0	?[c]	25.5	-
128	WN3b	112	5.44	0.0	-	-	-
129	WN3(h)a+O5V	79	6.20	0.2	x	2.77	1.64
130	WN11h	28	5.68	0.4	-	-	-
131	WN4b	71	5.67	0.0	-	-	-
132	WN4b(h)	79	5.58	0.0	-	-	-
133	WN11h	28	5.69	0.4	-	-	-
134	WN4b	79	5.51	0.0	-	-	-

[a] Values adopted from Hainich et al. (2014). [b] Values taken from Shenar et al. (2019). [c] Showing X-ray emission (see Hainich et al. (2014)).

Table 2: Parameters for WC stars in the LMC.

BAT99	spectral subtype [a]	M_V [a] [mag]	$\log(L)$ [$L_\odot$]	$\log(L_{lit})$ [$L_\odot$]	Binary? [a]	P [b] [d]
9	WC4	-4.4	5.49	5.44 [c]	-	-
8	WC4	-4.2	5.41	5.42 [c]	-	-
10	WC4(+O9.5II:)	-5.1	5.77	-	x	-
11	WC4	-5.5	5.93	5.70 [c]	-	-
20	WC4+O	-4.6	5.57	-	-	-
28	WC6+O5-6V-III(+O)	-6.5	6.33	-	x	14.926
34	WC4+OB	-5.8	6.05	-	?	-
38	WC4(+O8I:)	-7.2	6.61	-	x	3.0328
39	WC4+O6V-III(+O)	-6.1	6.17	-	x	1.9169
52	WC4	-4.5	5.53	5.65 [c]	-	-
53	WC4(+OB)	-5.4	5.89	5.35 [d]	x	-
61	WC4	-5.0	5.73	5.68 [c]	-	-
70	WC4(+OB)	-5.3	5.85	-	x	-
85	WC4(+OB)	-7.7	6.81	-	x	-
84	WC4(+OB)	-5.4	5.89	-	x	-
87	WC4+OB	-4.8	5.65	-	?	-
90	WC4	-4.6	5.57	5.44 [c]	-	-
115	WC4(+OB)	-5.7	6.01	-	x	-
101	WC4(+WN6+O)	-7.5	6.73	-	x	-
121	WC4	-4.7	5.61	-	-	-
125	WC4(+OB)	-5.6	5.97	-	x	-
127	WC4(+O)	-6.2	6.21	-	x	-

[a] Values adopted from Bartzakos et al. (2001a). [b] Values taken from Bartzakos et al. (2001b).
[c]Calculated by Gräfener et al. (2013). [d] Calculated by Ramachandran et al. (2018).

List of Figures

List of Tables